Pore Water Pressure Response of a Soil

Subjected to Traffic Loading under Saturated and Unsaturated Conditions

by

Carlos Cary

A Dissertation Presented in Partial Fulfillment
of the Requirements for the Degree
Doctor of Philosophy

Approved November 2011 by the
Graduate Supervisory Committee:

Claudia Zapata, Co-Chair
Matthew Witczak, Co-Chair
Kamil Kaloush
Sandra Houston

ARIZONA STATE UNIVERSITY

December 2011

ABSTRACT

This study presents the results of one of the first attempts to characterize the pore water pressure response of soils subjected to traffic loading under saturated and unsaturated conditions. It is widely known that pore water pressure develops within the soil pores as a response to external stimulus. Also, it has been recognized that the development of pores water pressure contributes to the degradation of the resilient modulus of unbound materials. In the last decades several efforts have been directed to model the effect of air and water pore pressures upon resilient modulus. However, none of them consider dynamic variations in pressures but rather are based on equilibrium values corresponding to initial conditions. The measurement of this response is challenging especially in soils under unsaturated conditions. Models are needed not only to overcome testing limitations but also to understand the dynamic behavior of internal pore pressures that under critical conditions may even lead to failure. A testing program was conducted to characterize the pore water pressure response of a low plasticity fine clayey sand subjected to dynamic loading. The bulk stress, initial matric suction and dwelling time parameters were controlled and their effects were analyzed. The results were used to attempt models capable of predicting the accumulated excess pore pressure at any given time during the traffic loading and unloading phases. Important findings regarding the influence of the controlled variables challenge common beliefs. The accumulated excess pore water pressure was found to be higher for unsaturated soil specimens than for saturated soil specimens. The maximum pore water pressure always increased when the high

bulk stress level was applied. Higher dwelling time was found to decelerate the accumulation of pore water pressure. In addition, it was found that the higher the dwelling time, the lower the maximum pore water pressure. It was concluded that upon further research, the proposed models may become a powerful tool not only to overcome testing limitations but also to enhance current design practices and to prevent soil failure due to excessive development of pore water pressure.

DEDICATION

This work is dedicated to my beloved mother Zulma,

my grandparents Elva and Ernesto,

and all my family in Peru.

ACKNOWLEDGMENTS

I would like to thank Dr. Claudia Zapata for her continuous support and guidance throughout this long journey.

I would also like to thank Dr. Matthew Witczak for the invaluable help offered in this research effort.

I would like to express my gratitude to Dr. Sandra Houston and Dr. Kamil Kaloush for all the knowledge shared during these years and for their important contribution to my formation as graduate student.

Last, I would like to thank my aunt Lia Ricalde for showing me the way to success.

TABLE OF CONTENTS

CHAPTER Page

CHAPTER Page

CHAPTER Page

CHAPTER Page

APPENDIX Page

LIST OF TABLES

Table Page

LIST OF FIGURES

Figure Page

Figure Page

Figure Page

Figure Page

Figure Page

CHAPTER 1. INTRODUCTION

Overview

The evaluation of the response of plastic soils subjected to dynamic loading is fundamental for the design of pavements. The Resilient Modulus (M_R) used for characterization of unbound materials has been found to be affected by the increase of pore water pressure under dynamic loading. Among the variety of unbound materials used by the engineering community for roads construction, materials with plastic components are the ones that have more potential for high excess pore pressure development. Commonly, the natural subgrade soil used as foundation of pavement systems is found to be a material with some to high degree of plasticity. Therefore, degradation of the pavement stiffness due to buildup of pore water pressure is expected under traffic loading.

Even though some methodologies to assess the impact of environmental changes upon the resilient response of unbound materials have been developed, the models currently used for the prediction of M_R consider moisture content variations as the main driver of the change in the response instead of a more fundamental stress state variable. Some authors have proposed models that introduce matric suction as a fundamental stress state variable to explain the effects of moisture variations in the M_R. However, most of these models neglect the effect that pore water pressure buildup under the traffic loading might have upon the stiffness of the material.

In 2008, Cary developed a predictive model for the M_R of unbound materials which not only incorporates matric suction stress to account for the effect of moisture variations but also accounts for dynamic changes in pore pressures due to traffic loading (*1*). However, given that measuring negative pore water pressures and its variation under applied dynamic load is still a challenging task, the capability of measuring the M_R for unsaturated materials is very limited at this time. Even though such test capabilities are available, the characterization of unbound materials when unsaturated and under dynamic loading condition is not quite ready to be implemented by partitioning engineers. It is believed that if our understanding of the behavior of these materials increases, the implementation of models such as the full stress state model proposed by the author in 2008 would be widely accepted among the pavement engineering community.

An alternative way to overcome testing limitations is by developing models capable of predicting pore water pressure variations during the M_R test. Such models may provide a shortcut for more accurate M_R predictions when pore water pressure variation measurements are either highly challenging or not possible at all.

A predicting model will not substitute laboratory measurements by any means but will be useful to obtain reliable estimates of pore water pressure variations due to traffic loading; and very important, it would be used to predict the M_R at any time during the service life of the pavement structure. In this way, the influence of varying pore water pressures or suction for unsaturated conditions

can be incorporated when estimating the cumulative damage of the pavement structure. As a consequence modeling of the development of pore water pressure under traffic loading will contribute to optimize the design of pavements.

Under dynamic loading, some soils develop higher excess pore pressures than others. It is well known that soil gradation and porosity determine the hydraulic conductivity of the material. Materials are more prone to excess pore pressure development as their plasticity increases. Therefore, plastic soils become materials of particular interest for this study. Not only properties inherent of the material type should be considered as potential variables for pore water pressure buildup modeling but also other parameters related to the loading pattern and the stress state.

Among others, the following parameters should be considered of particular interest for evaluation as predictive variables: hydraulic conductivity, deviator stress, confining stress, matric suction, loading time and dwelling time.

In this study, an exploratory testing program was conducted to characterize the pore water pressure response of a low plasticity coarse grained soil subjected to dynamic loading. Some of the previously mentioned parameters were evaluated as potential predictive variables. The effect that the selected parameters have upon the response of the material is investigated and an attempt to describe the dynamic response of the material by mathematical models is presented. This preliminary study is aimed at providing basic understanding of the role that both externally applied dynamic loading and matric suction stress play on the change of pore water pressure of subgrade materials under pavement

systems. Results will hopefully constitute the basis for future efforts aimed at the development of predictive models that describe the material resilient modulus response to stresses generated by dynamic loading under saturated and unsaturated soil conditions. Being able to fully understand the development of pore water pressure buildup within the soil structure due to dynamic loading will definitely enhance the characterization of unbound materials and hence, improve the currently available pavement design procedures.

Objectives

The objectives of this dissertation are aimed at answering the following questions:

1) What is the relative importance of matric suction and externally applied loads on the buildup of pore water pressure in plastic materials subjected to dynamic loading?

2) How important is the dwelling time (time between applied loads) in the buildup/dissipation of pore water pressures of saturated and unsaturated soils subjected to dynamic loading? Can it be related to vehicle speed or daily traffic?

3) Is it possible to find a model capable of predicting the buildup/dissipation of pore water pressures that is suitable to saturated and unsaturated soil conditions?

4) How important is the buildup of pore water pressure on the resilient modulus when the material is saturated or unsaturated?

5) Does the buildup of pore water pressure indicate changes in the stiffness of the material?

In order to answering the posted questions, the following objectives were pursued:

- Obtain measurements of pore water pressure buildup under repeated load for a low plasticity soil under both saturated and unsaturated conditions (two levels of suction) and at different levels of deviator stress and dwelling times.
- Find suitable mathematical models for the prediction of dynamic pore water pressure buildup considering the variables controlled in the laboratory testing program.
- Assess the importance of the pore water pressure buildup/dissipation on the resilient modulus of unsaturated soils subjected to dynamic loading conditions.
- Assess the importance of the pore water pressure buildup as indicator of changes in the stiffness of the material.

Relevant conclusions will define the basis for future research efforts aimed not only at the improvement of existing models but also at the faster implementation of unsaturated soil mechanics and principles into the design of pavement engineering practice.

Organization

The present study documents an investigation leading to the understanding of the pore water pressure buildup behavior for low plasticity soils under repeated traffic loading conditions. Following this introduction, Chapter 2 presents background information covering the basic concepts necessary to understand how the pore

water pressure generated under traffic load affects the resilient behavior of unbound materials and hence the performance of pavement systems. Prior research efforts that focused on understanding the influence of pore water pressure buildup upon the stiffness degradation of unbound materials are presented. Different approaches and interpretations by several authors of how certain variables may determine the magnitude of the excess pore pressure developed are commented as well. Finally some attempts to modeling the pore water pressure buildup are covered in this chapter.

Chapter 3 provides details about material handling and covers the first stage of the laboratory testing program which comprises both the preliminary routine soil classification tests and the special testing performed for unsaturated soils. The methodology followed as well as the testing results are presented.

Details regarding the triaxial systems utilized for the dynamic load testing on both saturated and unsaturated specimens are presented in Chapter 4. Besides the description of the triaxial systems, several enhancements done to the systems in order to successfully run the tests under the desired conditions are commented. Chapter 4 also presents a discussion about the conditions of the triaxial tests performed and provides details of the procedure followed to obtain the results presented in Chapter 5.

In Chapter 5, the dynamic load testing program is presented. Then, detailed information about specimen preparation and the different stages of the triaxial test is provided. At the end of this chapter, the results obtained from the dynamic load testing are presented.

Chapter 6 presents the analysis performed on the results from the dynamic load testing program. Remarkable findings including proposed mathematical models as well as the influence of the different variables evaluated in this study are discussed.

The most important findings are summarized and relevant conclusions of the overall study are provided in Chapter 7. Finally, recommendations for future research efforts are provided in Chapter 8.

CHAPTER 2. LITERATURE REVIEW

This chapter presents a brief summary of the currently available resilient modulus M_R predictive techniques, followed by a discussion on how the implementation of a model for prediction of pore water pressure buildup becomes an alternative way for overcoming testing limitations particularly encountered when dealing with unsaturated soils. The fundamental factors that govern the pore water pressure buildup within the soil structure are presented. This literature review also incorporates the few attempts completed to date, for modeling pore water pressure buildup in plastic soils subjected to dynamic loading.

Resilient Modulus (M_R)

Hveem stated in the late 40's the importance of pavement fatigue failures caused by resilience in the supporting soils (*2*). Hveem suggested that a comprehensive pavement design procedure must provide a structure that will either be capable of surviving the fatigue resulting from continuous flexing or have sufficient stiffness to reduce the flexing to an acceptable value. Hveem found the resilience of soils to be one of the driving factors for the development of fatigue cracking on the pavement surface (*3*). The concept of resilient modulus (M_R) was conceived by Seed et al. as the ratio of applied dynamic deviatoric stress σ_d, to the resilient (recovered) strain component ε_r under a transient dynamic pulse load (*4*). Analysis of actual field data showed that the elastic pavement deflection (measured with a Benkelman beam, La Croix deflectometer and/or California deflectometer) provided a better correlation to field performance than the total

pavement deflection (*5*). Therefore the pavement community accepted the resilient modulus value proposed by Seed et al. as a good indicator of the soil response to traffic load. Further detailed information about the history of the resilient modulus can be found in the research study presented by Cary in 2008 (*1*).

The literature reveals that the M_R has been traditionally modeled by following a total stress approach in which externally applied stresses are taken into account but internal stresses such as matric suction and positive pore water pressures are neglected. Among the models based on total stresses, a modification of the widely known "Universal Model" proposed by Witczak and Uzan in 1988 has been incorporated for the prediction of the M_R in the AASHTO Mechanistic Empirical Pavement Design Guide (MEPDG) (*6 , 7*). Nowadays, the modified version of the Universal Model constitutes perhaps the most widely accepted predictive model, which is expressed as follows:

$$M_R = k_1 \cdot p_a \cdot \left(\frac{\theta}{p_a} \right)^{k_2} \cdot \left(\frac{\tau_{oct}}{p_a} + 1 \right)^{k_3} \qquad (2\text{-}1)$$

Where,

p_a = atmospheric pressure

k_1, k_2, k_3 = regression constants

θ = bulk stress

τ_{oct} = octahedral shear stress

In Equation 2-1, the state of stress is described in terms of total stresses through the use of two stress invariants: the bulk stress (θ) or total volumetric component,

and the octahedral shear stress (τ_{oct}) or total deviator component. The bulk stress is defined as:

$$\theta = \sigma_1 + \sigma_2 + \sigma_3 \tag{2-2}$$

Where σ_1, σ_2 and σ_3 are the major, intermediate and minor principal stresses, respectively. The octahedral shear stress can be obtained from:

$$\tau_{oct} = \frac{1}{3} \cdot \sqrt{(\sigma_1 - \sigma_2)^2 + (\sigma_1 - \sigma_3)^2 + (\sigma_2 - \sigma_3)^2} \tag{2-3}$$

For triaxial conditions, the intermediate and the minor principal stresses have the same magnitude ($\sigma_2 = \sigma_3$) and therefore, the expressions can be reduced to:

$$\theta = \sigma_1 + 2\sigma_3, \tag{2-4}$$

and,

$$\tau_{oct} = \frac{\sqrt{2}}{3} \cdot (\sigma_1 - \sigma_3) \tag{2-5}$$

Different from unsaturated soils, the mechanical behavior of saturated soils can be expressed by using a stress state variable (conformed by two independent stresses) called the effective stress:

$$\sigma' = \sigma - u_w \tag{2-6}$$

Where,

σ' = effective normal stress

σ = total normal stress

u_w = pore-water pressure

The mechanical behavior of unsaturated soils is expressed by using one additional independent stress representing the air phase; this is, the pore air

pressure. In 1977, Fredlund and Morgenstern postulated that there are three possible normal stress variables that can be used to define the stress state in unsaturated soils: the net normal stress, the effective stress and the matric suction (*8*). Two out of those three mentioned stress state variables, which define the unsaturated soils behavior, were proposed by Fredlund and Fredlund and Rahardjo as commonly used in the formulation of unsaturated soil problems (*9, 10*). Furthermore, Fredlund et al. proposed that the resilient modulus could be expressed as a function of three stress state variables for the case of triaxial loading (*10, 11*):

$$M_R = f[(\sigma_3 - u_a), (u_a - u_w), (\sigma_1 - \sigma_3)] \quad (2\text{-}7)$$

Where,

$(\sigma_1 - \sigma_3)$ = deviator stress

$(\sigma_3 - u_a)$ = net normal stress

$(u_a - u_w)$ = matric suction

u_a = pore air pressure

u_w = pore water pressure

Note that different from the total stress approach used by Witczak and Uzan to develop the Universal Model, the approaches for both saturated and unsaturated soils represented by equations 2-6 and 2-7 are characterized for the presence of new fundamental stress state variables as shown in Figure 2-1. These variables are the pore water pressure (u_w) and the pore air pressure (u_a). The pore water pressure ranges from negative to positive values depending on whether the soil condition is unsaturated or saturated respectively. The pore air pressure (u_a) is

equal to zero under field conditions but can be manipulated to positive values under laboratory controlled conditions, as discussed in the following sections.

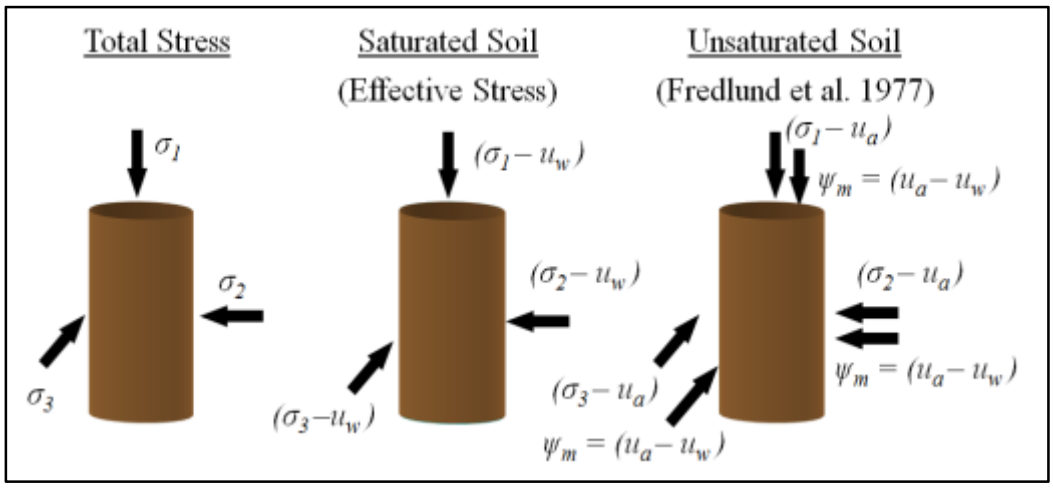

FIGURE 2-1 Different approaches to define the soil stress state

Several attempts have been made to incorporate the effect of moisture changes due to environmental conditions upon the resilient response of unbound materials. Some of these attempts make use of an environmental factor that accounts for the contribution of moisture changes (*12, 13*), independently of the contribution of externally applied loads. The predictive model adopted by the MEPDG to estimate the effect of moisture variations upon the resilient response of unbound materials can be included within this category. The model is expressed as follows:

$$M_R = 10^{a+\frac{b-a}{1+EXP\left(\beta+k_S\cdot\left(S-S_{opt}\right)\right)}} \cdot k_1 \cdot p_a \cdot \left(\frac{\theta}{p_a}\right)^{k_2} \cdot \left(\frac{\tau_{oct}}{p_a}+1\right)^{k_3} \quad (2\text{-}8)$$

Where,

S = degree of saturation,

S_{opt} = degree of saturation at optimum conditions,

θ = bulk stress,

τ_{oct} = octahedral stress,

p_a = atmospheric pressure,

k_1, k_2, k_3, a, b, k_s = fitting parameters,

$\beta = ln(-b/a)$ = location parameter

Note that the model shown above lacks of an independent term accounting for changes in pore water pressure resulting from the application of dynamic loading and rather, the change in pore water pressure is implicitly taken into account by the stress invariants.

Following a different approach; Fredlund et al., Yang et al., Liang et al. and Parreira and Goncalves tried to incorporate matric suction as a fundamental stress state variable (*11, 14, 15 and 16*). However, these attempts did not give light to the relative importance of matric suction effect when compared to the externally applied load.

It should be noted that any increase in pore water pressure leads to either a decrease in the effective stress when the soil is saturated or a decrease of matric soil suction when the soil is unsaturated. In both cases the stiffness degradation of soils will occur as the repeated loading is continuously applied. Figure 2-2 shows how initial matric suction drops, due to the buildup of pore water pressure, for a granular base material subjected to dynamic loading under undrained conditions (*17*).

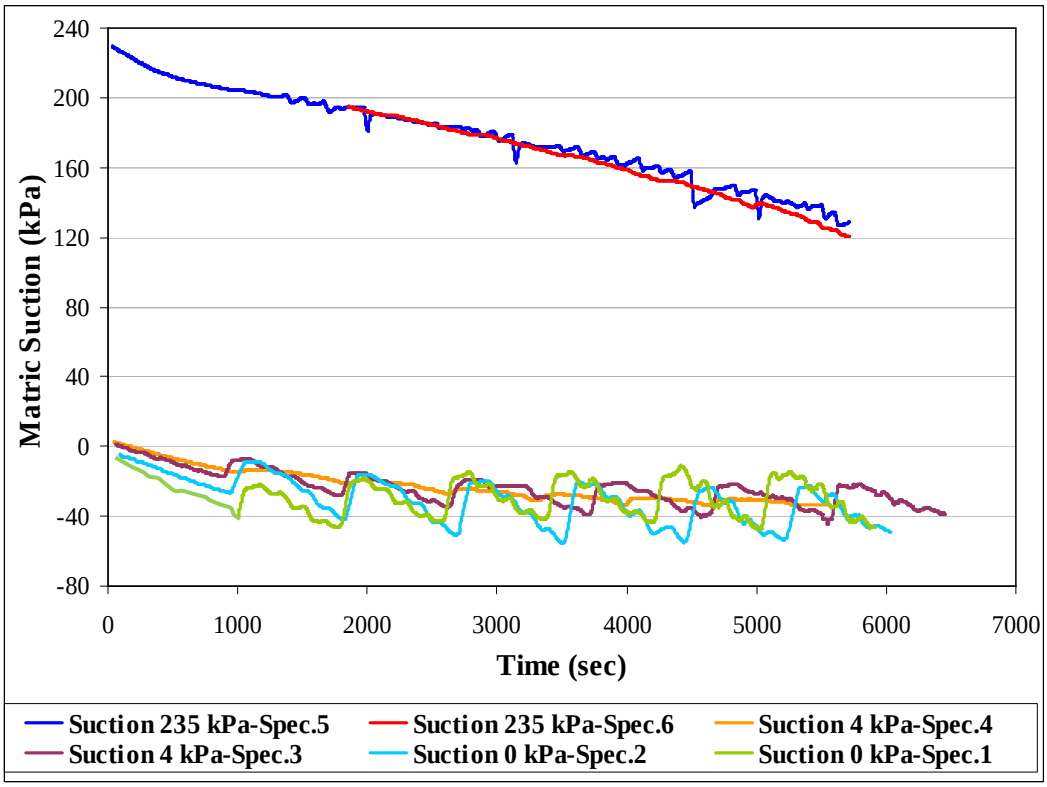

FIGURE 2-2 Decrease in matric suction due to pore water pressure buildup

Among the authors who tried to introduce the matric soil suction as a stress state, the model proposed by Cary in 2008 is the only one that accounts for the effect of dynamic pore water pressure buildup (*1, 17*). The model reads as follows:

$$M_R = k_1 \cdot p_a \cdot \left(\frac{\theta_{net} - 3 \cdot \Delta u_{w-sat}}{p_a} \right)^{k_2} \cdot \left(\frac{\tau_{oct}}{p_a} + 1 \right)^{k_3} \cdot \left(\frac{\left(\psi_{m_0} - \Delta \psi_m \right)}{p_a} + 1 \right)^{k_4} \qquad (2\text{-}9)$$

Where,

p_a = atmospheric pressurek_1, k_2, k_3 *and* k_4 = regression constants

$\theta_{net} = \theta - 3u_a$, net bulk stress

Δu_{w-sat} = buildup of pore water pressure under saturated conditions, in this case $\Delta \psi_m = 0$

τ_{oct} = octahedral shear stress

ψ_{m_0} = initial matric suction

$\Delta \psi_m$ = relative change of matric suction with respect to the initial matric suction due to buildup of pore water pressure under unsaturated conditions, in this case $\Delta u_{w-sat} = 0$

It should be noted that in equation 2-9, both variables Δu_{w-sat} and $\Delta \psi_m$ refer to changes in the pore water pressure for saturated and unsaturated conditions respectively. The presence of the mentioned variables in the model indicates that the modulus is not only a function of the externally applied stresses but also a function of the internal stresses generated by the pore pressures, and hence of matric suction. It should also be noticed that both stresses are considered independent of each other.

In preliminary analyses and in order to investigate the effect of suction changes brought by pore-water pressure buildup in the resilient modulus (Equation 2-9), Cary selected three different stress state levels represented by θ_{net} and τ_{oct} at a fixed confining pressure of 6 psi and computed M_R values by varying the suction level (*1*). The results are presented in Figure 2-3. The pore-pressure buildup has been considered as a negative suction, just for the sake of plotting the variation during saturated and unsaturated conditions altogether. In the figure, negative values of matric suction represent a positive pore-pressure buildup.

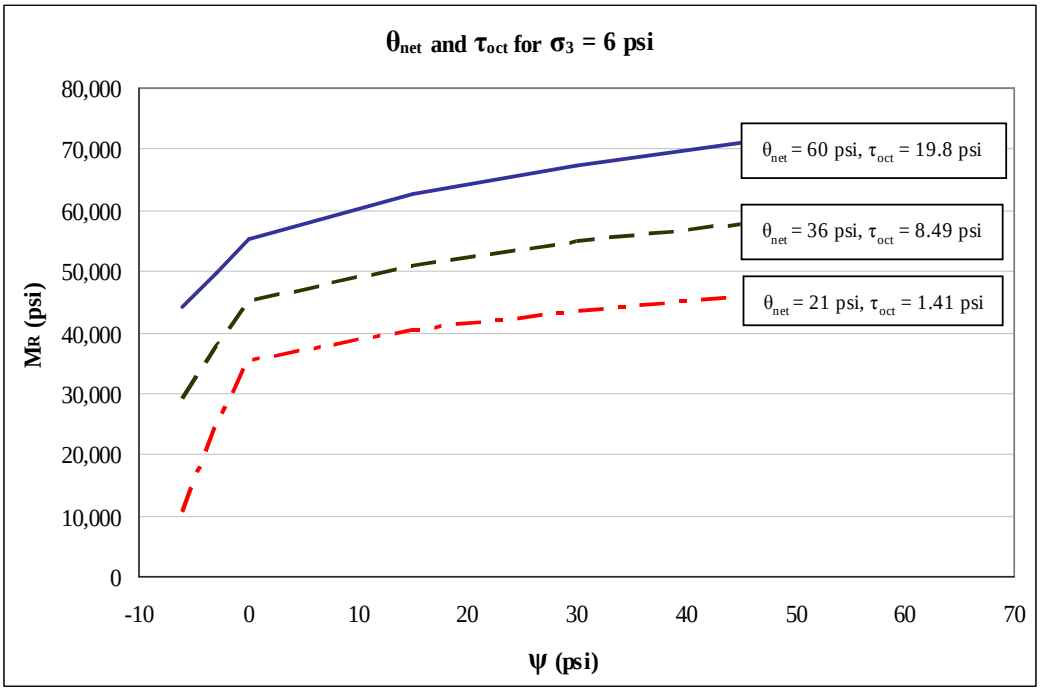

FIGURE 2-3 Variation of M_R as a function of $\Delta\psi_m$ for unsaturated conditions and Δu_w for saturated conditions (negative values shown in the graph)

The contribution of matric suction to the resilient response of the material can be observed at the three different state stress levels. It should be noted that as the matric suction increases the curve tends to get flat. This indicates that once the material gets dry enough, further increment in the matric suction of the material does not improve the resilient response of the material. On the other hand, when matric suction approaches to zero and pore-water pressure buildup occurs, the rate of drop in the resilient response of the material appears to be significantly greater than the rate of improvement in the resilient response due to the increment in the matric suction.

Figures 2-2 and 2-3 demonstrate how important are pore pressure changes within the soil stress state for the resilient response of unbound materials. Due to

cumulative **pore water pressure buildup**, under sustained repetitive loading conditions, the M_R may decrease to critical values that are not currently foreseen by pavement designers as the predictive techniques available do not explicitly contemplate this important variable even for saturated conditions. Most important, there is no clear understanding of the importance of suction changes in determining the stiffness of the material.

It is recognized that running a M_R test for unsaturated materials is a very challenging task because it requires special testing capabilities to measure variations in matric suction during the test. Such matric suction changes are result of the pore water pressure development under dynamic load. Therefore, modeling of pore water pressure buildup would be the best alternative to overcome testing limitations (*18*).

In a different scenario, besides being useful to substitute laboratory measured values, the same model could also be used by pavement designers to estimate the pore pressure buildup at multiple times along the pavement service life. These estimated values will contribute to determine with higher accuracy the real stress state that the material is being subjected to. Once the true stress state is determine, the predicted M_R values will capture the effect that the pore water pressure buildup has upon the resilient response of the material. As a consequence, higher accuracy in the prediction of M_R will contribute to optimize pavement design techniques.

Now that the importance of implementing a predictive model for pore water pressure buildup has been established, the predictive variables to be

controlled during the dynamic load testing need to be determined. In the following section, the factors considered by different authors to have influence upon the pore water pressure response are discussed. A review comprising what has been done in the topic during the last decades is presented.

Factors Governing the Pore Water Pressure Buildup on Plastic Soils

On this study, the factors governing the pore water pressure buildup of unbound materials are conveniently grouped in three categories:

- Factors related to the soil stress state
- Factors related to the repeated loading pattern
- Factors related to soil type

Factors Related to the Soil Stress State

As suggested by Fredlund, the stress state acting on unsaturated unbound pavement materials can be represented by three state stress variables: the deviator stress, net normal stress and matric suction (*9*). Fredlund also suggested that saturated soils should be considered as a special case of unsaturated soils. This statement is based on the fact that as an unsaturated soil approaches saturation, the pore water pressure approaches the pore air pressure, and as a consequence the matric suction approaches zero. When saturated, the pore air pressure is equal to the pore water pressure and the net normal stress is equal to the effective stress (*19*). Therefore, for this study, this sort of interchangeably stress state condition will be referred as a full stress state approach in which both unsaturated and saturated soil conditions are included.

Following this full stress state approach, three stress state variables can be controlled or measured depending on the drainage condition. The deviator stress $(\sigma_1 - \sigma_3)$, is the stress state variable that always remains unchangeable since it is independant upon internal pore pressure changes due to changes in water content. As previously mentioned, a second stress state variable could be defined either as net confining stress $(\sigma_3 - u_a)$, or effective confining stress $(\sigma_3 - u_w)$ depending on whether the soil is unsaturated or saturated. The third stress state variable considered is the matric suction $(u_a - u_w)$, which goes to zero when the soil becomes saturated.

The mentioned three stress state variables have been found to affect the pore water pressure buildup. In 1962, Larew and Leonards studied the impact of the repeated stress level upon the strength of unbound materials. They defined the "critical level of repeated stress" as the maximum repeated stress level that will not lead to failure (*20*). This concept suggested the importance of the repeated stress to the development of pore water pressure buildup. Subsequent studies by Sangrey (1968), Sangrey et al. (1969), Frances and Sangrey (1977) and Sangrey et al. (1978) validated the concept proposed by Larew and Leonards (*21, 22, 23 and 24*). In 1989, Ansal and Erken studied the undrained behavior of clay under cyclic shear stresses. In their studies, the cyclic shear stress amplitudes are presented as a ratio with respect to the consolidated undrained shear strength. Again, Ansal an Erken defined a critical shear stress ratio for dynamic loading

conditions which proved the influence of the cyclic stress magnitude on the development of pore water pressure (*25*).

Cyclic shear strains are induced by application of cyclic shear stresses. The cyclic shear strain amplitude has been identified as one of the principal parameters governing the changes in the soil microstructure due to dynamic loading. The cyclic shear strain amplitude that divides the domains of permanent cyclic pore water pressure development and virtually no pore pressure development at all is known as the threshold shear strain. At cyclic shear strain amplitudes larger than the threshold shear strain, the pore water pressure accumulates continuously and relatively rapidly with the number of cycles (*26*). The particles of soils subjected under undrained conditions to strains larger than the threshold shear strain, are irreversibly displaced with respect to each other. These displacements lead to a tendency for permanent volume change, the volume change that would have occurred if the conditions were drained. Under undrained conditions, any tendency toward volume change in saturated soils como translates into the development of cyclic pore water pressure. As a consequence, the deviator stress becomes one of the fundamental stress state variables driving the magnitude of the shear strain for soils subjected to repeated loading.

Additional proof of the influence of deviator stress upon the pore water pressure buildup was found by Brown et al. in 1975. Brown et al. performed a series of repeated load tests under undrained conditions involving the application of different levels of cyclic deviator stress. He found that the pore water pressure buildup increases along with the applied deviator stress (*27*).

In 1980, Andersen et al. found development of generated mean pore pressures in specimens subjected to triaxial cyclic shear test with one and two way cyclic loading. His results showed that increase in pore pressure is a function of the ratio τ_c/S_u. Where, τ_c is the cyclic shear stress and S_u is the undrained static strength (*28*). Later in 1994, Mendoza and Hernandez concluded from results of dynamic triaxial test on Mexico City clay specimens that there is an almost linear relationship between pore pressure and deviator stress up to a certain threshold shear stress; thereafter, pore pressure grows faster (*29*). As can be seen there is unanimous consensus on the significant influence of deviator stress upon the pore water pressure buildup.

Some authors studied the effect of confining pressure on the pore water pressure buildup. In 1954, Skempton proposed a model for prediction of excess pore pressure in saturated soils subjected to constant strain rate triaxial shear. The mentioned model is presented in the section dealing with attempts to predict the pore water pressure buildup. This widely known model is function of both changes in deviator stress and confining pressure. The contribution of these two variables to the excess pore pressure is dictated by the Skempton pore pressure coefficients *A* and *B*. The coefficients *A* and *B* are related to changes in deviator stress and confining pressure respectively. The *B* pore pressure parameter ranges from 0 to 1, and hence any increment in the confining pressure is expected to contribute to the increase in excess pore pressure (*30*). The same concept was presented in a book by Bishop and Henkel in 1957 (*31*).

In 1993, Fredlund and Rahardjo presented models to predict excess pore pressure in unsaturated soils for triaxial conditions and axially loaded at a constant strain rate (*19*). Again, the mentioned expressions are presented later in the document. Such expressions are very similar to those proposed by both Skempton and, Bishop and Henkel. The impact of the confining pressure upon the increase of excess pore pressure is also captured by the models.

In 1977, Ogawa et al. studied the dynamic strength of saturated cohesive soils. He performed cyclic loading triaxial tests on silty clay specimens and observed that the relationship between the applied cyclic stress and the number of stress cycles at yield are uniquely related in spite of the difference of the magnitude of the confining stress (*32*). Ogawa et al. observation implies that apparently ther is no effect of confining pressure upon the pore pressure buildup. Recently in 2009, Kim et al. performed a series of triaxial tests on silty sand specimens at different initial suction and confining stresses. He found higher development of pore water pressure for lower levels of confining pressure (*33*). The results observed by both Ogawa et al. do not seem to be in agreement with Kim et al., Skempton, Bishop and Henkel, and Fredlund and Rahardjo findings. It is evident that further investigation upon the effect that confining pressure has upon the pore water pressure buildup, especially under repeated load, is needed.

The third stress variable is the matric suction. It is observed that when the matric suction increases, the strength of the soil increases. When the soil is loaded under undrained conditions for the water phase, an increase in the pore water

pressure is expected, which leads to a decrease in the matric suction. As a consequence, degradation of the soil strength is expected.

Results from recent studies have shown that the magnitude of the maximum change in pore water pressure due to loading is related to the initial matric suction of the soil. In 2006, Minh Thu et al. performed shear strength triaxial tests on high plasticity silt specimens under constant water content conditions (*34*). He tested specimens under 8 different net confining stresses and 5 different matric suction levels. Figure 2-4 shows an example of Minh Thu et al. results. He found greater changes in pore water pressure at failure as initial matric suction values increased up to certain point. Thereafter, a gradual decrease in the pore water pressure change was observed in Minh Thu et al. results. The results were attributed to the fact that the void ratio of the soil decreased when the initial matric suction increased. As a result, the magnitude of the pore-water pressure response during shearing increased.

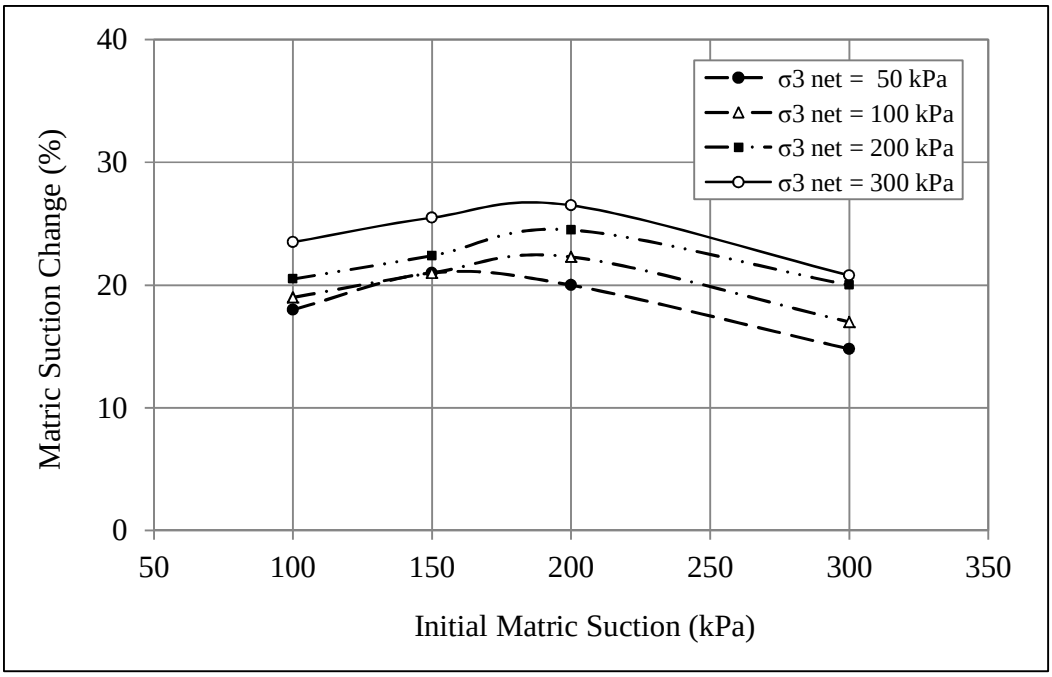

FIGURE 2-4 Matric suction change versus initial matric suction by Minh Thu et al. *(34)*

In 2008, Yang et al. performed resilient modulus test on A-6 and A-7-6 partially saturated soil specimens at a constant confining pressure and 3 different initial matric suction levels (*35*). He monitored the increase in excess pore pressure during constant water content resilient modulus tests. In general, matric suction decreased gradually with the increasing number of loading applications. The rate of decrease was found to be more pronounced for specimen with higher initial matric suction. These results were attributed to high pressures in pore water exerted by high air pressures at high matric suction levels. It was also observed that pore water pressure gradually achieves steady state at low matric suctions. On the other hand the pore water pressure kept building up for high initial matric

suction levels. Figures 2-5 and 2-6 show the results reported by Yang et al. for an A-6 soil.

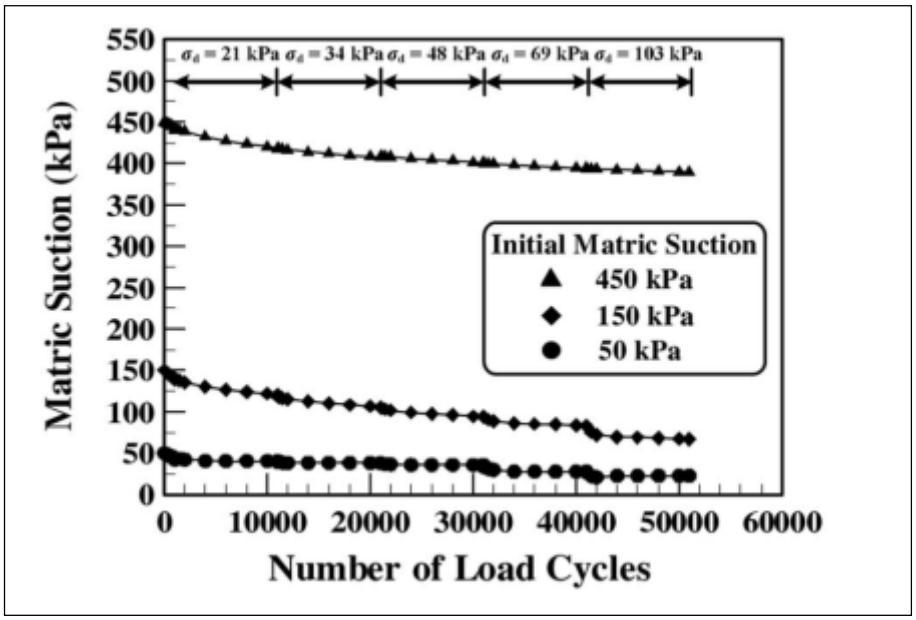

FIGURE 2-5 Variation of matric suction under M_R test by Yang et al. *(35)*

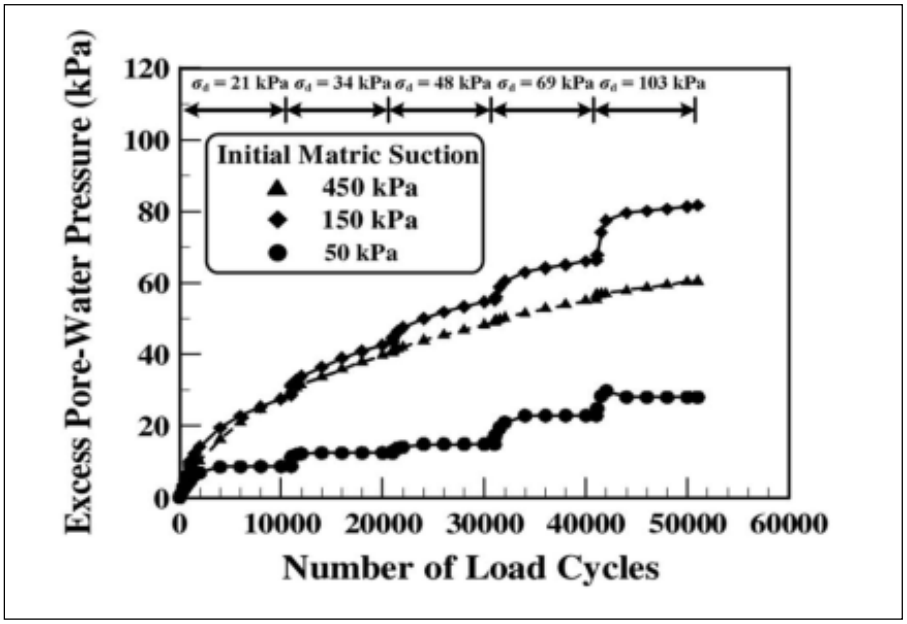

FIGURE 2-6 Variation of excess pore pressure under M_R test by Yang et al. *(35)*

In 2008, Zapata and Cary performed resilient modulus tests under constant water content conditions on A-1-a granular material specimens (*17*). As observed in Figure 2-1, they also found higher changes in pore water pressure as the initial matric suction increased.

Evidence presented in this section clearly suggests that all three stress state variables may have direct impact upon the change in pore water pressure due to repeated loading such that experienced by soils underlying pavements.

Factors Related to the Repeated Loading Pattern

Different from field situations such as typical earthquakes or marine waves impacting on offshore platforms, the stress pulse experienced by pavements subjected to traffic load has particular characteristics. In 1971, Barksdale conducted a study to determine the appropriate shape and duration of the compressive stress pulse experienced by flexible pavement systems (*36*). Barksdale affirms that typically stress pulses last for only a short period of time, and the magnitude and duration of the pulse are function of the vehicle type and speed, the pavement structure type and geometry, and the depth of the element of material under consideration.

Barksdale concluded that the variation in pulse time with depth should be considered for laboratory testing. That explains why the currently available protocol for resilient modulus testing NCHRP 1-28A uses pulse times of 0.1 and 0.2 seconds for granular base materials and subgrade soils respectively (*37*).

Barksdale also suggested that near the surface the pulse shape can be reasonably approximated as a half sinusoid. However, as depth to the material

element increases, the stress pulse flattens out significantly. Therefore, for elements located in the subgrade, the stress pulse would be better represented by a triangular pulse shape. He stated that if the pavement performs as an elastic system, an increase in vehicle speed would tend to linearly decrease the stress pulse time.

Diagrams to obtain stress pulse times as function of depth beneath the pavement surface and vehicle speed were developed by Barksdale. On these diagrams, principal stress pulse times ranged from about 0.02 seconds at the surface for vehicles traveling as fast as 45 mph, to about 6 seconds at a depth of 28 inches for vehicles traveling as slow as 1 mph. From these numbers, it can be concluded that any stress pulse time smaller than about 0.01 seconds and greater than about 6 seconds would not be representing field conditions.

In 1971, Lashine while studying some aspects of the characteristics of Keuper marl under repeated loading found out that no frequency effect over the range 0.01 to 10 Hz should be expected upon the pore pressure buildup (*27*, *38*). These frequencies correspond to stress loading pulses ranging from 100 seconds down to 0.1 seconds respectively. Stress pulses corresponding to such a low frequency as 0.01 Hz would not represent any field condition of repeated loading. On the other hand, stress pulses corresponding to frequencies higher than 10 Hz seems hard to be accurately reproduced in the laboratory. Therefore, based on Lashine statement, it would be reasonable to neglect the stress pulse loading time as a variable driving the development of excess pore pressure under repeated loading.

The traffic loading experienced by pavement systems is characterized for having a resting period following the load pulse as observed in Figure 2-7. According to the currently available protocol for resilient modulus testing NCHRP 1-28A, the assigned resting period for granular base and sub-base materials is 0.9s. For subgrade soils, the time specified in the guidelines is 0.8s. In both cases, the total cycle duration is 1s (*37*).

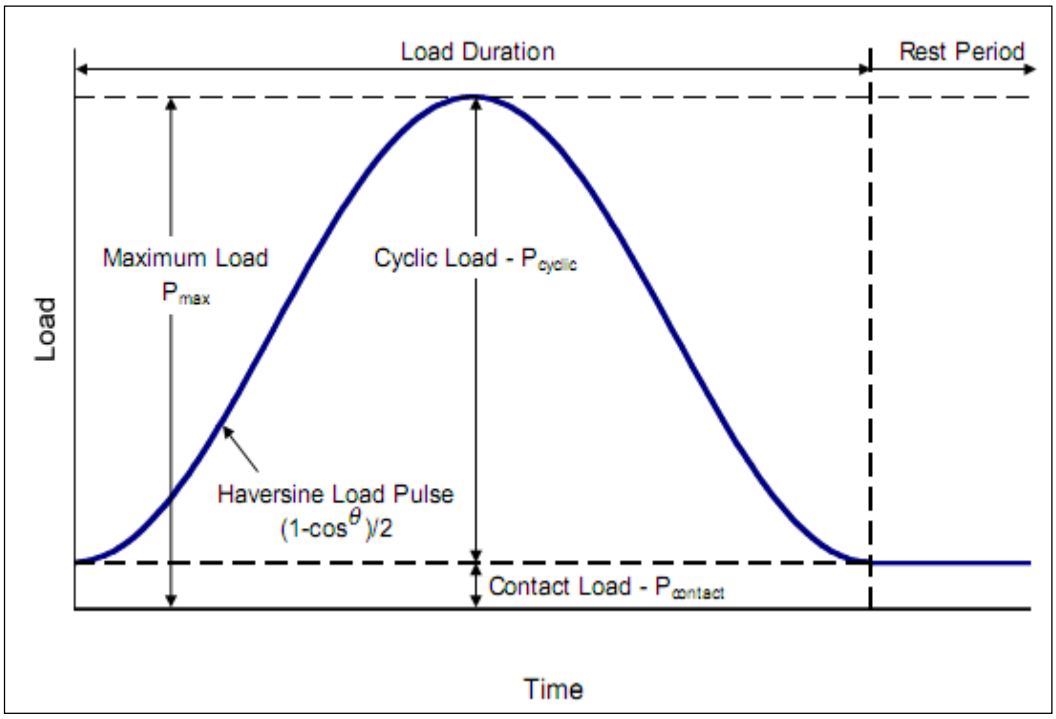

FIGURE 2-7 Stress pulse characteristics for resilient modulus testing *(37)*

The duration of the rest period is directly related to the mean daily traffic (*ADT*) of the road which reflects, in average, how busy the road is during a 24 hours period. For instance, according to the protocol NCHRP 1-28A, one loading cycle (including load pulse and rest period) is expected to occur every second. Since one day is equivalent to 86,400 seconds; then the loading pattern of the

protocol NCHRP 1-28A represents a road for which a total of 86,400 load repetitions are expected to occur in one day.

During the rest period at every loading cycle, some excess pore pressure is expected to be dissipated. The amount of excess pore pressure dissipated in this period will be a function of the soil hydraulic conductivity which is dictated by the soil type. Therefore, by varying the rest period some difference on the excess pore pressure response should be expected.

The other important parameter controlling the cyclic stress-strain characteristics of plastic soils is the number of cycles. Ansal and Erken defined a threshold cyclic shear stress level below which no excess pore pressure will develop. Even if the applied cyclic shear stress goes beyond that critical level, the accumulated excess pore pressure and cyclic shear strain amplitudes may not be significant if the number of cycles is relatively small (*24*).

Hsu and Vucetic coincide with Ansal and Erken on the importance of the number of cycles. They stated that at cyclic shear strain amplitudes larger than the threshold shear strain, the excess pore water pressure accumulates continuously and relatively rapidly with the number of cycles (*25, 26*). Repeated load triaxial testing performed by Brown et al. on a silty clay, suggested that pore pressures build up to constant positive values for lightly overconsolidated samples within about 10,000 cycles. For highly overconsolidated samples, the pore pressure leveled out at 1’000,000 (*27*). Andersen et al. also suggested that the excess pore pressure increases with both cyclic stress ratio and number of cycles (*28*). Furthermore, Ogawa in 1977 when evaluating the dynamic strength of saturated

cohesive soils observed that pore water pressure was still increasing after ceasing cyclic loading suggesting that failure may be possible even after pore pressure excitation is over (*32*).

In summary, three parameters related to the repeated loading pattern may be considered important in the prediction of the excess pore pressure for plastic soils: stress pulse time, rest period and number of cycles.

Factors Related to the Soil Type

Besides the grain size distribution and Atterberg limits, the hydraulic conductivity (*k*) is a good indicator of the soil type. The rate of the excess pore water pressure dissipation experienced by any soil subjected to repeated load will depend basically on the hydraulic conductivity of the material. Therefore this soil property becomes a good candidate to be a predictive variable capturing the effects of soil type in the development of a model for prediction of excess pore water pressure.

When the repeated load is applied under undrained conditions for the water phase, and the soil specimen is saturated, little to no volume change is expected to occur. Therefore any pore pressure dissipation will be due to removal of the transient load. The remaining excess pore pressure will gradually dissipate only under drained conditions. Drained conditions in the field will only take place when the repeated load is stopped and pore pressure dissipation may occur at very low rates depending on the hydraulic conductivity of the soil.

Usually, the materials encountered in the field have plastic components and are used as pavement foundations. It is hard to think that a saturated plastic

subgrade underlying a pavement structure will experience load resting periods sufficiently long such as to achieve any significant pore water pressure dissipation. Therefore, any pore water pressure dissipation under this condition will occur as a consequence of water drainage to deeper layers due to suction or gravitational gradients. On this aspect, the saturated hydraulic conductivity of the soil plays an important role on the potential of the material to dissipate excess pore water pressure.

Different from saturated soils, some internal dissipation of excess pore water pressure under undrained conditions occurs in unsaturated soils since there is available space in the pores filled with compressible air. Therefore, the unsaturated hydraulic conductivity is also an important factor to be considered in the development of a model for excess pore pressure prediction.

Attempts to Predict the Pore Water Pressure Buildup

Some attempts have been pursued to develop models that predict the pore water pressure buildup in soils. However, most of them do not include parameters accounting for the case of repeated loading. In this section, some of the models encountered in the literature are presented.

In 1954, Skempton presented a model to predict the pore pressure buildup for triaxial conditions (*30*). The same model was presented in a book by Bishop and Henkel in 1957 (*31*). In this model, the change in pore water pressure is in general shown as result firstly from a change in all-round stress or confining pressure and secondly from a change in uniaxial loading or deviator stress. The

corresponding changes in pore water pressure are expressed in terms of two empirical parameters *A* and *B*. The model reads as follows:

$$\Delta u = B \cdot \left(\Delta\sigma_3 + A \cdot \left(\Delta\sigma_1 - \Delta\sigma_3\right)\right) \quad (2\text{-}10)$$

Where,

B = tangent pore pressure parameter during isotropic, undrained compression

A = tangent pore pressure parameter during uniaxial, undrained compression

$\Delta\sigma_3$ = change in confining pressure

$\Delta\sigma_1$ = change in principal vertical pressure

When the soil is fully saturated the value of *B* is equal to 1. On the other hand, when the soil is partly saturated the value of *B* is less than 1 and varies with the stress range. Also, it was found more convenient to keep the terms of the product *AB* together and denote it as $\bar{A}$. Equation 2-10 is then better expressed as:

$$\Delta u = B \cdot \Delta\sigma_3 + \bar{A} \cdot \left(\Delta\sigma_1 - \Delta\sigma_3\right) \quad (2\text{-}11)$$

As can be seen, the stress state of the soil is considered in this expression but loading pattern parameters as well as the soil type are not considered. Furthermore, equation 2-11 does not consider the effects of repeated loading.

In 1993, Fredlund and Rahardjo presented an equation to predict the change in pore water pressure that has the same form as the pore water generation equations proposed by Skempton and Bishop and Henkel (*19, 30 and 31*). Again, the change in pore pressure is presented in terms of pore pressure parameter *B* for isotropic loading but for uniaxial loading, the parameter utilized is the pore

pressure parameter called *D*. Therefore, the generation of pore water pressure under triaxial conditions is expressed as follows:

$$du_w = B_w \cdot d\sigma_3 + D_w \cdot d(\sigma_1 - \sigma_3) \quad (2\text{-}12)$$

Where,

D_w = tangent pore water pressure parameter for uniaxial, undrained loading

B_w = tangent pore water pressure parameter during isotropic, undrained compression

$d\sigma_3$ = change in confining pressure

$d(\sigma_1 - \sigma_3)$ = change in deviator stress

By rearranging equation 2-12 and using $A_w = D_w / B_w$ as a new pore pressure parameter, the same expression is presented by Fredlund and Rahardjo as follows:

$$du_w = B_w \cdot (d\sigma_3 + A_w \cdot d(\sigma_1 - \sigma_3)) \quad (2\text{-}13)$$

The last expression results to be basically the same as the expression proposed by Skempton or Bishop and Henkel.

A good attempt to include the loading pattern parameters as well as the soil type into a pore-pressure generation model for repeated loading was presented by Ansal and Erken in 1989 (*25*). Ansal and Herken defined the parameter *m* as the rate of change of pore pressure with cyclic stress ratio as function of the number of cycles *N*. The expression that defines *m* is expressed as:

$$m = k + \log N \quad (2\text{-}14)$$

Where *k* is a material constant obtained from a regression analysis.

The threshold cyclic stress ratio $(S.R.)_t$ is defined as a stress ratio level below which no pore water pressure will develop. Once *m* is evaluated and knowing $(S.R.)_t$, it is possible to estimate the magnitude of the pore water pressure buildup *u*, by using the following equation given by Ansal and Herken:

$$u = \left(\frac{\tau}{\tau_f} - (\text{S.R.})_t \right) \cdot m \qquad (2\text{-}15)$$

Where, the ratio of the cyclic shear stress (τ), to the consolidated undrained shear strength (τ_f) defines the cyclic shear stress ratio.

Among the models presented in this section, only the one proposed by Ansal and Herken considers important parameters for repeated loading such as the number of repetitions and somehow the soil type. Therefore it is evident that a suitable model for application to pavement loading conditions is needed.

CHAPTER 3. LABORATORY ROUTINE SOIL CLASSIFICATION AND ADVANCED UNSATURATED SOIL TESTING

This chapter deals with all of the routine material testing completed prior to the dynamic load testing. The routine soil classification tests performed on the material included:

- Grain Size Distribution (includes Hydrometer Test)
- Atterberg Limits
- Specific Gravity
- Standard Compaction Curves

In addition, the saturated hydraulic conductivity (k_{sat}) of the material tested was measured and reported in this chapter. Finally, the results of the advanced unsaturated soil testing performed in order to obtain the *SWCC* of the material are presented.

Handling Materials

A total of 10 five gallon buckets of coarse grained subgrade were obtained from field sampling close to the intersection of Indian School Rd and Old Litchfield Rd in Avondale, Phoenix Metro area. This soil was denominated IOSG. The material was initially air dried, thoroughly powdered using mortar and pestle, and then mixed in order to achieve a uniform gradation before starting the testing program. Standard sampling procedures were followed in selecting material samples for the different tests to be performed.

Grain Size Distribution, Atterberg Limits and Soil Classification

ASTM Standard D 422-63 (2002) was followed to obtain the grain-size distribution of the material. Three replicates of the sieve analysis were completed for the IOSG plastic subgrade soil. The results of the tests are shown in Table 3-1.

TABLE 3-1 Sieve analysis results for IOSG subgrade soil

Sieve	Opening (mm)	Percent Passing (%)		
		Replicate 1	Replicate 2	Replicate 3
2"	50.800	100.0	100.0	100.0
1.5"	38.100	100.0	100.0	100.0
1"	25.400	100.0	100.0	100.0
¾"	19.100	100.0	100.0	100.0
½"	12.700	98.0	98.6	99.4
3/8"	9.520	97.4	97.2	98.6
#4	4.750	95.2	95.0	97.1
#10	2.000	93.7	93.1	95.5
#40	0.425	84.7	85.0	86.7
#60	0.250	73.5	75.5	77.2
#80	0.178	64.7	67.6	69.9
#100	0.149	60.2	63.4	65.9
#200	0.074	30.1	37.5	47.4

The curve obtained in test replicate number 2 was selected to be the average representative of the material. The result of this replicate was used in posterior classification of materials for further tests like compaction curves. Grain size distribution curves from the three replicates are plotted in Figure 3-1.

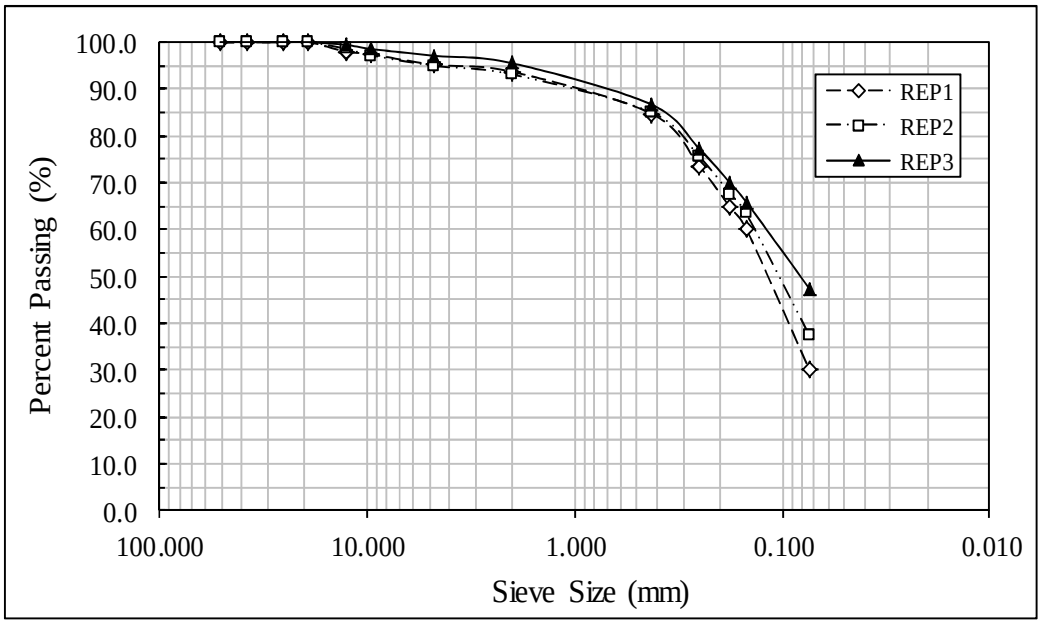

FIGURE 3-1 Grain size distribution of IOSG subgrade soil

Three replicates of hydrometer analysis were performed on the IOSG subgrade soil as part of the grain size distribution study. The result from replicate 2 of grain siza distribution was selected to extend the study to hydrometer analysis. It can be observed in replicate 2 that 37.5% of the material passes through sieve #200. Particle size distribution for the material passing sieve #200 of IOSG soil is based on this representative percentage.

Results of the hydrometer analysis are shown in Table 3-2. Figure 3-2 shows the extended grain size distribution curve including results from hydrometer analysis for the representative test result (replicate 2).

TABLE 3-2 Hydrometer analysis results for IOSG soil

Particle Diameter (mm)	Adjusted Percent Finer (%)			
	Replicate 1	Replicate 2	Replicate 3	Average
0.032	14.7	15.1	14.5	14.8
0.025	13.2	13.6	13.0	13.3
0.018	11.0	8.3	11.5	10.3
0.012	7.9	4.6	8.4	7.0
0.009	6.2	3.1	7.7	5.7
0.006	5.3	2.4	6.1	4.6
0.003	3.1	1.6	3.8	2.9
0.001	2.4	0.9	3.1	2.1

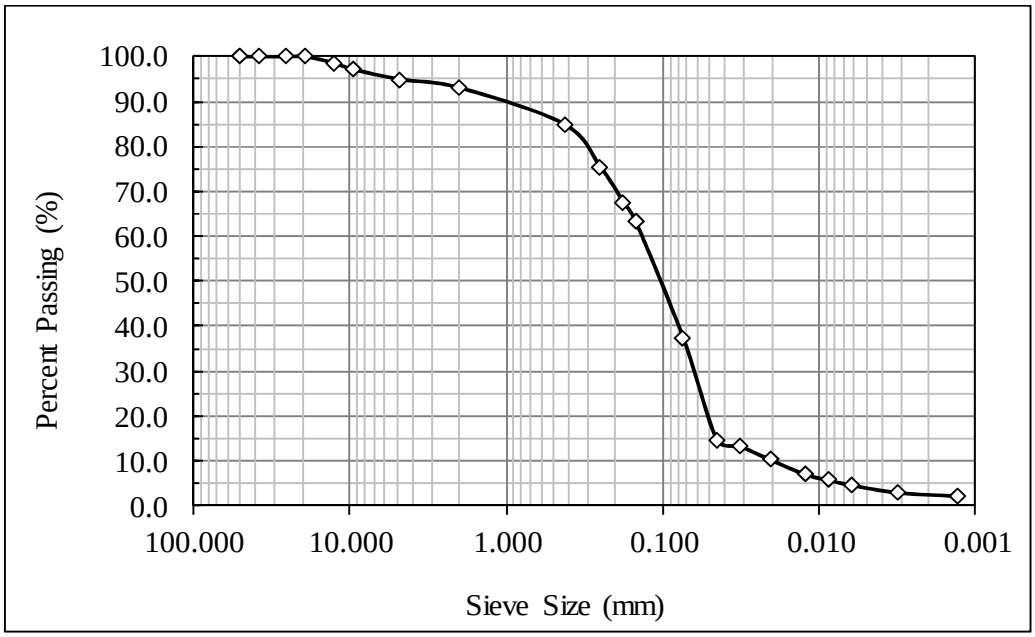

FIGURE 3-2 Extended grain size distribution of IOSG soil

The IOSG soil was classified as clayey sand (SC) according to the Unified Soil Classification System (USCS). According to the AASHTO classification, the

soil was classified as A-4 with a Liquid Limit of 23.9 and a Plasticity Index of 7.2. Two replicates of Atterberg limits tests were performed on the IOSG soil. The results from those two replicates and the final averaged values considered for classification are shown in Table 3-3.

TABLE 3-3 Atterberg limits for IOSG soil

Replicate	1	2	Average
LL	24.0	23.8	23.9
PL	16.8	16.6	16.7
PI	7.2	7.2	7.2

Specific Gravity

Two replicates were obtained for the specific gravity of the IOSG soil. The test for specific gravity of the solids was performed following the ASTM Standard C 128-04a.

Table 3-4 presents the results of the specific gravity test for the IOSG soil.

TABLE 3-4 Specific gravity for IOSG soil

Replicate	1	2
Specific Gravity, G_s	2.724	2.714
Average Specific Gravity,	2.719	
Standard Deviation	0.008	

Compaction Curves

The Standard Proctor Compaction test was performed by applying 12400 ft-lbs/ft^3 of compaction energy to determine the moisture-density relation for the materials investigated in this study. The test followed the guidelines of the ASTM Standard

D 698-00 method A for the IOSG soil. The IOSG soil samples were compacted at different water contents in molds of 4 inches in diameter and 4.5 inches in height. A rammer of 5.5 lbf and 12 inch of droop height was used to apply 25 blows per layer for a total of three layers per sample. Two replicates of standard compaction test were performed for the IOSG soil. The compaction curves were defined by 4 points in both curves. Table 3-5 and Figure 3-3 show the results of two replicates of the compaction test and the plot of the compaction curves for the IOSG soil respectively.

TABLE 3-5 Standard compaction for IOSG soil

Standard Compaction				
	Replicate 1		Replicate 2	
Specimen	Water Content (%)	Dry Density (g/cm^3)	Water Content (%)	Dry Density (g/ cm^3)
1	11.30	1.88	11.18	1.90
2	12.29	1.91	12.20	1.91
3	13.27	1.88	13.23	1.88
4	14.12	1.86	14.13	1.85
Average Optimum Water Content (%)				12.1
Average Maximum Dry Density (g/cm^3)				1.91

As can be observed from Table 3-5, an average value was obtained from the results of the two replicates. The optimum moisture content for the material evaluated is 12.1% and the maximum dry density 1.91 g/cm^3 in average.

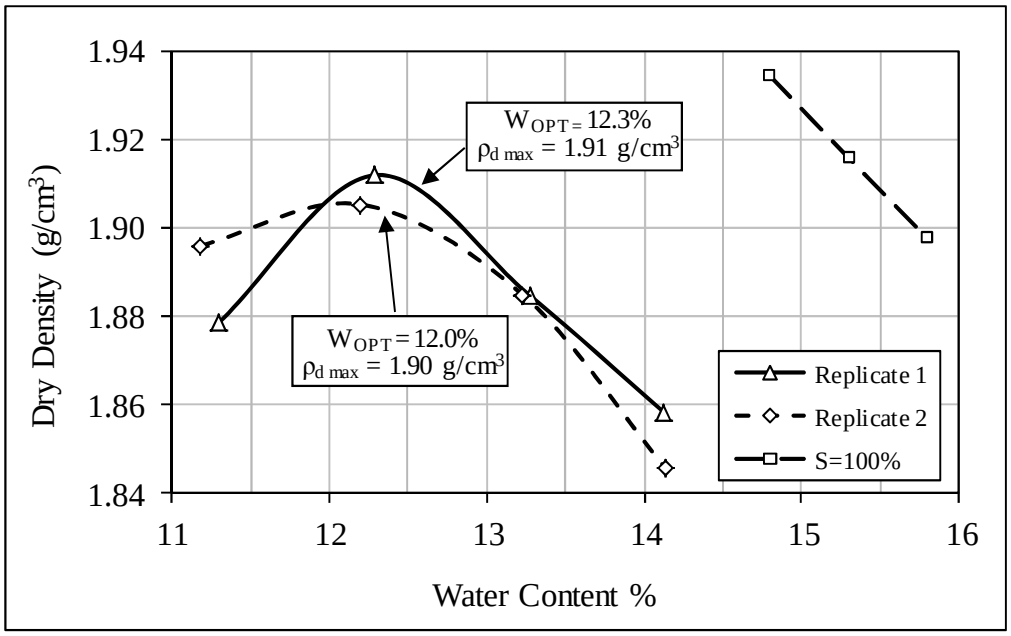

FIGURE 3-3 Standard compaction curves for IOSG soil

Saturated Hydraulic Conductivity

The coefficient of permeability (hydraulic conductivity) with respect to the water phase, k_w, is a parameter that indicates the availability of space for water to flow through the soil. It is known that for saturated conditions, the Constant Head Permeability Test and the Falling Head Permeability Test are usually performed for granular and plastic soils respectively.

For the present study, an alternative method was used to measure the saturated hydraulic conductivity of the material. With this alternative method, a water head gradient is imposed on a saturated cylindrical specimen using a triaxial cell.

The specimen used in this test is 2.8 inches diameter and 0.5 inches in height. This sample was prepared at optimum moisture conditions to achieve the maximum dry density estimated for the material. Then, the specimen was

mounted in a triaxial chamber and covered with a latex membrane that isolates the material from the confining fluid. Porous stones were placed at both ends of the specimen between. Filter paper was used between the porous stones and the top and bottom surfaces of the specimen to prevent clogging of the pores. Rubber o-rings were used to provide an effective seal between the membrane and the end platens.

Once the specimen was properly installed and the cell was filled up with water, back pressure was applied to saturate the specimen. The Skempton *B* parameter was controlled to determine whether the specimen reached saturation. When the *B* parameter reached 0.92, it was assumed that the specimen was saturated.

After that, a head gradient of 50 kPa was applied to the specimen and the total water volume discharged during a fixed time interval was measured using a glass tube of 1 cm in diameter. Using the known geometric characteristics and the data recorded from the test, the following Equation 3-1 was utilized to obtain the saturated hydraulic conductivity of the subgrade material:

$$k_{sat} = \frac{Q.L}{h.A.t} \tag{3-1}$$

Where; Q is the total discharged volume in m^3 during a time interval of t seconds, A and L are the specimen area in m^2 and thickness in meters respectively, and h is the applied head gradient in meters. Figure 3-4 shows the setup of the specimen for this test and Table 3-6 summarizes the test results.

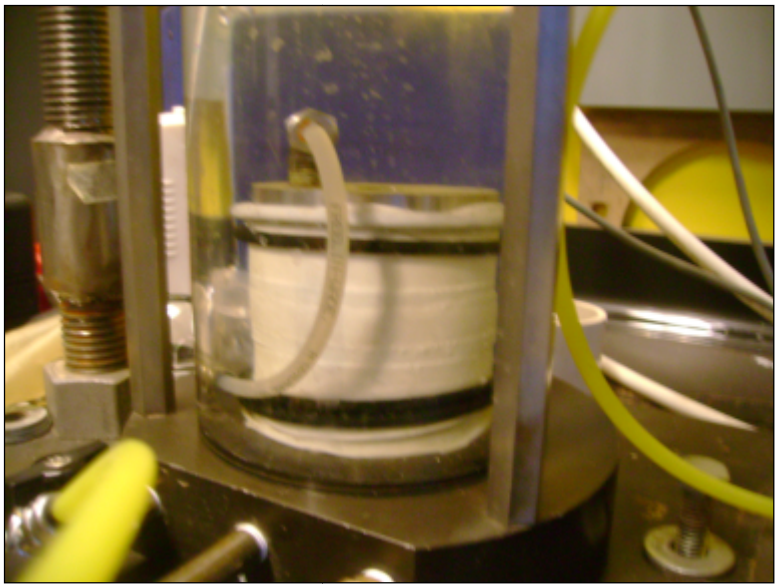

FIGURE 3-4 Specimen setup for hydraulic conductivity test

TABLE 3-6 Saturated hydraulic conductivity test results

Parameter	Value
Specimen diameter (cm)	7.06
Specimen height (cm)	1.25
Dry densty (g/cm^3)	1.84
Cross sectional area (cm^2)	39.2
Head gradient (m)	5.0
Average ksat (m/s)	2.724×10^{-8}
Standard Deviation (m/s)	2.889×10^{-9}

Soil-Water Characteristic Curve

The soil suction is defined as the free energy state of soil water measured in terms of the partial vapor pressure of the soil water. The thermodynamic relationship between soil suction and the partial pressure of the pore water vapor is defined by Equation 3-2:

$$\psi = -\frac{RT}{\upsilon_{w0}\omega_{\upsilon}} \ln\left(\frac{\bar{u}_{\upsilon}}{\bar{u}_{\upsilon 0}}\right) \quad (3\text{-}2)$$

Where,

ψ = total soil suction (kPa)

R = universal (molar) gas constant

T = absolute temperature

υ_{w0} = specific volume of water or the inverse of the density of water

ω_{υ} = molecular mass of water vapor

$\bar{u}_{\upsilon}$ = partial pressure of pore water vapor

$\bar{u}_{\upsilon 0}$ = saturation pressure of water vapor over a flat surface of pure water at the same temperature

It can be observed that soil suction is a function of temperature and the term $\bar{u}_{\upsilon}/\bar{u}_{\upsilon 0}$ called relative humidity, RH (%).

When quantified in terms of the relative humidity the soil suction is called "total suction". The total suction has two components called matric and osmotic suction, and can be expressed as shown in Equation 3-3:

$$\psi = (u_a - u_w) + \pi \quad (3\text{-}3)$$

Where,

$(u_a - u_w)$ = matric suction

π = osmotic suction

The matric suction component is commonly associated with the capillary phenomenon. In the soil, the pores with small radii act as capillary tubes that

cause the soil water to rise above the water table. The relative humidity in a soil decreases due to the presence of curved water surfaces (meniscus) produced by the capillary phenomenon. The radius of curvature of meniscus is inversely proportional to the difference between the air and water pressures across the surface which is called matric suction. It means that the matric suction as a component of total suction contributes to a reduction in the relative humidity.

Generally, the pore water present in soils contains dissolved salts. The relative humidity decreases with increasing dissolved salts in the pore water of the soil. The decrease in relative humidity due to the presence of dissolved salts in the pore water is known as the osmotic suction which is the other component of the soil suction (*31*).

The matric suction can be measured in direct or indirect ways. The use of tensiometers and pressure plates are two common devices for direct measuring of matric suction. The tensiometer uses a high air entry ceramic cup as an interface between the measuring system and the negative pore-water pressure in the soil. This device could be used either in the laboratory or in the field and measures only negative pore water pressures when air pore pressure is atmospheric. Difficulties with cavitation and air diffusion through the ceramic cup limit the measuring capability of tensiometers to -90 kPa.

Pressure plates can also be used to obtain the Soil-Water Characteristic Curve (*SWCC)* based on matric suction by applying the axis translation technique. A soil specimen should be placed on top of either a saturated high air entry ceramic disk or a saturated cellulose membrane with an air entry value higher

than the matric suction to be measured. The pressure plate chamber is closed as fast as possible and air pressure is applied keeping the pore water pressure in the compartment below the ceramic disk or cellulose membrane as close as possible to zero. By obtaining the moisture content of the specimen at equilibrium under several air pressure levels, it is possible to construct the *SWCC*. The positive air pressure at equilibrium should be numerically equal to the negative pore water pressure at the corresponding moisture content of the specimen. The measuring capability of the pressure plates depends on the air entry value of the ceramic disk or the cellulose membrane used. Ceramic disk and cellulose membranes with a maximum air entry value of up to 1500 kPa are commercially available.

An indirect way of measuring the matric suction is by using a standard porous block as a sensor. The matric suction can be inferred from the water content of the porous block. The thermal properties of the soil could be indicative of the water content of the soil through the use of calibration curves. Therefore, the thermal conductivity sensor is the most promising device for indirect measurements of matric suction. The measuring capability of the thermal sensor goes up to 400 kPa.

The equipment used for testing the IOSG soil in this study was a pressure plate of 3 inches in diameter and 3.5 inches high. A ceramic stone is used in this kind of equipment to allow the flow of water under applied pressure but impeding the flow of air through it.

The ceramic stone used in this test has a high air entry value of 5 bars (500 kPa). The ceramic stone used in this apparatus is glued into a ring that is fitted

into a recess on the bottom base plate which has a grooved water compartment to keep the stone saturated and to facilitate the flushing of diffused air. The base has two external ports that connect the water compartment to the drainage system.

The drainage system consists of two volumetric tubes to measure the amount of water that is released or absorbed for the specimen. In this case, the volumetric tubes were only used to determine when the water stopped flowing out of the sample while getting the drying path of the *SWCC*. Figure 3-5 shows the set up of the pressure plate used to obtain the *SWCC* of the IOSG soil.

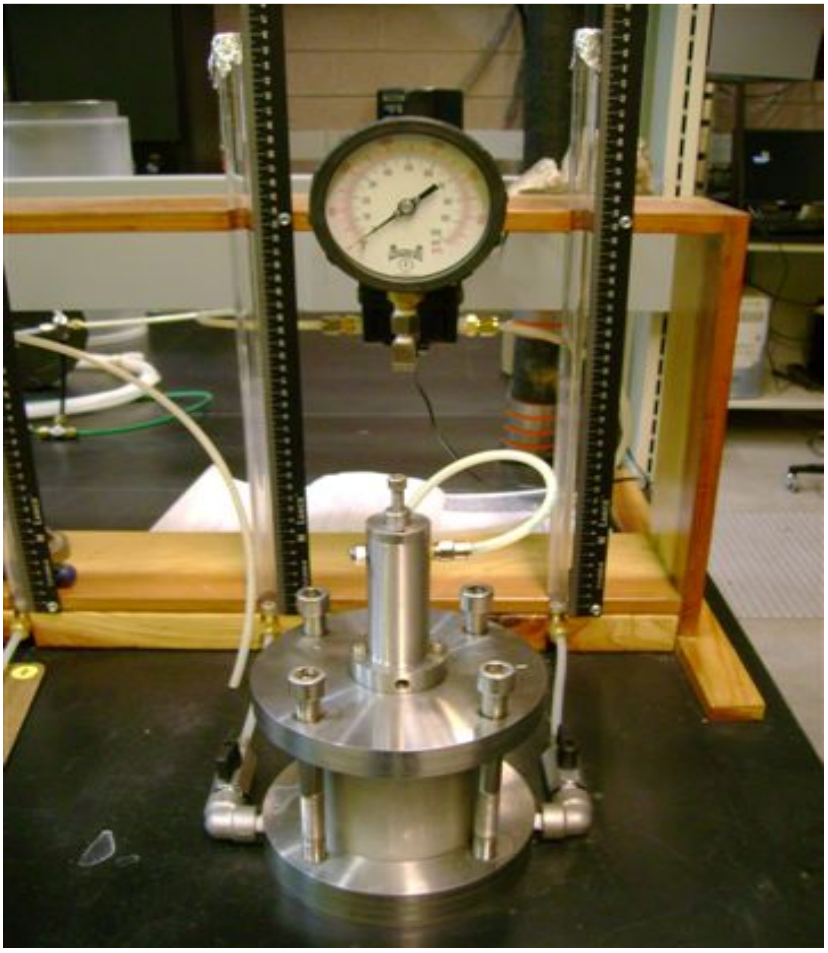

FIGURE 3-5 Pressure plate setup to obtain the *SWCC* of the soil

One IOSG soil sample of 2-inch diameter by 1-inch height compacted at optimum moisture content and maximum dry density and previously saturated was tested in the pressure plate apparatus. The same sample was removed from the pressure plate, weighted and replaced back whenever water stopped coming out under applied pressures. Pressures of 50, 120, 220, 350 and 450 kPa were applied to get the drying path of the *SWCC*. Water contents of 15.4, 14.1, 13.1, 11.3 and 11% were found for each pressure value, respectively. The results of the suction test are shown in Table 3-6.

TABLE 3-7 Soil water characteristic curve results for the IOSG soil

Soil Water Characteristic Curve					
Matric Suction Level	1	2	3	4	5
Matric Suction (kPa)	50	120	220	350	470
Water Content (w%)	15.4	14.1	13.1	11.3	11.0
Degree of Saturation (S%)	95.1	87.2	82.4	71.7	70.2

The dataset was then fitted with the nonlinear equation proposed by Fredlund and Xing (*39*). The *SWCC* plot is shown in Figure 3-6.

Unsaturated Hydraulic Conductivity

For unsaturated soils, the task of measuring permeability becomes challenging since methods utilized are highly prone to error if extremely care is not taken. Additionally the water flow rates during such tests are extremely low and therefore very long time is required to complete a series of permeability measurements.

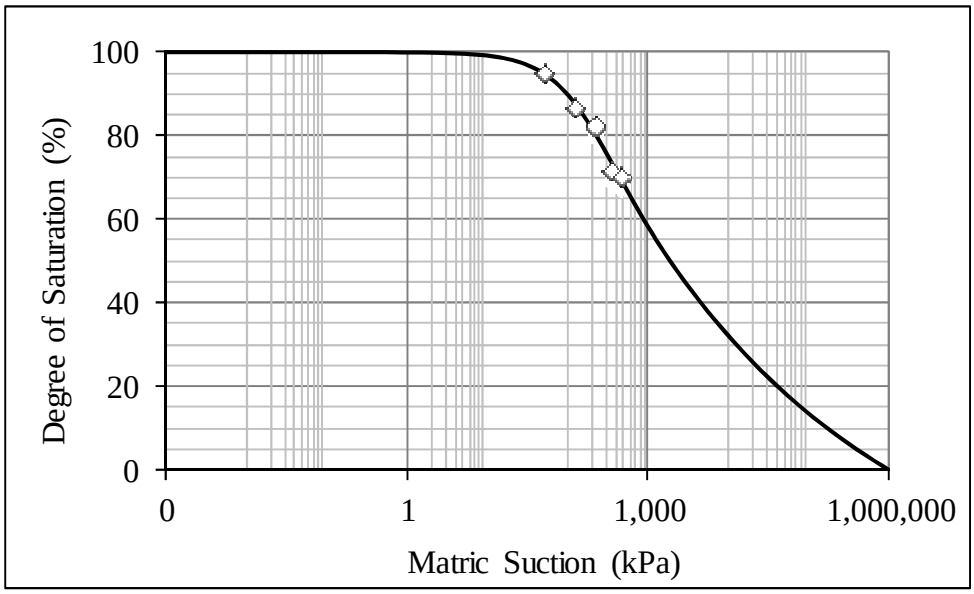

FIGURE 3-6 *SWCC* for the IOSG soil

The different testing procedures available to measure the permeability on unsaturated soils are categorized in two groups. The first group, called steady-state methods, comprehends those methods in which the quantity of flow is time-independent. For the second group, called unsteady state methods, the quantity of flow is time dependent. In general lines, the steady state methods are performed by maintaining a constant hydraulic head gradient across an unsaturated soil specimen. In the same way, matric suction and water content of the specimen are kept constant. These conditions produce a steady state water flow through the specimen. The steady state condition is reached when the flow rate entering the soil is equal to the flow rate coming out of the soil. A single coefficient of permeability can then be calculated and it corresponds to the applied matric suction or water content. Different values at different matric suction or water content values can be obtained by repeating the same procedure.

The unsteady state methods use a cylindrical soil specimen subjected to a continuous water flow from one end of the specimen. Different variations of the test method differ mainly in the flow process used and in the measurement of the hydraulic head gradient and the flow rate. The flow process can follow either the wetting path or the drying path. Some optional procedures can be followed to obtain the hydraulic gradient and flow rate at different points along the specimen. However, all variations in this kind of procedure are based on the same theoretical principles. After the flow of water has commenced, both the hydraulic head gradient and the flow rate are obtained concurrently and instantaneously at different elapsed times.

Given that direct measurements of the unsaturated hydraulic conductivity is difficult to perform, alternatives procedures referred to as indirect methods have been developed by some authors. These indirect methods can be performed provided that good measurements of both the *SWCC* and the saturated hydraulic conductivity, k_{sat}, are available.

The model proposed by Jacquemin in 2011 was utilized to estimate the unsaturated hydraulic conductivity k_{unsat} corresponding to the matric suction applied to the specimens in this laboratory testing program (*40*). The equation proposed by Jacquemin reads as follows:

$$k_{unsat} = \sqrt{k_{sat} k_{min}} \times 10^{\left[\frac{1}{2} log\left(\frac{k_{sat}}{k_{min}}\right) \times tanh\left(\frac{log\left(\frac{\psi}{\sqrt{b \times \psi_{AEV} \psi_{residual}}}\right)}{2 \times log\left(\frac{b \times \psi_{residual}}{\psi_{AEV}}\right)}\right)^{a}\right]} \quad (3\text{-}4)$$

Where,

k_{unsat} = unsaturated hydraulic conductivity

ψ = soil suction

k_{sat} = saturated hydraulic conductivity

k_{min} = minimum unsaturated hydraulic conductivity

ψ_{AEV} = soil air entry value

$\psi_{residual}$ = residual soil suction

a = fitting parameter related to the slope in the transition zone

b = fitting parameter related to the residual suction value

In this study, the suction level for unsaturated specimens was found to be 157kPa as explained in next sections. Using the model proposed by Jacquemin, the unsaturated hydraulic conductivity corresponding to 157kPa of initial suction was found to be 1.471×10^{-13} m/s. The input values used to estimate the unsaturated hydraulic conductivity of the material utilized in this study are presented in Table 3-8.

TABLE 3-8 Input parameters for the unsaturated hydraulic conductivity function

Parameter	Value
Air Entry Value (kPa)	50
$\psi_{Residual}$ (kPa)	12,000
k_{min} (m/s)	6.1×10^{-15}
k_{sat} (m/s)	2.724×10^{-8}
a	0.608
b	0.345

CHAPTER 4. DYNAMIC LOAD TRIAXIAL TEST

This chapter details the testing conditions established for this special study. The main features of the last generation testing equipment available at the ASU Geotechnical Laboratory, which were used for dynamic load testing of the IOSG subgrade material, are outlined. Two different systems were utilized to test either saturated or unsaturated soil specimens.

Some necessary enhancements done to the testing systems used for dynamic load are also detailed. All the different available types of triaxial tests are discussed and the triaxial test procedures selected for this study are defined.

Triaxial System for Dynamic Load Testing

The Geotechnical group at Arizona State University has up to 8 triaxial units available for testing. Three of them are less sophisticated than the rest but useful for testing on saturated specimens.

Tests on unsaturated soil specimens can be conducted in 5 out of the 8 available units. Even when all of them are capable of measuring and/or controlling matric suction, only three of these advanced unsaturated triaxial systems have unique features that make of them special for unsaturated soil testing.

At the beginning of the laboratory testing program, it was desired to run the dynamic load tests using the most sophisticated triaxial units available. Furthermore, some enhancements were performed to the mentioned triaxial units in order to condition them for this particular testing program as discussed in next

sections. However, due to problems arose with the system controllers and electronics in general, it was possible to utilize only one of the most sophisticated units available.

In order to achieve saturation of specimens in reasonable time frames, capability of the triaxial system for reaching high levels of confining pressure and backpressure is required. Because they make use of special pressure/volume controller devices, only the most sophisticated triaxial units have the capability to impart confining pressure levels that go beyond the maximum hose pneumatic pressure available in the Geotecnical Lab. This was the main reason for running the test on saturated specimens using the most sophisticated triaxial unit available

A second triaxial system utilized only for testing on unsaturated specimens is considered less sophisticated but still capable of measuring and/or controlling matric suction. In the next sections, some detailed information about both systems used in this testing program is presented.

Triaxial Unit used for Saturated Soil Specimens

A fully integrated system capable of applying repeated cycles of a haversine-shaped load pulse was used for the dynamic load testing on saturated specimens of IOSG subgrade material. Except for the specimen preparation and pressure cell assembly, essentially all functions are executed from the system control computer.

This Special Triaxial Unit (*STU*) used for testing of the saturated specimens is an electro-hydraulic system with closed- loop digital servo control. With this system, one can get direct control/measurement of pore water pressure (u_w) at the top/bottom of the specimen and direct control/measurement of pore air

pressure (u_a) at the top of the test specimen if unsaturated soil specimens are being tested. Different from most standard triaxial systems, which have only three ports for cell pressure and top and bottom pressure, the Special Triaxial Unit used in this study has two additional pressure ports for the pore air pressure and inner pressure measurements.

This system was originally developed to test 100mm (4 inch) diameter specimens and modified for this study to test 71mm (2.8 inch) diameter specimens. This system can also test 100mm (4 inch) diameter specimens by using specially-manufactured bottom platens. The system has a load cell capacity of 22.24 kN (5000 lbs) and the load reaction frame is capable of supporting up to 45 kN (10,000 lbs) in tension or compression. Figure 4-1 shows the Special Triaxial System used for testing on saturated soil specimens.

FIGURE 4-1 Special triaxial unit used for testing of saturated specimens

Two special features of the system are the high precision pressure/volume controllers (*PVC*) and the soil suction measuring device for unsaturated soils testing. In order to test unsaturated soils, an extremely precise method of measuring the pressure and volume change of both pore fluids air and water is required. The *PVC* are fully integrated into the system and controlled by the main system computer. The *PVC* is nothing but a pressure cylinder with two smooth bored coaxial chambers in its interior, one filled with hydraulic oil and the other with water. The oil chamber provides computer control via the servo valve. The other chamber is connected to a pressure chamber and provides the capability of measuring pressures via a pressure transducer. This last chamber can be filled with the fluid (air or water) for which the pressure or volume change is desired to be measured. By assuming a constant bore diameter, the volume change is measured by a linear movement of the rigid cylinder shaft. The amount of linear movement is captured by a linear variable differential transducer (*LVDT*) directly to the shaft. A schematic diagram of the pressure volume controller is shown in Figure 4-2.

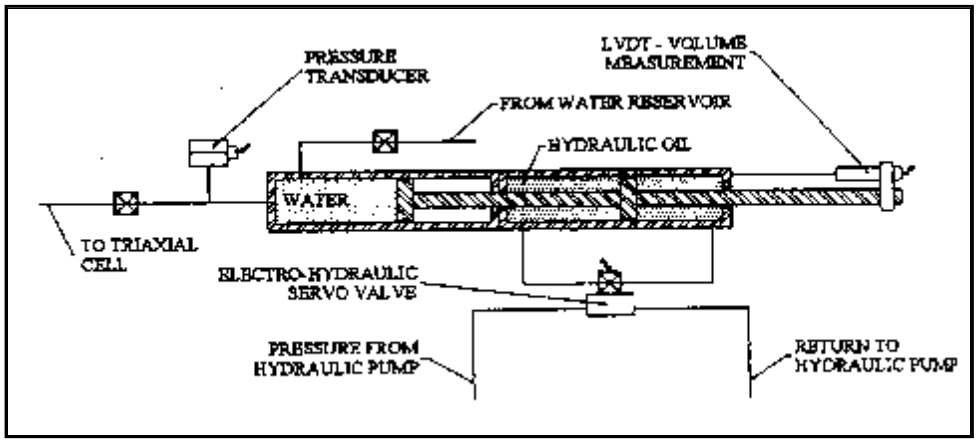

FIGURE 4-2 Schematic of pressure/volume controller

The *STU* counts with 5 of these pressure cylinders. Each one of the pressure cylinders is used for: cell pressure, inner pressure (in the center of hollow cylinder specimens), bottom pore water pressure, top pore water pressure, and pore air pressure. The pressure cylinders can be either controlled statically in constant pressure or constant volume, or dynamically, with a user defined function of either pressure or volume.

The soil suction measurement device consists of load platens with high air entry value (*HAEV*) ceramic disks bonded to them and connected directly to the *PVC* controllers. This allows matric soil suction to be measured or controlled at both the top and bottom of the soil specimen simultaneously and independently. However, in this study the soil suction measuring device was not used as the *STU* was used to test only saturated soil specimens. Only a porous stone was attached to a specially manufactured bottom platen as detailed in next sections.

The mechanism of the *HAEV* is similar to that described, in previous sections of this report, for the cellulose membrane used to obtain the *SWCC*. The *HAEV* ceramic disk allows the flow of water under applied pressure but impeding the flow of air through it. The best way to concisely describe the soil suction measuring device is as a system consisted of an extremely precise water pressure/volume control device connected to *HAEV* ceramic disks with a differential pressure sensor mounted between them.

Triaxial Unit used for Unsaturated Soil Specimens

A similar but less sophisticated triaxial system was used for testing on unsaturated soil specimens. The system is capable to control/measure automatically both the

axial load and the confining pressure, and provides direct manual control and automatic measurement of pore air pressure (u_a) at the top of the test specimen and pore water pressure (u_w) at top/bottom of the specimen. This system was originally designed to test 100 mm (4 inch) and 150 mm (6 inch) diameter specimens. The system has a load cell capacity of 22.24 kN (5000 lbs) and the load reaction frame is capable of supporting up to 45 kN (10,000 lbs) in tension or compression. The disadvantage of this system is that air pressure and water pressure control/monitoring is not integrated into the system and manual control is required for applying these pressures as previously mentioned.

Due to the fact that none of the other two sophisticated triaxial units were ready to use at the time the triaxial testing program started, it was decided to utilize the described system for testing on unsaturated specimens. The testing system described in this section is presented in Figure 4-3.

Enhancement on the Triaxial Test Systems

Some pilot dynamic load tests were conducted at the beginning of the study to evaluate the feasibility of the testing procedure. Valuable conclusions regarding the triaxial unit suitability for performing this kind of test were obtained.

In a first attempt, a specimen of 4 inches in diameter and 8 inches high was saturated, consolidated and then subjected to dynamic load. The first important conclusion obtained was related to the time for reaching saturation and consolidation. Given the size of the specimen, the long time to complete the initial

stages of saturation and consolidation were found to be impractical. Then, the size of the soil specimen became a matter of concern.

FIGURE 4-3 Triaxial unit used for testing of unsaturated specimens

In a second attempt, a specimen of 2.8 inches in diameter and 5.6 inches high was tested and it was observed that the conditioning times were substantially reduced. It was clear that all samples should be prepared with smaller dimensions. However, only one bottom pedestal designed for flushing air bubbles out of the system was available. Furthermore, additional problems with the design of the available pedestal were identified. Thus, there was a need of not only

manufacturing new bottom pedestals but also revising the original design. Figure 4-4 shows a picture of the bottom pedestal available for the pilot testing.

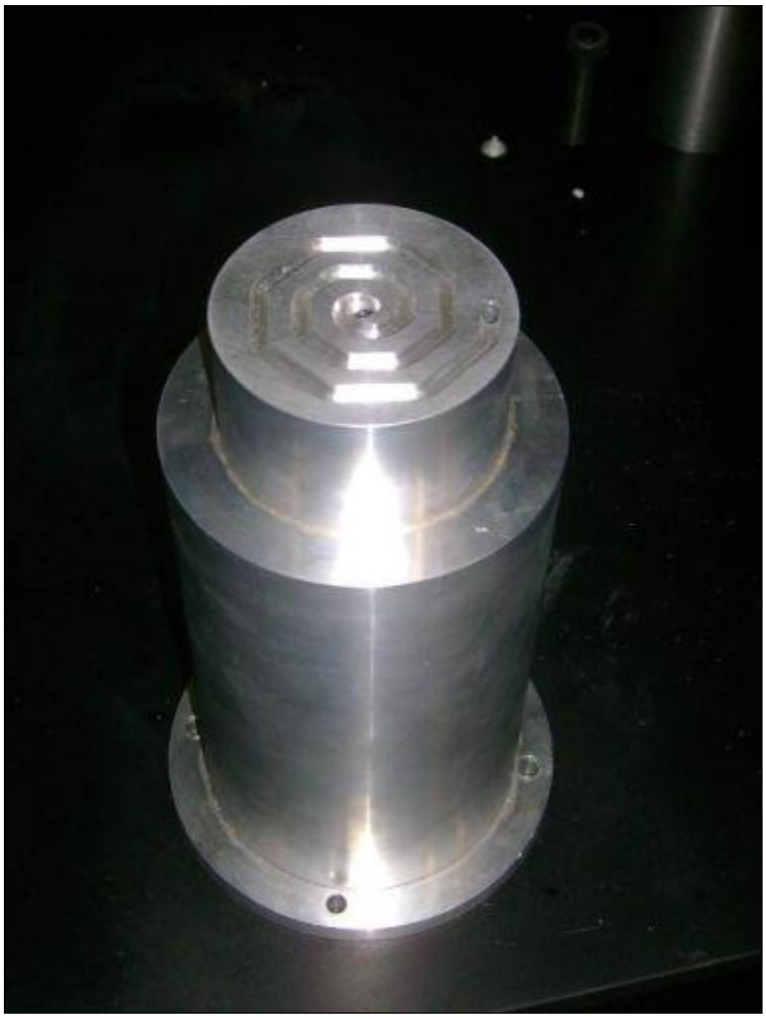

FIGURE 4-4 Bottom pedestal available for pilot testing

Different from conventional bottom pedestals, the water compartment underneath the ceramic disk is elevated 6 inches from the base of the pedestal as can be seen in Figure 4-4. In addition, this design requires the ceramic disk to be directly glued to the top of the pedestal in face to face manner as shown in the left hand drawing in Figure 4-5. As a result, the gap left by the existing epoxy

bonding the top face of the pedestal to the bottom face of the ceramic becomes a spot where air bubbles can be easily trapped.

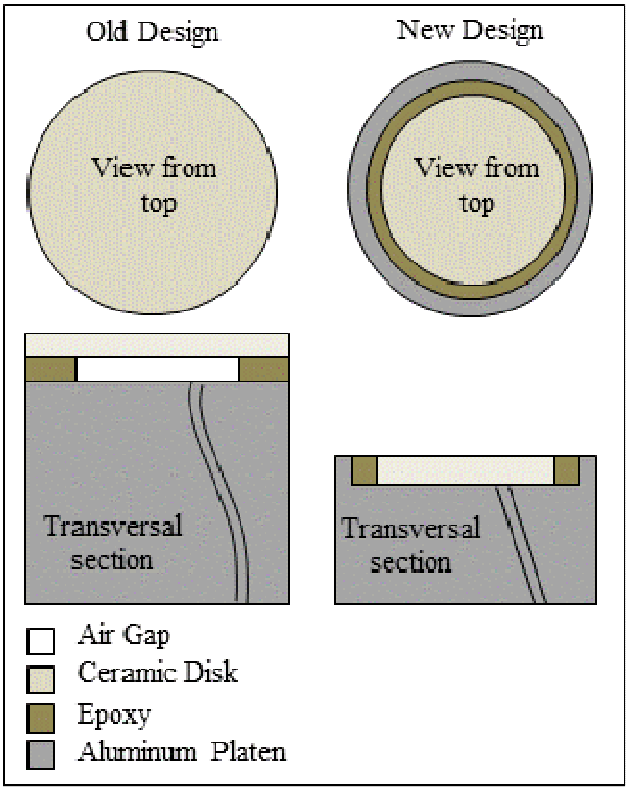

FIGURE 4-5 Simple schematics of the old and new bottom pedestal designs

When flushing the water from reservoir of the bottom pedestal used for the pilot testing, it was observed that air bubbles did not stop coming out even though the system was repeatedly flushed. A possible presence of leaks driving air towards the *PVCs* was discarded by performing a constant water volume test (once the system was free of air bubbles) under air confining pressure acting on the top of the saturated ceramic disk.

It was observed that bubbles came out only from the bottom pedestal towards the flushing line but not towards the *PVC*. In other words, surprisingly, bubbles were coming out only in one way. When checking for possible reasons,

any chance for internal leaks within the epoxy surrounding the ceramic disk or for cracks in the ceramic disk was discarded by checking the response of the pore water pressure transducer to increases in the confining pressure.

The only possible reason for the presence of air bubbles was a deficiency in the bottom pedestal design. The considerable length and non-linear path of water feeding bored holes increase the possibility for internal manufacturing imperfections. These internal imperfections in the bored holes along with the gap left by the epoxy as previously discussed were determined to be the reasons for the difficulties experienced when flushing the air bubbles out of the system. Then, manufacturing of new bottom pedestals with changes in the design were required before performing further testing.

The requirements for the new revised design were: to eliminate the face to face mechanism for bonding the ceramic disk to the pedestal, and to reduce the elevation of the water reservoir with respect to the base of the pedestal. On the right hand drawing of Figure 4-5, a preliminary idea of what was wanted for new design is presented.

Finally, the part was completely redesigned and the drawings were sent to the ASU machine shop for the manufacture of two new bottom pedestals. The revised design drawings are included in Appendix A. Figures 4-6 and 4-7 show the new manufactured bottom pedestals that were utilized in the dynamic load testing program for this study. Note that the pedestal in Figure 4-6 has a porous stone attached for testing on saturated soil specimens while the pedestal in Figure 4-7 has a ceramic disk bonded for testing on unsaturated soil specimens. A third

bottom pedestal of 4 inches diameter from a third triaxial unit was machined to 2.8 inches diameter. However, it could not be used due to problems encountered in the unit when conditioning the triaxial system.

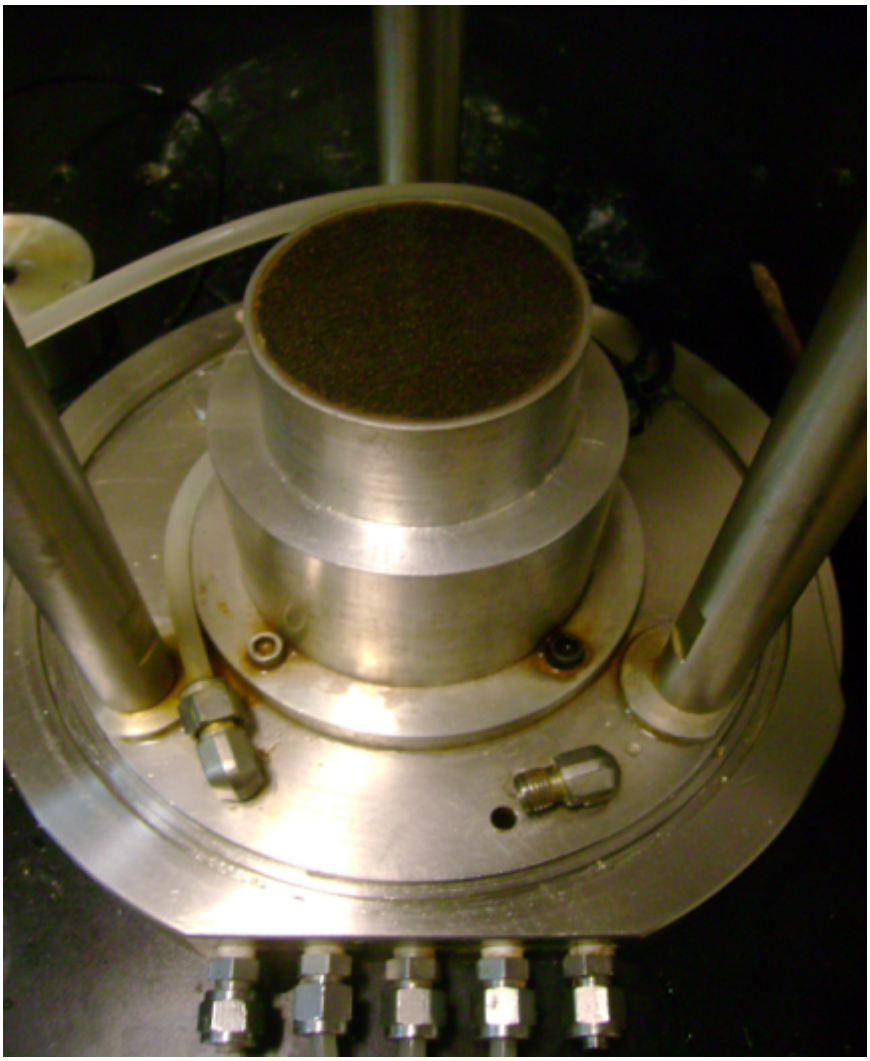

FIGURE 4-6 New bottom pedestal used for saturated testing

FIGURE 4-7 New bottom pedestal used for unsaturated testing

Triaxial Tests on Saturated and Unsaturated Soils

The triaxial test is the most common method used to measure the stiffness of soils in the laboratory. Cylindrical soil specimens isolated from the confining fluid by latex membranes are placed and tested in triaxial cells. The cell is filled with a confining fluid and pressurized in order to apply a uniform all-around confining pressure. Then, the soil specimen is subjected to axial stresses (static or dynamic) through a loading ram that is in contact with the top of the specimen.

Different procedures, associated with the drainage conditions imposed during test, are available for triaxial testing. Such procedures are summarized and compared in the next sections.

It should be recognized that these procedures were originally conceived for use in shear strength test. However, there are basic principles used in the triaxial shear strength test that apply to all other triaxial test types including those that involve dynamic load.

Consolidated Drained Test (CD)

- After saturation is achieved (when required), the soil specimen is consolidated to a stress state representative of field conditions and then sheared under drained conditions (drainage valves open) for both the pore-air and pore-water phases.
- The consolidation is performed under isotropic confining pressure, the pore air and the pore water pressures are controlled (at positive values-axis translation technique).
- During shear, the deviator stress increases until reaching the failure condition, the net confining pressure and matric suction remain constant throughout the test.

Constant Water Content Test (CW)

- After saturation is achieved (when required), the soil specimen is consolidated first and then sheared under drained conditions for the air phase and undrained mode for the water phase.

- The consolidation is performed under isotropic confining pressure, the pore air and the pore water pressures are controlled (at positive values-axis translation).
- During shear, the deviator stress increases until reaching the failure condition, the pore air is under drained conditions (valve opened) and the pore water is under undrained conditions (valve closed).
- The net major principal stress reaches a failure value, the net confining pressure remains constant throughout the test and matric suction changes to a failure value.

Consolidated Undrained Test with Pore Pressure Measurements (CU)

- After saturation is achieved (when required), the soil specimen is consolidated first and then sheared under undrained conditions for the air phase and water phase.
- The consolidation is performed under isotropic confining pressure, the pore air and the pore water pressures are controlled (at positive values-axis translation).
- During shear, deviator stress increases until the failure condition, the drainage valves are closed for both the pore air and the pore water phases. Excess pore air and pore water are developed during undrained loading.
- The net major principal stress reaches a failure value, the net confining pressure and matric suction changes to a failure value due to the development of pore air and pore water pressures.

- It is difficult to maintain a fully undrained condition for the pore air because air diffuses through the pore water, rubber membrane, and other parts of the triaxial apparatus.

Undrained Test

- The soil specimen is subjected to a net confining pressure and matric suction first and then sheared under undrained conditions for the air phase and water phase (not consolidated). The volume of the specimen may change due to compression of pore air.
- During shear, the deviator stress increases until the failure condition and the drainage valves are closed for both the pore air and the pore water phases. Excess pore air and pore water are developed during loading but are not commonly measured. Results are commonly used with a total stress formulation of a problem.
- The net major principal stress reaches a failure value, the net confining pressure and matric suction changes to a failure value due to the development of pore air and pore water pressures.
- It is difficult to maintain a fully undrained condition for the pore air. Air diffuses through the pore water, rubber membrane, and other parts of the triaxial apparatus.

Unconfined Compression Test (UC)

- The soil specimen is not subjected to a net confining pressure. The pore air pressure is assumed to be atmospheric and the specimen has a negative pore water pressure.

- During shear, the deviator stress increases until the failure condition and the deviator stress is equal to the major principal stress. The load is applied quickly in order to simulate undrained conditions. Excess pore air and pore water are developed during loading but are not measured.
- There are three possible stress paths depending on whether the matric suction increase, decrease or remains constant.
- Generally the matric suction will decrease, when this occurs, the pore air pressure is assumed to increase slightly and therefore the net confining pressure will decrease to a negative value. The net major principal stress reaches a failure value.
- In the case of constant matric suction, the pore air and pore water are assumed to remain constant during compression. In this case the net confining pressure at failure will be equal to the initial one and the major principal stress will reach a failure value.
- Unconfined compression tests on unsaturated soils commonly underestimate the available shear strength since confining pressure contribution to strength is not considered.

Triaxial Test Procedures Selected for the Study

Among the triaxial test procedures available for soil testing; the dynamic loading tests performed in this study can be defined as either consolidated undrained (*CU*) or constant water content test (*CW*) depending on whether the test is performed on saturated or unsaturated soil specimens. When running the test on saturated specimens, the test procedure will include a saturation stage.

When required, after the saturation stage was completed, a consolidation stage at the desired initial conditions was conducted. These stages will be discussed in detail in following sections.

The confining pressure in a conventional shear strength test remains constant through the whole test. In the dynamic load test conducted for this study the confining pressure was also constant through the whole test.

The drainage conditions are exactly the same as in the *CU* or *CW* shear strength tests. Ideally, it would be desirable to run the test for both saturated and unsaturated specimens under undrained conditions. However, due to the need for maintaining the air pressure positive and constant when applying the axis translation technique, the test condition on unsaturated specimens becomes drained for the air phase. Therefore, the *CW* test is the suitable procedure to follow for unsaturated conditions.

Since under saturated conditions the matric suction is equal to zero, there is no need for the application of the axis translation technique. In this case, both the air phase and water phase were set undrained. Therefore, under saturated conditions the procedure followed corresponds to a *CU* triaxial test.

CHAPTER 5. DYNAMIC LOAD TESTING PROGRAM

This chapter deals with the second stage of the laboratory program that covers the dynamic load testing. The selection of the levels for the variables to be controlled in the test is discussed. Details of sample preparation and every single stage of the test are also presented. The dynamic load test results are summarized at the end of the chapter.

Dynamic Load Testing Program

This second part of the lab testing program included dynamic load testing on a low plasticity coarse grained soil. Specimens molded at optimum conditions were conditioned and tested using two different drainage conditions as discussed in previous sections. In this section, the selection of variables to control and their corresponding levels are discussed. A table summarizing the laboratory testing program is provided at the end.

As discussed in previous sections, pavements systems are subjected to a stress state characterized by three stress variables: deviator stress, confining pressure (net or effective) and matric suction. In the pavement materials field, traffic load is usually simulated by applying repeated load to a cylindrical soil specimen.

Subgrade soils containing fines in their composition are likely to experience undrained conditions for the water phase when subjected to repeated load. As a result, excess pore pressure is expected to develop and accumulate as the repeated loading process progresses. Knowing that the pavement is subjected

to atmospheric pore air pressure which remains constant in the field, it is expected that the buildup of pore water pressure will produce either a decrease in the effective stress under saturated conditions or a decrease in matric suction under unsaturated conditions. Both conditions in the practice translate into degradation of the soil stiffness.

It has been discussed in this study that traffic loading has singular characteristics which makes of this dynamic loading pattern different to those observed in the case of earthquakes or offshore platforms. Even though some predictive techniques have been found in the literature, none of them includes all factors presumed to be of importance when estimating excess pore pressure as a result of traffic loading.

The effect of some of the most important variables that discussed in previous sections was evaluated in this laboratory testing program. Some others were left aside for future research. However, it is believed that results of this testing program will greatly contribute to the understanding of the effect of traffic loading upon the buildup of pore water pressure in subgrade soils.

Controlled Variables

Six variables were considered as potential predictors for the pore water pressure buildup in cohesive soils subjected to dynamic load. The six variables were divided into two groups: the first one includes variables related to the stress state and the second one relates the dynamic behavior of the excess pore pressure to the load configuration. A third important group of variables are related to the soil type. However, due to the time demanding nature of the tests performed, it was

not possible to evaluate the influence of the soil type as only one material was tested.

Variables Related to the Soil Stress State

The first group of variables includes the cyclic deviator stress σ_d and the **initial** matric suction ψ_{mo} which define the state of stress acting on the soil. The confining stress σ_3 was set constant for all tests.

The cyclic deviator stress was controlled at two levels. These two levels are defined by the ratios of major principal cyclic stress (σ_1) to minor principal stress (σ_3). The ratios selected are 2 and 4 for low and high levels of cyclic deviator stress respectively.

Both ratios were selected from the loading procedure for coarse grained subgrades observed in the new resilient modulus test protocol NCHRP 1-28A. The ratio of 2 is intended to represent an average condition within the range of stresses applied in such procedure. The ratio of 4 is the highest level considered in the resilient modulus loading procedure. In order to make use of the maximum stress magnitudes found in the procedure, the confining stress for both ratios 2 and 4 was set at 83 kPa. As a result, the high level of deviator stress applied in the tests was 248 kPa and corresponds to the maximum value from the resilient modulus loading procedure. For a stress ratio of 2, the corresponding deviator stress was 83 kPa, which is also equivalent to the confining stress.

The deviator stress magnitudes applied were translated in terms of the bulk stress invariant. It should be mentioned that an additional contact load equal to 12.4 kPa was used in the dynamic load test. Thus, the low deviator stress level

corresponded to a bulk stress of 344 kPa and the high deviator stress level corresponded to a bulk stress of 509 kPa. From this point on, the bulk stress will reflect in reality the deviator stress level utilized in the testing program. Table 5-1 presents the breakdown for the two levels of external stresses applied in the dynamic load test. Note that the stresses shown below are the effective or net magnitudes applied during the test, meaning that the effects of internal stresses are already reflected in the values. The total stresses magnitudes actually applied during the test are detailed in following sections.

TABLE 5-1 Breakdown of external applied stresses

Stress Ratio, $\sigma_{1Cyclic} / \sigma_3$	2	4
Cyclic Deviator Stress, $\sigma_{d\ cyclic}$ (kPa)	83.4	248.4
Contact Deviator Stress, $\sigma_{d\ contact}$ (kPa)	12.4	12.4
Total Deviator Stress, $\sigma_{d\ total}$ (kPa)	95.8	260.8
Vertical Stress, σ_1 (kPa)	178.6	343.6
Confinning Stress, σ_3 (kPa)	82.8	82.8
Bulk Stress, θ (kPa)	344.2	509.2

In a similar way, the initial matric suction corresponding to two different moisture conditions was selected to be controlled in the test. The initial matric suction values were obtained out of the *SWCC* measured in the preliminary laboratory testing presented in Chapter 3. The levels of matric suction selected were meant to correspond to saturated conditions and 85% degree of saturation. Initial matric suction values of 0 kPa corresponding to 100% degree of saturation and 157 kPa corresponding to 85% degree of saturation were used in the tests.

Variables Related to the Repeated Load Pattern

The second group includes the number of cycles *N*, stress pulse loading time t_L and dwelling time t_D which define the load configuration. The number of cycles for the test was not fixed constant. The number of load repetitions applied for each test varied depending on different factors like: premature failure of the sample, problems encountered with the equipment prior to test completion, etc. In general, the number of load repetitions applied ranges from 16,000 to 96,000.

The loading time was fixed constant as some evidence of no influence upon the pore pressure buildup (within a range of interest for pavement applications) was found in the literature. When selecting the loading time, it was considered a priority to use a frequency that allows time to the triaxial system to properly reproduce the wave shape and record reliable data. Also this value was meant to fall within a range representing field conditions.

In order to determine a reasonable loading time a numerical analysis was performed. When a wheel load is at a considerable distance from any point of interest within the pavement system, the stress acting on that particular point is zero. As the load approaches to the considered point, the stress increases becoming maximum when the load is directly above that point. Then, it is reasonable to assume that the load wave has a haversine shape (*7*). The duration of such load can be determined using Equation 5-1 which is function of both the vehicle speed and the depth of the point below the surface of the pavement.

$$t_L = \frac{L_{eff}}{17.6 v_s} \tag{5-1}$$

Where:

t_L = time of load in seconds

L_{eff} = effective length in inches

v_s = velocity in miles per hour

The effective length defines de duration of the load pulse and can be determined using Equation 5-2:

$$L_{eff} = 2.\left(a_c + Z_{eff}\right) \tag{5-2}$$

Where:

a_c = radius of the contact area in inches

Z_{eff} = effective depth in inches

The effective depth is obtained by following the method of equivalent thicknesses proposed by Odemark and assuming the Poisson's ratio the same for all layers (*41*). According to Odemark, the equivalent thickness is function of the elastic modulus and layer thicknesses of the pavement system. The effective depth for a particular point of interest within the pavement structure can be obtained using the Equation 5-3:

$$Z_{eff} = \sum_{i=1}^{n-1}\left(h_i \sqrt[3]{\frac{E_i}{E_{SG}}}\right) + h_n \sqrt[3]{\frac{E_n}{E_{SG}}} \tag{5-3}$$

Where:

E_{SG} = elastic modulus of the subgrade

E_i = elastic modulus of the i^{th} layer above the point of interest

h_i = thickness of the i^{th} layer above the point of interest

E_n = elastic modulus of the n layer where the point of interest is located

h_i = depth from the top of the *n* layer to the point of interest

The equations presented above where used to estimate the loading time for different vehicle speeds and at a point of interest located 2 inches below the top of the subgrade. The following input data was assumed in order to perform the computations:

- The radius of contact area is equal to 3.5 inches for a single axle configuration.
- The pavement system has three layers: asphalt concrete, granular base and subgrade.
- The asphalt concrete layer has a modulus of 500,000 psi and thickness of 8 inches.
- The granular base layer has a modulus of 40,000 psi and thickness of 8 inches
- The subgrade has a modulus of 10,000 psi and infinite thickness.

The results of the analysis are presented in Table 5-2.

TABLE 5-2 Loading time as function of vehicle speed

Vehicle Speed (mph)	Z_{eff} (in)	L_{eff} (in)	t_L (s)	f (Hz)
5	44.2	95.3	1.08	1
15	44.2	95.3	0.36	3
40	44.2	95.3	0.14	7
70	44.2	95.3	0.08	13
100	44.2	95.3	0.05	18

According to the results in Table 5-2, the maximum loading time observed is 1.08 seconds corresponding to a vehicle traveling at 5 mph on a pavement system with the characteristics assumed for this exercise. At very high speeds the loading time is below 0.1 seconds. Therefore, by using a loading time of 1 second, one of the worst case scenarios (slow moving load) expected in the field can be reproduced in the laboratory. Also, a loading time of 1 second is a reasonable time for the triaxial system to reliably reproduce the required haversine shaped pulse and provide accurate data at the same time.

The dwelling time was controlled at 4 and 8 seconds corresponding to low and high level for this variable. Since the loading time selected for the dynamic load test is 1 second, when adding the dwelling time the resulting total time per load cycle is either 5 or 9 seconds. The dwelling times proposed simulate traffics of 17,280 (low dwelling time level) and 9,600 (high dwelling time level) number of traffic load repetitions per day. These numbers may also correspond to traffic levels of about 63.1 and 35 millions of repetitions respectively for a pavement service life of 10 years.

Such numbers represent traffic levels higher than those actually registered in the field. Therefore, it is concluded that the values selected for dwelling time are reasonable and represent the extreme conditions that a pavement may experience during a life span of 10 years. Also, these values allow the testing system to acquired data for a duration of time long enough to capture pore water pressure dissipation trends and differences between responses at different dwelling times.

Variables Related to the Soil Type

The third group includes the indicators of soil type. Among the potential parameters to be considered as predictive variables are the hydraulic conductivity *k* (permeability) and the plasticity index *PI* of the soil. As presented in previous chapters, the *PI* of the material evaluated is 7 and the saturated hydraulic conductivity is 2.724×10^{-8} m/s.

Unfortunately, due to the time demanding nature of the test, only one soil type was evaluated in this study. Therefore, the influence of soil type is not evaluated. However, even when the *PI* is the same for all the specimens tested, the hydraulic conductivity for the saturated specimens was different from the one for unsaturated specimens. Based on that, in reality the effect of hydraulic conductivity was evaluated at two levels.

If the influence that soil type has upon the pore water pressure response was exclusively a function of the hydraulic conductivity regardless of the material *PI*, then it would be likely that the difference in response between two specimens of the same soil type but tested at different suction levels (therefore different hydraulic conductivities) is similar to the difference in response between two specimens of different soil types (having hydraulic conductivities similar to those found for a single soil type at different suction levels) and tested at the same suction level. The previous hypothesis is explained in Figure 5-1.

If the hypothesis discussed above were true, then the effect of the soil type upon the pore water pressure development would be indirectly evaluated. Some conclusions based on this assumption are presented in following sections.

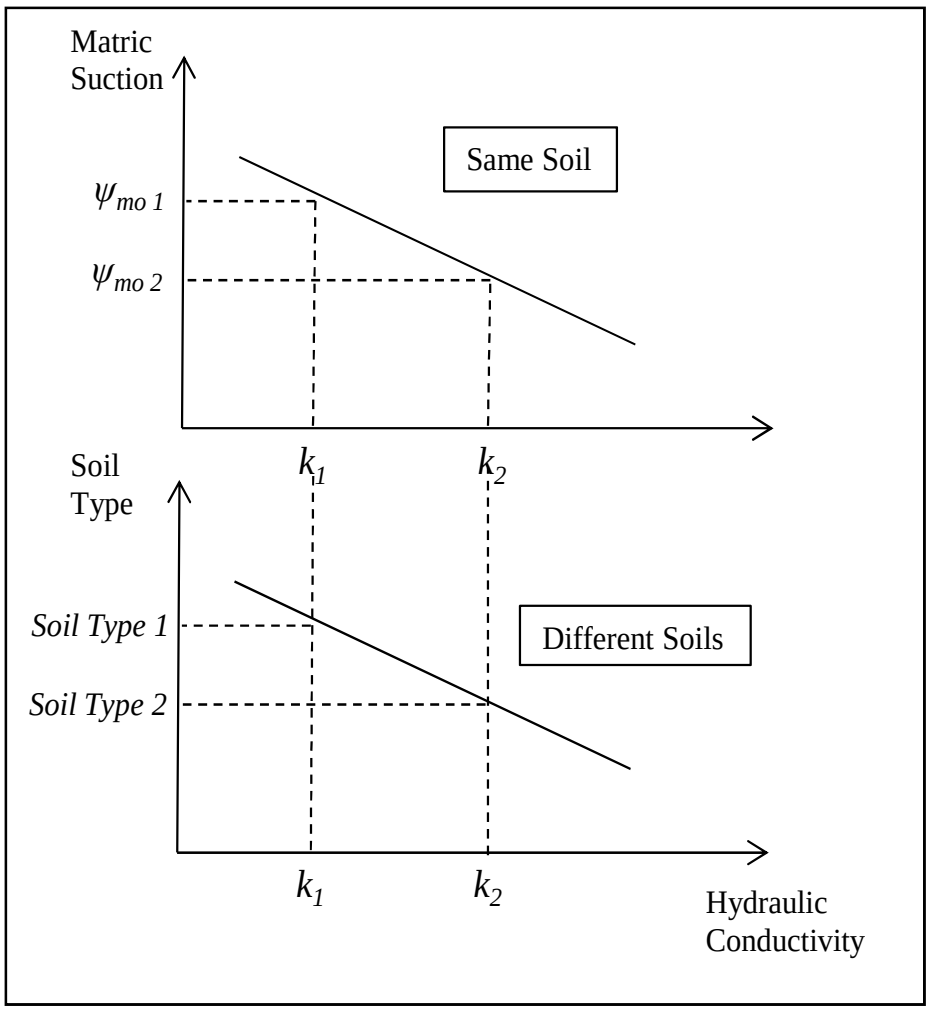

FIGURE 5-1 Hypothetical correspondence of k to both soil type and ψ_{mo}

Dynamic Load Test Factorial

No replicates are contemplated for this testing program as every single test was expected to be highly time consuming. According to the variables established for the testing program, the test factorial is summarized as follows:

- 2 bulk stress levels - θ
- 2 initial matric suction levels - $\psi_{mo} \approx$ 2 permeability – k_w (soil type)
- 1 loading time levels - t_L
- 2 dwelling time levels – t_D

A total of 8 dynamic triaxial tests would be required to complete the factorial. However, due to the difficulties encountered, only **6 tests** were successfully conducted. A better arrangement of the complete factorial is presented in Table 5-3. The details about the test conditions applied to the 6 specimens that were tested are presented in next sections.

TABLE 5-3 Dynamic load test factorial

Controlled Variables					
Variable	Symbol	Group	Levels	Low	High
Bulk Stress	θ	Stress State	2	344 kPa	509 kPa
Initial Matric suction	ψ_{mo}	Stress State	2	0 kPa	157 kPa
Loading Time	t_L	Load Conf.	1	1s	1s
Dwelling Time	t_D	Load Conf.	2	4s	8s
Number of Runs Performed					6 tests

Specimen Preparation

According to the dynamic load testing program, 6 specimens were prepared for testing the IOSG subgrade material. The dry material was wetted and mixed to get a homogeneous condition in the soil. The prepared mix was then stored in a sealed plastic Ziploc bag and was left to equilibrate in a controlled temperature room for about not less than 3 days. Once the material was ready, the compaction of the specimen was performed.

As previously mentioned, the specimen dimensions for the pilot testing performed to evaluate the condition of the triaxial units were 4 inches in diameter and 8 inches in height. Then, based on the pilot testing results it was determined

that using smaller dimensions would help to reduce either the saturation or equilibration time. Therefore the dimensions utilized to compact the specimens for dynamic load test are 2.8 inches in diameter and 5.6 inches in height. The mold and tools utilized for compaction are shown in Figure 5-2.

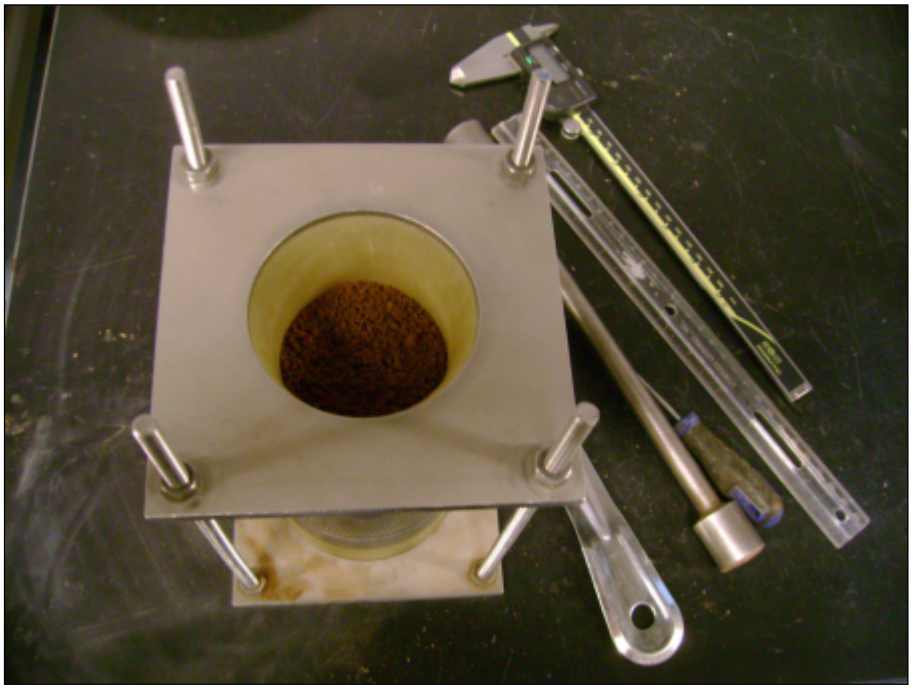

FIGURE 5-2 Split mold and tools used for compaction

Each specimen was compacted in 8 layers of 0.7 inches using a plastic split mold and a latex membrane to avoid the specimen sticking to the plastic surface of the mold during its extraction.

Since the contact area of a standard compaction hammer was found to be large compared to the cross sectional area of the specimen, it was decided to compact the specimen using a small tamper. The density of the specimen was controlled for each layer of 0.7 inches by compacting the estimated weight of material necessary to achieve the desired density for such height.

The target moisture content and dry density was the average optimum and maximum obtained from both standard compaction curve replicates ($w\%_{opt}$ = 12.1%, $\rho_{d\ max}$ = 1.906g/cm^3). At the end of the compaction of the 8th layer, the top face of the specimen was leveled to get a flat contact surface for testing as shown in Figure 5-3.

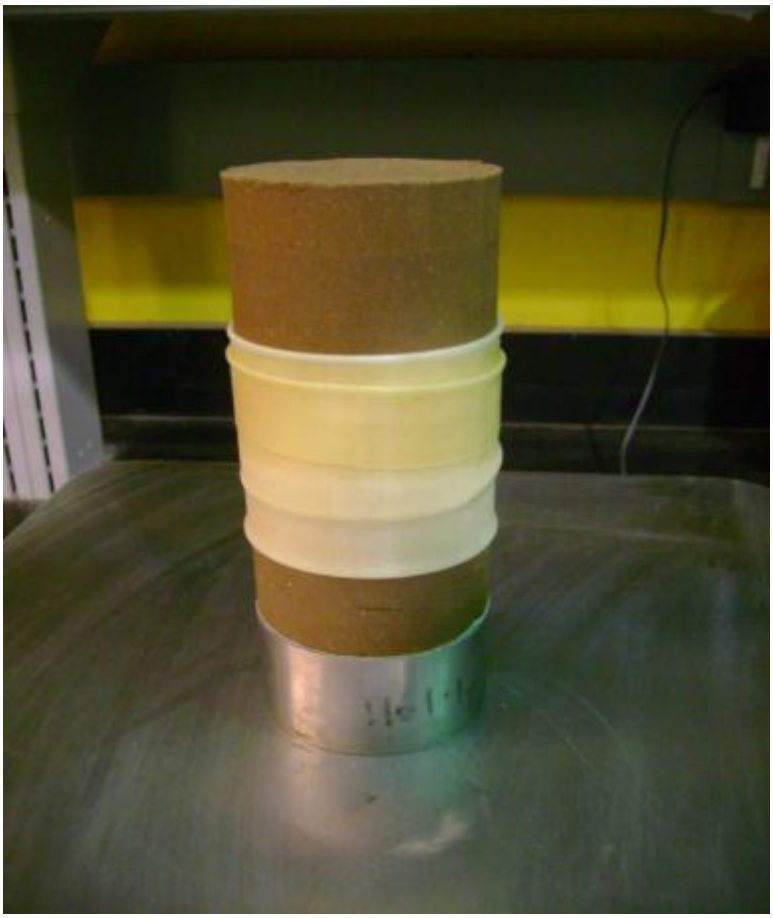

FIGURE 5-3 Leveled top surface of specimen after compaction

Once compacted; the specimen was weighted, and the diameter and height were accurately measured using a caliper in order to control the dry density achieved as shown in Figures 5-4 and 5-5. The same procedure was repeated for all the 6 specimens.

Once the measurements were taken after compaction, the specimens to be tested under unsaturated conditions were wetted on a scale using a sprayer filled with de-aired water and controlling the weight. The objective of the pre-wetting procedure was to get as close as possible to the estimated moisture content corresponding to the desired initial matric suction according to the *SWCC*. However, later it was found that actually these specimens dried up when subjected to the 153 kPa of matric suction.

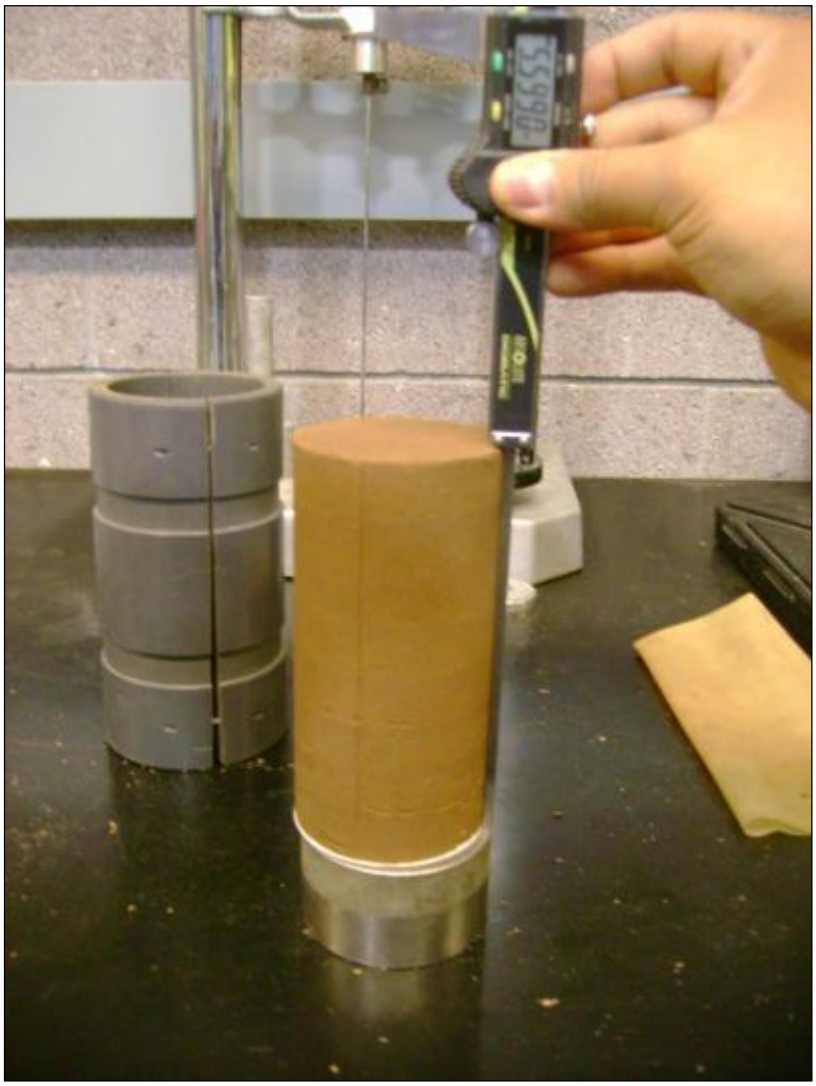

FIGURE 5-4 Measurement of specimen height after compaction

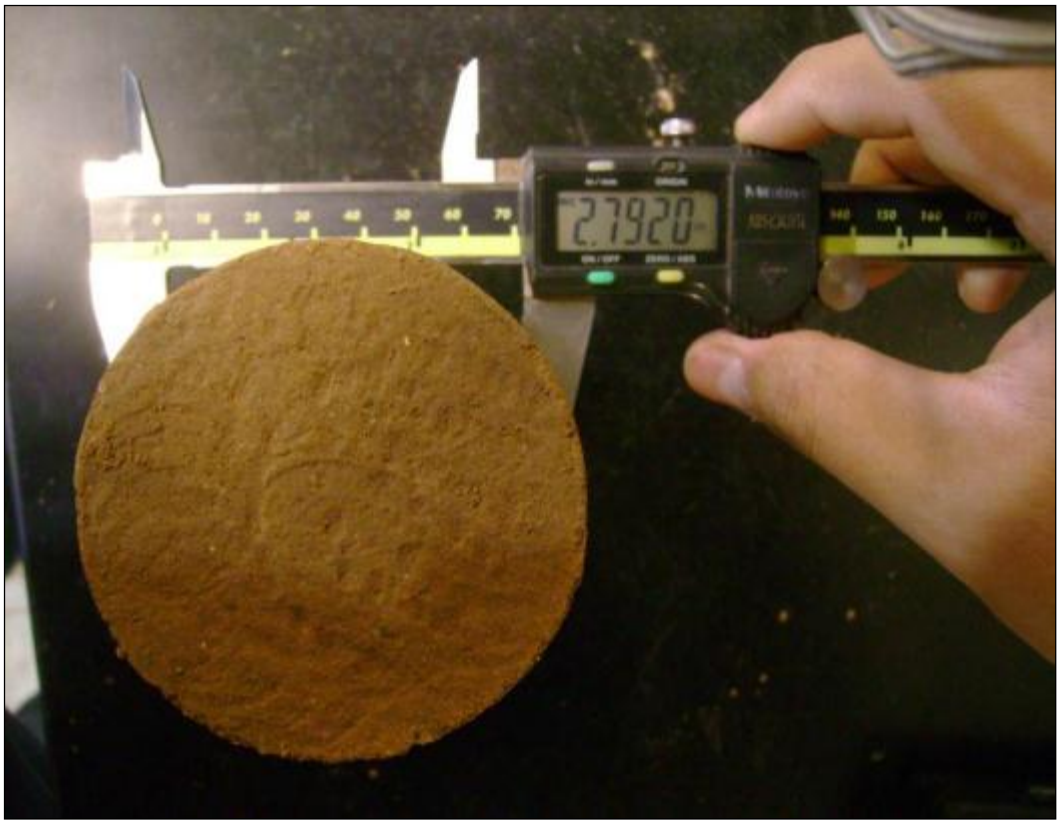

FIGURE 5-5 Measurement of specimen diameter after compaction

Then, the pre-wetted specimens were covered with the latex membrane and placed between aluminum platens. Rubber o-rings were used as seals between the membrane and the platens to prevent loss of moisture. After that the specimens were carefully placed in Ziploc bags and left to equilibrate for achieving uniform moisture distribution in a controlled temperature room for 24 hours. Once equilibrated, the specimens were mounted in the triaxial cell for testing.

Different from the specimens to be tested under unsaturated conditions, those to be tested under saturated conditions were directly covered with the latex membrane and mounted immediately in the triaxial cell.

Table 5-4 shows the moisture content *w%*, dry density ρ_d, and degree of saturation *S%*, obtained after compaction as well as the test conditions that were applied for each specimen. Note that the volumetric stress invariant could be defined either as net bulk stress ($\theta_{net} = \theta - 3u_a$) for unsaturated conditions or effective bulk stress ($\theta' = \theta - 3u_w$) for saturated conditions. Also, for triaxial conditions, the bulk stress is: $\theta = \sigma_1 - 2.\sigma_3$, as previously presented in Equation 2-4.

TABLE 5-4 Density control and test conditions for specimens

Specimen	1	2	3	4	5	6
Diameter (in)	2.78	2.77	2.79	2.76	2.77	2.78
Height (in)	5.58	5.58	5.57	5.59	5.57	5.60
Volume (cm^3)	553.0	552.6	553.1	548.1	549.8	547.8
Weight (g)	1199.6	1181.9	1200.7	1183.9	1182.6	1182.3
w (%)	12.14	12.43	12.14	12.02	13.03	12.15
ρ_d (g/cm^3)	1.934	1.902	1.907	1.928	1.903	1.925
$\rho_{d\ target}$ (g/cm^3)	1.906	1.906	1.906	1.906	1.906	1.906
S (%)	81	79	78	80	83	80
θ_{net} or θ' (kPa)	509	344	509	344	509	344
ψ_{mo} (kPa)	157	157	0	0	157	157
t_D (s)	4	4	4	4	8	8

Specimen Conditioning

Different procedures were followed for conditioning depending on whether the specimen was saturated or unsaturated. In the following sections these conditioning procedures are discussed.

Conditioning for Saturated Specimens

The conditioning conducted on these specimens consisted basically in the saturation and consolidation procedures. These procedures are subdivided in three steps as follows.

Mounting the Specimen on the Triaxial Cell

The specimen, which is already covered by the latex membrane, is mounted on the triaxial cell. Filter paper is placed between the porous stone (bonded to the bottom pedestal) and the base of the specimen. The use of the filter paper is basically intended to prevent clogging of the porous stone. In the same way, filter paper is used between the top of the specimen and a top porous stone that is also placed on top of the specimen. Finally, the aluminum platen if placed on top of the porous stone.

Before rolling the membrane over the top platen and bottom pedestal, it is necessary to make sure that the surface area of the platens to be in contact with the membrane is clean. Then the contact area is coated with some vacuum grease to enhance the sealing. After sliding the membrane over both the top and bottom platens; o-rings are placed on the platens, which are already covered by the membrane, to provide an efficient seal and to make sure that the specimen will be isolated from the confining fluid. Figure 5-6 shows how a specimen should be properly mounted on the triaxial pedestal and isolated.

Once the specimen is ready in place, the cell wall must be installed and properly tightened to ensure an efficient pressurization when applying the confinement. The confining fluid utilized for this series of dynamic load tests is

de-aired water. The water should be de-aired by heating and applying a vacuum to the water tank for a period of 24 hours. With the specimen ready and the water de-aired, the next step is to proceed to saturate the specimen by applying backpressure.

FIGURE 5-6 Specimen mounted on the triaxial pedestal

Saturation of the Specimen

As previously mentioned, de-aired water is used as confining fluid to prevent migration of air through the latex membrane. Once the triaxial cell is filled up with de-aired water, it is important to make sure that every single house in

the system is free of air bubbles. After flushing the air bubbles out of the system, the specimen is progressively back-pressurized from bottom to top until saturation is successfully achieved.

During back-pressurization, the difference between the confining pressure and the back-pressure should be always positive. For the specimens tested on this study, during back-pressurization the effective stress was kept at 30 kPa. Both the confining pressure and backpressure should be progressively increased to allow for a uniform pressurization and distribution of water within the soil structure. Also, back-pressurization is conducted stepwise to ensure that most of the air is successfully removed from the specimen.

The pore pressure *B* parameter should be determined to check for saturation of the soil. This is done by increasing the confining pressure and measuring the increase of pore pressure in the specimen. If the ratio of the increment in confining pressure to the increment in pore pressure is greater than 0.92, then it can be assumed that the specimen is saturated. In the present study, the time needed to achieve saturation was about one month for each specimen.

Consolidation of the Specimen

The next step is to consolidate the specimen to the desired initial confining effective stress. Consolidation is assumed to be achieved when the change in water volume under the applied confining stress becomes negligible. For the present study, the initial effective confining stress σ_3' was 83 kPa as

discussed in previous sections and the consolidation of saturated specimens was achieved in 24 to 48 hours.

Conditioning for Unsaturated Specimens

The conditioning conducted on these specimens consisted basically in the consolidation of the soil under the desired initial conditions for dynamic test. This procedure is subdivided in two steps as follows.

Mounting the Specimen on the Triaxial Cell

For unsaturated specimens, the procedure for mounting the specimen on the triaxial cell is basically the same except for some slight differences. Different from the saturated specimens, the bottom pedestal does not have a porous stone. Instead, a high air entry ceramic disk is glued to the pedestal to provide the triaxial unit with the capability to measure matric suction.

Also, the ceramic disk should be properly saturated prior to starting the test as discussed in previous sections. The saturation of the disk is achieved by pushing de-aired water through the ceramic disk applying a small pressure. In order to do that, the bottom pedestal with the ceramic disk bonded to it, must be submerged under de-aired water inside the triaxial cell. Then, low confining pressure is applied overnight. Saturation of the ceramic disk is achieved when water without air bubbles comes consistently out of the bottom pedestal thorugh the drainage line.

The rest of the procedure for mounting the specimen is basically the same as for saturated specimens.

Consolidation of the Specimen

For unsaturated specimens, the procedure for consolidation of the specimen has a particularity which is the application of the axis translation technique. This technique is used to be able to apply matric suction levels greater than 90 kPa which is the limit negative pore water pressure that can be measured by conventional devices.

As previously discussed, the difference between the pore air pressure and the pore water pressure is defined as matric suction of the soil. In the field, when the air pressure is atmospheric (zero gauge pressure), the matric suction is equal to the negative pore water pressure. By applying the axis translation technique, the origin of reference for the pore water pressure is translated from atmospheric conditions to the positive air pressure applied in the triaxial cell. In this way, the decrease in matric suction does not become highly negative and the problem of air going into solution due to cavitation is prevented.

. Under constant applied matric suction ψ_{mo}, and net confining pressure $\sigma_{3\,net}$, the specimen is expected to reach equilibrium when the change in pore water volume becomes insignificant. As previously discussed, the net stresses are used when dealing with unsaturated soils tested with axis translation technique. The net confining stress $\sigma_{3\,net}$ is the difference between the total confining stress σ_3 applied to the specimen and the pore air pressure u_a imposed internally. Since all the test are intended to conducted under the same confining stress, the net confining stress $\sigma_{3\,net}$ for unsaturated

specimens is exactly the same as the effective confining stress σ_3' used for saturated material: 83 kPa.

The initial matric suction desired for unsaturated specimens is 157 kPa as mentioned in previous sections. This means that under field conditions the pore water pressure would be -157 kPa. In order to apply such level of suction, the origin of reference for the pore water pressure was translated to 177 kPa, meaning that pore air pressure u_a of that magnitude was imposed from the top of the specimen. As a consequence, in order to maintain a matric suction of 157 kPa, the pore water pressure u_w was increased to 20 kPa.

Under constant applied net confining pressure and matric suction the specimen is left to undergo consolidation and reach equilibrium under the desired initial stress state. For this study, equilibration or end of consolidation was assumed to be achieved when the change in pore water volume was equal or less than 0.2 cm^3. Such state was generally reached by the unsaturated specimens in 7 to 10 days.

Dynamic Load Test

Once the conditioning phase was completed, the dynamic load test was performed on the specimens. GCTS CATS v1.6 is the software available for the operation of the testing systems useid in this study. It is a user-friendly Windows 98, XP™ compatible software for automated test control.

The Resilient Modulus Module of the software was utilized to run the dynamic load test. With this module, both the pore water and pore air pressure can be recorded while applying dynamic load. Besides a pre-conditioning sequence, up to 40 different sequences with different stress configuration can be applied per test. The loading configuration (loading and dwelling times) used throughout the test can be customized by the user. In every sequence, data for the last 5 load repetitions is recorded. About 202 data points can be recorded for each single cycle. Half of the data points are collected within the loading time and the other half during the dwelling time.

In general, the higher the number of repetitions applied to the specimen, the better the trend of pore water pressure build up recorded. Based on the experience gained in this study, it was observed that ideally a test run for 90,000 to 100,000 repetitions would provide an important amount of useful data for analysis. However, as shown in next sections, it was not always possible to reach that number of repetitions for all the tests.

Since the triaxial system only records data for the last five cycles of every sequence, it was determined that several tests should be conducted on the same specimen. In this way, a high number of loading cycles can be applied and sufficient amount of data can be collected to appropriately capture the trend of pore pressure development.

For instance, if one single test of 100,000 repetitions was run, then data for the last 5 cycles from 40 sequences of 2,500 repetitions would be collected. This

means that we would be obtaining information only for 5 cycles every 2,500 cycles. In that case, it is possible that valuable data would be missed.

Therefore, in order to obtain representative data, it was decided to run 40 sequences of 400 cycles per test which gives a total of 16,000 load repetitions. Besides, the Resilient Modulus Module utilized to control the test imposes a mandatory pre-conditioning sequence. This sequence was set to only 10 repetitions. Then, a total of 16,010 load repetitions were applied per test.

Obviously, to achieve a high number of load repetitions, consecutive tests should be run. For this study, always a new test was started on the same specimen immediately after the previous test concluded.

The total duration of the dynamic load test varied from one specimen to the other depending on both the number of 16,000 cycles tests performed per specimen and the total duration of the loading cycle (5 or 9 seconds). It can take up to 10 days to apply about 96,000 cycles of 9 seconds per cycle. On the other hand, it only takes 22 hours to complete about 16,000 cycles of 5 seconds per cycle. Table 5-5 shows an estimate of the total duration for tests conducted using different load configurations and different levels of load repetitions. Table 5-5 is intended to give the reader an idea of the duration of the tests performed for this study.

Finally, the test conditions as well as the stress state applied to each specimen in this study are presented in Table 5-6. It should be recalled that the

TABLE 5-5 Dynamic load test duration

Number of Tests per Specimen	Total Duration (days)	
	$t_L + t_D = 5$ s	$t_L + t_D = 9$ s
1	0.9	1.7
2	1.9	3.3
3	2.8	5.0
4	3.7	6.7
5	4.6	8.3
6	5.6	10.0

TABLE 5-6 Specimens stress state and test conditions

Stress (kPa)	Specimen					
	1	2	3	4	5	6
$\sigma_{d\ Total}$	261	96	261	96	261	96
$\sigma_{d\ Contact}$	12	12	12	12	12	12
$\sigma_{d\ Cyclic}$	248	83	248	83	248	83
$\sigma_{1\ net} / \sigma_1'$	344	179	344	179	344	179
$\sigma_{3\ net} / \sigma_3'$	83	83	83	83	83	83
θ_{net} / θ'	509	344	509	344	509	344
ψ_{mo}	157	157	0	0	157	157
S_{target} (%)	85	85	100	100	85	85
t_D (s)	4	4	4	4	8	8

Test Results

In this section, the results of the dynamic load testing are presented. As mentioned in the previous section, a large amount of data was collected for each specimen. For every single test 40 sequences of 400 loading cycles are conducted. Data for

the last 5 cycles from every sequence was recorded. Therefore, information for a total of 200 cycles was obtained.

Considering that about 200 data points were recorded per cycle, the total number of data points per test is about 40,000. It should be recalled that more than one test was conducted for most of the specimens. As a consequence, for obvious reasons it was not possible to show the totality of the data recorded in the laboratory test.

Figure 5-7 shows as an example the type of data obtained for each specimen. In this figure, 202 data points corresponding to one loading cycle are plotted. The data corresponds to a load configuration of 1 second loading time and 4 seconds dwelling time. It should be mentioned that the time origin in the "x" axis was translated to zero in order to show the data example in a friendly scale.

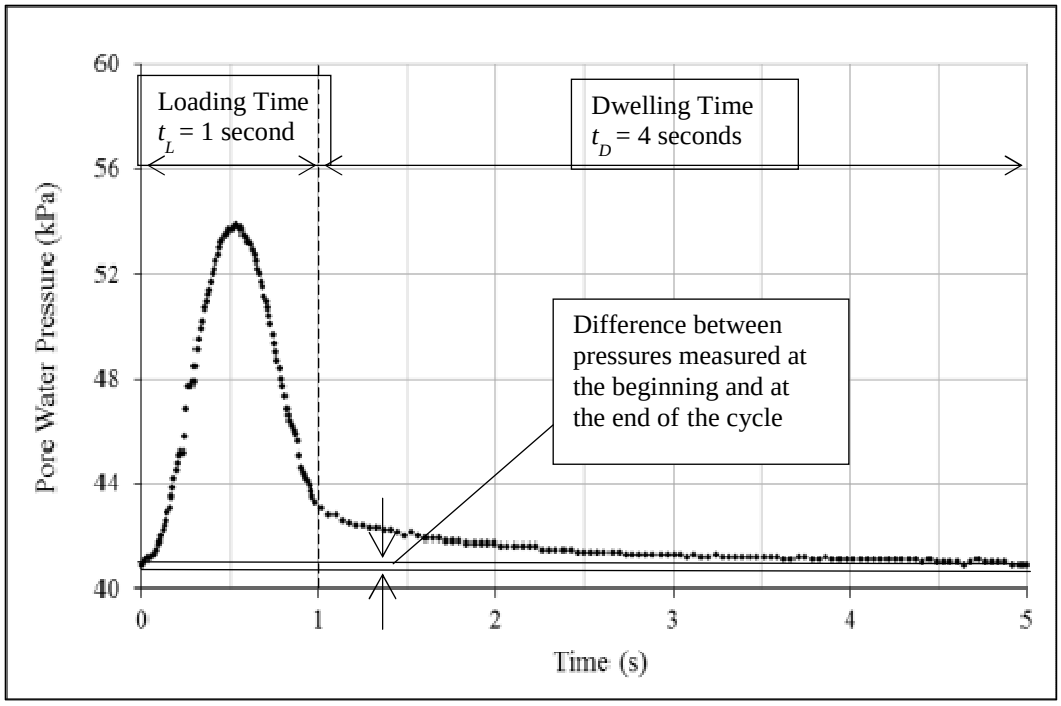

FIGURE 5-7 Example of data collected

As observed, the data clearly shows that the two components of the load configuration: loading time t_L and dwelling time t_D are reflected in the pore pressure response. It is noticeable that there is a peak pore pressure u_p' occurring close to the middle of the loading time. It should be noted that besides the peak pore pressure there are three notable pore water pressure points in the curve: at the beginning of the cycle u_0', at the end of loading time u_1' and at the end of the cycle u_2'.

Also, a slight difference between the pore water pressures measure at the beginning and at the end is observed. Such difference could be considered insignificant when looking at only one cycle but after several cycles, all the small residual accumulated turn out to be a significant buildup of pore water pressure.

Figure 5-8 shows a schematic of the pore water pressure characteristic elements identified by the observation of results. It should be recognized that the pore pressure elements presented in this figure do not represent global accumulated pressures but represent pressures obtained by translating the origin of the "y" axis to zero.

Figure 5-9 shows a representation of how the schematic from Figure 5-8 fits in a global perspective of the measured data. As can be observed, u_0' in Figure 5-8 is the starting point of the pore water pressure buildup cycle *N*. This starting point corresponds to a value $u_{2\text{-}1}$ from the "Global End Cycle Excess Pressure Curve" in Figure 5-9. At the end of the loading cycle *N*, the measured global excess pore pressure $\Delta u_{2\text{-}1}$ is incremented by the resulting residual pore pressure equal to u_2' and becomes a new global excess pressure $\Delta u_{2\text{-}2}$ that belongs to the

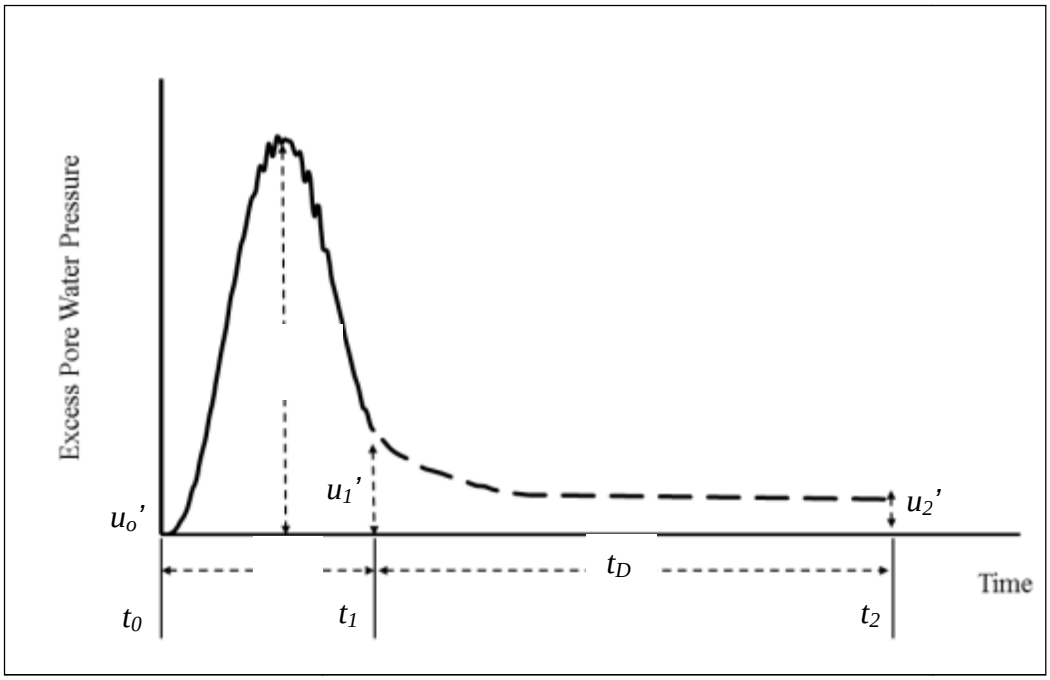

FIGURE 5-8 Pore pressure characteristic elements

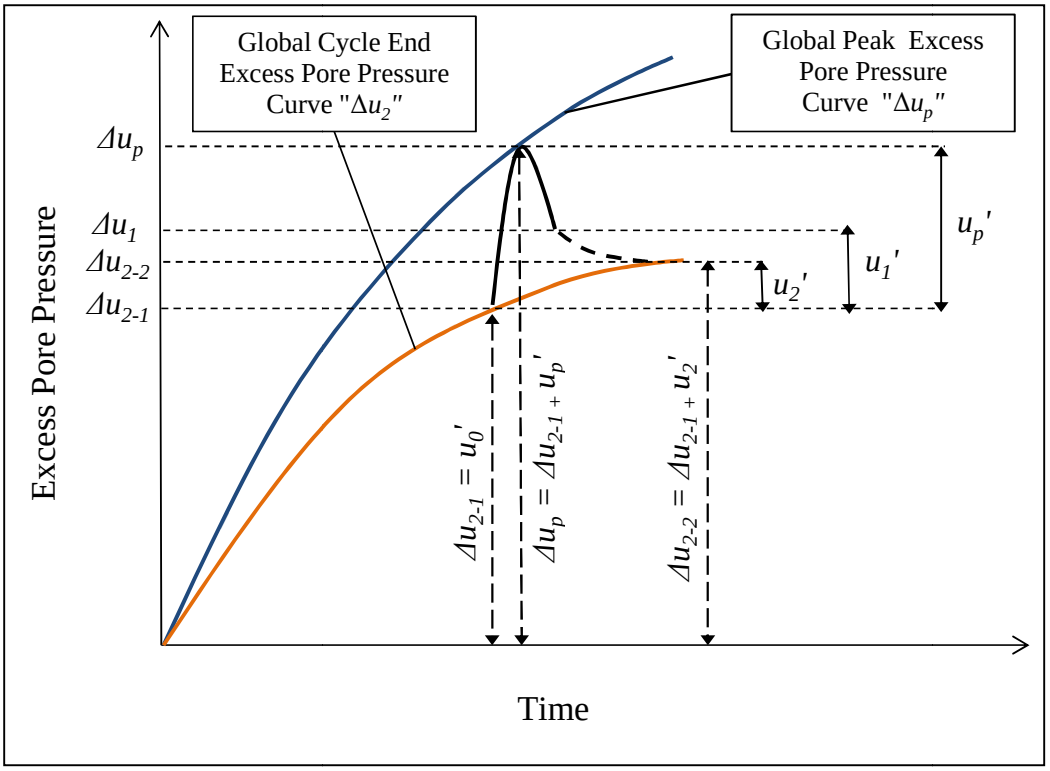

FIGURE 5-9 Global perspective of the pore pressure characteristic elements

same “Global Cycle End Excess Pore Pressure Curve”. A second curve observed in Figure 5-9 is called the “Global Peak Excess Pressure Curve”. This curve captures the maximum global excess pressures registered during the test for each loading repetition. At any cycle *N*, the global peak excess pressure Δu_p is the sum of the measured global excess pressure at the beginning of the cycle $\Delta u_{2\text{-}1}$ and the peak pore pressure u_p’ generated due to the load applied at that particular cycle. Following the same reasoning, the global excess pressure at the end of the loading time Δu_1 can be obtained by adding the pore pressure buildup at the end of the loading time generated due to the load applied at that particular cycle u_1’ to the global excess pressure at the beginning of the cycle $\Delta u_{2\text{-}1}$.

In order to obtain representative data to be presented as a sample of the tests results, both the Global Peak Excess Pressures Δu_p and the Global Cycle End Excess Pressures $\Delta u_{2\text{-}2}$ were extracted from the raw data files. Figures 5-10 to 5-23 were generated using the extracted data and are intended to represent the results obtained from the dynamic load testing program. These plots show the buildup of excess pore pressure versus time.

Figures 5-10 to 5-21 were plotted using the same scale to facilitate the comparison of measured values for different conditions. The figures presented provide results for the 6 specimens tested in this study.

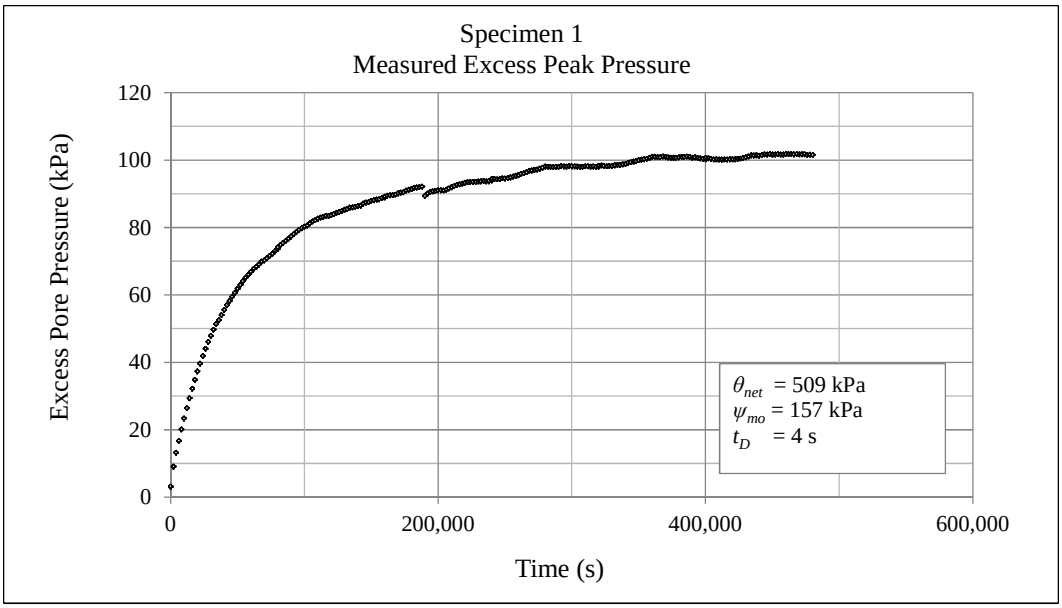

FIGURE 5-10 Measured excess peak pressure for specimen 1

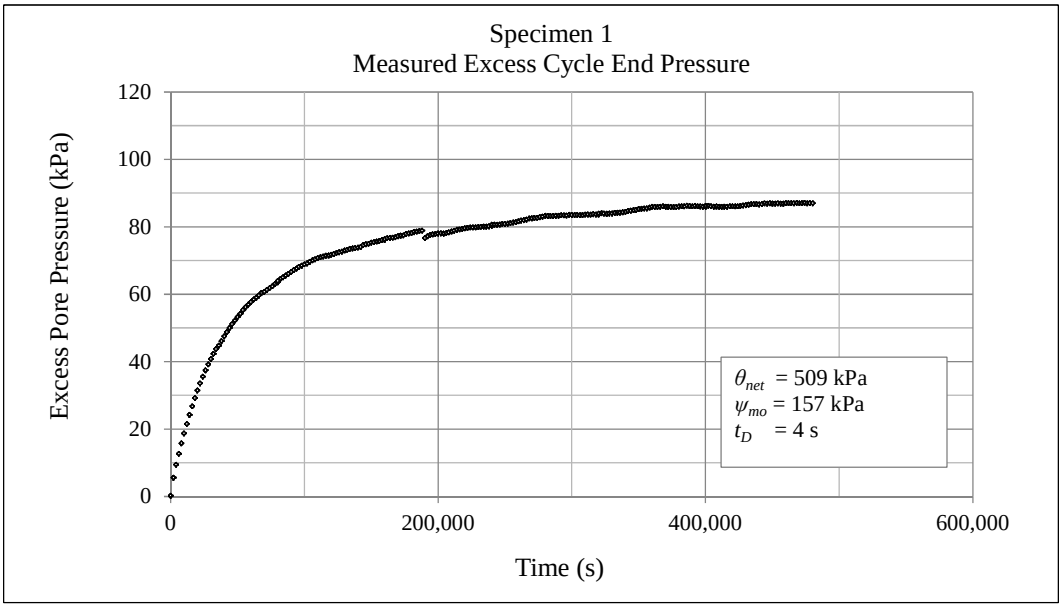

FIGURE 5-11 Measured excess cycle end pressure for specimen 1

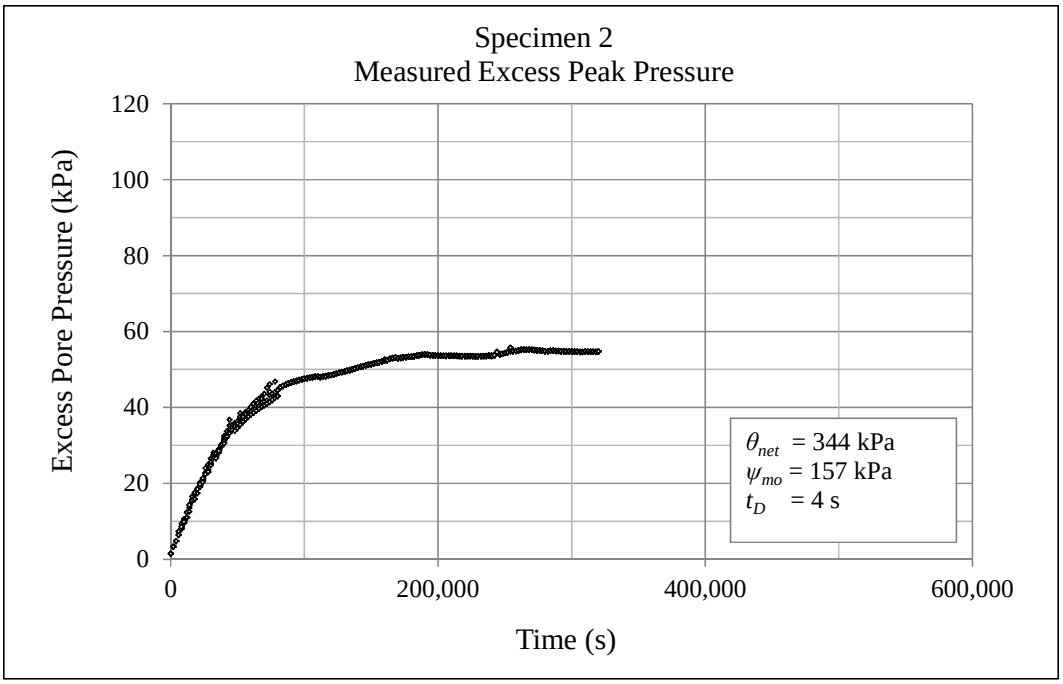

FIGURE 5-12 Measured excess peak pressure for specimen 2

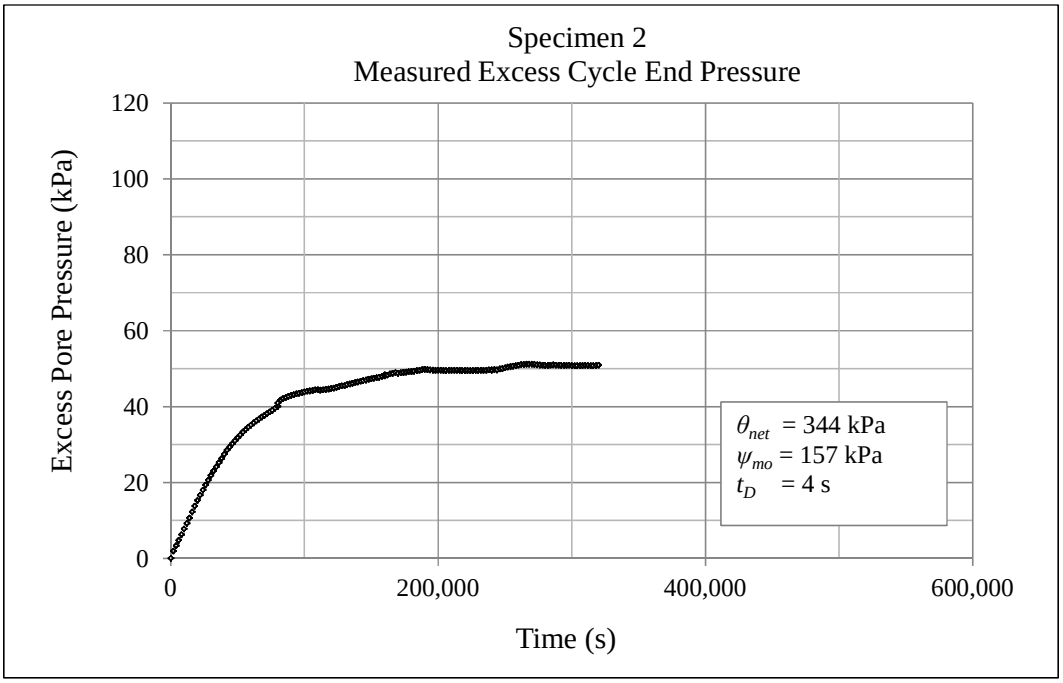

FIGURE 5-13 Measured excess cycle end pressure for specimen 2

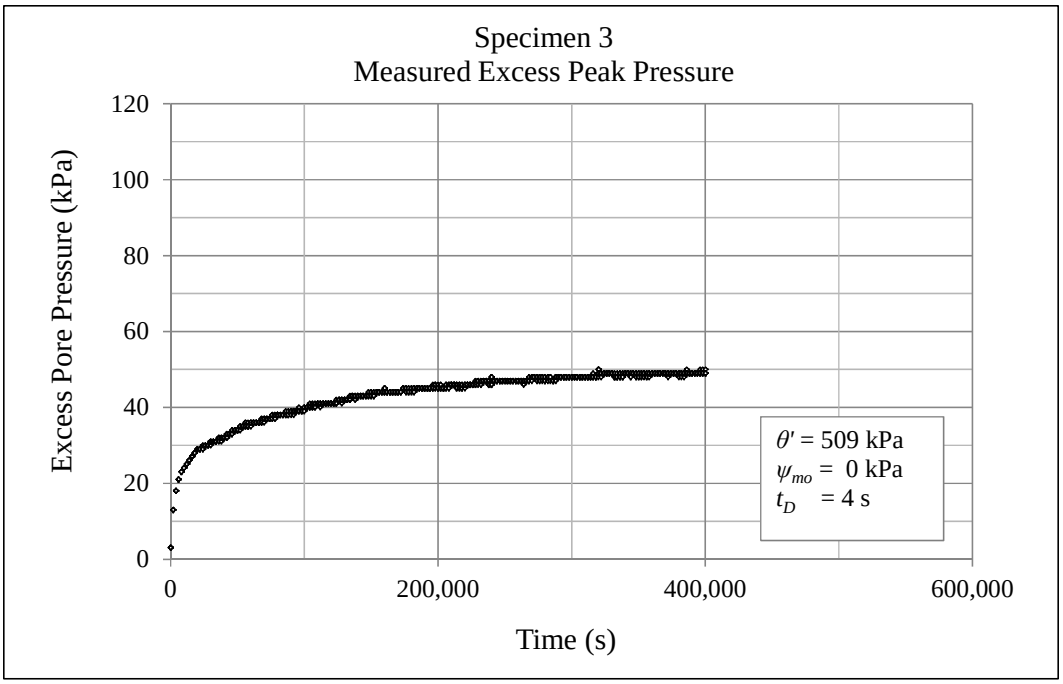

FIGURE 5-14 Measured excess peak pressure for specimen 3

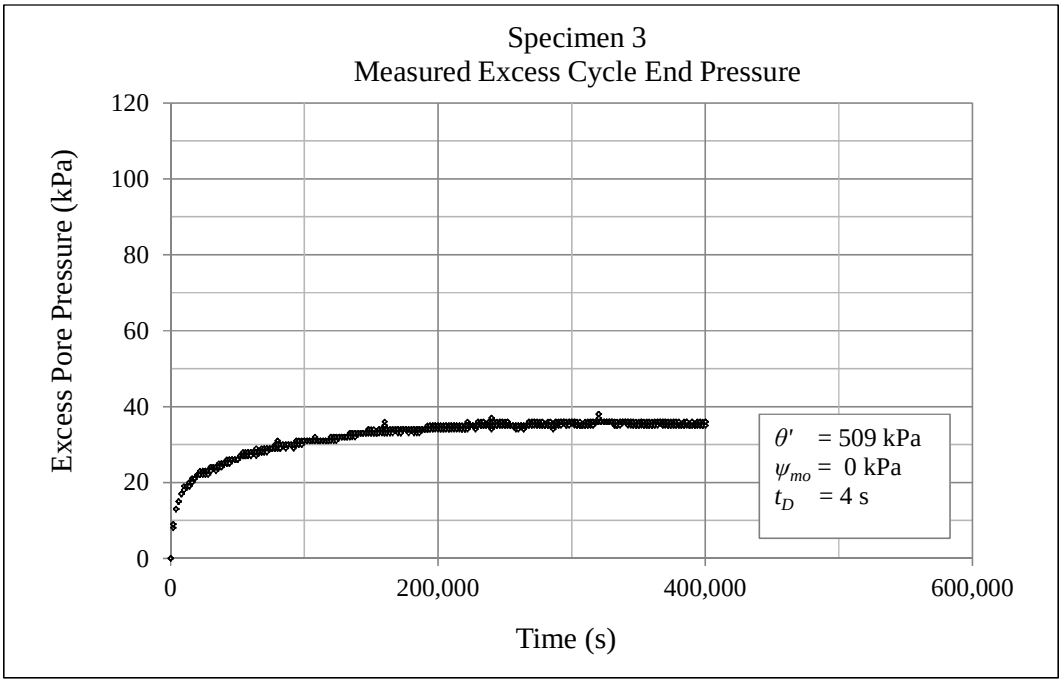

FIGURE 5-15 Measured excess cycle end pressure for specimen 3

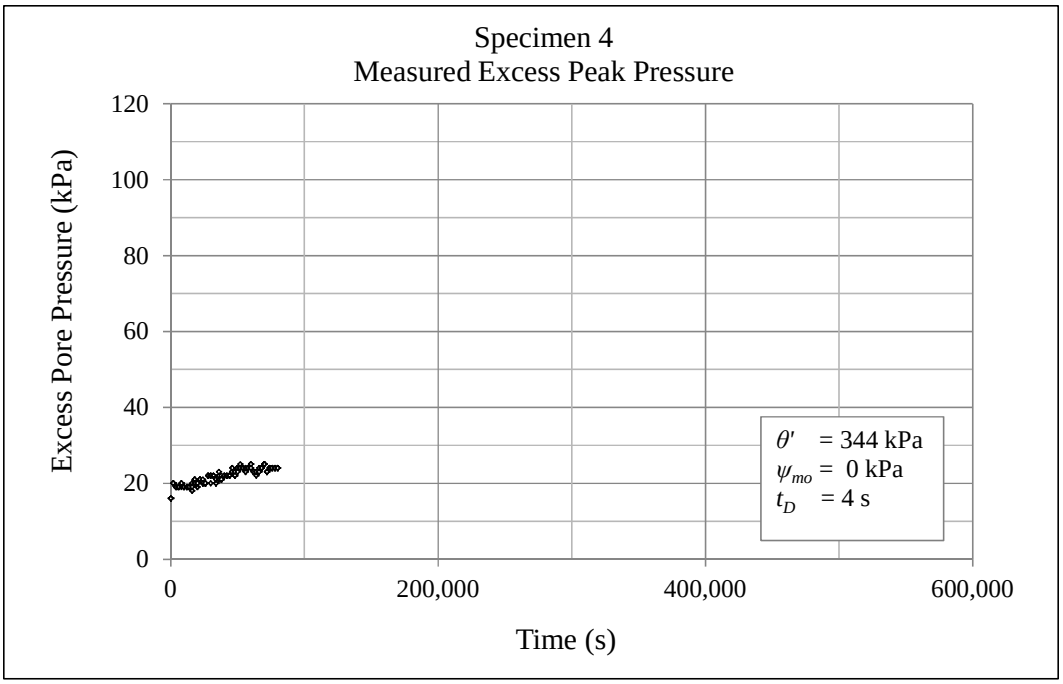

FIGURE 5-16 Measured excess peak pressure for specimen 4

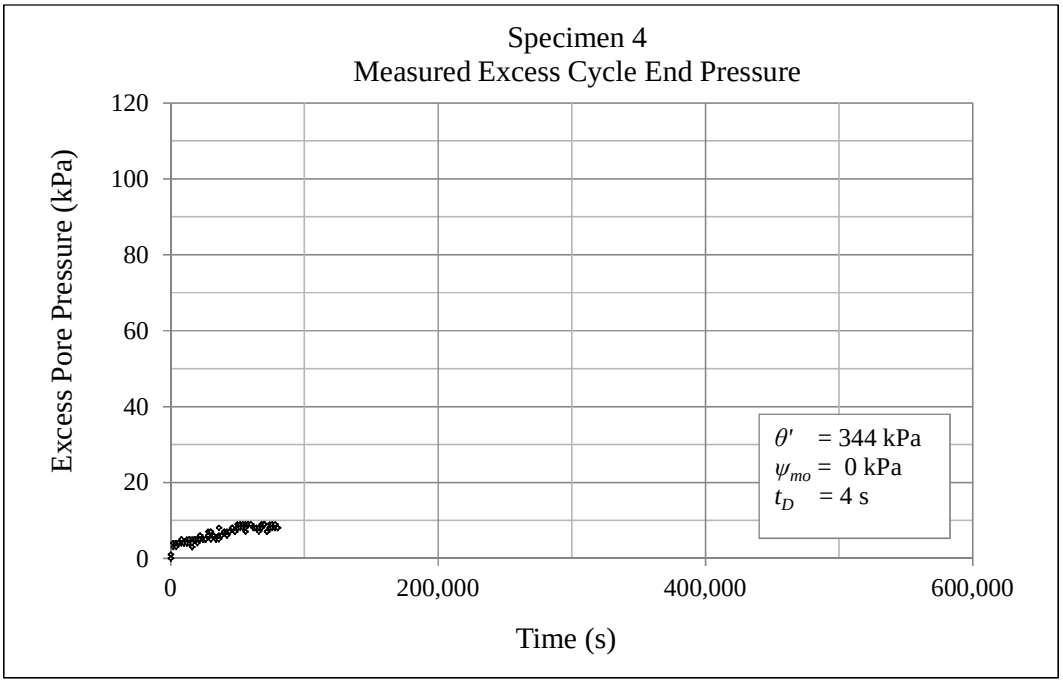

FIGURE 5-17 Measured excess cycle end pressure for specimen 4

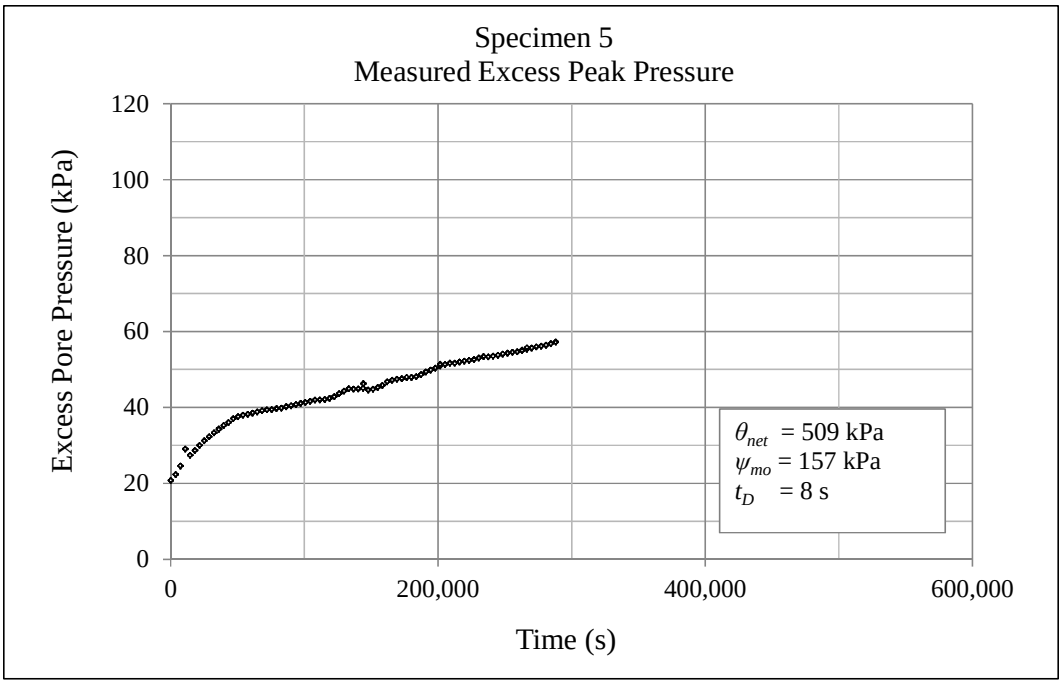

FIGURE 5-18 Measured excess peak pressure for specimen 5

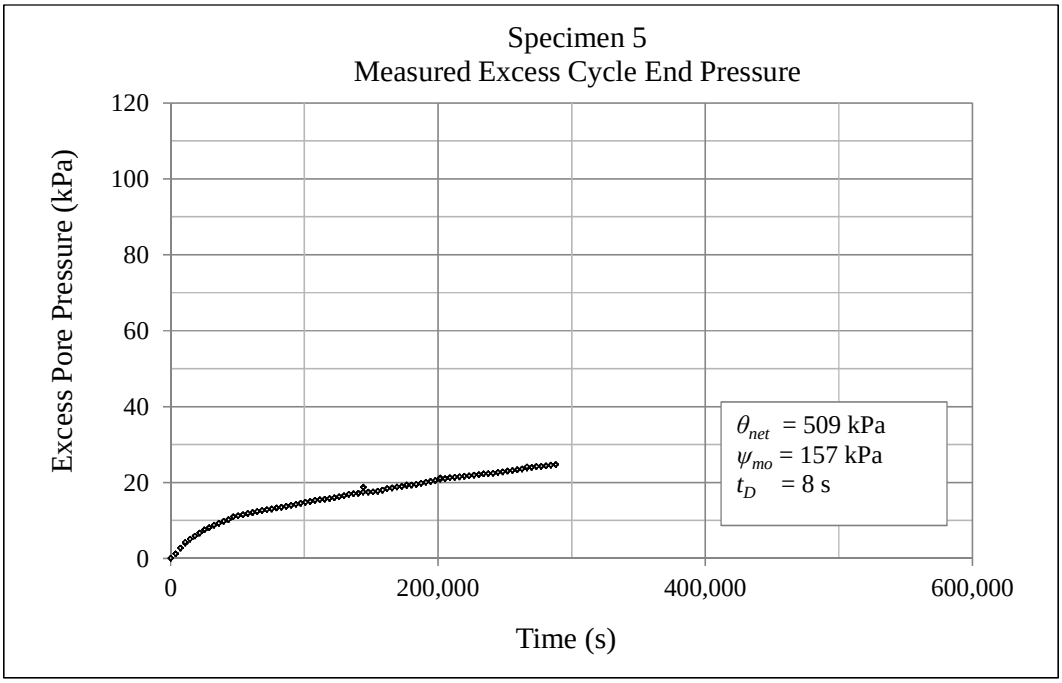

FIGURE 5-19 Measured excess cycle end pressure for specimen 5

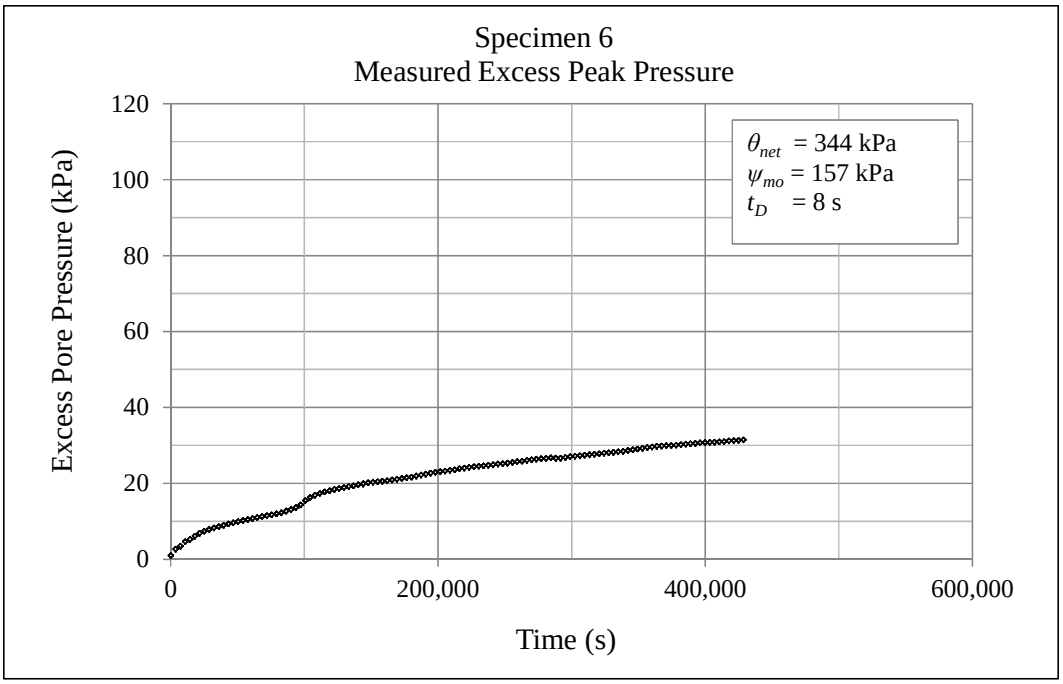

FIGURE 5-20 Measured excess peak pressure for specimen 6

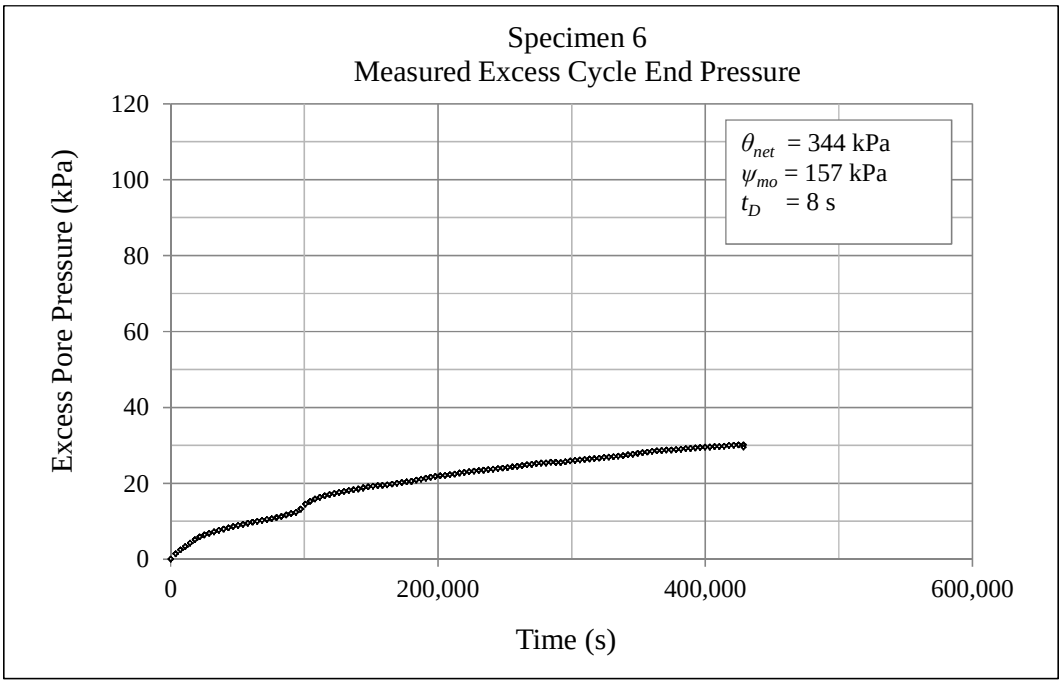

FIGURE 5-21 Measured excess cycle end pressure for specimen 6

In the following sections, the analysis of the data obtained from the dynamic test program is elaborated.

CHAPTER 6. ANALYSIS AND DISCUSSION OF RESULTS

In this chapter the results of the dynamic load testing program are analyzed and discussed. Models for the prediction of pore water pressure buildup are proposed. The influence that the controlled variables have upon the pore water pressure buildup is studied. Also, the principal findings are commented.

Preliminary Modeling Attempts

As previously discussed, the drainage conditions established for the dynamic load test in this study correspond to *CU* and *CW* tests for saturated and unsaturated specimens, respectively. For both conditions, the water phase is undrained which means that no water volume change is allowed during axial load. Excess pore water pressure is developed due to the tendency towards volume change induced by the repeated load.

Under undrained conditions, positive pore water pressures are expected to develop in normally consolidated cohesive soil specimens *(42)*. Positive pore water pressure buildup takes place during the loading time t_L instantaneously. When the load is removed, pore water pressure dissipates during the dwelling time t_D. However, all the pressure developed is not able to dissipate. There is a residual pore water pressure that remains at the end of the loading cycle. This happens at every cycle

The residual pore water pressure gets accumulated as the number of cycles increases. This process can be represented by Equation 6-1:

$$\Delta u_{wN} = \sum_{i=1}^{N} u_2{}'_i \qquad (6\text{-}1)$$

Where,

$u_2{}'_i$ = residual pore water pressure in the i^{th} cycle

Δu_{wN} = accumulated excess pore water pressure in the N cycle

It should be recognized that under loading conditions, positive pore water pressures develop whether the soil is partially or fully saturated. When the soil is partially saturated, the pore pressure development will result in a positive increase from negative pore water pressure levels, which is equivalent to a reduction in matric suction. On the other hand when the soil is fully saturated, the development of pore water pressure will add to existing neutral or positive pore water pressures. In the present study the mentioned changes in either saturated or unsaturated soil specimens will be referred to as excess pore pressure development.

In order to predict the excess pore water pressure development, proper mathematical models need to be assumed. Different attempts to model this parameter using the results observed in the laboratory tests are presented in the following sections.

First Modeling Attempt

Results from a pilot test were used in a first attempt to find models for the prediction of excess pore pressure development. A total of 24,030 load repetitions were applied to an unsaturated specimen with similar testing conditions as those shown in the previous chapter for Specimen 1. The net initial matric suction ψ_{mo}

was 157 kPa, loading time t_L of 1 second and dwelling time t_D of 4 seconds. The only difference with respect to Specimen 1 was the applied net bulk stress θ_{net}, which was equal to 496 kPa, rather than 509 kPa applied to Specimen 1.

The results of the pilot testing are shown in Figure 6-1. The "Global Peak Excess Pressure Curve" and "Global Cycle End Excess Pressure Curve" are plotted versus number of cycles. It should be noted that for this first preliminary modeling attempt, only a sample of the test results was used. The sample includes data measured from one cycle every thousand cycles. Therefore, only data for 25 load cycles was analyzed.

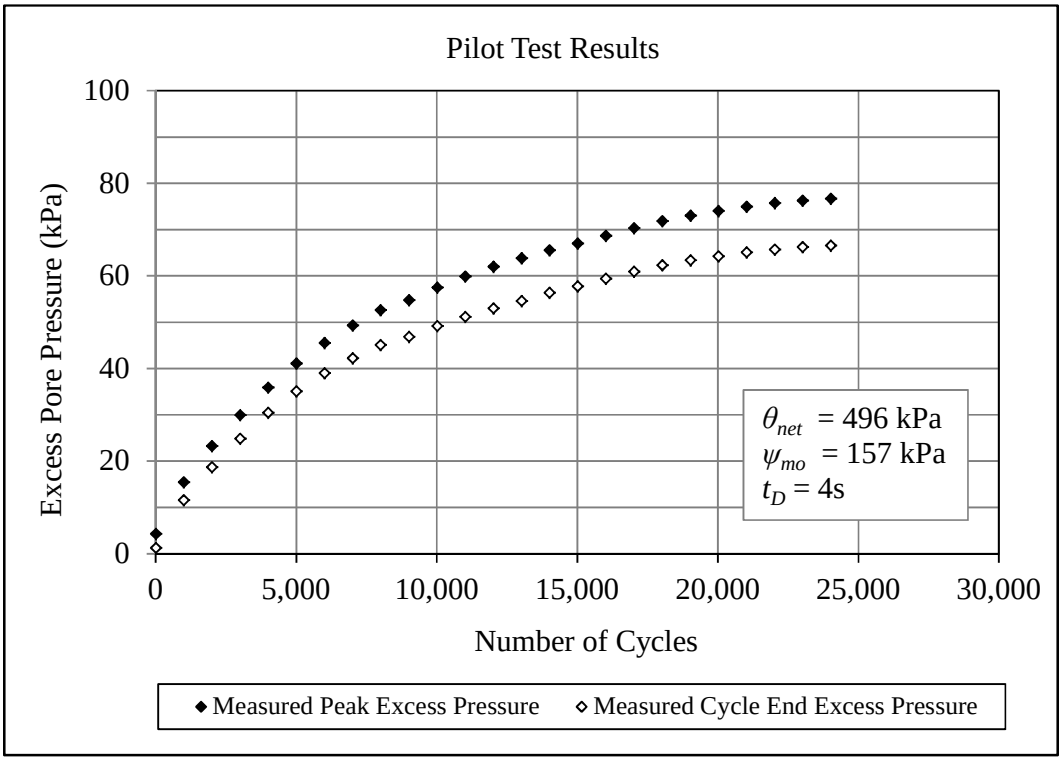

FIGURE 6-1 Results of pilot testing

Careful observation of the data led to the decision of using three different functions to model the pore water pressure development for every single cycle

and therefore, each individual cycle of pore water pressure development was broken down in three segments as shown in Figure 6-2.

The first segment represents the pore pressure development from the beginning of the cycle until a time equal to 0.92 seconds, at which time a slightly different behavior in the pore water pressure dissipation was observed from this point until the end of the loading time t_L. Therefore, for that particular time interval, a second model was utilized. For the entire dwelling time t_D, a third mathematical model was used.

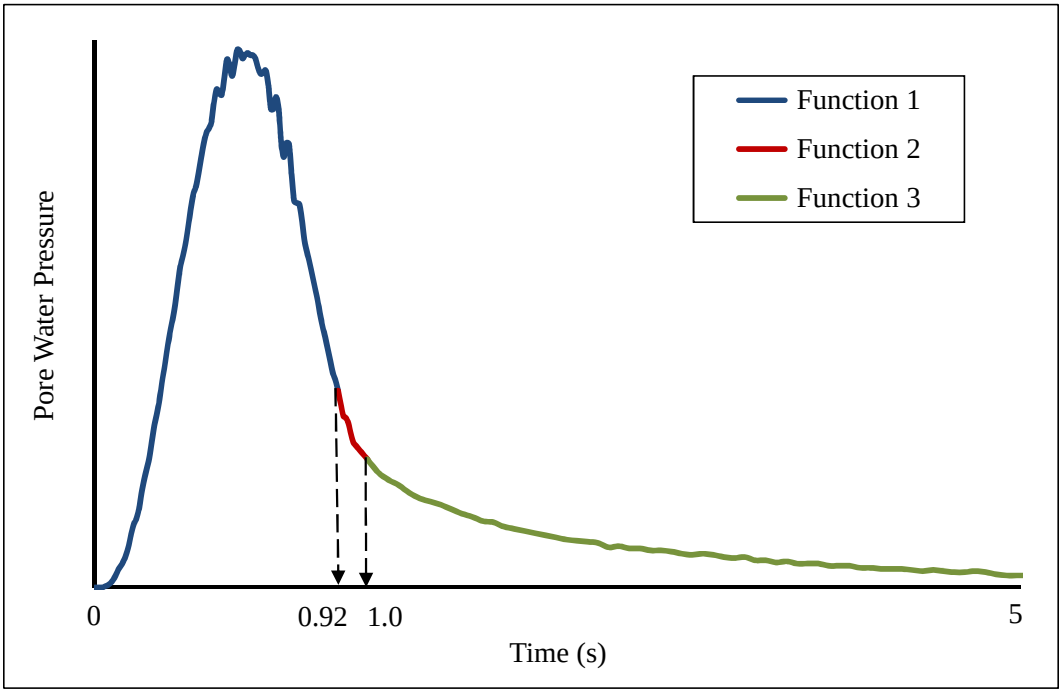

FIGURE 6-2 First attempt for modeling the i^{th} cycle

Function 1

Non-linear regression analysis was conducted using the data for the 25 cycles considered in this preliminary attempt. Data points corresponding to a time range between 0 and 0.92 seconds were used. From several non-linear functions

evaluated, the Weibull function shown in Equation 6-2 provided the best fit to the measured data:

$$u_w' = \alpha \left(\frac{\delta-1}{\delta}\right)^{\left(\frac{1-\delta}{\delta}\right)} \left[\frac{t-\beta}{\lambda} + \left(\frac{\delta-1}{\delta}\right)^{\frac{1}{\delta}}\right]^{\delta-1} exp\left[-\left(\frac{t-\beta}{\lambda} + \left(\frac{\delta-1}{\delta}\right)^{\frac{1}{\delta}}\right)^{\delta} + \left(\frac{\delta-1}{\delta}\right)\right] \quad (6\text{-}2)$$

Where,

u'_w = pore water pressure

t = time; valid for 0s $\leq t \leq$ 0.92s

α = pore water pressure pulse amplitude

β = time at maximum pore water pressure

λ and δ = regression constants

Figure 6-3 shows the elements of the Weibull function for a single pore water pressure pulse. Note that Equation 6-3 can be used to estimate the pore water pressure buildup within an interval of time going from 0 to 0.92 seconds, including the three reference pore water pressures u_0', u_p' and u_1' as can be seen in Figure 6-3

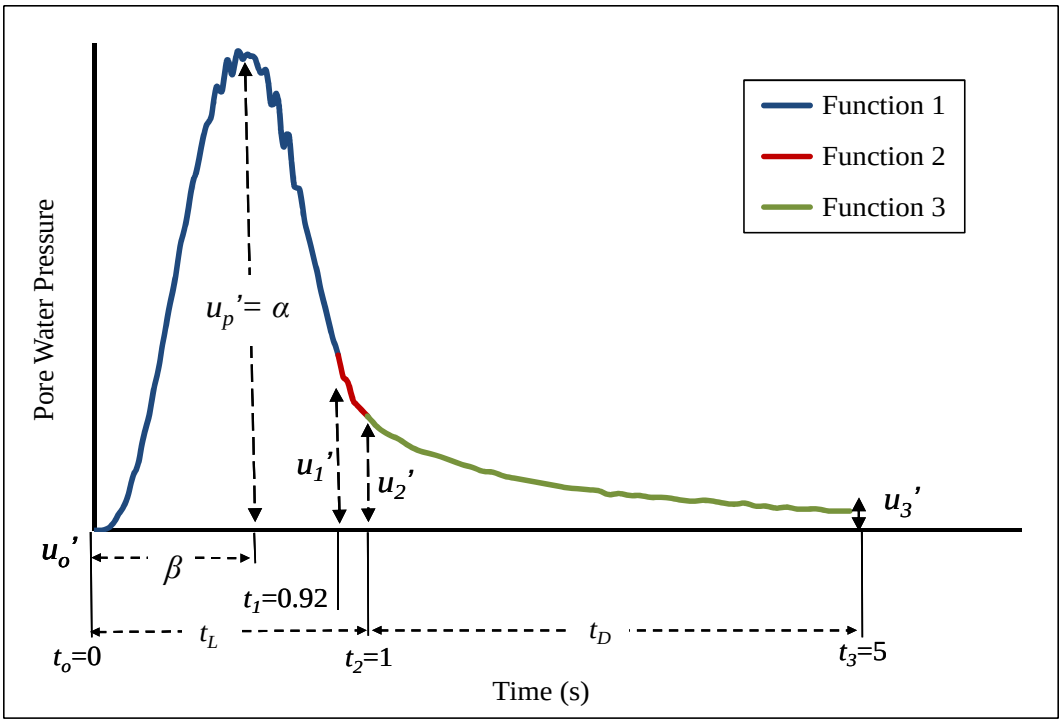

FIGURE 6-3 Weibull function parameters for the i^{th} cycle

The results of the regression analysis suggest that the model provides good prediction of pore water pressures within the time interval established. The adjusted coefficient of determination R^2_{adj} values obtained ranged from 0.998 to 1 for the 25 pore water pressure pulses analyzed.

The next step was to determine relationships between the regression coefficients α, β, λ and δ and the number of repetitions N.

Figures 6-4 to 6-7 show relationships between the Weibull regression constants and the number of repetitions N. Relationships for α and λ were obtained, whereas for β and not well defined patterns were observed. It was then decided to assume β and to be constant regardless of the number of repetitions and average values were obtained and used to predict the pore water pressure buildup.

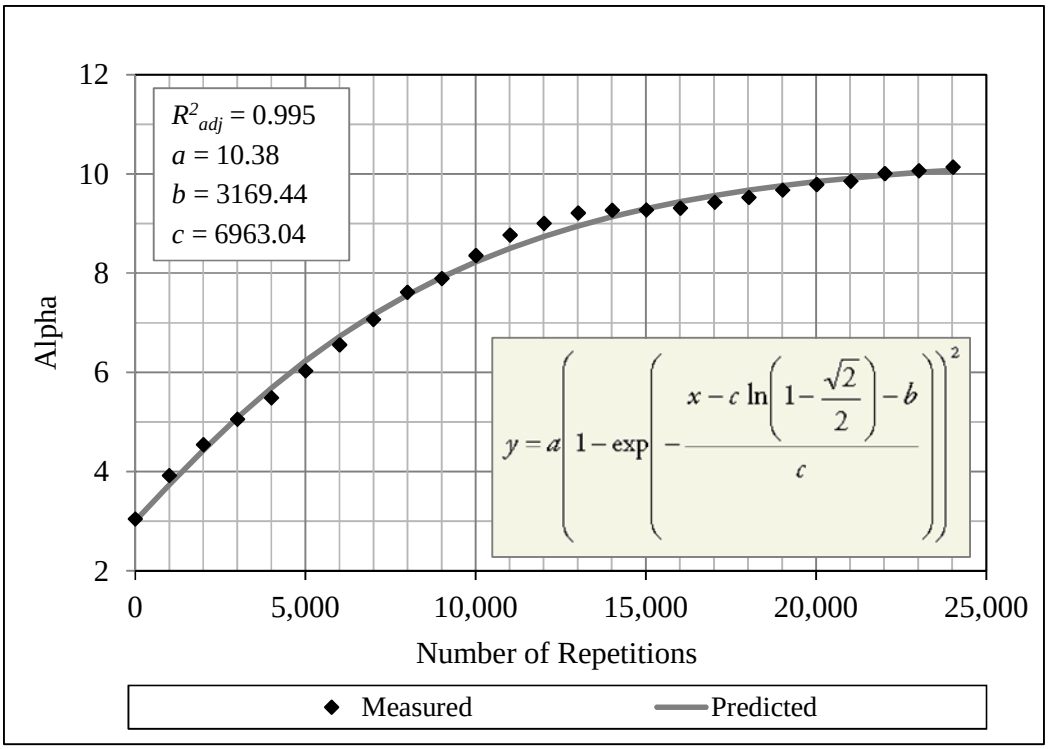

FIGURE 6-4 Alpha versus number of repetitions – first attempt

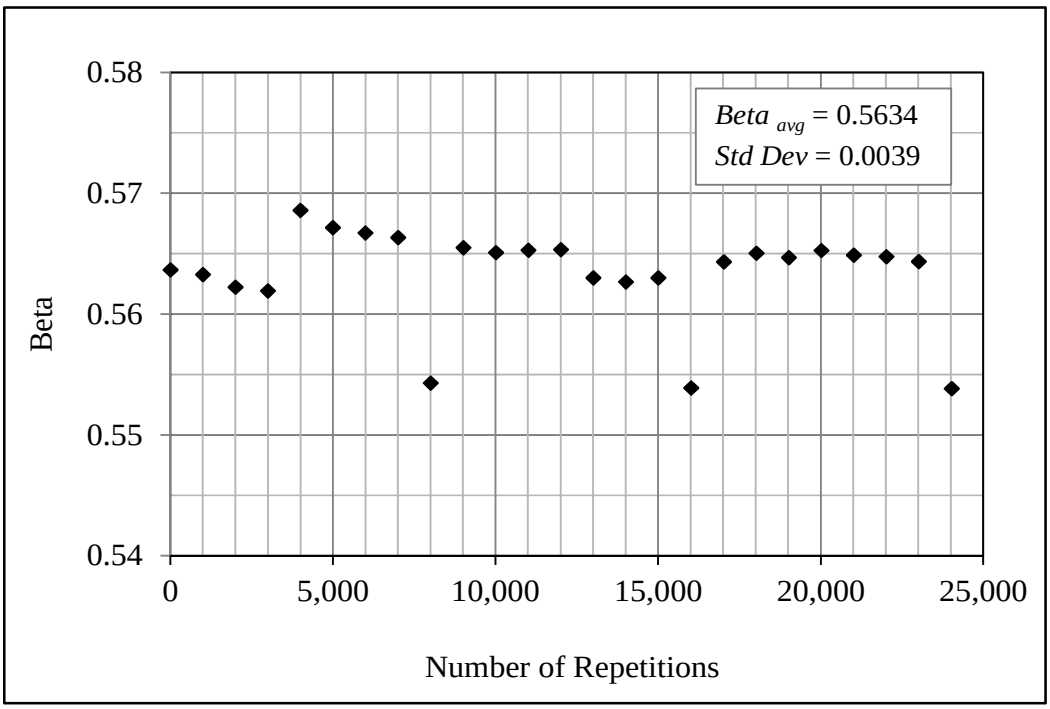

FIGURE 6-5 Beta versus number of repetitions – first attempt

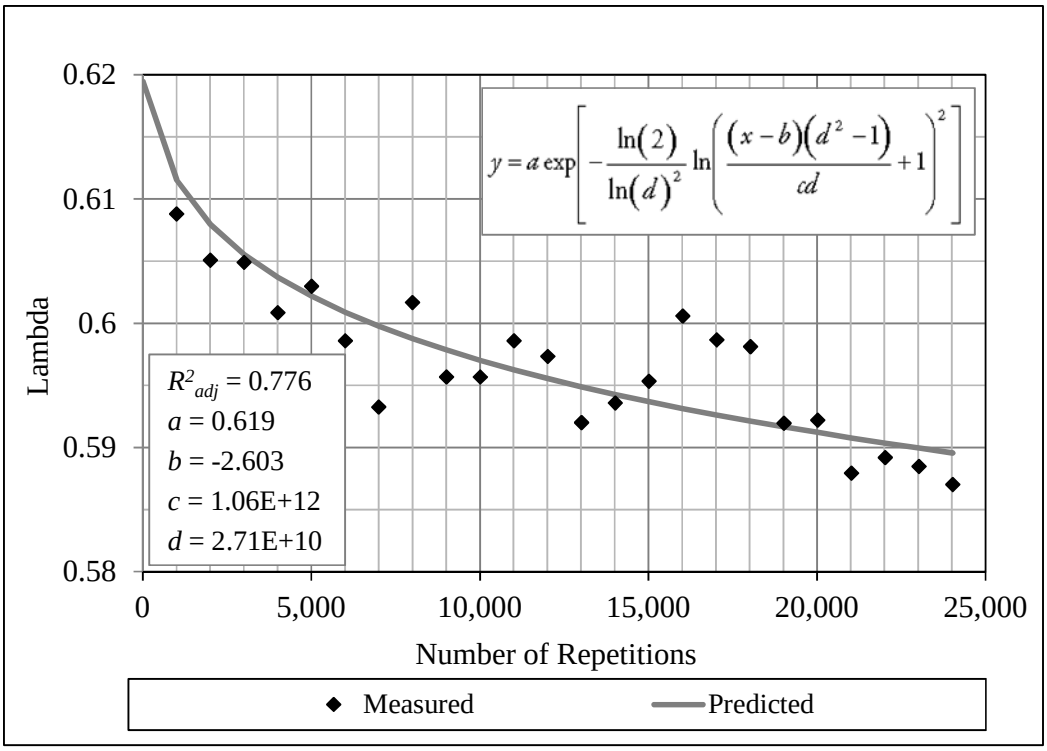

FIGURE 6-6 Lambda versus number of repetitions – first attempt

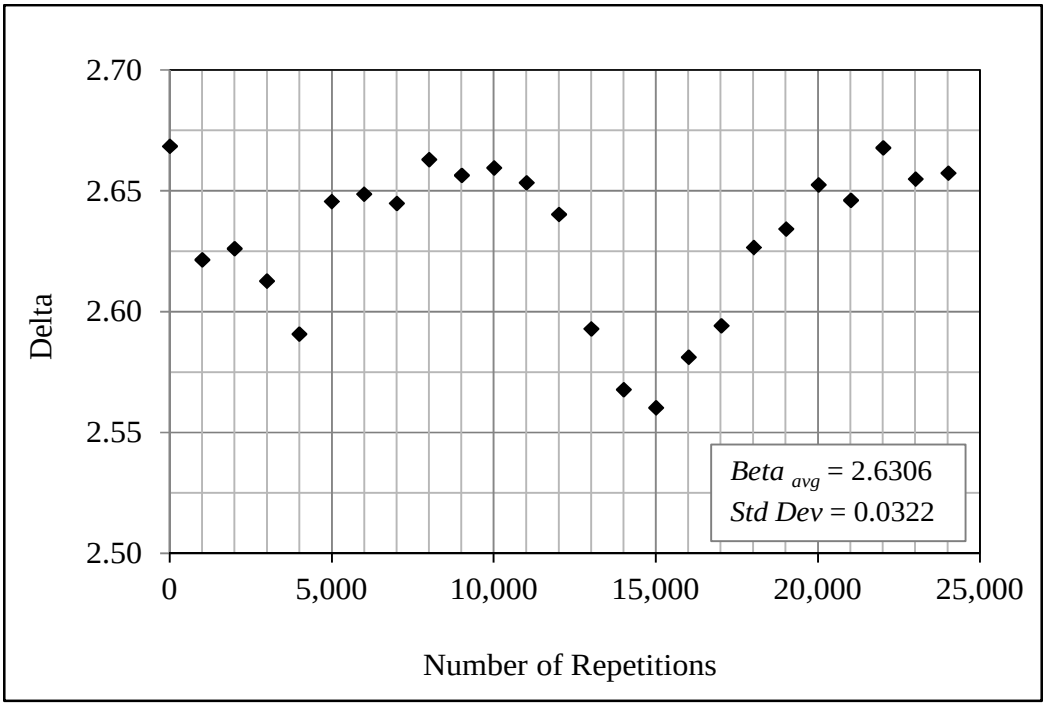

FIGURE 6-7 Delta versus number of repetitions = first attempt

Function 2

From several non-linear functions evaluated, the function shown in Equation 6-3 provided the best fit to the measured data corresponding to a time range between 0.92 and 1 second. The adjusted coefficient of determination R^2_{adj} values obtained for this function ranged from 0.959 to 0.997 for the 25 data points observed.

$$u_w' = [\vartheta + \rho . t(Ln\ t)]^{0.5} \quad (6\text{-}3)$$

Where,

u'_w = pore water pressure

t = time; valid for 0.92s $\leq t \leq$ 1s

$\vartheta = (u_1')^2$

ρ = regression constant

Note that in Equation 6-3, ϑ is the square intercept. This intercept is the pore water pressure value obtained when using Equation 6-2 at a time equal to 0.92 (see Figure 6-3). The regression parameter ρ was found to be related to the number of repetitions N through the relationship shown in Figure 6-8.

Equation 6-3 can be used to estimate the pore water pressure buildup u_w' = u_2' at t_2 = 1 second (see Figure 6-3). Note that the origin of the time line must be translated to zero and as consequence, u_2' must be estimated using t = 0.08 seconds. In order to obtain the parameter ϑ, u_w' = u_1' should be estimated using Equation 6-2 for $t = t_1$ = 0.92 seconds.

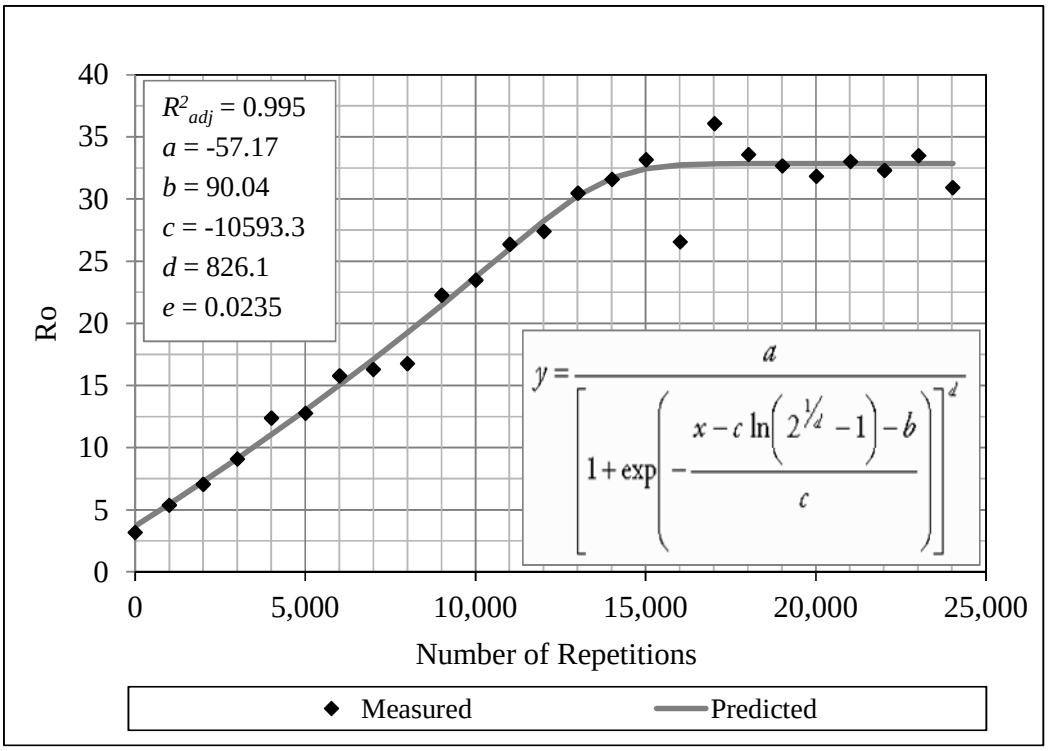

FIGURE 6-8 Ro versus number of repetitions – first attempt

Function 3

From several non-linear functions evaluated, the function shown in Equation 6-4 provided the best fit to the measured data. The adjusted coefficient of determination R^2_{adj} values obtained for this function ranged from 0.987 to 0.997.

$$u_w' = (\varphi + \omega . t^{0.5})^2 \qquad (6\text{-}4)$$

Where,

u'_w = pore water pressure

t = time; valid for 1s ≤ t ≤ 5s

$\varphi = (u_2')^{0.5}$

ω = regression constant

Note that in Equation 6-4, φ is the square root of the intercept. The regression parameter ω is related to the number of repetitions N through the relationship shown in Figure 6-9.

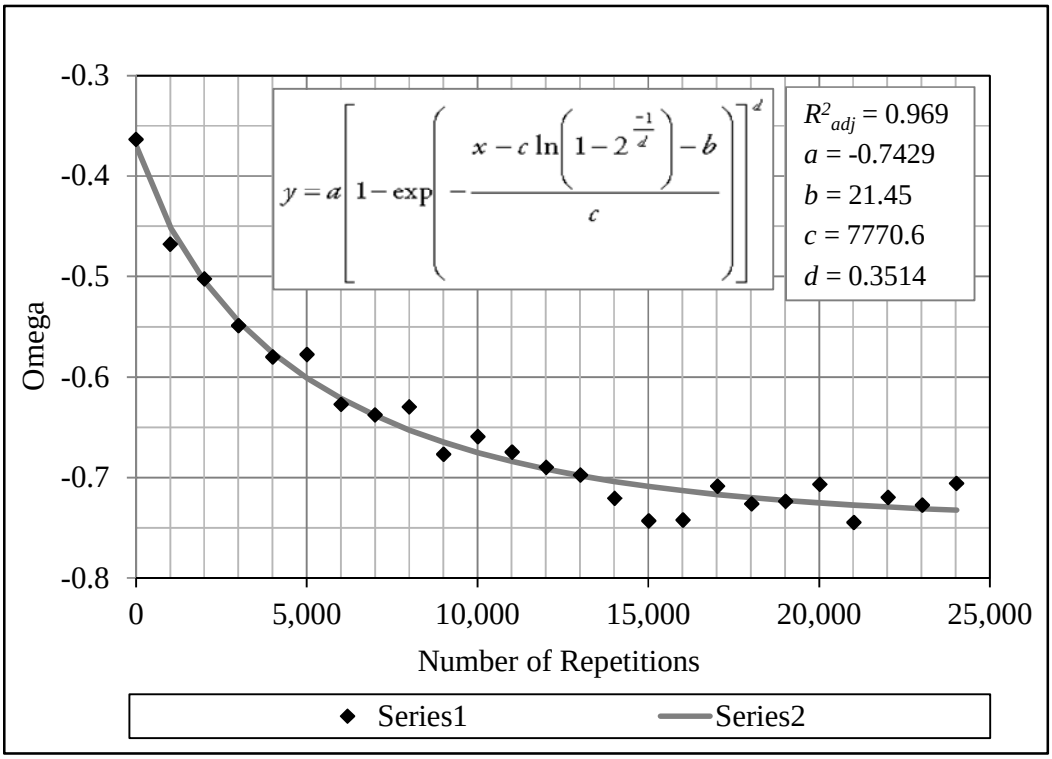

FIGURE 6-9 Omega versus number of repetitions – first attempt

The intercept for the Function 3 is the pore water pressure buildup $u_w' = u_2'$ estimated for the time $t = t_2 - t_1 = 0.08$ seconds by using Equation 6-3. The residual pore water pressure $u_w' = u_3'$ for the i^{th} cycle can be estimated by using Equation 6-4 for $t = t_D = t_3 - t_2 = 4$ seconds. Finally, the accumulated excess pore water pressure $\Delta u_w^{\ i}$ for the i^{th} cycle Δu_{wi}, can be obtained by adding the residual pore water pressure u_3' for the i^{th} cycle to the accumulated excess pore water pressure for the $(i\text{-}1)^{th}$ cycle Δu_{wi-1}. Note that Δu_{wi-1} is the initial pore water pressure $u_w' = u_0'$ for the i^{th} cycle in Figure 6-3.

Following the approach depicted in Figure 6-3, the expression presented in Equation 6-1 can be re defined as follows:

$$\Delta u_{wN} = \sum_{i=1}^{N} u_3{}'_i \tag{6-5}$$

Where,

$u_3{}'_i$ = residual pore water pressure in the i^{th} cycle

Δu_{wN} = accumulated excess pore water pressure of the N cycle

Using Equations 6-2 to 6-5 and the relationships found to predict the regression constants as function of number of repetitions, a simulation of pore water pressure buildup for 24,000 cycles was performed. The results for the accumulated peak pore pressure Δu_p and cycle end pore pressures Δu_3 obtained from the simulation are presented in Figures 6-10 and 6-11, respectively. It can be observed that the predictions do not match the measured values and discrepancies of up to 45 kPa between the predicted and measured values can be observed in both figures. Besides, the predicted curves do not show continuous trends which indicate that the relationships used to predict the regression constants for Equations 6-2 to 6-4 are not properly defined.

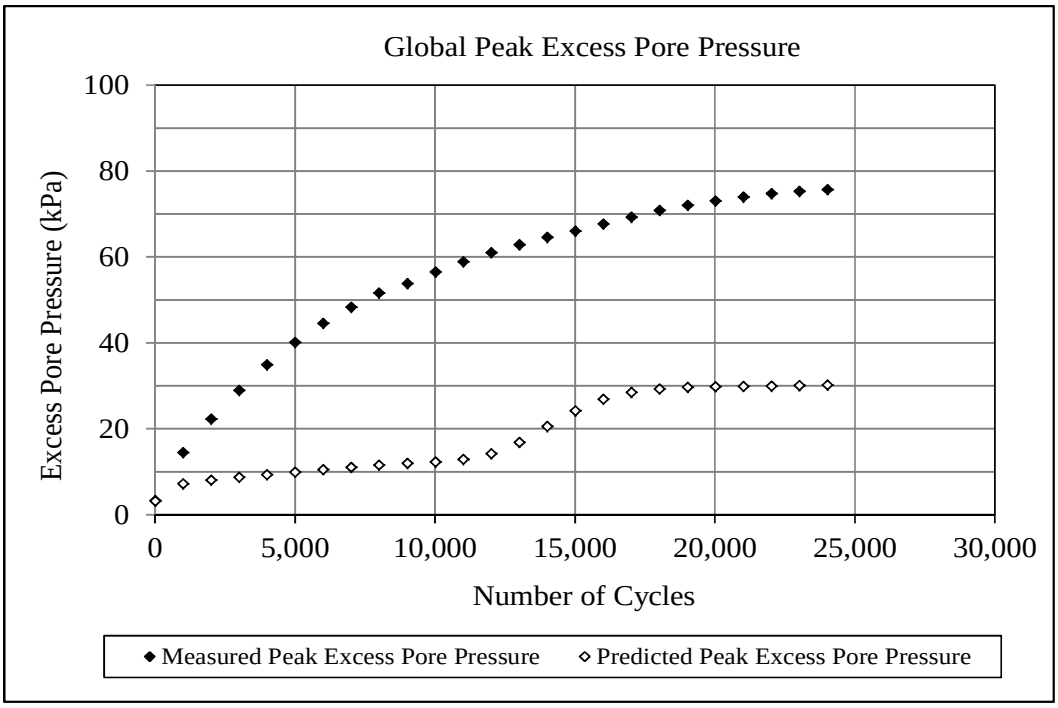

FIGURE 6-10 Simulation results for the global peak excess pore pressure

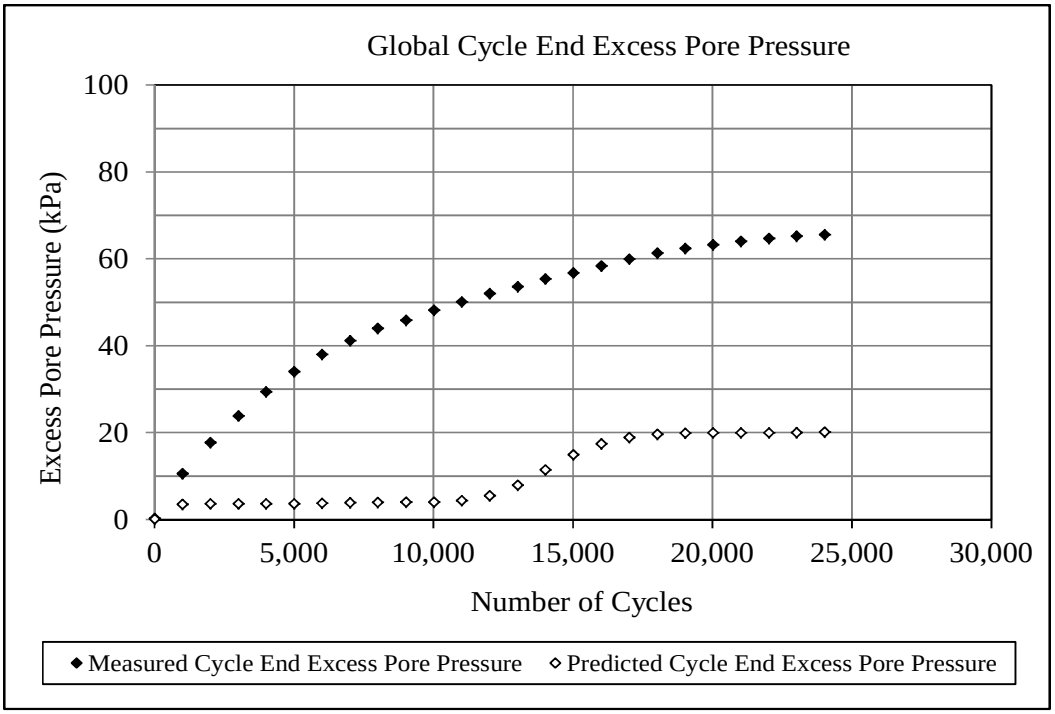

FIGURE 6-11 Simulation results for the global peak excess pore pressure

Also, it was observed that even though the R^2_{adj} values indicate that the functions provide good predictions, a marginal error in the residual pore pressure predicted for each cycle, accumulates as the number of cycles increases, making the final accumulated error significantly enough to explain the differences between predicted and measured values.

Some changes in the analytical methodology were considered to overcome the mentioned problems as explained in following sections.

Second Modeling Attempt

Results from the main dynamic load experiment were available by the time the second model was attempted. Therefore, testing results from Specimen 1 were used in this analysis. A total of 96,060 load repetitions were applied to Specimen 1 but only data from 1,230 cycles was recorded.

The test conditions for Specimen 1 were: net bulk stress θ_{net} = 509 kPa net initial matric suction ψ_{mo} = 157 kPa, loading time t_L = 1 second and dwelling time t_D = 4 seconds. The results of the test for Specimen 1 were shown in Figures 5-10 and 5-11 in Chapter 5, in which the "Global Peak Excess Pressure Curve" and "Global Cycle End Excess Pressure Curve" are plotted versus time. It should be noted that for this second modeling attempt, data recorded from 1230 cycles was used.

In this second attempt, it was decided to use two different functions to model the pore water pressure development for every single cycle instead of three, as it was done for the first attempt. That was intended to minimize the sources of error affecting the prediction of the cumulative excess pore water

pressure. In addition, by using data from 1,230 cycles instead of only 25 cycles used during the first attempt, better relationships between the number of repetitions and the regression parameters were expected to be obtained. Figure 6-12 shows the schematic of the new pore water pressure pulse. Note that this time, the first and second mathematical functions described the pore pressure development during the entire loading and dwelling time, respectively; that is, the first function is valid from 0 to 1 second and the second function from 1 to 5 seconds.

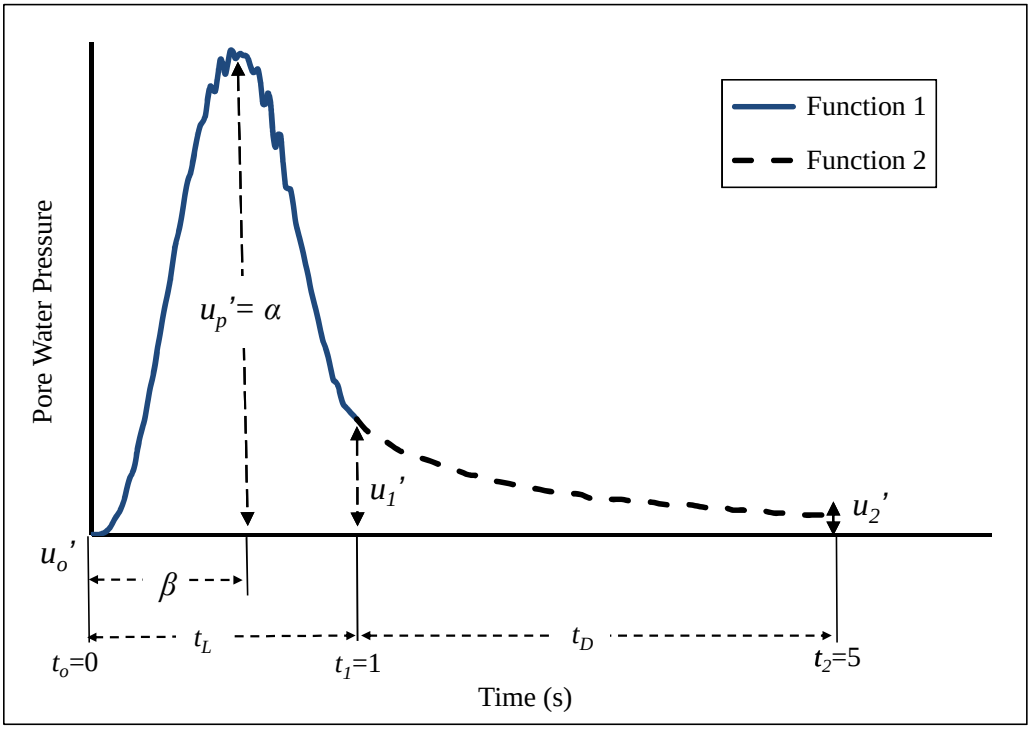

FIGURE 6-12 Second attempt for modeling the i^{th} cycle

In this opportunity, the measured data used for the regression analysis was replaced by predicted values. Different from the first attempt, instead of using about 200 measured data points per cycle, only 9 points were used. Five of them were used to perform regression analysis for the first function and 4 were used for

the second function. Such points were obtained by fitting the measured data corresponding to the reference pore pressures identified in Figure 6-12 to predictive functions. For instance, the cumulative peak pore pressure Δu_p points (measured from the origin of the pore pressure axis for the test) from all the 1,230 cycles were extracted and fitted to a mathematical function. The same procedure was followed using the points corresponding to the cumulative initial pore pressure Δu_0, cumulative pore pressure at the end of the load time Δu_1 and cumulative pore pressure at the end of the cycle Δu_2.

In addition, predicted Global Curves were obtained for two extra intermediate points within each function in order to complete the data sets needed for performing the regression analysis. In this way, predicted reference pressure values as function of time could be obtained and used instead of measured values. Again, it was expected to enhance the predictions by analyzing data points obtained directly from a global predicted curve rather than using values oscillating around it. Figure 6-13 shows the global predicted excess pore pressure curves for Specimen 1 corresponding to the reference pore pressures u_p', u_1', and u_2'. Details about the functions used to fit the data and their goodness of fit are provided in the following sections.

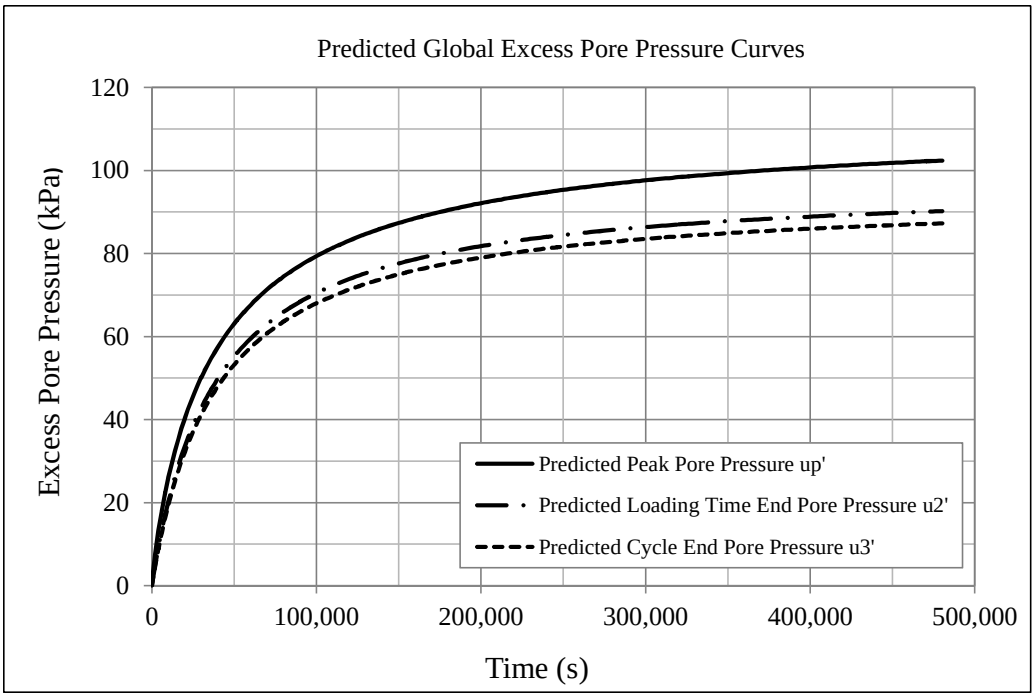

FIGURE 6-13 Global predicted excess pore pressure curves for specimen 1

Function 1

Non-linear regression analysis was conducted using the data from the 1,230 cycles considered. That means, 1,230 non-linear regressions were conducted. Data points corresponding to a time range between 0 and 1 second were used. The same Weibull function used from the first attempt was utilized. Function 1 is presented again in Equation 6-6.

$$u_w' = \alpha \left(\frac{\delta-1}{\delta}\right)^{\left(\frac{1-\delta}{\delta}\right)} \left[\frac{t-\beta}{\lambda} + \left(\frac{\delta-1}{\delta}\right)^{\frac{1}{\delta}}\right]^{\delta-1} exp\left[-\left(\frac{t-\beta}{\lambda} + \left(\frac{\delta-1}{\delta}\right)^{\frac{1}{\delta}}\right)^{\delta} + \left(\frac{\delta-1}{\delta}\right)\right] \quad (6\text{-}6)$$

Where,

u'_w = pore water pressure

t = time; valid for 0s $\leq t \leq$ 1s

α = pore water pressure pulse amplitude

β = time at maximum pore water pressure

λ and δ = regression constants

Figure 6-12 shows the Weibull function parameters for the i^{th} pore water pressure pulse. Note that Equation 6-6 can be used to estimate the pore water pressure development within an interval of time going from 0 to 1 second, including the three reference pore water pressures u_0', u_p' and u_1' shown in Figure 6-12. The adjusted coefficient of determination R^2_{adj} values obtained for 1,230 data sets ranged from 0.998 to 1 indicating that the predictions were good.

Figures 6-14 to 6-17 show the relationship between the Weibull regression constants and the number of repetitions *N*. Relationships for α, β, λ and δ were obtained. It can be observed that only the parameter α has a high R^2_{adj} = 0.9998. The rest of the parameters, however, were not accurately predicted. Even though the functions adjusted to the parameters β, λ and , followed rational trends, the variability of the values yielded R^2_{adj} lower than desired.

Furthermore, for the parameters λ and δ, it was required to use two functions in order to describe the trends. The use of the functions presented in the figures becomes impractical because a significant number of regression constants might need to be introduced in the general predictive model for excess pore water pressure.

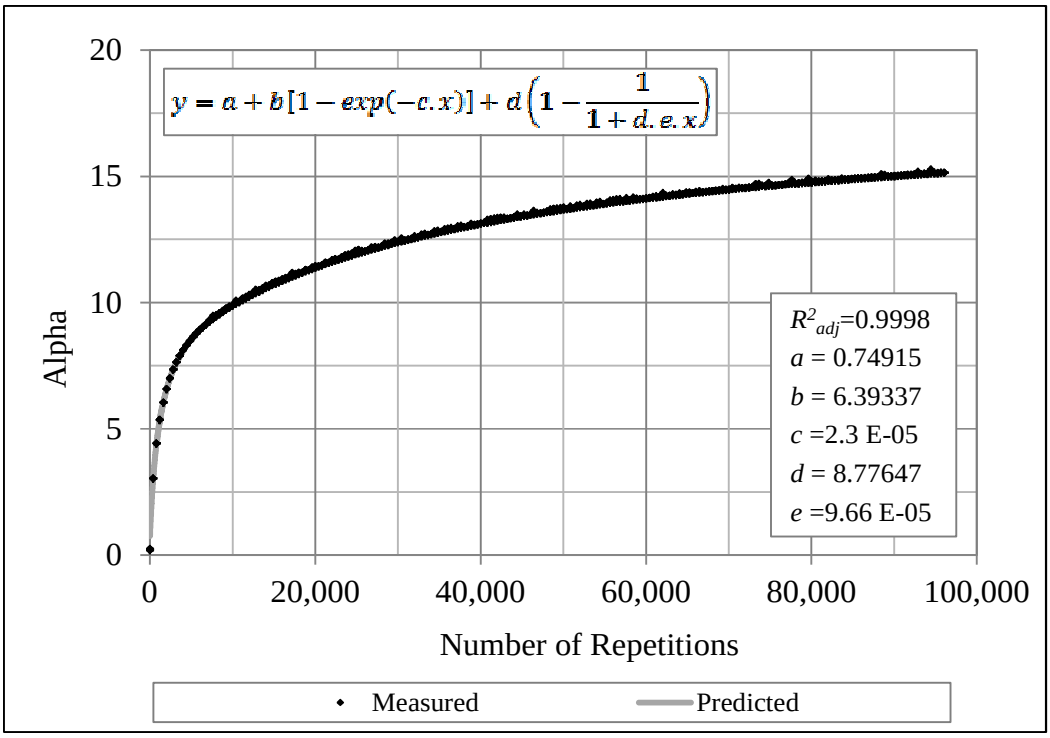

FIGURE 6-14 Alpha versus number of repetitions – second attempt

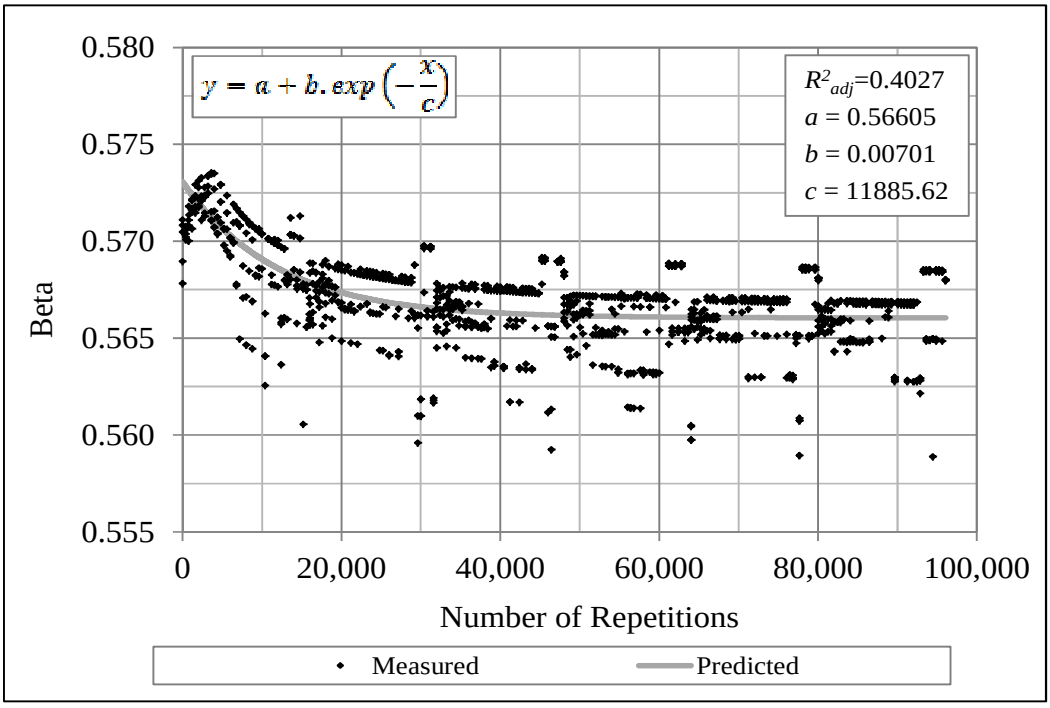

FIGURE 6-15 Beta versus number of repetitions – second attempt

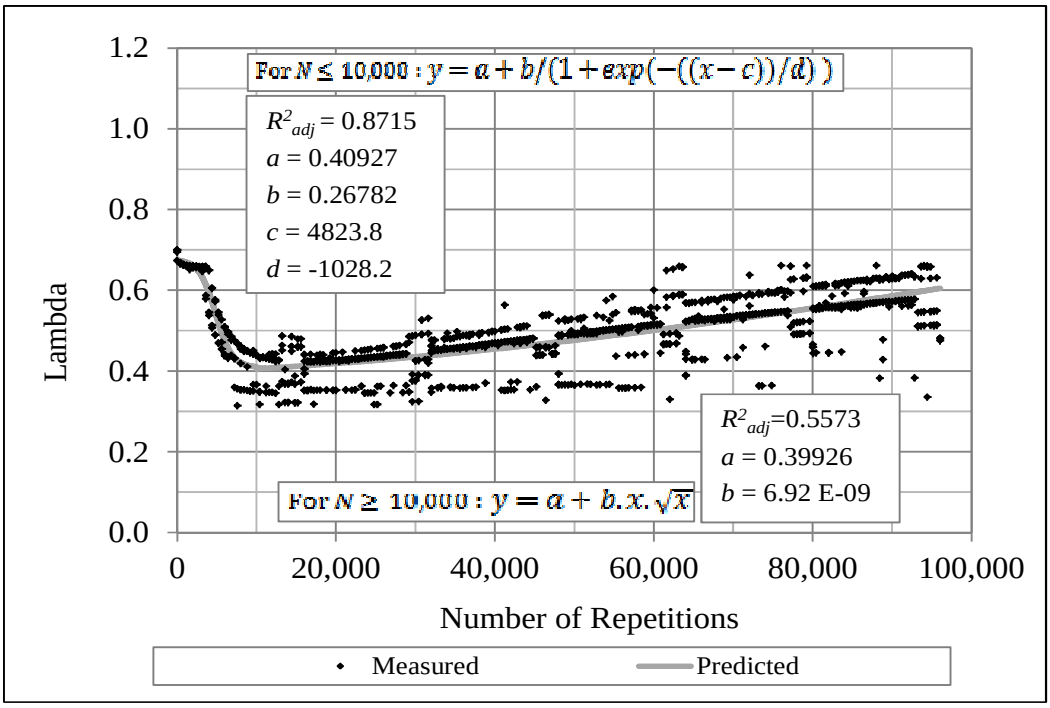

FIGURE 6-16 Lambda versus number of repetitions – second attempt

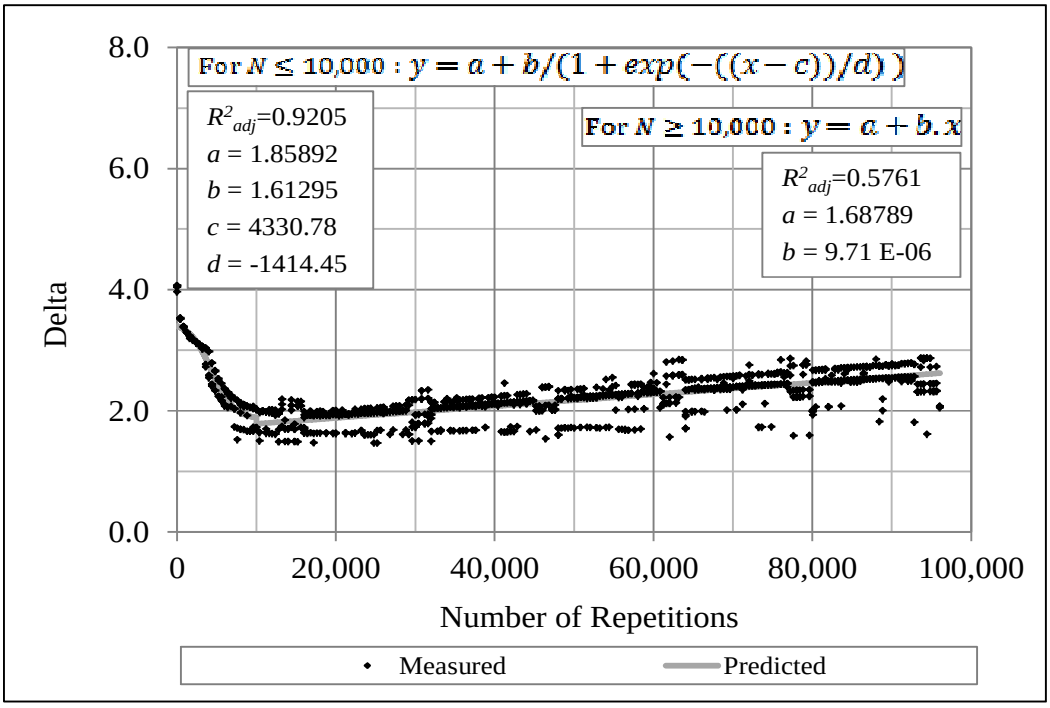

FIGURE 6-17 Delta versus number of repetitions – second attempt

Function 2

In order to find a model for the pore water pressure dissipation, non-linear regression analysis was conducted using the data from the 1,230 cycles used in this attempt. Data points corresponding to a time range between 1 and 5 seconds were used. From several non-linear functions evaluated, the Third Order Decay function shown in Equation 6-7 provided the best fit to the data.

$$u_w' = \vartheta + \frac{\rho}{\sqrt{1+2\rho^2\omega.t}} \quad (6\text{-}7)$$

Where,

u'_w = pore water pressure

t = time elapsed from the beginning of the unloading phase; valid for 1s $\leq t \leq$ 5s

ϑ and ω = regression constants

$\rho = u_1' - \vartheta$

The adjusted coefficient of determination R^2_{adj} values obtained for this function ranged from 0.9997 to 1; which indicates that very good predictions can be obtained by using Equation 6-7.

Note that in Equation 6-7, ρ is the difference between the intercept or pore water pressure developed at the end of loading time u_1' and the regression constant ϑ. This intercept is the pore water pressure value obtained when using Equation 6-6 at a time equal to 1 second as shown in Figure 6-12. The parameter ϑ is a regression constant and is related to the number of repetitions N through the relationship shown in Figure 6-18. Figure 6-19 shows the same relationship for the parameter ω.

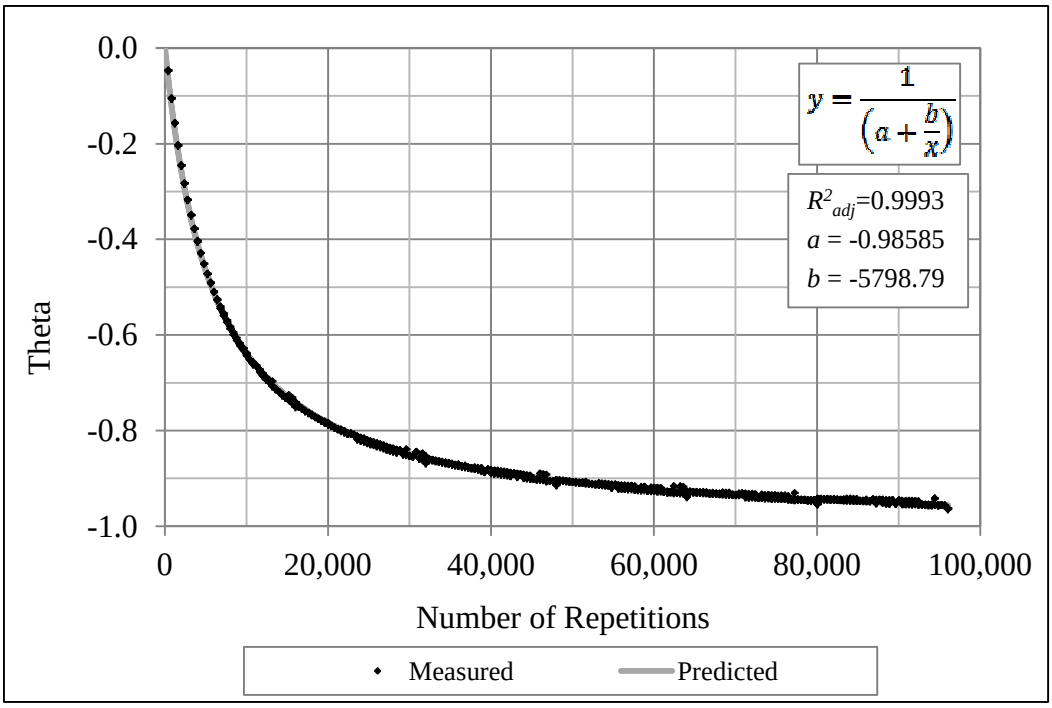

FIGURE 6-18 Theta versus number of repetitions – second attempt

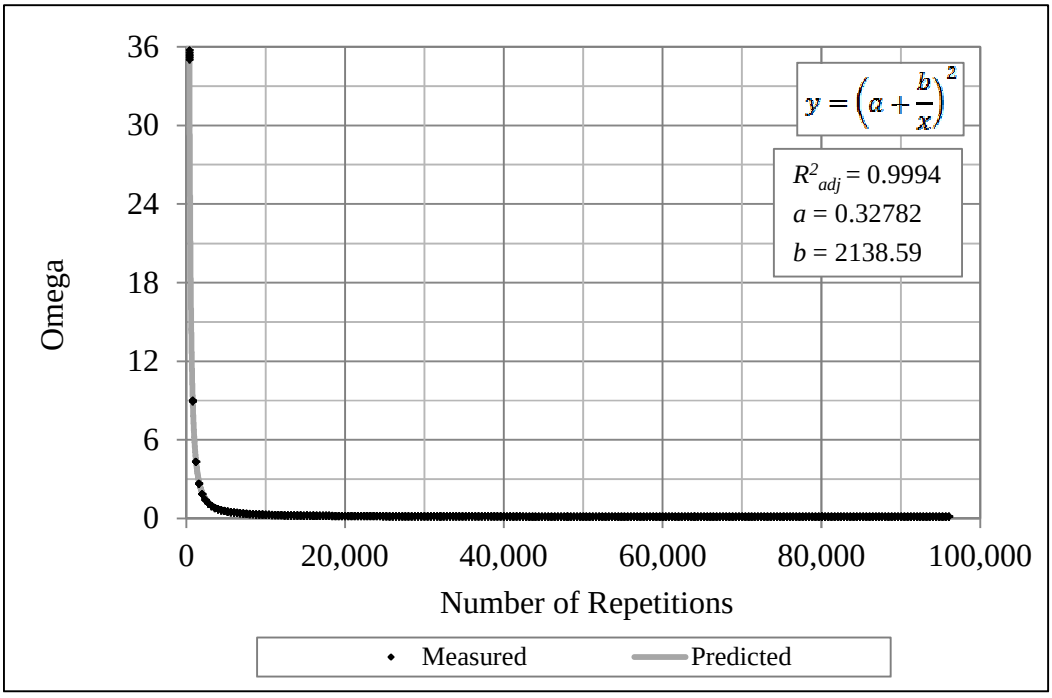

FIGURE 6-19 Omega versus number of repetitions – second attempt

The residual pore water pressure $u_w' = u_2'$ for the i^{th} cycle can be estimated by using Equation 6-7 for $t = t_D = t_2 - t_1 = 4$ seconds. Finally, the cumulative excess pore water pressure for the i^{th} cycle, Δu_{wi}, can be obtained by adding the residual pore water pressure u_2' for the i^{th} cycle to the excess pore water pressure accumulated in the $(i\text{-}1)^{th}$ cycle Δu_{wi-1}.

Following the approach proposed in Figure 6-12, the expression presented in Equation 6-1 can be re defined as follows:

$$\Delta u_{wN} = \sum_{i=1}^{N} u_2{}'_i \tag{6-8}$$

Where,

$u_2{}'_i$ = residual pore water pressure in the i^{th} cycle

Δu_{wN} = cumulative excess pore water pressure at the N cycle

Similar to the work done during the first attempt, a simulation of pore water pressure buildup for 96,060 cycles was performed using Equations 6-6 to 6-8 and the relationships found to predict the regression constants as function of number of repetitions. The results for the accumulated peak pore pressure Δu_p and cycle end pore pressures Δu_2 obtained from the simulation are shown in Figures 6-20 and 6-21. It can be observed that the predictions do not match the measured values. Nor the use of more complex functions to estimate the regression constants for the models neither the use of collected data from all cycles helped improving the results.

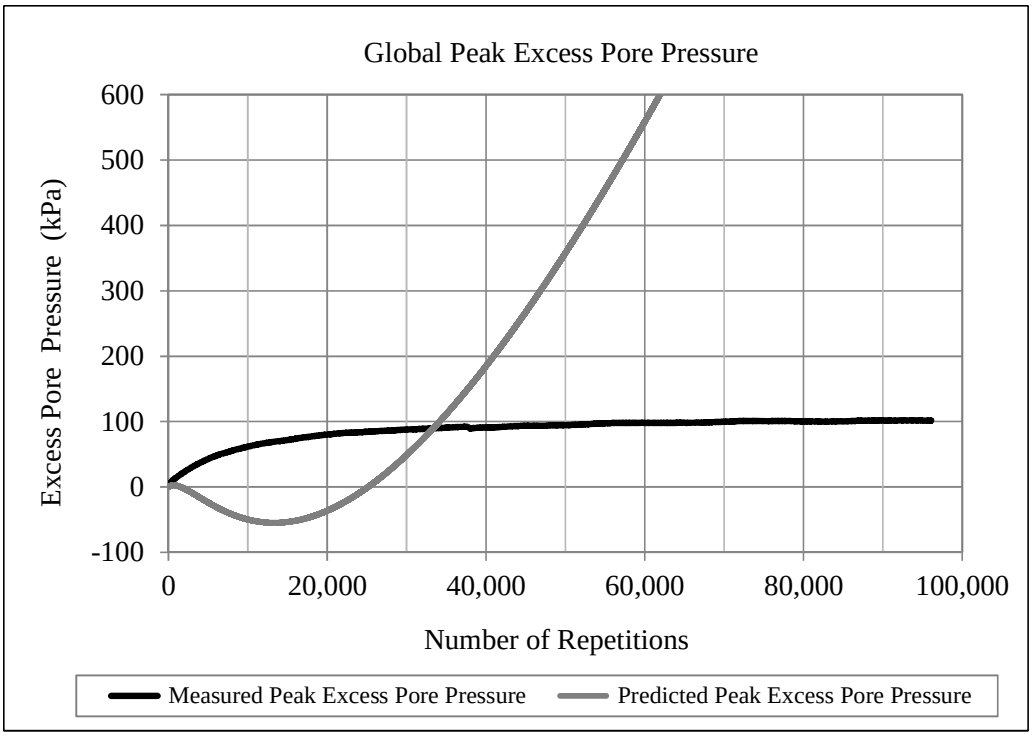

FIGURE 6-20 Simulation results for the global peak excess pore pressure

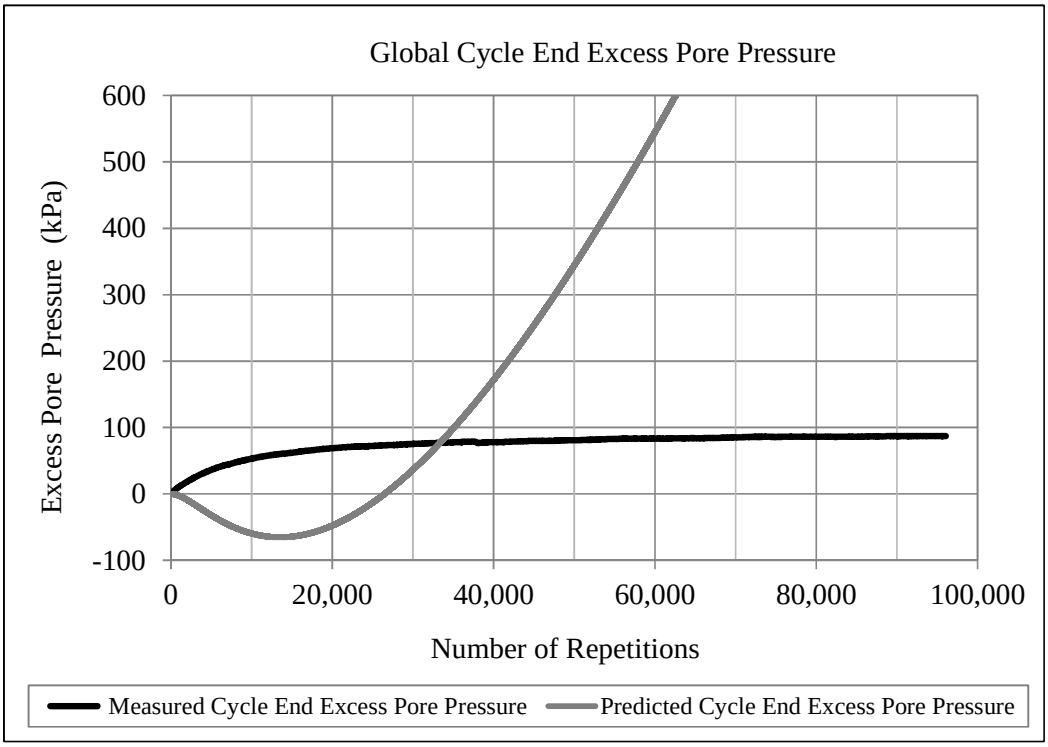

FIGURE 6-21 Simulation results for the global cycle end excess pore pressure

The error observed when estimating the residual pore water pressure u_2' for each i^{th} cycle may seem to be marginal but in fact it becomes significant when accumulated as the number of repetitions increases, as shown in Figure 6-22. Even though the R^2adj observed for functions 1 and 2 suggest that the predictions are very good, the models do not fit the pore pressures perfectly. Thus, the greater the number of repetitions involved in the analysis, the greater the error is likely to occur.

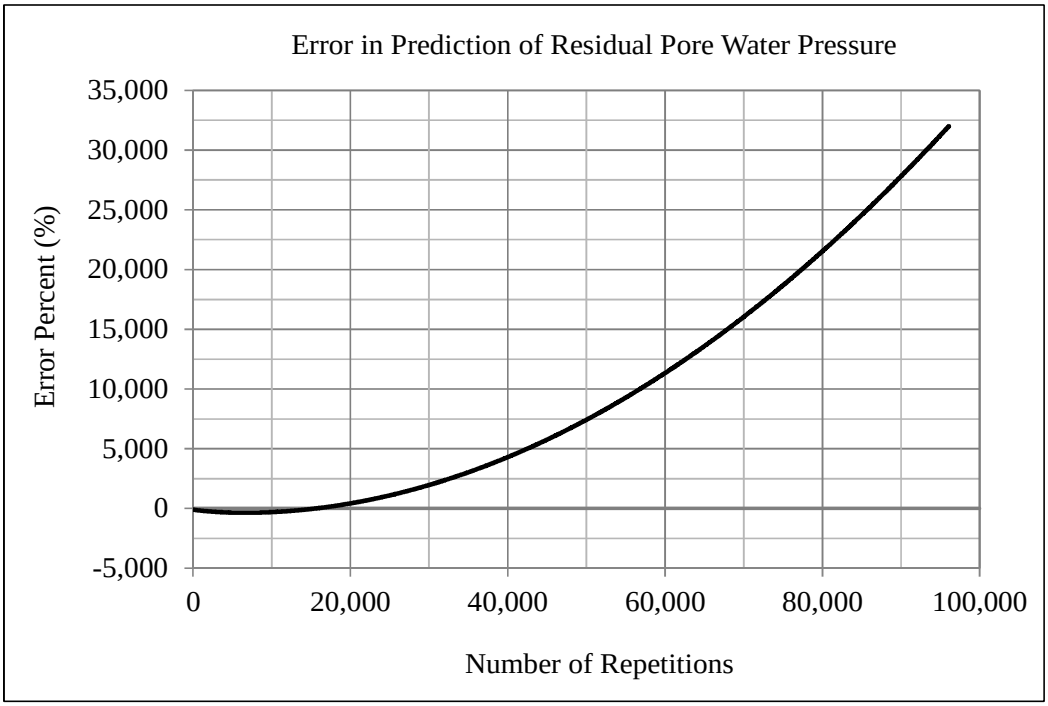

FIGURE 6-22 Error in prediction of residual pore pressure u_2' for the i^{th} cycle

Figure 6-23 shows that the magnitude of the residual pore pressure for each cycle is very small compared to the final excess pore pressure accumulated. As previously mentioned, even though predictions are very good according to the R^2adj values, the small marginal error observed in the i^{th} cycle becomes very significant as it accumulates as the number of repetition increases.

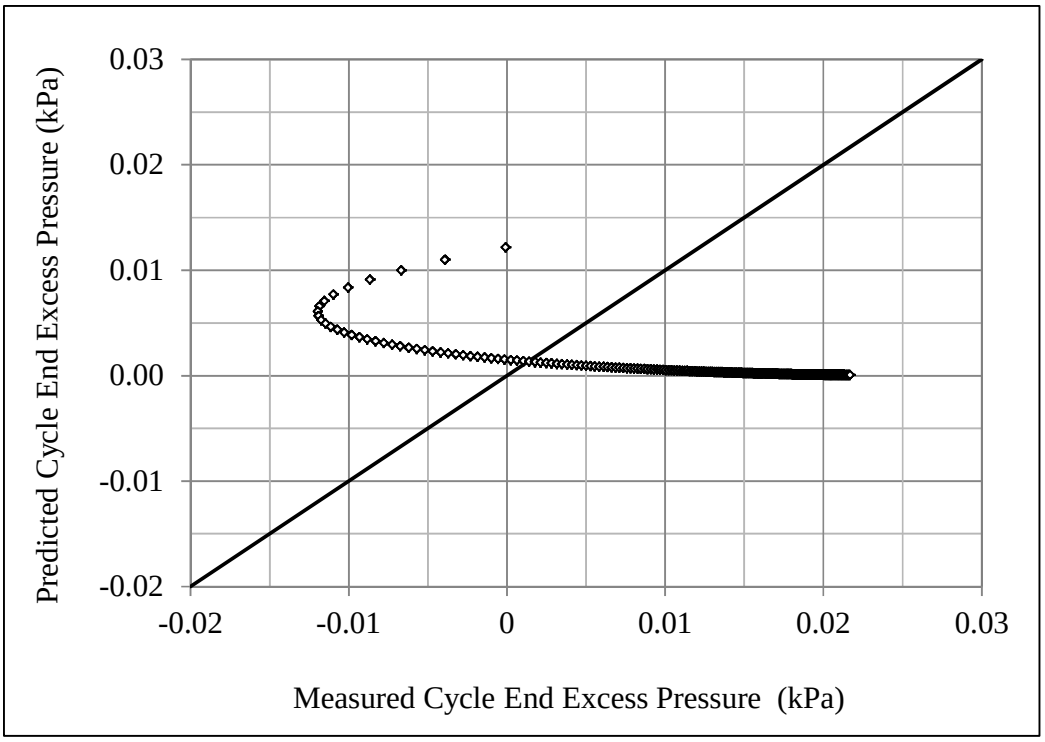

FIGURE 6-23 Measured versus predicted residual pore pressure u_2' at the end of each cycle

Third Modeling Attempt

Based on the results obtained in the first two modeling attempts, it was evident that a different approach ought to be followed to obtain a predictive model.

For this third attempt, the approach followed to break down the pore water pressure pulse is the same as that followed for the second approach (see Figure 6-12). Again, two functions are used to describe the pore water pressure development: the first one represents loading conditions during time t_L and the second one represents unloading conditions during the dwelling time t_D.

Firstly, it was decided to look for a different mathematical model to predict the pore water pressure development during the loading time t_L. Unlike the

Weibull function used originally, the new function has less than 4 regression constants, which may contribute to reduce the uncertainty of the predictions.

It was also decided to set the limits for maximum and minimum pore water pressures developed within the i^{th} cycle to correspond to the values defined by the Global Excess Pore Pressure Curves shown in Figure 6-13. For instance, if the predicted pore water pressure at the end of loading time u_1' resulted to be either greater or less than the value observed in the Global Loading Time End Excess Pressure Curve, then the pore pressure corresponding to the Global Curve was the prevailing value to be used as the intercept when applying the second function. In the same manner, u_p' and u_2' were adjusted before computing the pore pressure for the next cycle in the simulation.

Function 1

Non-linear regression analysis was conducted using the data from the 1,230 cycles available for Specimen 1. In other words, 1,230 non-linear regressions were conducted. Similar to the previous modeling attempt, data points corresponding to a time range between 0 and 1 second were used. In this case, instead of using 5 data points as it was done for the second attempt, only data corresponding to the three reference pore water pressure values u_0', u_p' and u_1' were included in each data set. That is, 1,230 data sets of 3 points were used to conduct the regression analysis.

As previously mentioned, a new function with only 3 regression constants was found to fit the data points. The function selected is called Logistic Dose Response Pulse (*LDR*) and is presented in Equation 6-9.

$$u_w' = \frac{4\alpha t^{-\lambda-1}\beta^{\lambda+1}\lambda^2}{\left(\lambda-1+\lambda t^{-\lambda}\beta^{\lambda}+t^{-\lambda}\beta^{\lambda}\right)^2} \quad (6\text{-}9)$$

Where,

u'_w = pore water pressure

t = time; valid for 0s ≤ t ≤ 1s

α = pore water pressure pulse amplitude

β = time at maximum pore water pressure

λ = regression constants

Similar to the Weibull function, the *LDR* function has a pulse amplitude α and a time at maximum pore water pressure β. Figure 6-12 shows the elements of the *LDR* pulse which are similar to those of the Weibull function. Equation 6-9 can be used to estimate the pore water pressure development during the loading time, including the three reference pore water pressures u_0', u_p' and u_1' shown in Figure 6-12.

In this case, measured values for the pulse amplitude α and the time at maximum pore water pressure β were used. The pulse amplitude α is the peak pore pressure u_p' for the i^{th} cycle. The u_p' values used as α to perform the regressions were obtained from the Predicted Global Peak Excess Pore Pressure Curve. The time values at maximum pore water pressure β were obtained from the measured data. Thus, only the values of λ remained unknown. The adjusted coefficient of determination R^2_{adj} values obtained for the 1,230 data sets were equal to 1 indicating exceptional predictions.

Figures 6-24 to 6-26 show the relationship between the *LDR* regression parameters and the number of repetitions *N*. Functions to predict α, and λ were obtained. As observed in Figure 6-25, it was considered reasonable to use an average value for the β parameter in the final simulation.

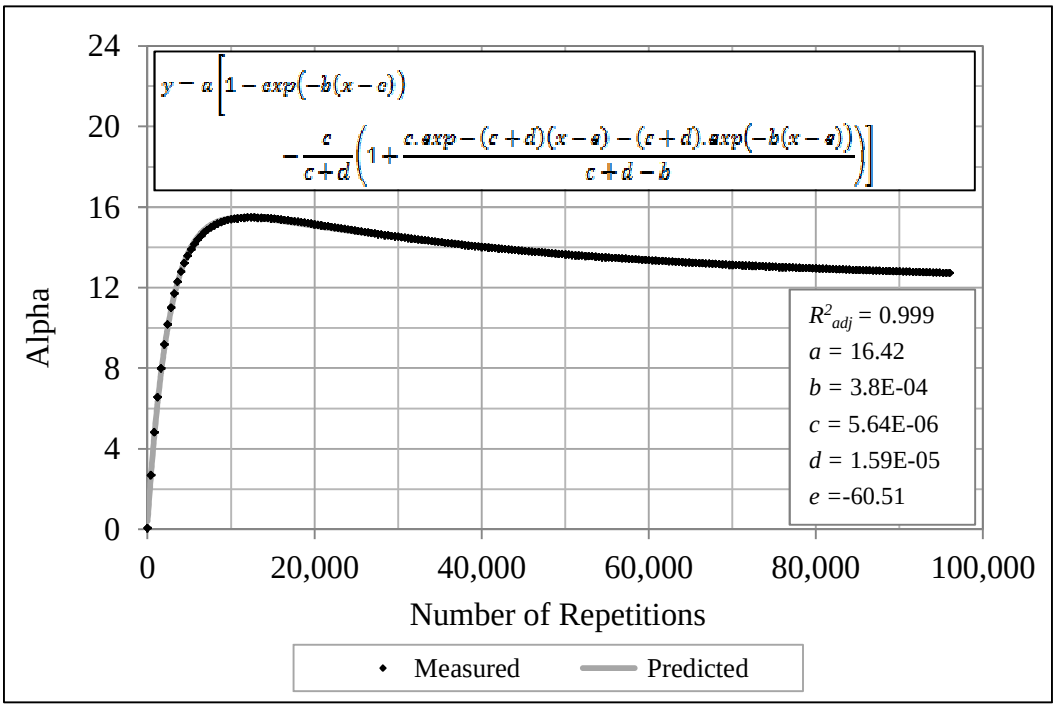

FIGURE 6-24 Alpha versus number of repetitions – third attempt

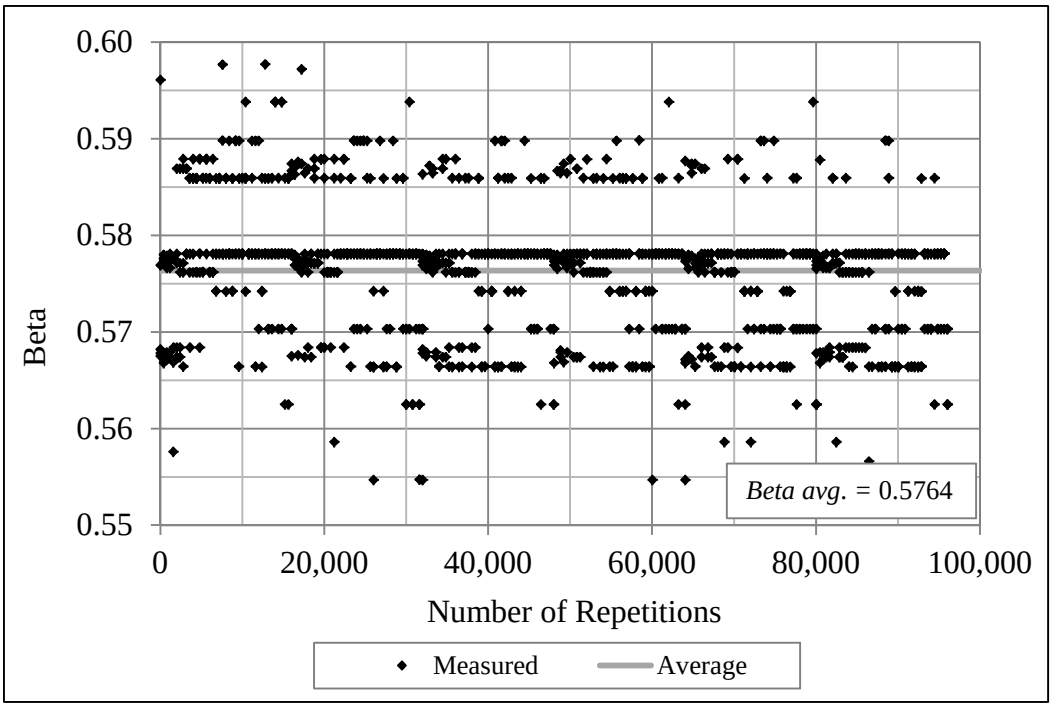

FIGURE 6-25 Beta versus number of repetitions – third attempt

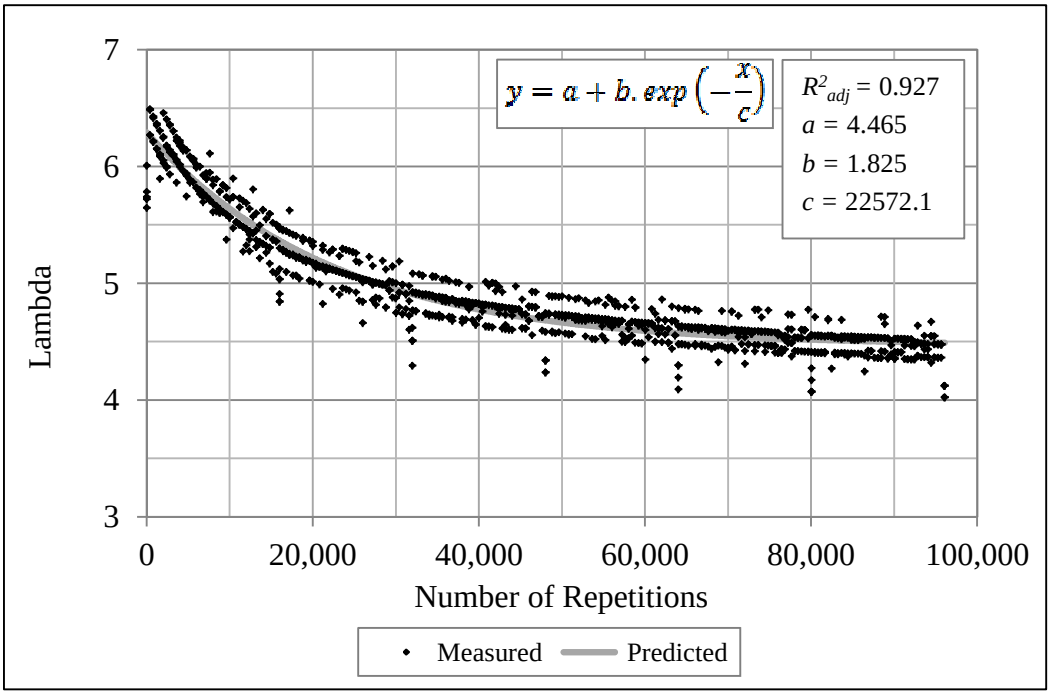

FIGURE 6-26 Lambda versus number of repetitions – third attempt

It is observed that the function to predict the *LDR* pulse amplitude α presented in Figure 6-24 has a high degree of complexity. A total of 5 regression constants are required to predict α as function of the number of repetitions *N*. Besides, different from the functions for α obtained in the previous modeling attempts, this time the pulse amplitude does not show a sustained increasing trend. It shows an increasing trend up to a maximum value and then it starts decreasing. Mathematically, the amplitude of the *LDR* pulse should be the difference between the pore pressure at the beginning u_0' and the peak pore pressure u_p' of the i^{th} cycle. It is expected that such difference shows an increasing trend up to a point where trend starts to level off. This observation was taken into account for the final modeling exercise presented in next sections.

The time at maximum pore pressure seems to oscillate around an average value of 0.5764 seconds. Therefore it was considered reasonable to use this average in this modeling attempt. The predictive function for λ shows a good R^2_{adj} of 0.927 even though some scatter is observed. All these observations were taken into consideration for the development of the final model presented in following sections.

Function 2

The same Third Order Decay function used in the second modeling attempt was used for this attempt. Therefore, the results and conditions of the analysis previously conducted apply also to this section. The Equation 6-7 defines the function utilized in this attempt, and Figures 6-18 and 6-19 show the relationships

between the regression parameters for such function and the number of repetitions.

Following the approach proposed in Figure 6-12, the expression to estimate the excess pore water pressure for *N* number of repetitions is again presented in Equation 6-10:

$$\Delta u_{wN} = \sum_{i=1}^{N} u_2{}'_i \tag{6-10}$$

Where,

$u_2{}'_i$ = residual pore water pressure in the i^{th} cycle

Δu_{wN} = accumulated excess pore water pressure in the *N* cycle

Taking into account that u_2' is estimated by using Equation 6-7, and also is a function of u_1' (which is estimated by using Equation 6-9), Equation 6-10 when used to estimate $\Delta u_{w\,N}$ for "the cumulative cycle end pressure" can be rewritten as follows:

$$\Delta u_{2\,N} = \sum_{i=1}^{N} \left[\vartheta + \frac{\left[\frac{4\alpha t_L{}^{-\lambda-1}\beta^{\lambda+1}\lambda^2}{\left(\lambda-1+\lambda t_L{}^{-\lambda}\beta^{\lambda}+t_L{}^{-\lambda}\beta^{\lambda}\right)^2} - \vartheta \right]}{\sqrt{1+2.\left[\frac{4\alpha t_L{}^{-\lambda-1}\beta^{\lambda+1}\lambda^2}{\left(\lambda-1+\lambda t_L{}^{-\lambda}\beta^{\lambda}+t_L{}^{-\lambda}\beta^{\lambda}\right)^2} - \vartheta \right]^2 .\omega.t_D}} \right]_i \tag{6-11}$$

In a similar way, when estimating $\Delta u_{w\,N}$ for "the cumulative peak pressure", Equation 6-10 can be rewritten as follows:

$$\Delta u_{p\,N} = \sum_{i=1}^{N-1} \left(\vartheta + \frac{\left[\frac{4\alpha {t_L}^{-\lambda-1} \beta^{\lambda+1} \lambda^2}{\left(\lambda-1+\lambda {t_L}^{-\lambda} \beta^{\lambda} + {t_L}^{-\lambda} \beta^{\lambda}\right)^2} - \vartheta \right]}{\sqrt{1+2.\left[\frac{4\alpha {t_L}^{-\lambda-1} \beta^{\lambda+1} \lambda^2}{\left(\lambda-1+\lambda {t_L}^{-\lambda} \beta^{\lambda} + {t_L}^{-\lambda} \beta^{\lambda}\right)^2} - \vartheta \right]^2 .\omega.t_D}} \right)_i + \alpha_N \qquad (6\text{-}12)$$

It can be observed that Equation 6-9 was inserted into Equation 6-7 to generate Equations 6-11 and 6-12. However, as commented in the beginning of this section, whenever the accumulated pore pressure at the transition between functions for the i^{th} cycle does not match the value from the Global Excess Pore Pressure Curves, any result obtained using Equations 6-7 and 6-9 should be replaced by its corresponding value from the respective Global Curve. Therefore, the solely use of Equations 6-11 and 6-12 without adjusting the results is not useful to obtain good predictions.

As in previous attempts, a simulation of pore water pressure buildup for 96,060 cycles was performed. The results for the pore pressure accumulated at the peak of cycles Δu_p and pore pressure accumulated at the end of cycles Δu_2 obtained from the simulations are shown in Figures 6-27 and 6-28.

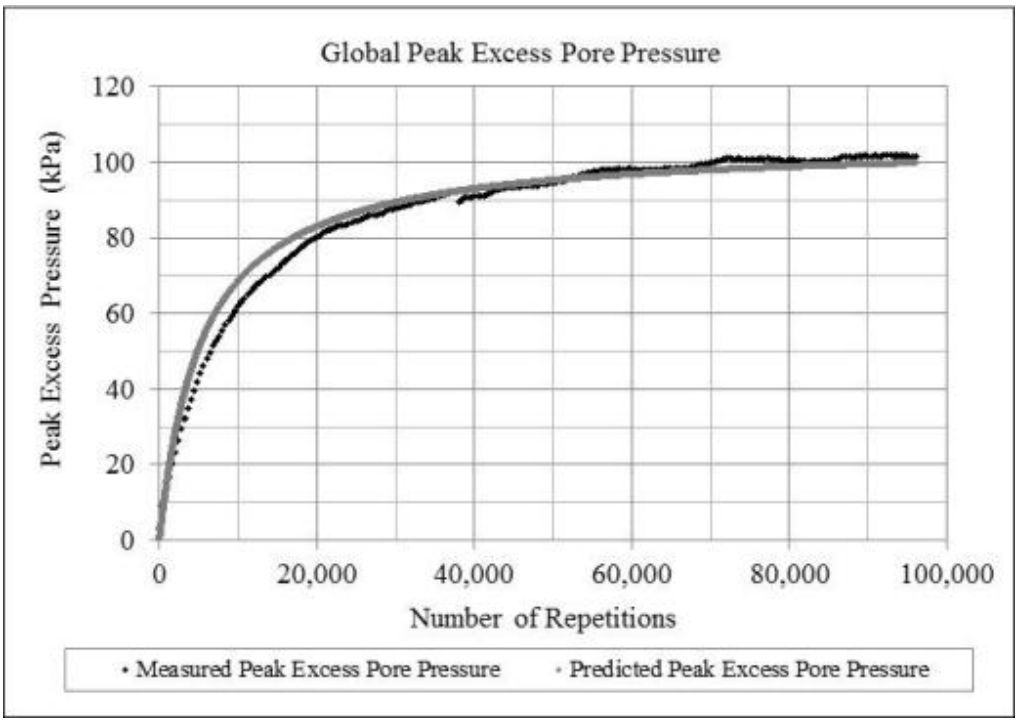

FIGURE 6-27 Simulation results for the global peak excess pore pressure

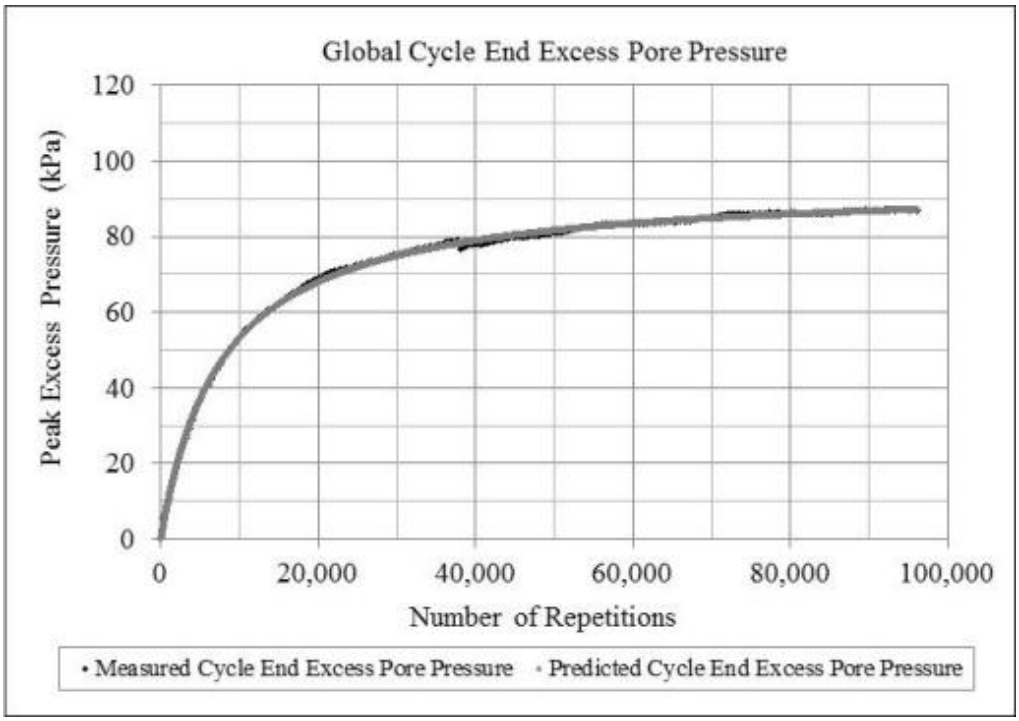

FIGURE 6-28 Simulation results for the global cycle end excess pore pressure

It can be observed that the predictions closely match the measured values. This is due to the adjustment applied to the estimates from the simulation. Since the results are adjusted to match the predicted Global Curves shown in Figure 6-13, the difference between the predicted values and the measured values are basically the same as the difference between the predicted Global Curves and the measured values.

Figures 6-27 and 6-28 may not the best plots to judge the accuracy of the predictions obtained because the points observed correspond to adjusted values that will always fall on predicted Global Curves. In order to emit a better judgment on how well the models presented in this section describe the pore water pressure development, a close view on the predictions for only 5 cycles is presented in Figure 6-29.

In this figure, the gray dashed line corresponds to the pore water pressure measured in the lab. It can be seen that the predictions represented by the black continuous line are very close to the measured values. Also, it should be noted that the Global Curves govern the limits of the predictions as a result of the applied adjustments previously described. The difference between the measured peak points and the predicted peak points basically reflects the error induced by the mathematical equation selected to model the Global Peak Pore Pressure Curve. The same applies for the pressure values at the end of cycles. Details about the mathematical functions used to model Global curves are provided in next sections.

The error induced by using both the *LDR* pulse and the Third Order Decay functions is also captured in Figure 6-29 even if it is not too noticeable. However, such error does not accumulate anymore due to the applied adjustment to the values predicted at the transition between the two functions.

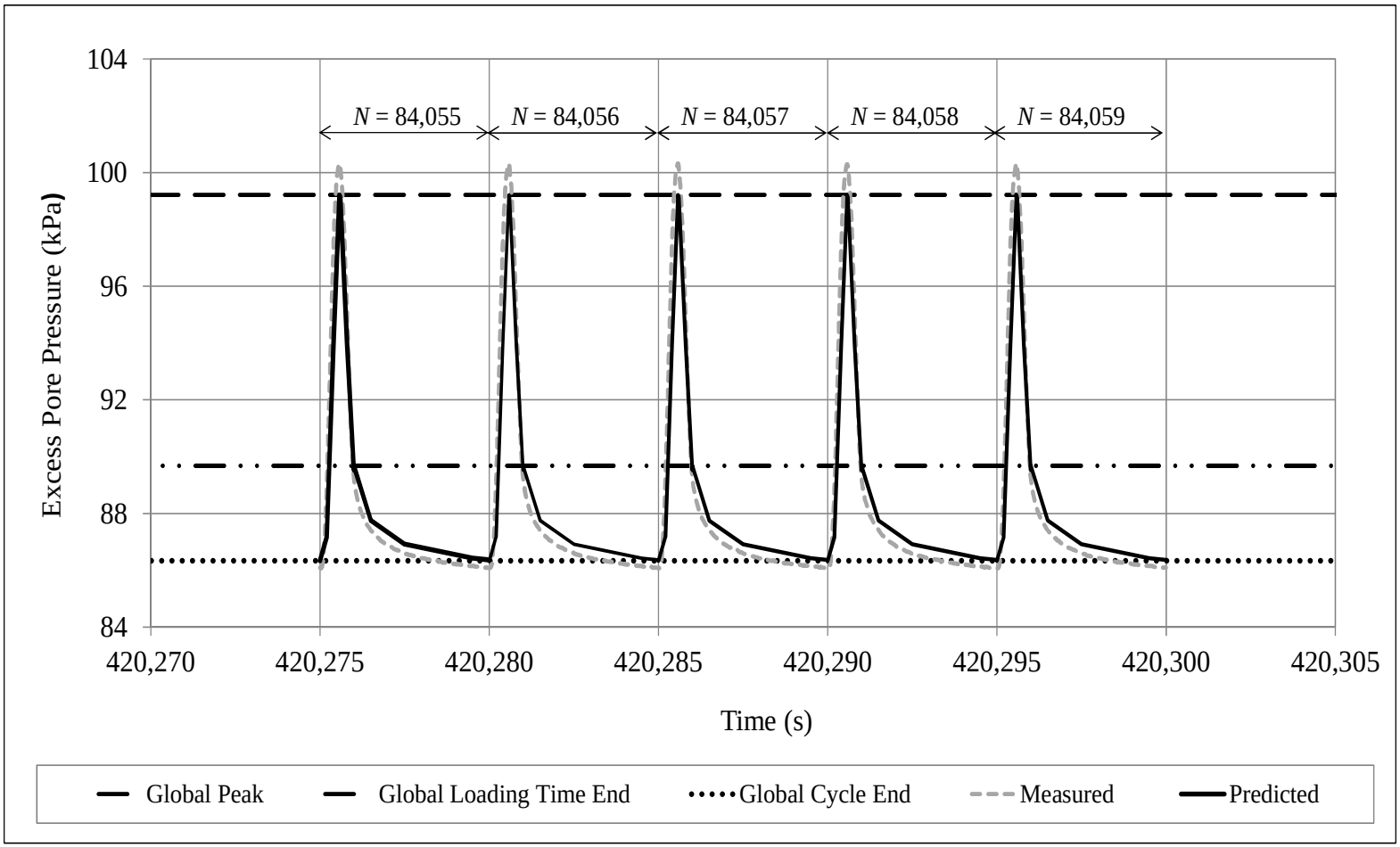

FIGURE 6-29 Close view of excess pore pressure predictions – third modeling attempt

One of the problems encountered in this modeling attempt had to do with the complexity of the model found to predict the amplitude α of the *LDR* pulse. Therefore, a more practical solution was needed.

Final Model

In this section, the final approach followed to analyze the data obtained from the laboratory testing program is presented. The analysis was performed by using all the specimens tested. The main enhancement in the modeling methodology was the use of the predicted Global Curves to set boundary conditions for solving the functions that describe the pore pressure development for the i^{th} cycle. In this way, the final number of regression constants required for prediction was minimized and better results were obtained.

In order to model the laboratory test results, first it was necessary to find a mathematical function to describe the Global Excess Pore Water Pressure Curves. Then the boundary conditions for the functions were established and the final expression was developed.

Global Excess Pore Pressure Curves

The suitability of different simple mathematical models to fit the data from the specimens tested in the laboratory was evaluated. In the preliminary modeling attempts explained in previous sections, the Global Excess Pore Pressure data for Specimen 1 was fitted to hundreds of mathematical functions by using the statistical software Table Curve 2D. Table 6-1 shows an example of the software output obtained for both the Global Peak Excess Pressure and the Global Cycle

End Excess Pressure. A ranking of equations (expressed in a linear fashion) that best fitted the data is shown for the two mentioned curves. Based on the R^2_{adj}, the top ranked functions were selected as predictive equations. This means that for the preliminary analysis, the same equation was not used to predict all the Global Curves.

For the final modeling, it was considered convenient that the data from all specimens should fit the same mathematical function and therefore, the same regression exercise was conducted in all the data sets to identify a common function capable of predicting the Global Curves with reasonably high accuracy. For instance, in Table 6-1 it can be observed that the highest ranked equation for the Global Cycle End Pressure data is not the same as the highest ranked equation for the Global Peak Pressure data. However, no significant accuracy in the prediction of the Global Peak Pressure is lost if the highest ranked equation found for the Global End Cycle Pressure is used for predicting both curves. Therefore, it can be considered reasonable to use the equation grayed out in Table 6-1 as a common predictive function.

TABLE 6-1 Example of mathematical functions evaluation for specimen 1

Rank	Global Peak Pressure		Global Cycle End Pressure	
	R^2_{adj}	Equation	R^2_{adj}	Equation
1	0.9974	$y^{-1}=a+blnx/x$	0.9990	$y^{-1}=a+b/x$
2	0.9834	$lny=a+b/x^{0.5}$	0.9974	$y^{-1}=a+blnx/x$
3	0.9744	$y^{-1}=a+b/x$	0.9938	$lny=a+b/x^{0.5}$
4	0.9645	$y^{-1}=a+b/x^{0.5}$	0.9798	$lny=a+blnx/x$
5	0.9568	$lny=a+b/lnx$	0.9756	$y^{-1}=a+b/x^{1.5}$
6	0.9517	$y=a+b(lnx)^2$	0.9593	$y^{-1}=a+b/x^{0.5}$
7	0.9490	$y^{0.5}=a+blnx$	0.9523	$lny=a+b/lnx$
8	0.9342	Power(a,b,c)	0.9497	$y=a+b(lnx)^2$
9	0.9265	$y^{0.5}=a+b(lnx)^2$	0.9445	$y^{0.5}=a+blnx$
10	0.9202	$y=a+blnx$	0.9311	Power(a,b,c)
11	0.9191	Power_(a,b)	0.9299	$lny=a+b/x$
12	0.9117	$lny=a+blnx$	0.9216	$y=a+blnx$
13	0.8875	$y^{-1}=a+b/lnx$	0.9194	$y^{0.5}=a+b(lnx)^2$
14	0.8798	$lny=a+b(lnx)^2$	0.9128	Power_(a,b)
15	0.8263	$y=a+bx^{0.5}$	0.9030	$lny=a+blnx$
16	0.8197	$y^{-1}=a+blnx$	0.8780	$y^{-1}=a+b/lnx$
17	0.7973	$y=a+bx^{0.5}lnx$	0.8690	$lny=a+b(lnx)^2$
18	0.7807	$y^{-1}=a+b(lnx)^2$	0.8440	$y^{-1}=a+blnx/x^2$
19	0.7702	$y^{0.5}=a+bx^{0.5}$	0.8170	$y=a+bx^{0.5}$
20	0.7411	$y^{0.5}=a+bx^{0.5}lnx$	0.8076	$y^{-1}=a+blnx$

The same analysis exercise was performed considering the Peak, Loading Time End and Cycle End Global Excess Pore Pressure Curves from all specimens. It was concluded that Equation 6-13 is the model that best fits all data from every specimen tested. Equation 6-13 is an asymptotic function with two regression parameters and is expressed as follows:

$$\Delta u_w = \frac{1}{a+\frac{b}{t}} \quad (6\text{-}13)$$

Where,

Δu_w = cumulative Global Excess Pore Pressure

t = time in seconds

a and b = regression parameters

For practical purposes, convenient subscripts are used to differentiate between parameters a and b corresponding to the three different Global Excess Pressure Curves utilized as boundaries for modeling of the i^{th} cycle. The parameters a_p and b_p correspond to the Global Peak Excess Pressure Curves, parameters a_1 and b_1 correspond to the Global Load End Excess Pressure Curves and, parameters a_2 and b_2 correspond to the Global Cycle End Excess Pressure Curves.

Table 6-2 shows the a and b parameters obtained from the regression analysis and also recalls the test conditions for each specimen. It should be noted that $S\%_{AP}$ is the specimen degree of saturation after preparation, $S\%_{AC}$ is the specimen degree of saturation after consolidation and $S\%_{AT}$ is the specimen degree of saturation after testing.

TABLE 6-2 Test conditions and regression constants for the global curves

Specimen	1	2	3	4	5	6
$S\%_{AP}$	81	79	78	80	83	80
$S\%_{AC}$	75	76	95	96	78	73
$S\%_{AT}$	77	77	100	100	82	77
$\psi_{mo}\,(kPa)$	157	157	0	0	157	157
$\theta_{net/eff}\,(kPa)$	509	344	509	344	509	344
$t_D\,(s)$	4	4	4	4	8	8
a_p	0.0090	0.0157	0.0199	0.0398	0.0177	0.0233
a_1	0.0103	0.0164	0.0260	0.0936	0.0295	0.0243
a_2	0.0107	0.0167	0.0270	0.0981	0.0307	0.0252
b_p	359.2	613.9	391.2	180.3	452.7	3716.2
b_1	388.4	714.8	425.7	1016.9	2028.7	3873.0
b_2	400.3	732.4	440.1	1703.0	3449.3	3906.8

As an example of the results obtained from the regression analysis, Figure 6-30 shows the predicted Global Peak Excess Pressure Curve obtained for Specimen 1. In Figure 6-30, the data points are plotted along with the predicted curve. Figure 6-31 shows the goodness of fit for Specimen 1. It can be observed that the adjusted coefficient of determination R^2_{adj} and the standard error ratio S_e/S_y obtained are 0.998 and 0.040, respectively. These numbers indicate that the model selected provides excellent predictions.

Similar plots to those presented in Figures 6-30 and 6-31 were developed for the three Global Curves for every specimen. The totality of the plots is conveniently presented in Appendix B.

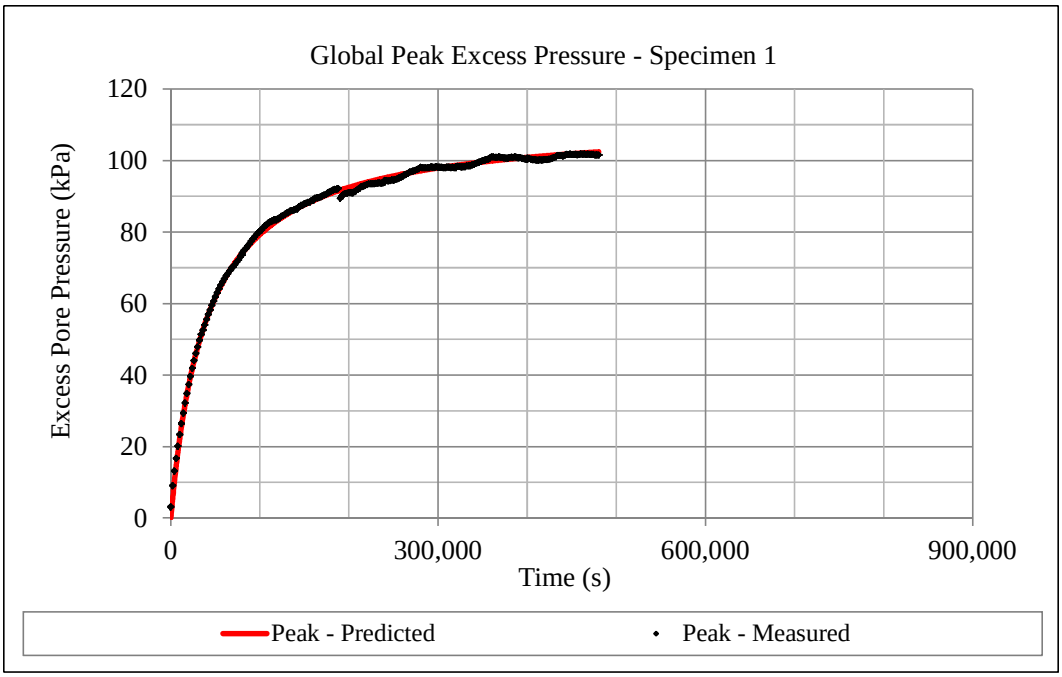

FIGURE 6-30 Predictions of global excess pore pressure

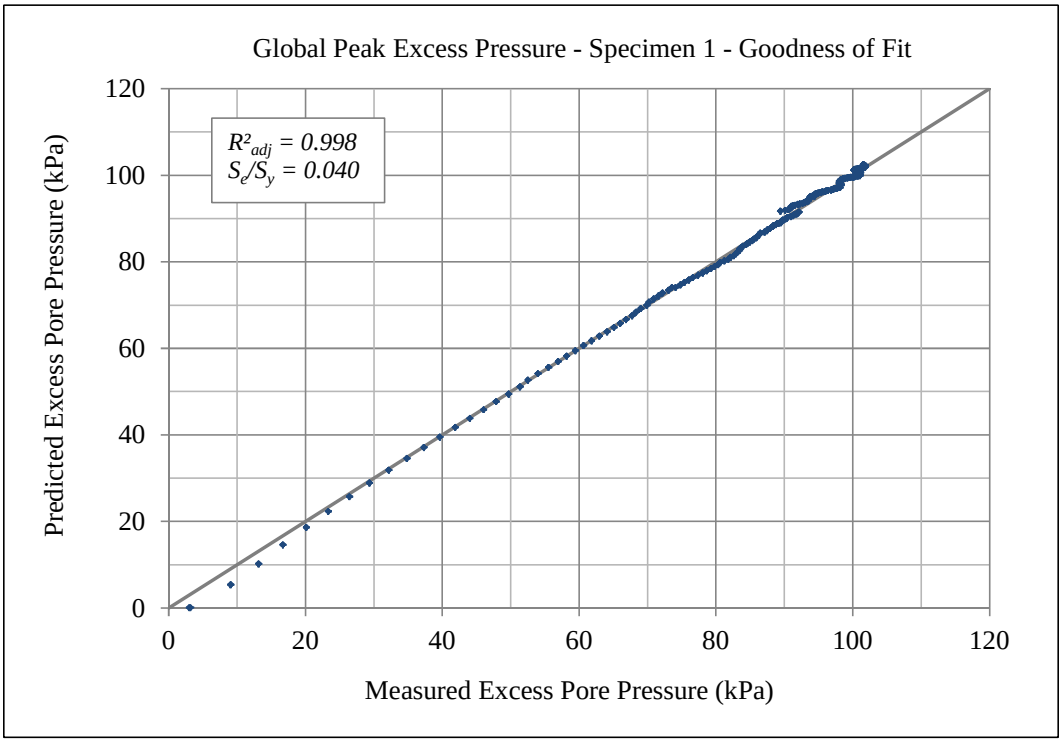

FIGURE 6-31 Goodness of fit for global excess pore pressure

Table 6-3 shows the regression constants but this time accompanied by the statistical parameters that indicate the goodness of fit of the data to the model selected. Both, the adjusted coefficient of determination R^2_{adj} and the standard error ratio are included in the table. The adjusted coefficient of determination R^2_{adj} ranges from 0.752 to 0.999, while the standard error ratio S_e/S_y ranges from 0.032 to 0.526. According to both parameters the predictions can be considered good to excellent.

Figure 6-32 shows a plot presenting the predicted Global Peak Pore Water Pressure Curves obtained as result of fitting the data to Equation 6-13. It was decided presenting the Peak Pressures only in order to keep the figure clear rather than presenting a crowded plot containing several curves that would not help for a good appreciation of the results.

TABLE 6-3 Statistical parameters for the predicted global curves

Specimen	Parameter											
	a_p	b_p	S_e/S_y	R^2_{adj}	a_1	b_1	S_e/S_y	R^2_{adj}	a_2	b_2	S_e/S_y	R^2_{adj}
1	0.00901	359.2	0.040	0.998	0.01027	388.4	0.032	0.999	0.01068	400.3	0.035	0.999
2	0.01572	613.9	0.113	0.987	0.01638	714.8	0.122	0.985	0.01666	732.4	0.123	0.985
3	0.01995	391.2	0.279	0.922	0.02597	425.7	0.225	0.949	0.02704	440.1	0.223	0.950
4	0.03985	180.3	0.485	0.766	0.09358	1016.9	0.526	0.725	0.09813	1703.0	0.499	0.752
5	0.01774	452.7	0.421	0.823	0.02951	2028.7	0.223	0.950	0.03072	3449.3	0.139	0.981
6	0.02334	3716.2	0.125	0.984	0.02434	3873.0	0.115	0.987	0.02524	3906.8	0.112	0.987

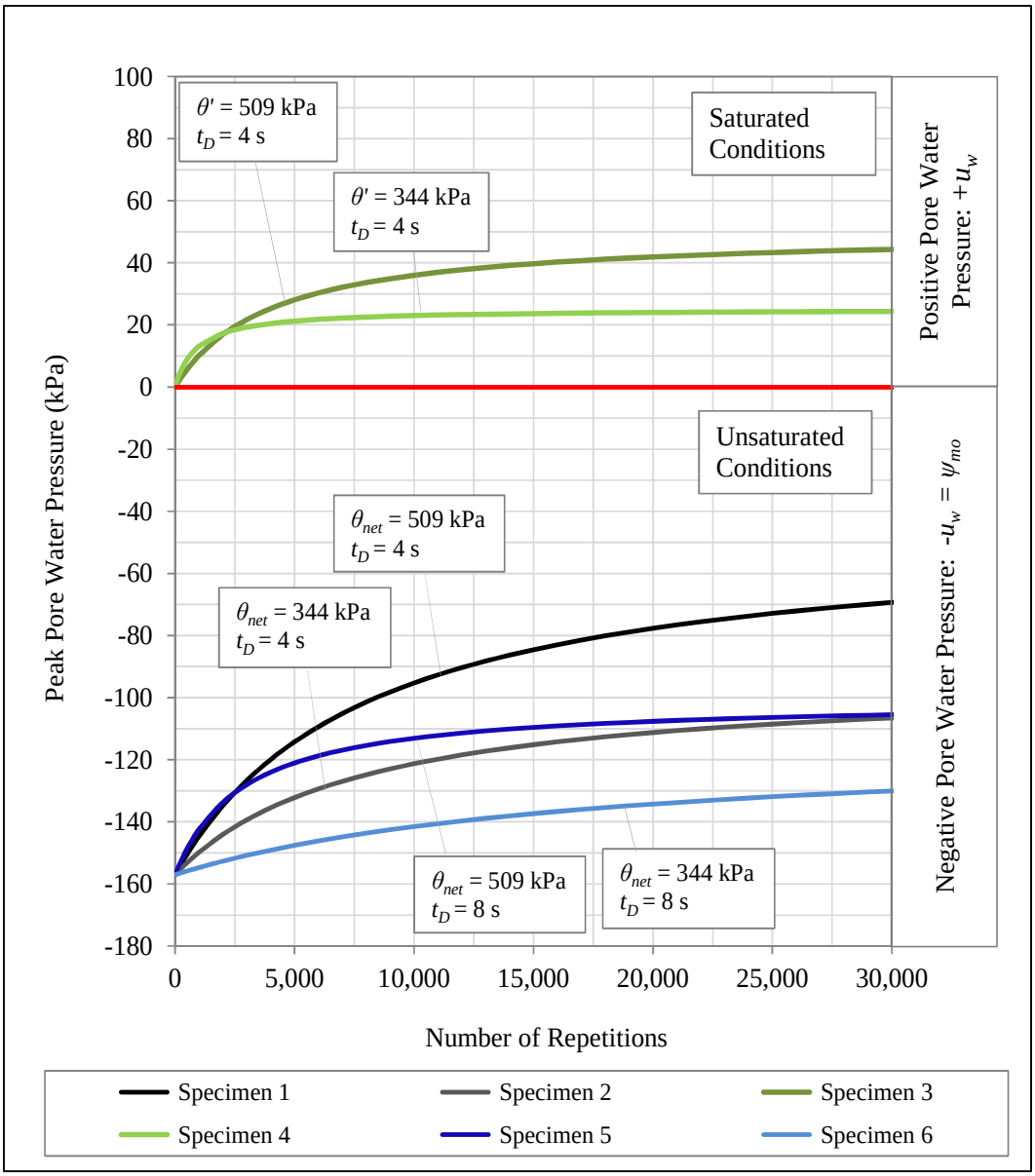

FIGURE 6-32 Results from regression analysis for the global peak pressure curves

Note that the values plotted in the figure correspond to **Pore Water Pressures** rather than **Excess Pore Pressure**. This means that for the unsaturated specimens, the origin of the predicted Excess Pore Pressure was translated to the Initial Negative Pore Pressure imposed to each specimen as the initial equilibrium

condition. The Initial Negative Pore Water Pressure is the negative value of the Initial Matric Suction.

When looking at the results presented in Figure 6-32, reasonable trends are found. It is observed that for constant initial matric suction ψ_{mo} and dwelling time t_D, the greater the bulk stress $\theta_{net/eff}$ applied, the grater the pore water pressure developed.

The influence of the dwelling time t_D is evident. The shorter the dwelling time t_D, the greater the pore water pressure buildup, which means less dissipation between cycles. Values of excess pore water pressure developed were found to be higher for the specimens tested with 4 seconds of dwelling time t_D. On the other hand, the specimens tested using a dwelling time t_D equal to 8 seconds developed lower excess pore water pressures.

Probably the most unexpected result was related to the initial matric suction ψ_{mo}. It is believed that specimens under saturated conditions develop higher excess pore pressures than those under unsaturated conditions. However it can be observed in Figure 6-32 that exactly the opposite effect was obtained.

It can be observed that Specimens 3 and 4 tested under saturated conditions with a dwelling time t_D of 4 seconds and effective bulk stresses θ' of 509 and 344 kPa respectively, developed lower pore water pressures than Specimens 1 and 2, which were tested at the same t_D and θ_{net} respectively but under unsaturated conditions. Even though these findings are surprising, they coincide with the results observed by Minh Thu et al. and Yang et al. (*34 and 35*). Such results were previously presented in Chapter 2.

Finally, it was also observed in Figure 6-32 that under the test conditions for this study, the pore water pressure buildup seems to gradually reach an asymptotic value for all specimens tested. Note that the unsaturated specimens do not even develop positive pore water pressures after thousands of repetitions. However, under extreme loading conditions (i.e., under unusual high loads) it cannot be ruled out that the rate of pore pressure buildup become high enough and significantly reduce the effective confining stresses leading the specimen to failure.

These preliminary observations are further elaborated and discussed towards the end of this chapter.

Significance of the Global Curves Regression Constants

The principal motivation for developing a model that describes the excess pore pressure buildup is aimed not only at predicting the response of the material but also to understand how the loading/unloading conditions affect such response. In order to evaluate the influence of the conditions present during the load application, the significance of the regression parameters that define the model needs to be understood.

The expression previously presented in Equation 6-13 describes the accumulation of excess pore water pressure as the number of load repetitions increases. Such accumulation occurs progressively until it approaches an asymptotic value that represents the maximum excess pore water pressure or maximum change in pore water pressure expected under a particular condition.

Figure 6-33 shows how the variation of the *a* parameter impacts the estimated excess pore pressure development. For this exercise, the value of the *b* parameter was held constant at 500 and the *a* parameter was varied within a range from 0.0075 to 0.0175.

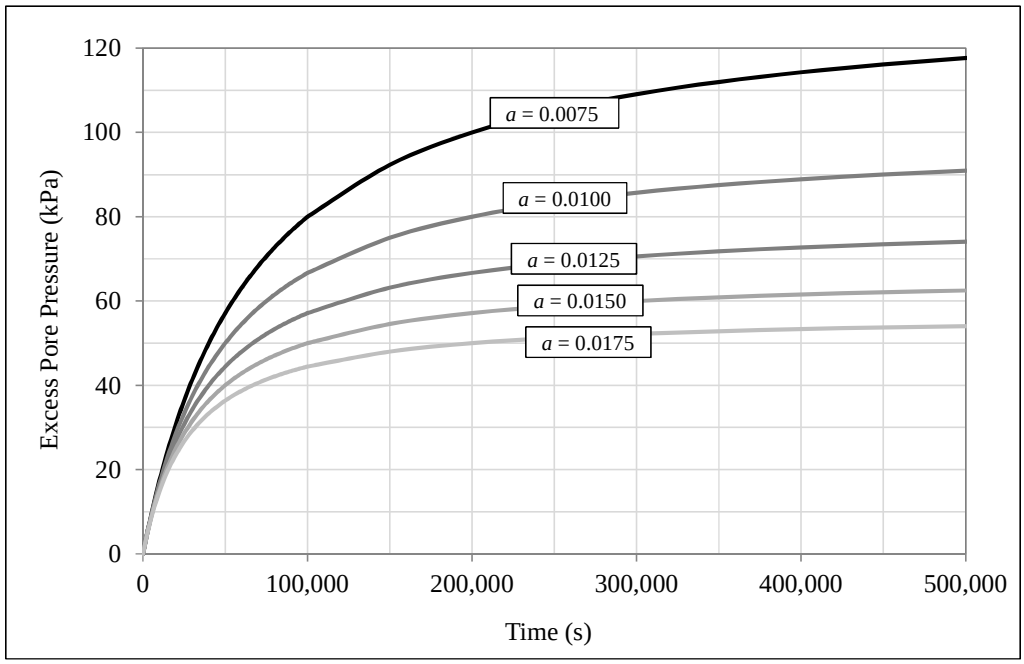

FIGURE 6-33 Influence of the *a* parameter upon excess pore pressure response

As can be observed, the expected maximum excess pore pressure development increases as the *a* parameter decreases. The relationship between the *a* parameter and the maximum excess pore pressure $\Delta \boldsymbol{u}_{\boldsymbol{w\,max}}$ buildup under dynamic load is expressed in Equation 6-14.

$$\Delta u_{w\,max} = \frac{1}{a} \tag{6-14}$$

Figure 6-34 represents graphically the relationship between *a* parameter and the maximum excess pore pressure $\Delta \boldsymbol{u}_{\boldsymbol{w\,max}}$.

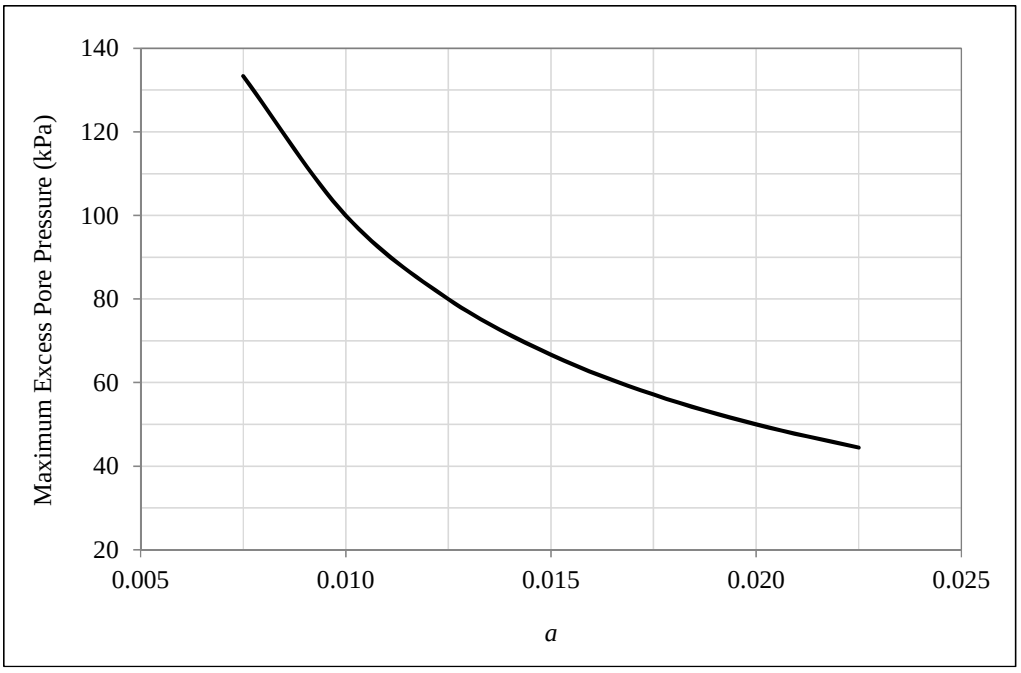

FIGURE 6-34 Relationship between *a* parameter and 99% of $\Delta \boldsymbol{u}_{\boldsymbol{w\,max}}$

The parameter *b* represents the time it takes to reach the maximum excess pore pressure. As it can be observed in Figure 6-35, the greater the *b* parameter, the longer the time to reach the maximum excess pore pressure. For this exercise, the value of the *a* parameter was held constant at 0.0085. This value corresponds to a maximum excess pore pressure of about 118 kPa. The *b* parameter was varied within a range from 100 to 1,200.

Figure 6-36 clearly shows the linear relationship between the b parameter and the estimated time to reach the 99% of $\Delta \boldsymbol{u}_{\boldsymbol{w\,max}}$corresponding to a value of 0.0085 for the *a* parameter. Such times correspond to the *b* values used to develop Figure 6-34.

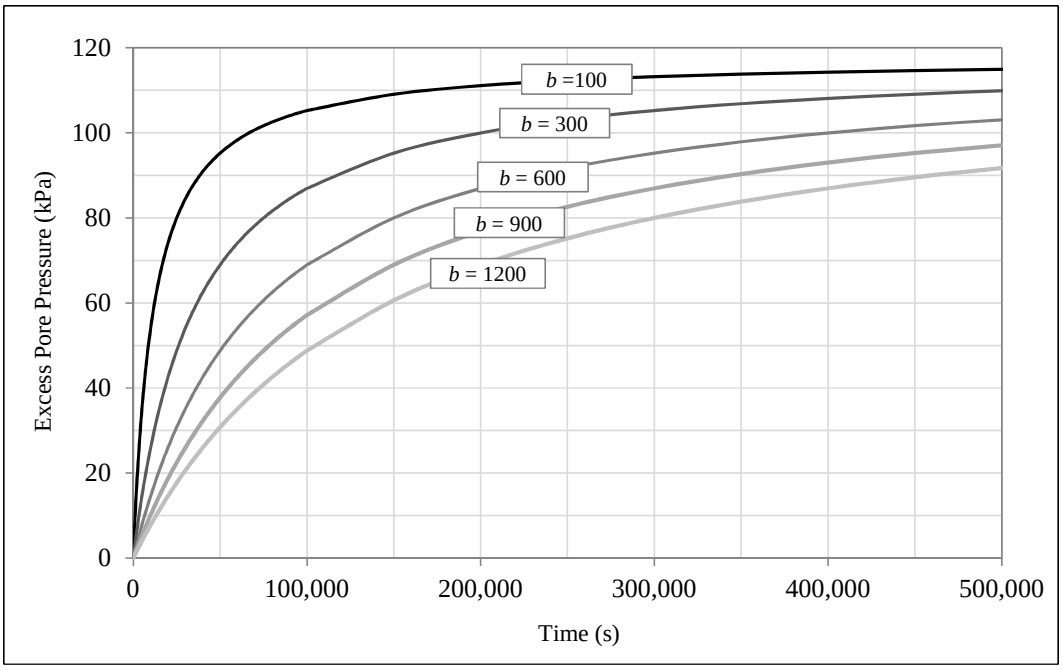

FIGURE 6-35 Influence of the *b* parameter upon the pore pressure response

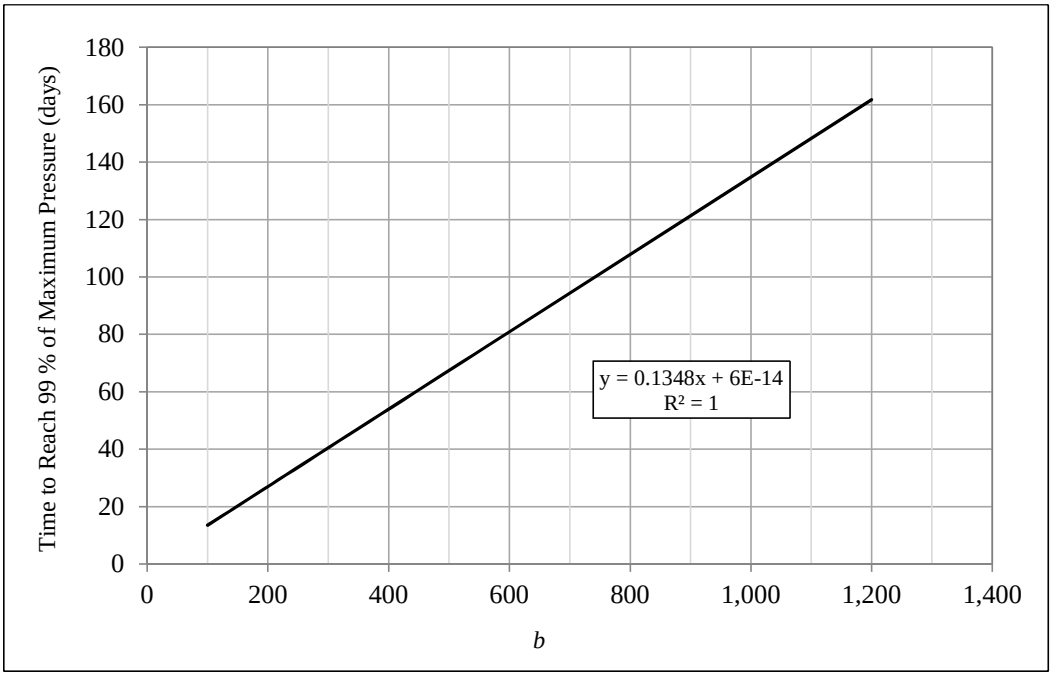

FIGURE 6-36 Relationship between *b* parameter and 99% of $\Delta \boldsymbol{u}_{\boldsymbol{w\,max}}$

Table 6-4 presents the estimated times required to reach 99% of $\Delta \boldsymbol{u}_{\boldsymbol{w\,max}}$ for all specimens tested. The parameters *a* and *b* from Table 6-3 were used to solve Equation 6-13 to find both, the $\Delta \boldsymbol{u}_{\boldsymbol{w\,max}}$ and the time required to reach 99% of it. Such times were also translated into number of repetitions N_{max}. As previously mentioned, the loading time t_L for all specimens tested was fixed to 1 second. The dwelling time t_D for each specimen can be found in Table 6-2. The total time per cycle is $t_{L+}\ t_D$.

TABLE 6-4 Maximum excess pressures and times

Specimen	1	2	3	4	5	6
ψ_{mo}*(kPa)*	157	157	0	0	157	157
$\theta_{net/eff}$*(kPa)*	509	344	509	344	509	344
t_D*(s)*	4	4	4	4	8	8
$\Delta u_{p\,max}$*(kPa)*	111	64	50	25	56	43
$\Delta u_{1\,max}$*(kPa)*	97	61	39	11	34	41
$\Delta u_{2\,max}$*(kPa)*	94	60	37	10	33	40
$t_{p\,max}$*(days)*	46	45	22	5	29	182
$t_{1\,max}$*(days)*	43	50	19	12	79	182
$t_{2\,max}$*(days)*	43	50	19	20	129	177
$N_{p\,max}$	788,973	773,340	388,281	89,568	280,697	1,751,489
$N_{1\,max}$	748,849	863,942	324,580	215,156	756,186	1,750,483
$N_{2\,max}$	742,201	870,612	322,189	343,612	1,235,176	1,702,900

The estimated values of maximum excess pore pressures from Table 6-4 reflect the influence of the *a* parameter on the predictions obtained with Equation 6-13. Within a single specimen, it can be observed in Table 6-3 that reasonably the a_p parameter from the Global Peak Excess Pressure Curve is always lower than the a_1 parameter for the Global Load End Excess Pressure Curve. This

observation is translated in terms of maximum excess pressure developed in Table 6-4. The maximum excess pressure developed for the Global Peak Excess Pressure Curve is always greater than the maximum excess pressure developed for the Global Load End Excess Pressure Curve. The same observation applies when comparing the *a* parameters between the Global Load End Excess Pressure Curve and the Cycle End Excess Pressure Curve. Such observations only reflect the fact that the maximum excess pressure is the reciprocal of the *a* parameter and that the prediction is rational.

In the same way, it can be observed that the reciprocal of the *a* parameter or maximum excess pressure for any of the three Global Curves is always greater for those specimens that were subjected to a high level of bulk stress when compared to their pairs tested at low bulk stress level. Also, when comparing Specimens 1 and 2 with Specimens 3 and 4 respectively, it can be observed that the unsaturated Specimens 1 and 2 developed higher excess pressures than Specimens 3 and 4. This means that the *a* parameter for Specimens 1 and 2 were found to be lower than those for Specimens 3 and 4.

The rationality of the *b* parameter is more complicated to evaluate at a first glance or by simply comparing the number of repetitions *N* required to reach the maximum excess pressures. This is due to the fact that when estimating either maximum time or maximum *N*, the parameter *a* varies from one specimen to the other. At this point it can only be said that as the *b* parameter increases, the time to reach the maximum excess pressure also increases when *a* is held constant. A deeper analysis of *a* and *b* regression parameters is presented in next sections.

Modeling the Pore Water Pressure Development for the i^{th} Cycle

In this second step of the modeling procedure, the three Global Excess Pore Pressure Curves are utilized to set boundary conditions for modeling the pore pressure development within each particular i^{th} cycle. The mathematical functions that describe the soil response for each period of load and rest are presented. The previously presented *LDR* function is used to model the loading period and a new exponential function is proposed to model the dwelling period.

The composition of the load cycle is the same shown in Figure 6-12 for the third attempt. The same schematic is conveniently presented again in Figure 6-37 to recall the composition of the i^{th} cycle.

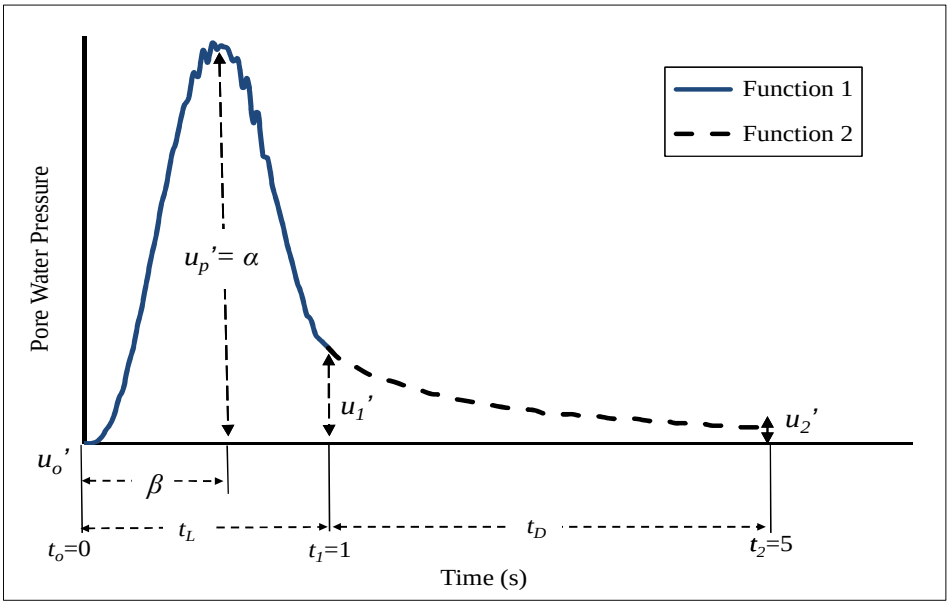

FIGURE 6-37 Final modeling of the i^{th} cycle

Function 1

As previously mentioned, a function with only 3 regression constants was found to fit reasonably well the data points corresponding to the loading period. The function selected is called Logistic Dose Response Pulse (*LDR*) and is presented again in Equation 6-15.

$$u_{wL}' = \frac{4\alpha t^{-\lambda-1}\beta^{\lambda+1}\lambda^2}{\left(\lambda-1+\lambda t^{-\lambda}\beta^{\lambda}+t^{-\lambda}\beta^{\lambda}\right)^2} \quad (6\text{-}15)$$

Where,

u'_{wL} = pore water pressure developed within the i^{th} cycle during the load period

t = time elapsed from the beginning of the cycle; valid for 0s $\leq t \leq t_L$

α = pore water pressure pulse amplitude

β = time at maximum pore water pressure

λ = regression parameters

The *LDR* function has a pulse amplitude α and a time at maximum pore water pressure β as shown in Figure 6-37. Note that if pore pressures accumulated from cycles applied prior to the i^{th} cycle were added, the new accumulated u_0' value would correspond to a point that lies on the Global Cycle End Excess Pressure Curve. Following the same reasoning, the accumulated pressure at u_2' falls on the Global Cycle End Excess Pressure Curve too. From a global perspective, the points corresponding to u_p' and u_1' would fall on the Global Peak and Global Load End Excess Pressure Curves, respectively. This approach can be better understood by looking at the global perspective of the pore pressure characteristic elements shown in Figure 5-9 in Chapter 5.

Following the same reasoning, the amplitude $\alpha = u_p'$ for the *LDR* function at any i^{th} cycle can be easily found if the *a* and *b* parameters corresponding to the Global Excess Pressure Curves are known. By applying Equation 6-13, the accumulated excess pore pressure from the Global Peak Excess Pressure Curve at any cycle can be found as follows:

$$\Delta u_{wp} = \frac{1}{a_p + \frac{b_p}{t_p}} \tag{6-16}$$

Where,

Δu_{wp} = accumulated Global Peak Excess Pore Pressure

$t_p = (i-1)(t_L + t_D) + \beta$, in seconds

$a_p$and b_p = regression constants corresponding to the Global Peak Excess Pore Pressure Curve

In a similar way, the cumulative excess pore pressure from the Global Cycle End Excess Pressure Curve at any cycle can be found as follows:

$$\Delta u_{w2} = \frac{1}{a_2 + \frac{b_2}{t_2}} \tag{6-17}$$

Where,

Δu_{w2} = cumulative Global Cycle End Excess Pore Pressure

$t_2 = (i-2)(t_L + t_D) + (t_L + t_D)$, in seconds

$a_2$and b_2 = regression constants corresponding to the Global Cycle End Excess Pore Pressure Curve

Following the global perspective of the pore pressure characteristic elements, the amplitude $\alpha = u_p'$ for the *LDR* function at any i^{th} cycle is equivalent

to the difference between Δu_{wp} and Δu_{w2}. Therefore, the solution for the amplitude α for any i^{th} cycle can be obtained as follows:

$$\alpha = \left(\frac{t_p}{a_p t_p + b_p}\right) - \left(\frac{t_2}{a_2 t_2 + b_2}\right) \quad (6\text{-}18)$$

The time at maximum pore water pressure within the i^{th} cycle is denominated as β. As shown in Figure 6-25, the high variability observed for this parameter makes the use of an average value the best alternative available. The β parameter for all specimens tested in this study showed high variability as well. The average values obtained for every specimen are shown in Table 6-5.

TABLE 6-5 Time at maximum pore water pressure within i^{th} cycle

Specimen	S_{AC}%	β_{avg} (s)
1	75	0.576
2	76	0.566
3	100	0.493
4	100	0.512
5	78	0.578
6	72	0.600

The average values shown in Table 6-5 were used for each specimen. It was observed that for saturated specimens the β_{avg}.value is 0.503 seconds while for unsaturated specimens, with S_{AC}% ranging from 72 to 78%, the β_{avg}.value is 0.580 seconds.

It appears that the β.value could be related to the initial degree of saturation. Considering that the t_L is 1 second for all tests and the haversine stress pulse applied reaches its maximum at 0.5 seconds, a β_{avg}.value of 0.503 seconds for the saturated specimens indicates that the pore pressure response of the

material to the load takes place immediately. On the other hand, for unsaturated soils a β_{avg}.value of 0.580 seconds indicates that there is a lag in the material response. Further investigation on the behavior of this parameter needs to be done for a broader range of S_{AC}%.

The λ parameter is a regression constant that defines the width of the bell shape of the *LDR* function. Figure 6-38 shows how the variation of λ affects the *LDR* function. In order to develop the curves shown in Figure 6-38, constant values for α = 3.574 and β = 0.576 were assumed.

As seen in Figure 6-38, the width of the bell increases as the value of λ decreases. Different values of λ for each specimen ranging from 3.3 to 7 were found. It should be recognized that the values of λ varies as the number of cycles increases. Even though the coefficient of variation *CV* for λ within each specimen was found to be smaller than 0.1, any small error, considered marginal within a single cycle is very significant when accumulated and therefore, it should be minimized. Again, the boundary conditions established by the Global Excess Pore Pressure Curves were used to obtain the most accurate estimate of λ possible.

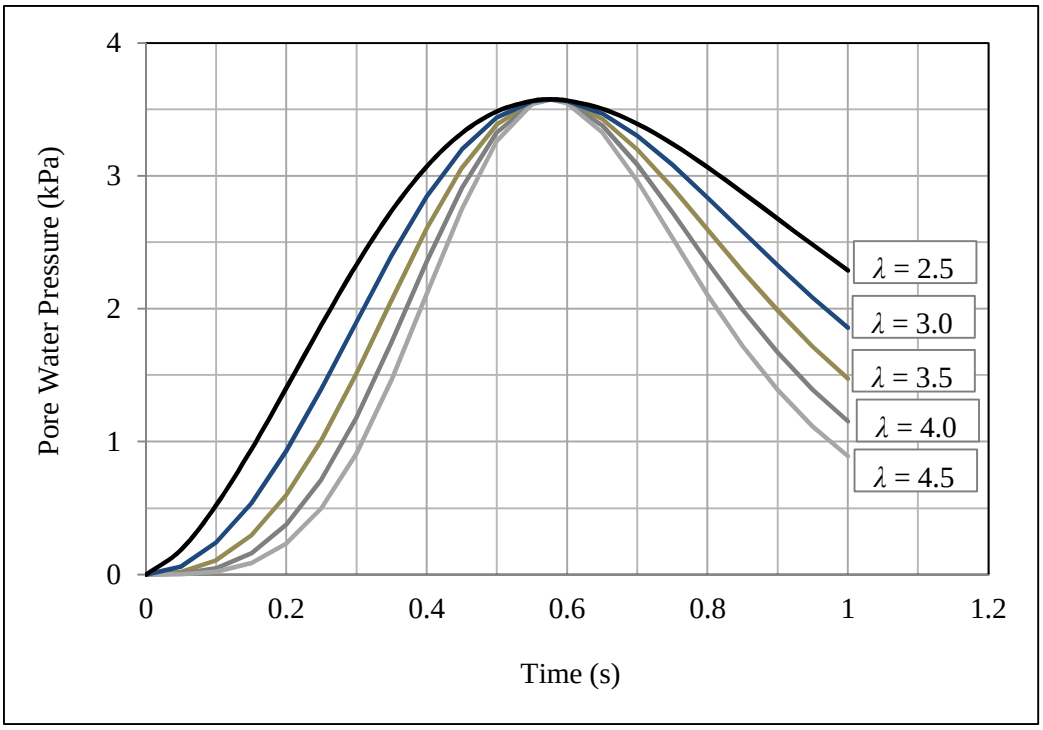

FIGURE 6-38 Influence of λ upon the *LDR* function

In order to find a solution for λ, first it is necessary to find the solution for u_1' which is nothing but u_{wL}' evaluated at the end of the loading time t_L by using Equation 6-15. Also, it should be noted that a solution for α was obtained in Equation 6-18. By substitution of Equation 6-18 into Equation 6-15, an expression to estimate u_1'evaluated at $t = t_L$ is obtained:

$$u_1' = \left[\left(\frac{t_p}{a_p t_p + b_p}\right) - \left(\frac{t_2}{a_2 t_2 + b_2}\right)\right]\left[\frac{4 t_L^{-\lambda-1}\beta^{\lambda+1}\lambda^2}{\left(\lambda - 1 + \lambda t_L^{-\lambda}\beta^{\lambda} + t_L^{-\lambda}\beta^{\lambda}\right)^2}\right] \qquad (6\text{-}19)$$

Also, an alternative solution for u_1' can be obtained by using the Global Excess Pressure Curves in the same way it was done to find the solution for α. Following the same approach, the alternative solution for u_1' reads as follows:

$$u_1' = \left(\frac{t_1}{a_1 t_1 + b_1}\right) - \left(\frac{t_2}{a_2 t_2 + b_2}\right) \qquad (6\text{-}20)$$

Where,

$t_1 = (i-2)(t_L + t_D) + t_L$, in seconds

a_1 and b_1 = regression constants corresponding to the Global Load End Excess Pore Pressure Curve

By making Equation 6-19 equal to Equation 6-20, the following expression is obtained:

$$\frac{\left(\frac{t_1}{a_1 t_1 + b_1}\right) - \left(\frac{t_2}{a_2 t_2 + b_2}\right)}{\left(\frac{tp}{a_p tp + b_p}\right) - \left(\frac{t_2}{a_2 t_2 + b_2}\right)} = \frac{4 {t_L}^{-\lambda-1} \beta^{\lambda+1} \lambda^2}{\left(\lambda - 1 + \lambda {t_L}^{-\lambda} \beta^{\lambda} + {t_L}^{-\lambda} \beta^{\lambda}\right)^2} \quad (6\text{-}21)$$

Where, all the variables, except for λ, are known. By solving Equation 6-21 through an iterative procedure, a solution for λ at every single i^{th} cycle can be obtained; and by using the proposed solution, the value of λ is adjusted to match the boundary Global Excess Pressure Curves. As a consequence, the sources of error in the prediction are minimized. The Equations presented were incorporated in the final general model presented in next sections.

Function 2

The Function 2 describes the pore pressure dissipation phase that takes place after the loading period. Based on the experience gained from the preliminary modeling attempts, it was recognized that no matter how accurate the predictions seem to be, a marginal error will always remain present after every single cycle. Regardless of whether several or few points were fitted to models of either medium or relatively high complexity, the accumulated error at the end of an excess pore pressure development simulation, after a high number of cycles, is likely to be significant.

Therefore, it was opted to use of a simple mathematical function that describes the pore water pressure dissipation by an exponential asymptotic curve. Obviously the asymptotic value should approach to zero in the case when all the pore water pressure is dissipated. Observation of laboratory tests suggests that the pore pressure dissipation phase can be modeled by the following mathematical function:

$$u_{wU}' = q.exp\left(\frac{-t}{p}\right) \quad (6\text{-}22)$$

Where,

u_{wU}' = pore water pressure developed within the i^{th} cycle during the unload period

t = time within the unloading phase in seconds; valid for $0s \leq t \leq t_D$

q = function intercept; obtained by solving Function 1 at $t = t_L$

p = regression constant

The fact that only one parameter is unknown, makes this function a simple approach to follow for estimating the pore water pressure dissipation. Similarly to the λ parameter required to estimate the excess pore pressure development, the p parameter vary from cycle to cycle. However, a solution of the same type as the one adopted to estimate λ is not useful for the modeling purposes as model parameters that can be related to the soil properties during the dwelling time are needed.

Nonetheless, only to develop a predictive model for p, a solution using the boundary Global Excess Pressure Curves was adopted to obtain estimates of p at different i^{th} cycles. The results obtained were then fitted to a model capable of predicting p as function of the number of repetitions. As a consequence new

parameters were introduced into Equation 6-22. Such parameters are expected to reflect the influence that soil properties have upon the dissipation of pore water pressure. At the same time the variation of *p* due to number of cycles is also captured.

Using the Global Excess Pressure Curves, the intercept $q = u_1'$ can be estimated by using Equation 6-20 with time $t_1 = (i-2)(t_L + t_D) + t_L$ and time $t_2 = (i-2)(t_L + t_D) + (t_L + t_D)$. In a similar way, u_{wU}' evaluated at time $t = t_D$ is equal to u_2'. The pore pressure u_2' is nothing but the difference between the Global Cycle End Excess Pressure Equation 6-20 evaluated at the end and beginning of the i[th] cycle. When both solutions are introduced in Equation 6-22, the following expression to estimate *p* for the i^{th} cycle is obtained

$$p = \frac{-t_D}{ln\left[\frac{\left(\frac{t_2'}{a_2 t_2' + b_2}\right) - \left(\frac{t_2}{a_2 t_2 + b_2}\right)}{\left(\frac{t_1}{a_1 t_1 + b_1}\right) - \left(\frac{t_2}{a_2 t_2 + b_2}\right)}\right]} \qquad (6\text{-}23)$$

Where,

$t_2 = (i-2)(t_L + t_D) + (t_L + t_D)$

$t_2' = (i-1)(t_L + t_D) + (t_L + t_D)$

Again, the solution for p presented in Equation 6-23 was not obtained with the purpose of being utilized as part of the final model but of being used as a mean to obtain a predictive equation for *p* as function of the number of load repetitions.

Solutions of *p* for several cycles in each specimen were obtained using Equation 6-23 and then the results were fitted to different potential predictive

functions. From all the functions evaluated, Equation 6-24 showed to be the best for predicting *p* as function of number of repetitions:

$$p = \frac{1}{m+n.\left(Ln(i)\right)^2} \quad (6\text{-}24)$$

Where,

i = the i^{th} cycle

m and *n* = regression constants

The results of the regression analysis performed on the *p* parameters obtained for each specimen are summarized in Table 6-6. As can be observed, the statistical parameters indicate that the model selected provides excellent predictions. The R^2_{adj} values range from 0.990 to 1.00 and the S_e/S_y from 0.010 to 0.101.

Figure 6-39 shows the predictions for Specimen 1. It can be seen that the points fit well the predictive function. Figure 6-40 shows the goodness of fit for the predictive model. These two figures are shown only as a sample of all the plots obtained. The totality of the figures generated for each sample was conveniently included in Appendix C.

TABLE 6-6 Results of the regression analysis for the *p* parameter

Specimen	Parameter			
	m	*n*	S_e/S_y	R^2_{adj}
1	-0.170	0.022	0.034	0.999
2	-0.195	0.021	0.052	0.997
3	-0.176	0.024	0.022	0.999
4	0.729	0.018	0.058	0.997
5	0.407	0.008	0.101	0.990
6	-0.229	0.011	0.010	1.000

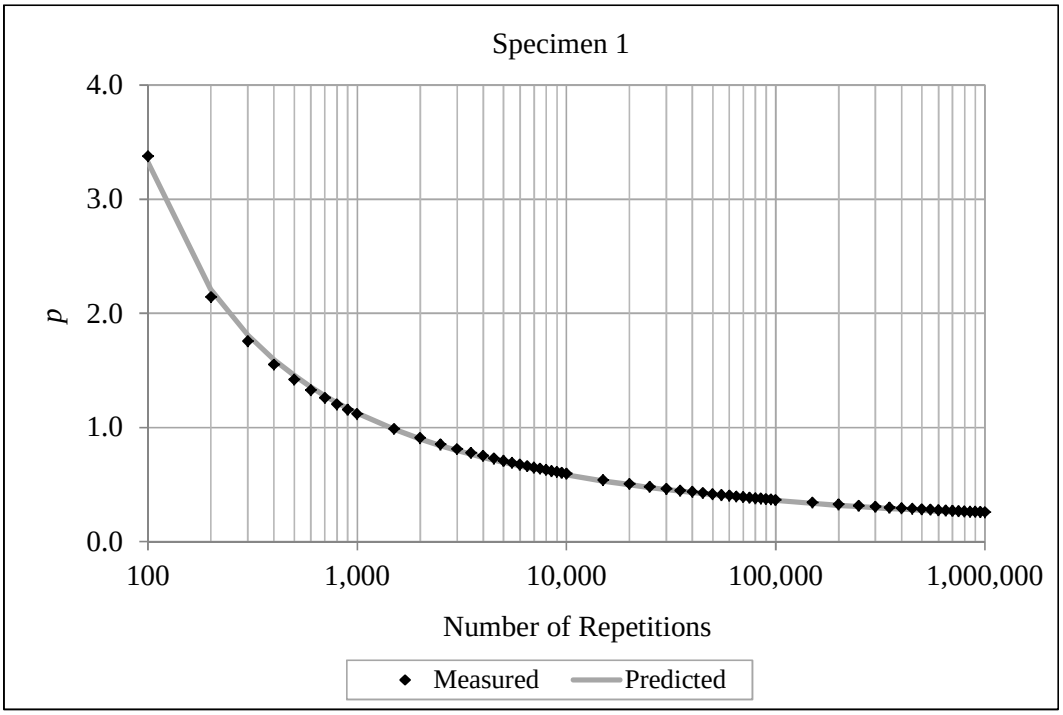

FIGURE 6-39 Results of prediction for parameter *p* – Specimen 1

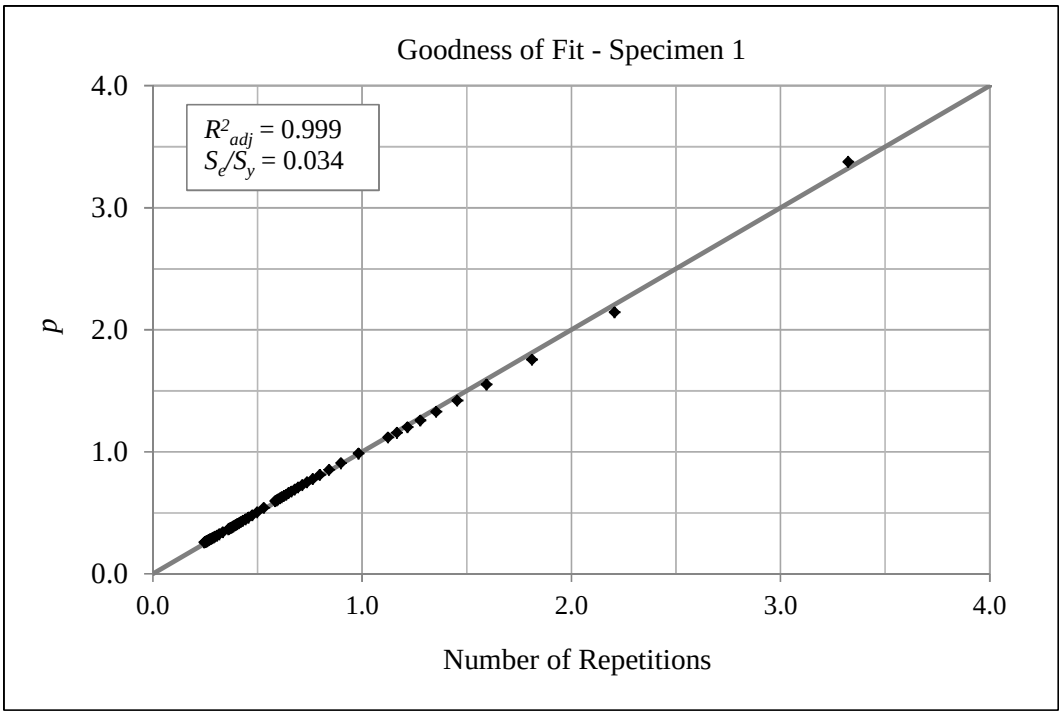

FIGURE 6-40 Goodness of fit for parameter *p* – Specimen 1

Even when Equation 6-24 showed to be a good model to predict the *p* parameter, problems were encountered with predictions at a low range of number of cycles. It was observed that the issue arises when the *m* regression constant is negative and the number of cycles is low enough to make the denominator of Equation 6-24 become a negative value. In that case, the *p* parameter would result in a negative value as well, and when applied to Equation 6-22, the predicted residual pore water pressure or pressure at the end of the cycle would become greater than the value predicted at the end of the loading time.

In order to overcome this issue, a constraint was established for Equation 6-23. Such constraint is determined by Equation 6-25:

$$Ln(i)^2 \geq -\frac{m}{n} \tag{6-25}$$

The minimum number of cycles required to comply with Equation 6-25 is defined as *i'*. The value of *i'* should be determined and set as constant to determine the *p* parameter corresponding to any *i* lower than *i'*. In this way, any irrationality in the results obtained with Equation 6-24 is prevented.

The details on the analysis of the influence of test conditions upon the regression constant *m* and *n* are discussed in detail in next sections.

Development of the General Predictive Model

Once the Global Excess Pore Pressure Curves and Functions 1 and 2 to model the pore pressure development in the i^{th} cycle were established, general models to predict the pore water pressure buildup at any time can be developed.

It is important to recognize that in order to predict the excess pore pressure at any time within any i^{th} cycle, the excess cycle end or residual pore pressure accumulated prior to the i^{th} cycle must be estimated by using Equation 6-1 presented at the beginning of this chapter. Equation 6-1 is conveniently presented again as follows:

$$\Delta u_{wN} = \sum_{i=1}^{N} u_2{}'_i \qquad (6\text{-}26)$$

Where,

$u_2{}'_i$ = residual pore water pressure in the i^{th} cycle

Δu_{wN} = accumulated excess pore water pressure at the *N* cycle

The functions selected to model both the loading and the dwelling phases are conveniently reviewed again. For the loading phase, the following Logistic

Dose Response Pulse equation can be used to predict the pore pressure development at any time within the loading phase in the i^{th} cycle:

$$u_{wL}{}' = \frac{4\alpha t^{-\lambda-1}\beta^{\lambda+1}\lambda^2}{\left(\lambda-1+\lambda t^{-\lambda}\beta^{\lambda}+t^{-\lambda}\beta^{\lambda}\right)^2} \quad (6\text{-}27)$$

Where,

u_{wL}' = pore water pressure developed within the i^{th} cycle during the loading phase

t = time within the loading phase; valid for 0s $\leq t \leq t_L$

α = pore water pressure pulse amplitude

β = time at maximum pore water pressure

λ = regression constants

For the dwelling phase, it was determined that the following exponential function can be used to predict the pore pressure dissipation at any time within the unloading phase i^{th} cycle:

$$u_{wU}{}' = q.exp\left(\frac{-t}{p}\right) \quad (6\text{-}28)$$

Where,

u_{wU} '= pore water pressure developed within the i^{th} cycle during the unloading phase

t = time in seconds elapsed form the end of load; valid for $0s \leq t \leq t_D$

q = function intercept; obtained by solving Equation 6-27 at $t = t_L$

p = function of the number of cycles as well as m and n regression constants as presented in Equation 6-24.

In the next sections, a series of equations proposed to predict the excess pore pressure development for a single cycle as well as for accumulated repetitions are presented.

Predictive Equation for *N*=*i*=1 during the Loading Phase

The general expression developed to estimate the excess pore water pressure during the loading phase within the first cycle is identical as Equation 6-27. Thus Equation 6-27 can be utilized to estimate the excess pore pressure development when *N*=*i*=*1* as follows:

$$u_{wL}{}' = \frac{4\alpha t^{-\lambda-1}\beta^{\lambda+1}\lambda^2}{\left(\lambda-1+\lambda t^{-\lambda}\beta^{\lambda}+t^{-\lambda}\beta^{\lambda}\right)^2} \quad (6\text{-}29)$$

Where,

u'_{wL} = pore water pressure developed within the 1st cycle during the loading phase

t = time elapsed from the beginning of the *1st* cycle; valid for 0s $\leq t \leq t_L$

α = pore water pressure pulse amplitude

β = constant that defines the time at maximum pore water pressure

λ = parameter that defines the width of the bell for the *LDR* pulse

The value for α and λ can be obtained by solving the following equations:

$$\alpha = \left(\frac{\beta}{a_p\beta+b_p}\right) - \left(\frac{t_2}{a_2 t_2+b_2}\right) \quad (6\text{-}30)$$

$$\frac{\left[\left(a_2+\frac{b_2}{t_2}\right)-\left(a_1+\frac{b_1}{t_L}\right)\right].\left(a_p+\frac{b_p}{\beta}\right)}{\left[\left(a_2+\frac{b_2}{t_2}\right)-\left(a_p+\frac{b_p}{\beta}\right)\right].\left(a_1+\frac{b_1}{t_L}\right)} = \frac{4{t_L}^{-\lambda-1}\beta^{\lambda+1}\lambda^2}{\left(\lambda-1+\lambda {t_L}^{-\lambda}\beta^{\lambda}+{t_L}^{-\lambda}\beta^{\lambda}\right)^2} \quad (6\text{-}31)$$

Where,

t_L = loading time in seconds

t_2 = time at the beginning of the first cycle in seconds

$a_p, a_1, a_2, b_p, b_1 and\ b_2$ = regression coefficients from the Global Excess Pressure Curves

As the equations shown above apply for the first loading cycle, t_2 should be in reality equal to zero. However, in order to avoid indeterminate results, a small value approaching zero like $1x10^{-20}$ seconds can be used only for the first cycle.

Predictive Equation for *N*=*i*=1 during the Unloading Phase

In order to estimate the excess pore water pressure during the unloading phase, an intercept value is required as indicated in Equation 6-28. Such intercept is nothing but the result of evaluating Equation 6-27 for $t = t_L$ within the cycle under analysis. Therefore, by substitution of Equation 6-24 and 6-27 into Equation 6-28, the following expression to estimate the excess pore pressure at any time during the unloading phase and within the first cycle, is obtained:

$$u_{wU}' = \frac{4\alpha {t_L}^{-\lambda-1}\beta^{\lambda+1}\lambda^2}{\left(\lambda-1+\lambda {t_L}^{-\lambda}\beta^{\lambda}+{t_L}^{-\lambda}\beta^{\lambda}\right)^2}.exp[-t.(m+n.Ln(i)^2)] \quad (6\text{-}32)$$

Where,

u_{wU}' = pore water pressure developed within the *1st* cycle during the unloading phase

t = time in seconds elapsed from the end of load in the *1st* cycle; valid for $t_L \leq t \leq t_D$

t_L = loading time in seconds

α = pore water pressure pulse amplitude

β = constant that defines the time at maximum pore water pressure

λ = parameter that defines the width of the bell for the *LDR* pulse

i = 1 if by evaluating the constraint presented in Equation 6-25, it is determined that the use of i' is not required; otherwise i' should be used.

The value for α and λ can be obtained by using the same equations presented for the case of the loading phase. The same regression constants and recommendations apply.

Predictive Equation for N>1 during the Loading Phase

In order to estimate the excess pore water pressure during the loading phase for any i^{th} cycle greater than 1, the excess pore water pressure accumulated prior to the occurrence of the i^{th} cycle needs to be considered.

In order to estimate the accumulated pressure, Equation 6-32 evaluated at the end of the unloading phase is incorporated into Equation 6-26. Then Equation 6-27 evaluated at the time the pressure is desired to be estimated is added to the accumulated excess pressure from prior cycles. Especial considerations should be taken into account with times and the λ parameter as the prediction is conducted for several consecutive cycles. The final expression reads as follows:

$$\Delta u_{wL} = \sum_{i=2}^{N-1}\left[\left(\frac{t_p}{a_p t_p + b_p}\right) - \left(\frac{t_2}{a_2 t_2 + b_2}\right)\right]\left[\frac{4{t_L}^{-\lambda-1}\beta^{\lambda+1}\lambda^2}{\left(\lambda - 1 + \lambda {t_L}^{-\lambda}\beta^{\lambda} + {t_L}^{-\lambda}\beta^{\lambda}\right)^2}\right] exp\left(-t_D.\left(m + n.Ln(i-1)^2\right)\right)$$

$$+\left[\left(\frac{{t_p}'}{a_p {t_p}' + b_p}\right) - \left(\frac{{t_2}'}{a_2 {t_2}' + b_2}\right)\right]\left[\frac{4t^{-\lambda'-1}\beta^{\lambda'+1}\lambda'^2}{\left(\lambda' - 1 + \lambda' t^{-\lambda'}\beta^{\lambda'} + t^{-\lambda'}\beta^{\lambda'}\right)^2}\right] \quad (6\text{-}33)$$

Where,

t_L = loading time in seconds

t_D = dwelling time in seconds

$t_p = (i-2)(t_L + t_D) + \beta$

$t_2 = (i-3)(t_L + t_D) + (t_L + t_D)$

${t_p}' = (i-1)(t_L + t_D) + \beta$

${t_2}' = (i-2)(t_L + t_D) + (t_L + t_D)$

t = time elapsed from the beginning of the i^{th} cycle; valid for 0s $\leq t \leq t_L$

β = constant that defines the time at maximum pore water pressure

λ = parameter that defines the width of the bell for the *LDR* pulse in the $(i\text{-}1)^{th}$ cycle

λ' = parameter that defines the width of the bell for the *LDR* pulse in the i^{th} cycle

$i = i$ if by evaluating the constraint presented in Equation 6-25, it is determined that the use of i' is not required; otherwise i' should be used.

$a_p, a_1, a_2, b_p, b_1 and\ b_2$ = regression coefficients from the Global Excess Pressure Curves

The parameters λ and λ' can be estimated by solving the following equations:

$$\frac{\left[\left(a_2+\frac{b_2}{t_2}\right)-\left(a_1+\frac{b_1}{t_1}\right)\right].\left(a_p+\frac{b_p}{t_p}\right)}{\left[\left(a_2+\frac{b_2}{t_2}\right)-\left(a_p+\frac{b_p}{t_p}\right)\right].\left(a_1+\frac{b_1}{t_1}\right)} = \frac{4{t_L}^{-\lambda-1}\beta^{\lambda+1}\lambda^2}{\left(\lambda-1+\lambda{t_L}^{-\lambda}\beta^{\lambda}+{t_L}^{-\lambda}\beta^{\lambda}\right)^2} \tag{6-34}$$

$$\frac{\left[\left(a_2+\frac{b_2}{t_2'}\right)-\left(a_1+\frac{b_1}{t_1'}\right)\right].\left(a_p+\frac{b_p}{t_p'}\right)}{\left[\left(a_2+\frac{b_2}{t_2'}\right)-\left(a_p+\frac{b_p}{t_p'}\right)\right].\left(a_1+\frac{b_1}{t_1'}\right)} = \frac{4{t_L}^{-\lambda'-1}\beta^{\lambda'+1}\lambda'^2}{\left(\lambda'-1+\lambda'{t_L}^{-\lambda'}\beta^{\lambda'}+{t_L}^{-\lambda'}\beta^{\lambda'}\right)^2} \tag{6-35}$$

Where,

$t_1 = (i-2)(t_L + t_D) + t_L$

$t_1' = (i-1)(t_L + t_D) + t_L$

Predictive Equation for *N*>1 during the Unloading Phase

In order to estimate the excess pore water pressure during the unloading phase for any i^{th} cycle greater than 1, the excess pore water pressure accumulated prior to the occurrence of the i^{th} cycle also needs to be considered. The accumulated excess pore pressure is estimated in the same way as for Equation 6-33. Different from Equation 6-33, this time expression 6-32 is added to the accumulated excess pore pressure to take into account the pressure developed during the i^{th} cycle within the unloading phase. The resulting equation reads as follows:

$$\Delta u_{wU} = \sum_{i=2}^{N-1}\left[\left(\frac{t_p}{a_p t_p + b_p}\right) - \left(\frac{t_2}{a_2 t_2 + b_2}\right)\right]\left[\frac{4{t_L}^{-\lambda-1}\beta^{\lambda+1}\lambda^2}{\left(\lambda - 1 + \lambda {t_L}^{-\lambda}\beta^{\lambda} + {t_L}^{-\lambda}\beta^{\lambda}\right)^2}\right] exp\left(-t_D.\left(m + n.Ln(i-1)^2\right)\right)$$

$$+\left[\left(\frac{{t_p}'}{a_p {t_p}' + b_p}\right) - \left(\frac{{t_2}'}{a_2 {t_2}' + b_2}\right)\right]\left[\frac{4{t_L}^{-\lambda'-1}\beta^{\lambda'+1}\lambda'^2}{\left(\lambda' - 1 + \lambda' {t_L}^{-\lambda'}\beta^{\lambda'} + {t_L}^{-\lambda'}\beta^{\lambda'}\right)^2}\right] exp\left(-t_D.\left(m + n.Ln(i)^2\right)\right)$$

(6-36)

Where,

t_L = loading time in seconds

t_D = dwelling time in seconds

$t_p = (i-2)(t_L + t_D) + \beta$

$t_2 = (i-3)(t_L + t_D) + (t_L + t_D)$

${t_p}' = (i-1)(t_L + t_D) + \beta$

${t_2}' = (i-2)(t_L + t_D) + (t_L + t_D)$

t = time elapsed from the load end within the i^{th} cycle; valid for 0s $\leq t \leq t_D$

β = constant that defines the time at maximum pore water pressure

λ = parameter that defines the width of the bell for the *LDR* pulse in the $(i\text{-}1)^{th}$ cycle

λ' = parameter that defines the width of the bell for the *LDR* pulse in the i^{th} cycle

$i = i$ if by evaluating the constraint presented in Equation 6-25, it is determined that the use of i' is not required; otherwise i' should be used.

$a_p, a_1, a_2, b_p, b_1 and\ b_2$ = regression coefficients from the Global Excess Pressure Curves

The parameters λ and λ' can also be estimated by solving equations 6-34 and 6-35.

Additionally, the times t_L and t_D can be expressed in terms related to the highway traffic characteristics. As discussed in Chapter 5, the loading time t_L is a function of both the vehicle speed v_s and the effective length L_{eff} that defines de duration of the load pulse. It was shown in Chapter 5 that L_{eff} is function of the pavement structure, radius of tire imprint and depth to the point of interest for analysis. The expression that can be used to estimate the loading time reads as follows:

$$t_L = \frac{L_{eff}}{17.6 v_s} \tag{6-37}$$

Therefore; if the pavement structure under analysis, tire imprint radius and particular depth to the point of interest are known; then t_L for the expressions previously proposed to estimate the excess pore pressure can be substituted by Equation 6-37.

It was also mentioned in Chapter 5 that the dwelling time t_D is related to the highway traffic frequency which is determined by the Average Daily Traffic

(*ADT*). Therefore, if the *ADT* for the highway under analysis were known, the following Equation would replace t_D in the predictive equations proposed.

$$t_D = \frac{86400}{ADT} - \frac{L_{eff}}{17.6 v_s} \tag{6-38}$$

In the next section, the validation of the models proposed for the prediction of the excess pore water pressure is presented.

Validation of the Proposed Equations

In this section, the results of the validation conducted for Equations 6-33 and 6-36 are presented. Using Excel spreadsheets a simulation of the excess pore water pressure development for each one of the six specimens was conducted.

As can be seen in the previous sections, a total of 9 parameters are needed to predict the pore water pressure response by using Equations 6-33 and 6-36. Six of them (a_p, a_1, a_2, b_p, b_1 and b_2) correspond to the Global Excess Pore Pressure Curves. The other three (β, m and n) characterize the behavior of the material within each cycle.

The parameters a_p, a_1, a_2, b_p, b_1 and b_2 from Table 6-3 were used. The values for parameters β were obtained from Table 6-5. The m and n values used can be found in Table 6-6. The simulation was conducted for the same number of cycles applied to each specimen during the test.

Equation 6-33 was evaluated for $t = \beta$ to obtain the accumulated peak excess pressures Δu_{pL} of each cycle developed during the loading phase. Equation 6-36 was evaluated for $t = t_D$ to obtain the accumulated excess pressures developed at the end of each cycle Δu_{2U} during the unloading phase.

The results of the simulations are presented in Table 6-7. As previously mentioned, the simulation was conducted for the number of cycles applied to each specimen during the test. By looking at the error in the prediction it can be realized that most of the time the proposed models under predict the values observed from the laboratory testing.

Numerically, the higher error magnitudes or difference between the measured and predicted values are observed for specimens 1 to 3. This makes sense since those specimens subjected to higher number of loading cycles accumulate more error. As discussed earlier in this study, the error is accumulated progressively with the number of cycles.

TABLE 6-7 Results of the simulations – numerical values

Specimen	N_{Total}	Peak Pressures			Cycle End Pressures		
		Measured	Predicted	Error	Measured	Predicted	Error
1	96,060	101.5	95.3	6.2	87.0	79.7	7.3
2	64,040	54.7	48.5	6.2	50.9	44.6	6.3
3	80,050	49.0	47.1	1.9	36.0	34.8	1.2
4	16,010	24.0	23.9	0.1	8.0	8.5	-0.5
5	32,020	57.2	54.0	3.1	24.7	25.7	-0.9
6	47,628	31.4	31.5	-0.1	29.4	29.4	0.0

Table 6-8 presents the results of the simulations in terms of statistical parameters. As can be observed, except for the peak pressure corresponding to Specimen 4 the R^2_{adj} ranges from 0.63 to 0.99. This indicates that the model provides fair to excellent predictions. The S_e/S_y values are good and range from 0.09 to 0.61. It can be noted that the highest errors relative to the measured values

correspond to Specimen 2 with 11 and 12% for the peak and cycle end pressures respectively. The best results are observed for Specimen 6 which shows low S_e/S_y and high R^2_{adj}. Also the relative error for Specimen for is lower than 0.5% for both accumulated peak and cycle end pressures.

TABLE 6-8 Results of the simulations – statistical parameters

Specimen	N_{Total}	Peak Pressures			Cycle End Pressures		
		S_e/S_y	R^2_{adj}	Error %	S_e/S_y	R^2_{adj}	Error %
1	96,060	0.307	0.907	6.2	0.372	0.862	8.4
2	64,040	0.506	0.746	11.3	0.525	0.727	12.4
3	80,050	0.295	0.914	3.9	0.256	0.935	3.3
4	16,010	1.731	-1.879	0.6	0.539	0.720	6.1
5	32,020	0.614	0.631	5.5	0.441	0.809	3.8
6	47,628	0.111	0.988	0.4	0.087	0.993	0.0

It is also observed that the R^2_{adj} for the accumulated peak pressure of Specimen 4 results to be negative and the S_e/S_y value is significantly high. This is due to the fact that the measured values did not fit well to the model at an early stage of the simulation. However, if one looks at Table 6-7, it can be seen that the absolute error is 0.5 kPa. Similarly, in Table 6-8 a low relative error of 0.6% indicates that the predictions towards the end of the test fit well the measured data. Furthermore, when not considering the first thirty predicted values, the calculated R^2_{adj} raises to 0.73. Since for traffic loading conditions, the results at high number of repetitions rather than low number of repetitions is a major concern, it is concluded that the predictions are still acceptable.

Figures 6-41 to 6-44 show the predictions and goodness of fit obtained for the accumulated peak and residual or cycle end pressures by using the proposed model for Specimen 1. Figures 6-45 to 6-48 show the same information for Specimen 3. Only the mentioned figures were conveniently included in the main text as an example. The totality of plots developed for all specimens are included in Appendix D.

It should be recognize that the simulations were performed for thousands of cycles. Therefore, it is not possible to include all the detailed work conducted in this document as space would become a serious issue. However, a short example of the simulation setup for one specimen is included in Appendix E. The example comprehends samples of the results for Specimen 1 from cycle 1 to 30 and from cycle 1,000 to 1,023.

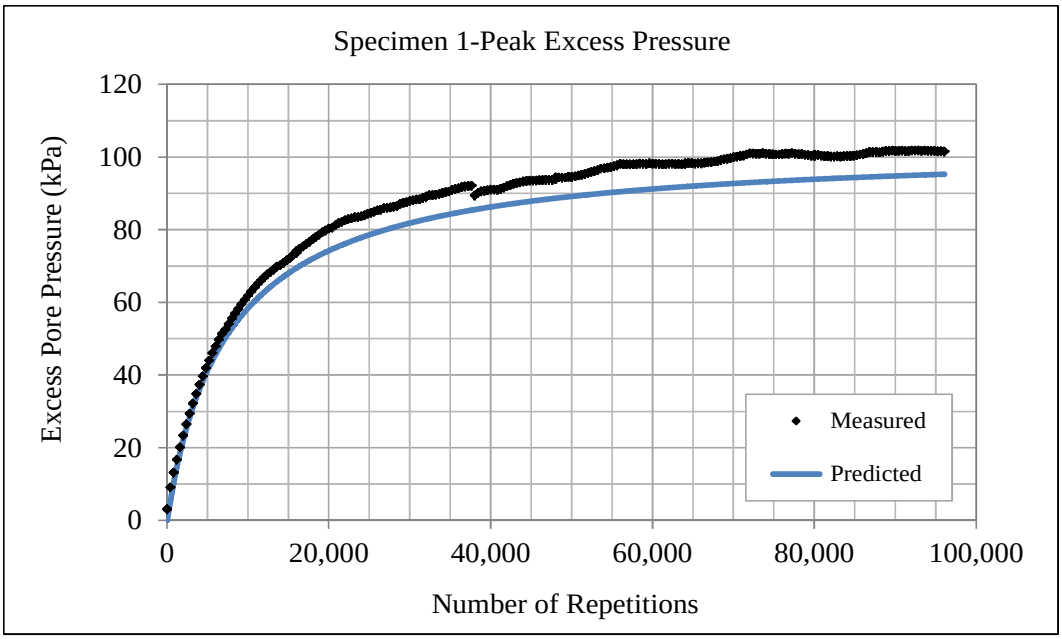

FIGURE 6-41 Simulation of peak excess pressure development – Specimen 1

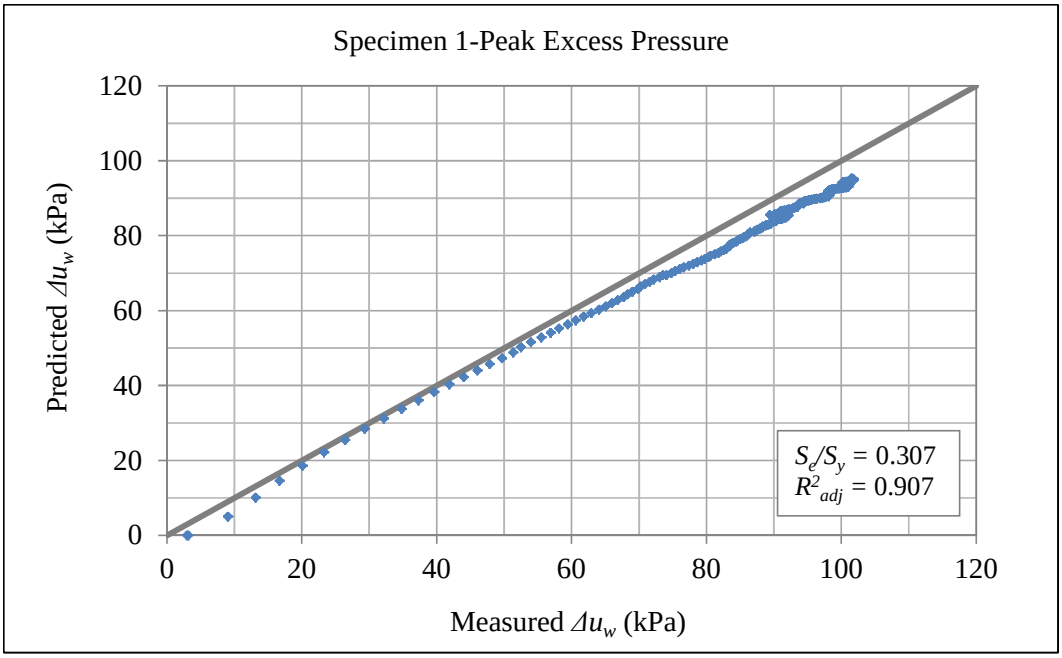

FIGURE 6-42 Goodness of fit - peak excess pressure – Specimen 1

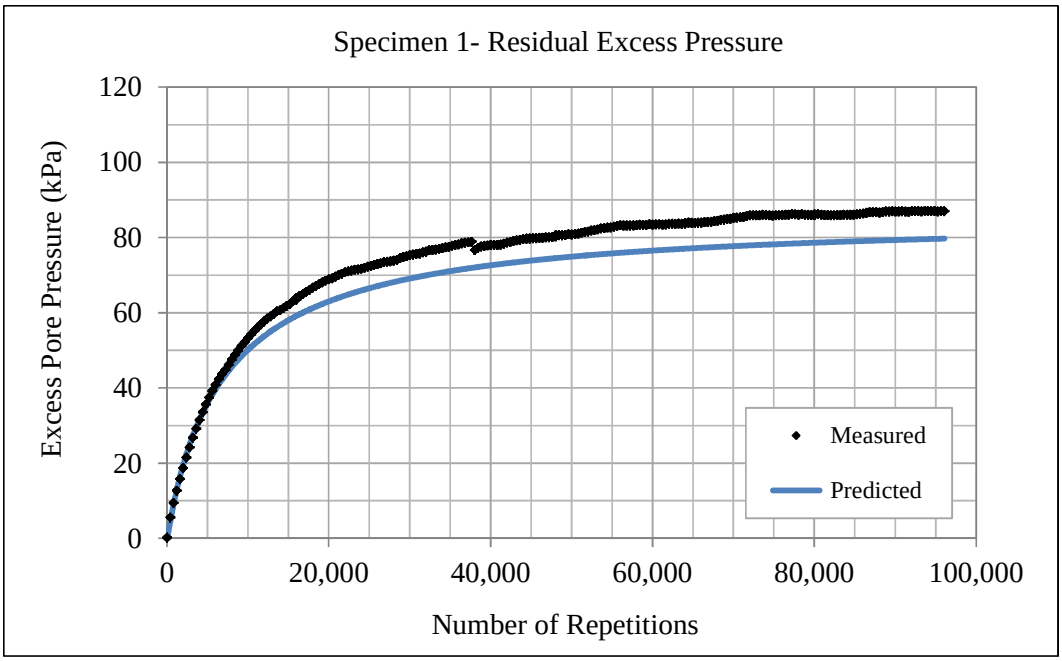

FIGURE 6-43 Simulation of residual excess pressure development – Specimen 1

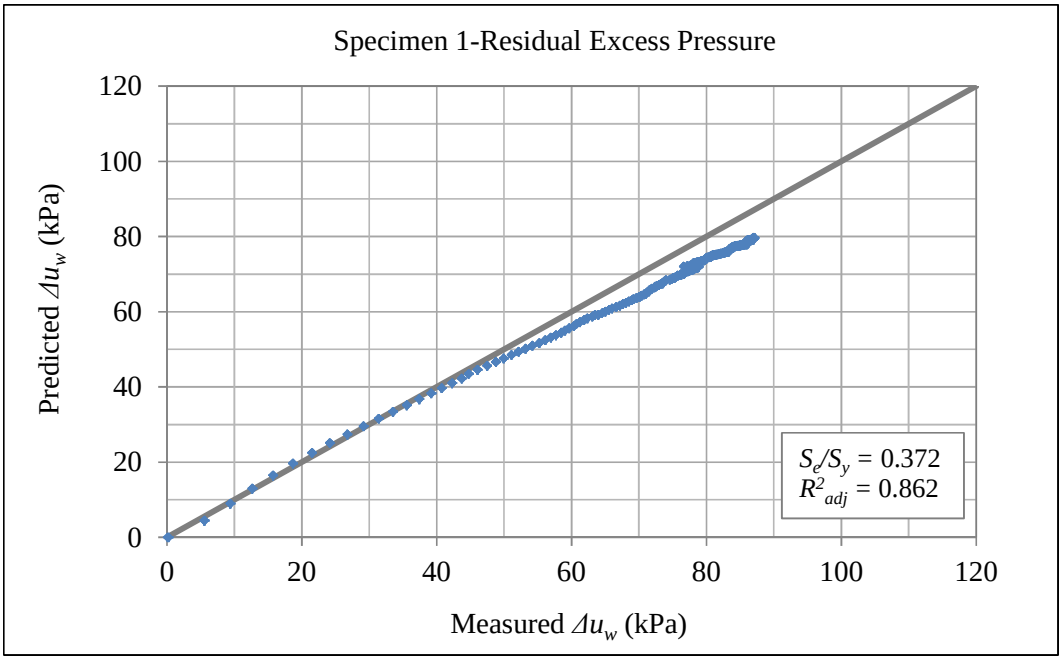

FIGURE 6-44 Goodness of fit - residual excess pressure – Specimen 1

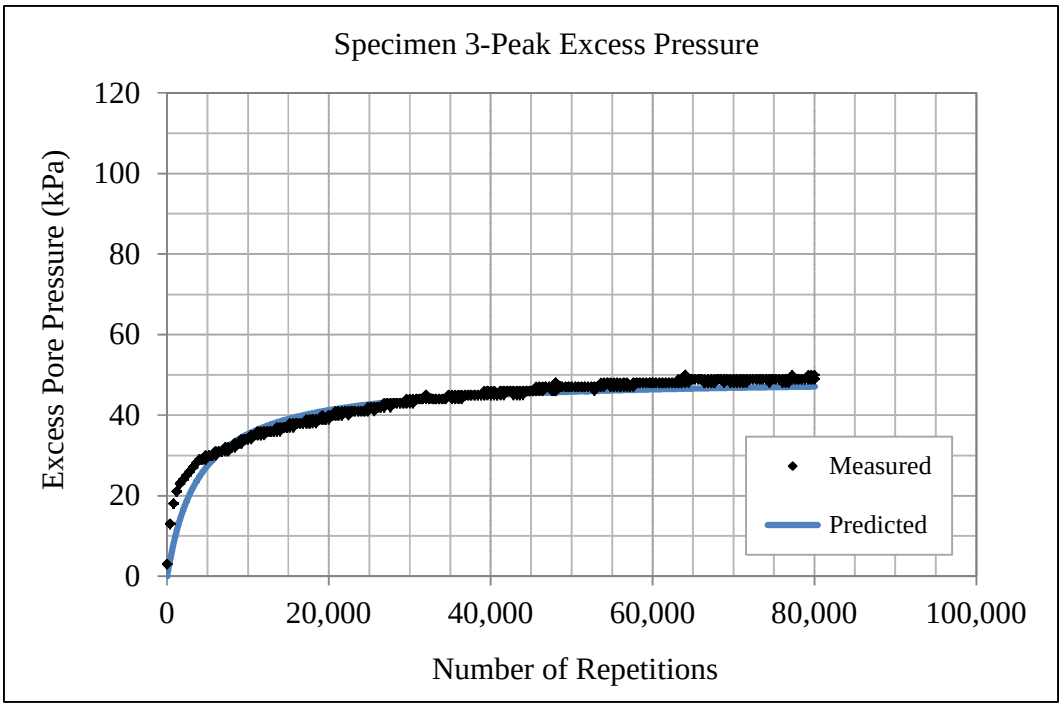

FIGURE 6-45 Simulation of peak excess pressure development – Specimen 3

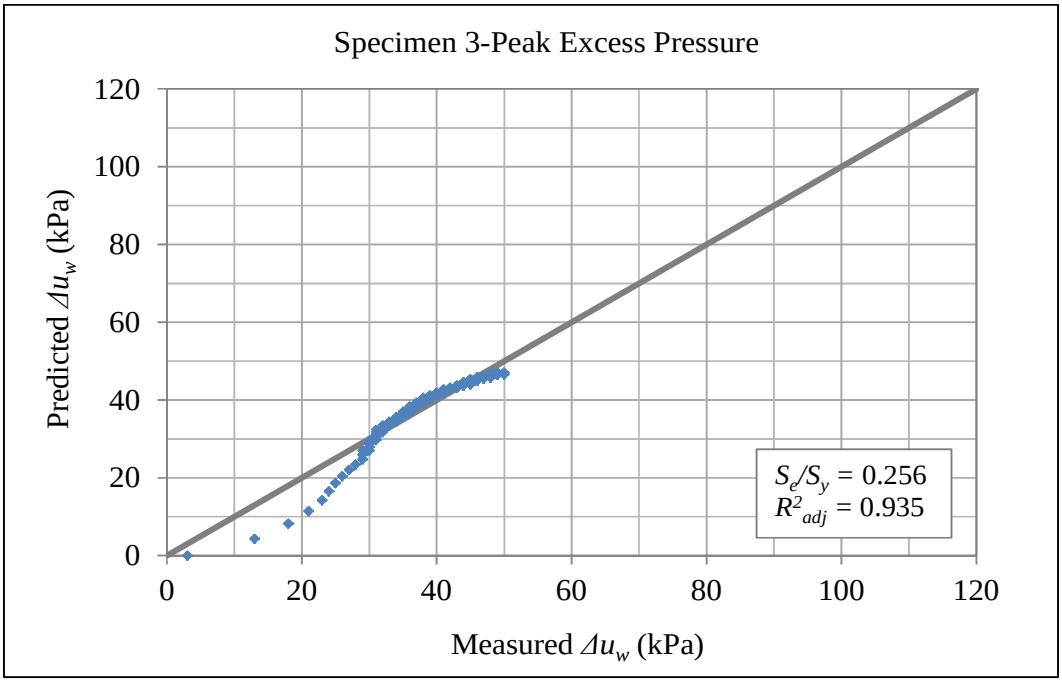

FIGURE 6-46 Goodness of fit - peak excess pressure – Specimen 3

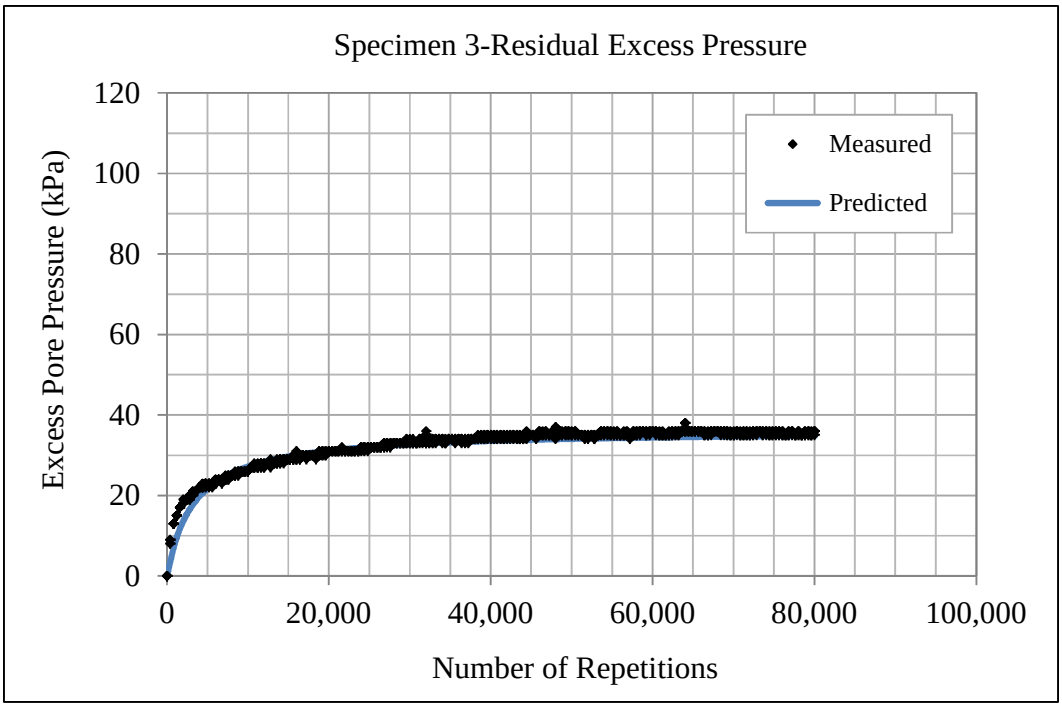

FIGURE 6-47 Simulation of residual excess pressure development – Specimen 3

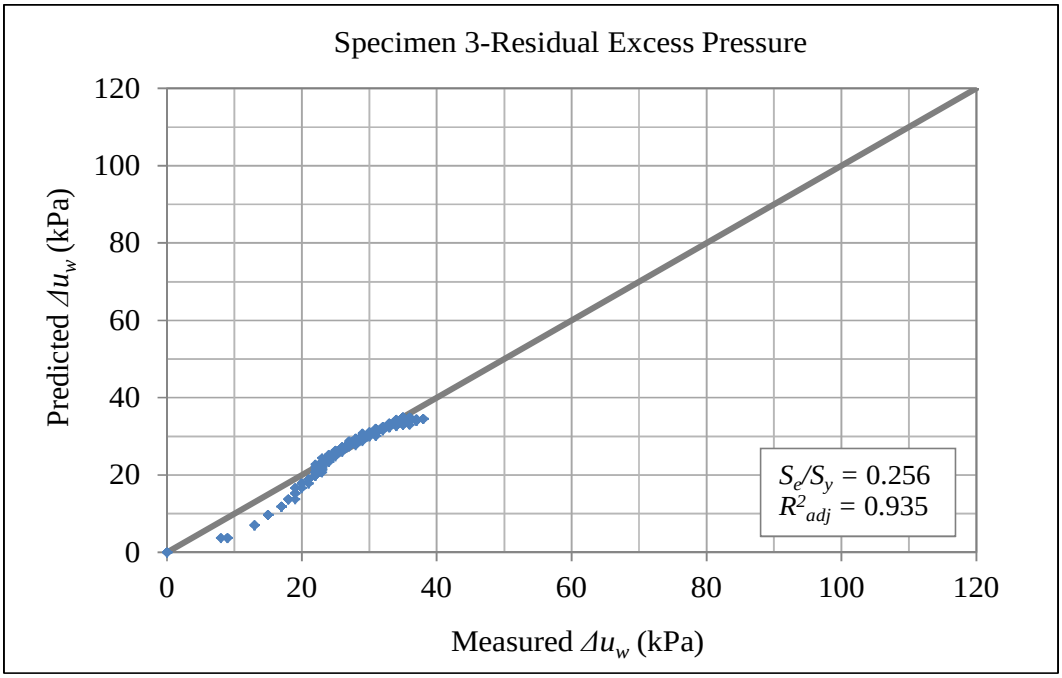

FIGURE 6-48 Goodness of fit - residual excess pressure – Specimen 3

Plots for specimens 1 and 3 were selected to be presented in the main document because they are representative of the worst and best results obtained from the simulations. Figures 6-41 and 6-43 show graphically an absolute error between 6 and 7 kPa as presented in Table 6-7. Even when the error in predictions is evident, the general trend of excess pore pressure developed for Specimen 1 seems to be well represented by the proposed models. Figures 6-42 and 6-44 also show the deviation of the predictions from the measured values, particularly when pore pressure is accumulated beyond 50 kPa. Also it is observed that for Specimen 1 the estimates under predict the real response of the material.

Figures 6-45 and 6-47, show the case when good predictions are obtained with the proposed models. As seen on Table 6-7 the absolute error for both the peak and residual excess pressures in Specimen 3 is less than 2 kPa, which is reasonably acceptable considering that more than 80,000 load repetitions were applied to the Specimen. Figures 6-46 and 6-48 reveal that the predictions do not follow the measured trend at low ranges of load repetitions. However, as previously mentioned, the major concern in pavement applications is the accumulation of excess pore pressures at high levels of number of cycles.

Figures 6-41 to 6-48 are good to visually analyze how well the results replicate the measured trends from a general point of view. Since it is also interesting to visualize how the proposed models simulate the pore pressure development within the i^{th} cycle, magnified views to the figures recently presented are shown in Figures 6-49 to 6-51 for Specimen 1. The figures show the detail at early, intermediate and advanced stages of the test.

Figures 6-49 to 6-51 present the results of the simulation for Specimen 1. Figure 6-49 details the predictions for cycles 4,806 to 4,810. These cycles obviously correspond to and early stage in the test for Specimen 1 that lasted for a total of 96,060. The Global Peak and Cycle End Excess Pore Pressure Curves used as boundaries to develop the model are shown in the figures. The measured data as well as the predictions are also displayed in the figures.

It can be observed that there is an error of roughly 1kPa in the Global Predicted Curves relative to the measured data.in that particular segment of the test. There is also an error of about 1.5kPa in the Global Predicted Curves relative to the predictions. It is interesting that in the test segment shown in Figure 6-49, the error of the predictions relative to the measured data is smaller than the error relative to the Global Curves. This is not necessarily representative of what is seen along the test as can be corroborated by looking at Figures 6-50 and 6-51. The differences between the predicted peaks and residual pressures seem to be roughly the same as the differences between the Global Curves which confirms that the Global Curves as boundaries for modeling serve their purpose.

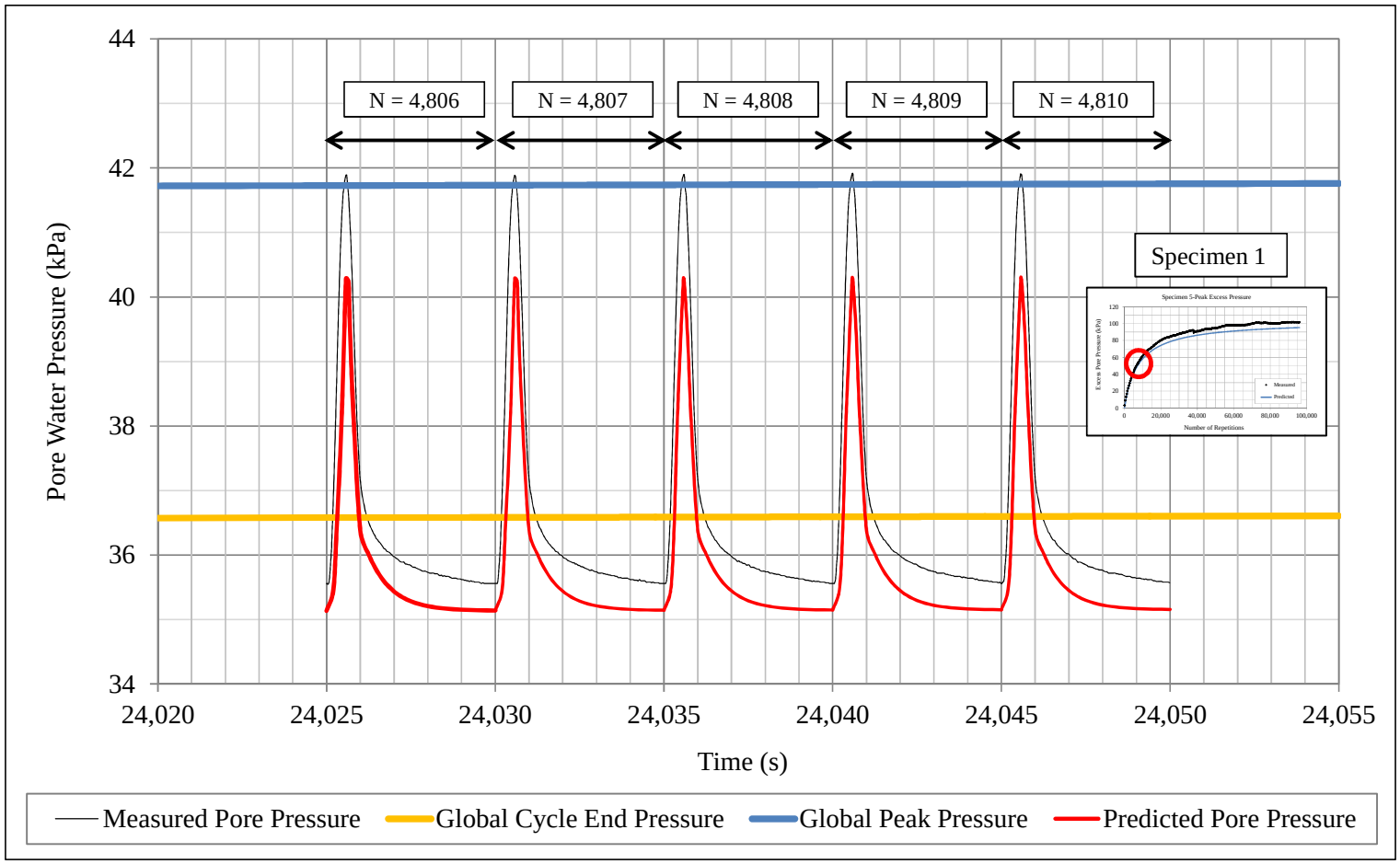

FIGURE 6-49 Magnified view of the pore pressure development at an early stage of the test for specimen 1

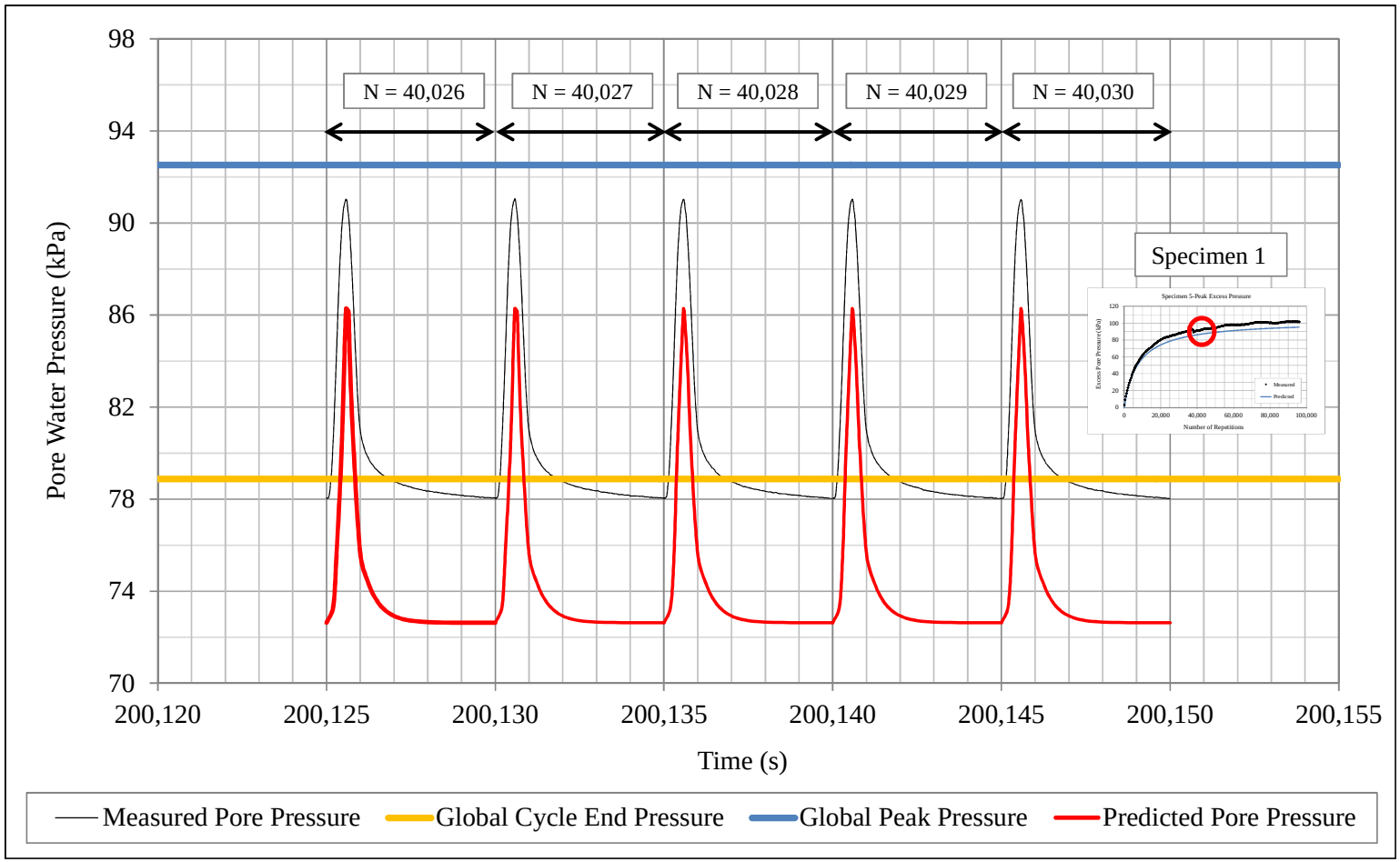

FIGURE 6-50 Magnified view of the pore pressure development at an intermediate stage of the test for specimen 1

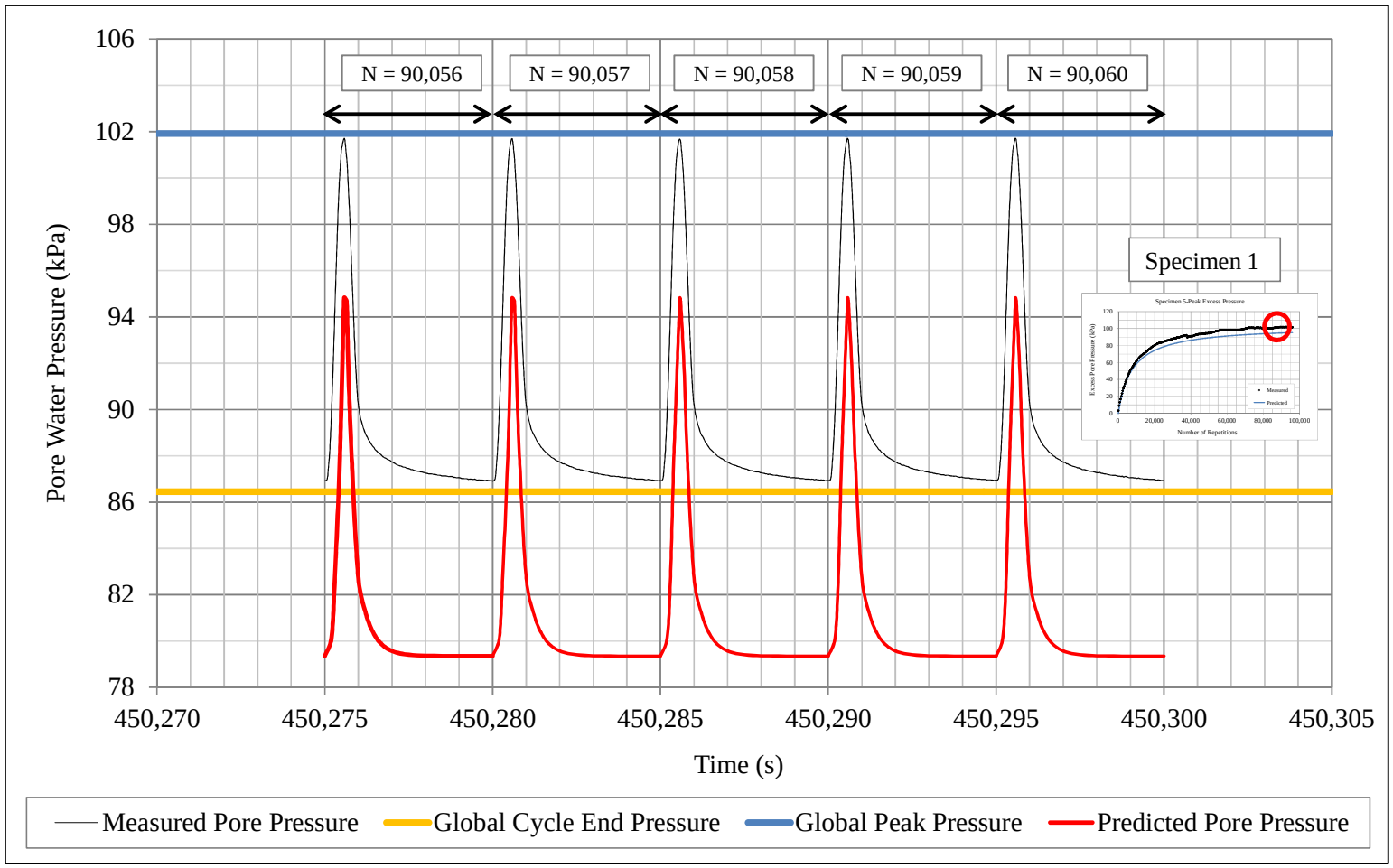

FIGURE 6-51 Magnified view of the pore pressure development at an advanced stage of the test for specimen 1

Note that as the number of cycles increase when going from Figure 6-49 to Figure 6-50 and then from Figure 6-50 to figure 6-51, the accumulation of error becomes more significant. If the predictions in all figures were shifted upwards in such a way the peak and residual pressures match the boundary limits, it would appear that the results fit the boundaries exceptionally. However, a marginal error in each cycle is always accumulated. Therefore, the increment in accumulated error observed in the figures confirms that even when the error is not perceived in a single cycle, it becomes significant as accumulated with the number of cycles. The error observed increases progressively from about 1.5kPa in Figure 6-49 to roughly 7kPa towards the end of the test as noticed in Figure 6-51. Generally, the results are always under predicting both the measured data and the Global Curves.

In Figures 6-52 to 6-54 it is observed that better predictions were obtained for Specimen 3. As the number of repetitions increases when moving from one figure to the next, the error seems to be relatively constant to less than 1kPa. The models over predict the measured values at early stages of the test as seen in Figure 6-52. At intermediate stages of the test, the predictions seem to match the measured results as seen in Figure 6-53. At advanced stages of the test the estimates under predict the measurements as seen in Figure 6-54. Generally it is concluded that for Specimen 3, the error is compensated along the test. It is also observed that the Global Curves boundaries again rule the shape of the pore pressure pulse at each cycle even when the predictions do not fall within the boundaries.

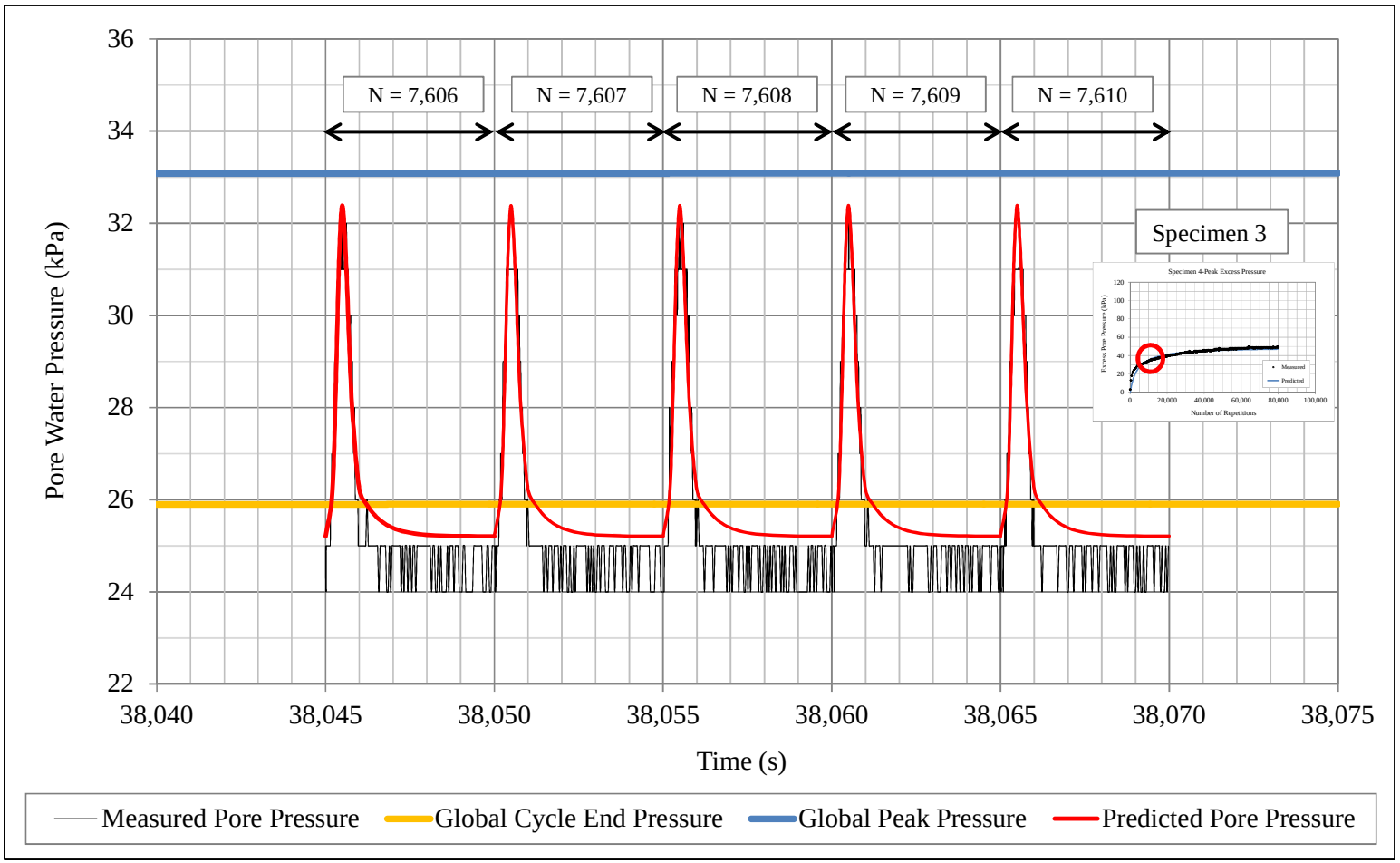

FIGURE 6-52 Magnified view of the pore pressure development at an early stage of the test for specimen 3

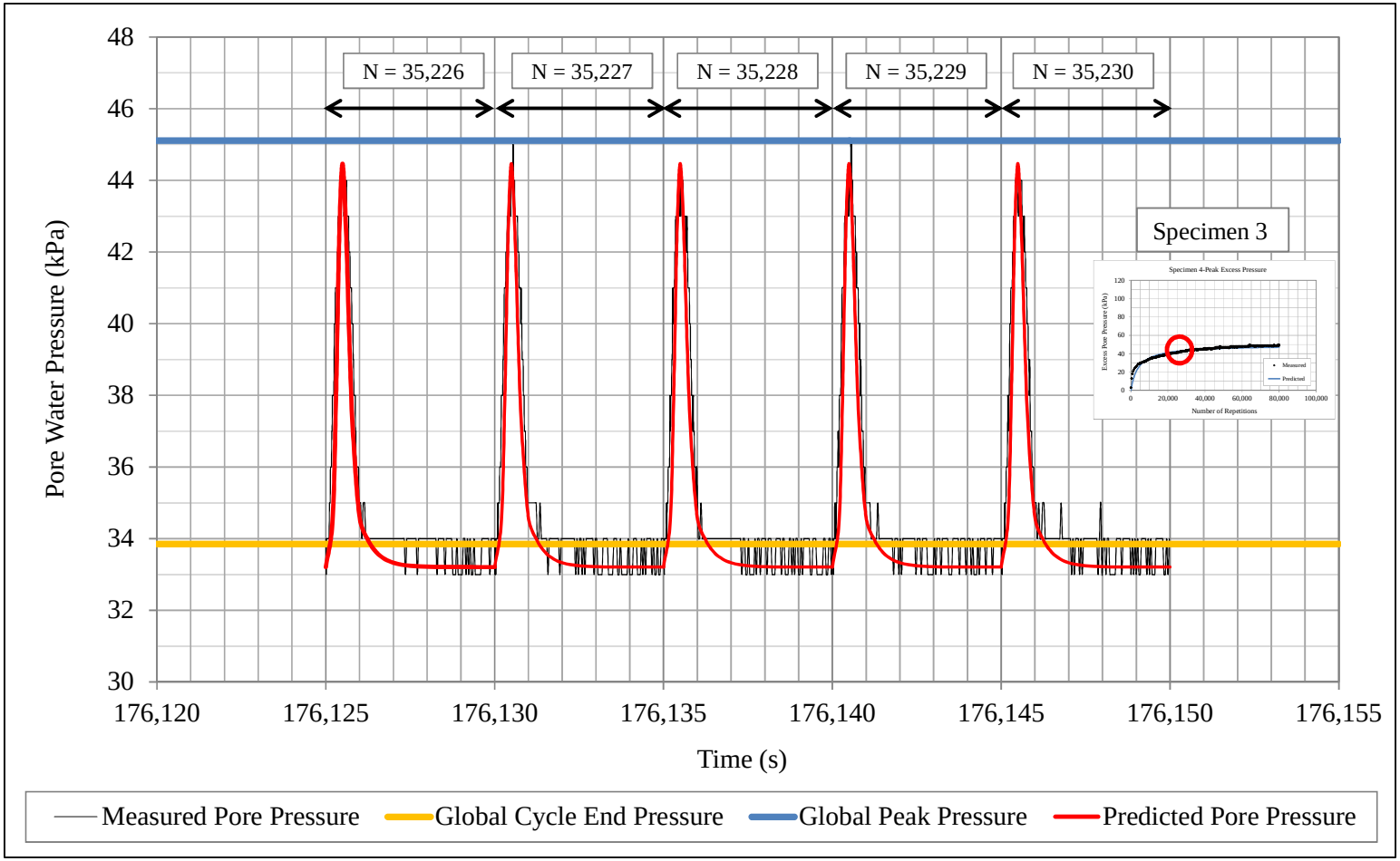

FIGURE 6-53 Magnified view of the pore pressure development at an intermediate stage of the test for specimen 3

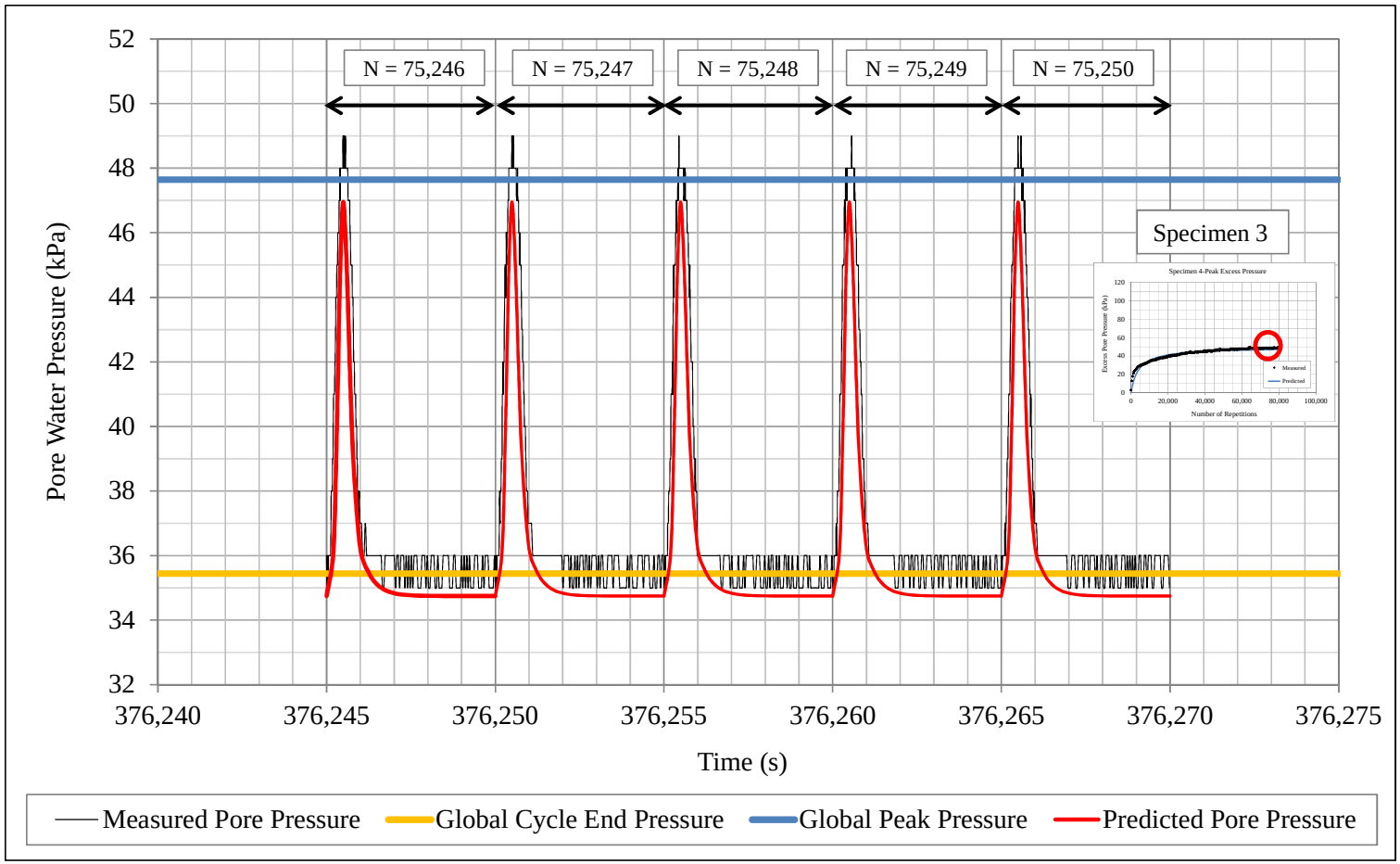

FIGURE 6-54 Magnified view of the pore pressure development at an advanced stage of the test for specimen 3

As observed in Figures 6-49 to 6-54, the problem with the predictions seems to be an accumulation of marginal errors throughout the test rather than major issues when predicting the pore pressure pulse within a single cycle. Therefore, a rule to adjust the predictions along the test can be imposed when running a simulation program. In this way, whenever the accumulated error goes beyond a reasonable critical value, the predicted pulses can be shifted either upwards or downwards in such a way the initial point for the next cycle lies on the Global Cycle End Excess Pressure Curve.

The error in accumulated residual pressure predictions ε_2 can be defined as the difference between the accumulated residual excess pore pressure Δu_{2U} obtained evaluating Equation 6-36 for $t=t_D$, and the excess pore pressure estimated from the Global Cycle End Excess Pressure Curve at the same global time by using Equation 6-13. The expression to estimate the error reads as follows:

$$\varepsilon_2 = \Delta u_{2U} - \frac{1}{a_2+\frac{b_2}{t}} \tag{6-39}$$

Where, $t = i.(t_L + t_D)$ and a_2 and b_2 are known parameters from the Global Cycle End Excess Pressure Curve. Then, if ε_2 results to be greater than +/- a critical value established for a particular analysis, the corrected residual excess pore pressure $\Delta u_{2U_{Adj}}$can be obtained by applying the following equation:

$$\Delta u_{2U_{Adj}} = \Delta u_{2U} - \left(\Delta u_{2U} - \frac{1}{a_2+\frac{b_2}{t}}\right) \tag{6-40}$$

Figure 6-55 shows a graphical example of the results adjustments performed on Specimen 1. It can be observed in the figure, that by applying the adjustment, the predictions are shifted upwards in such a way the predicted accumulated excess pressure at the beginning of the next cycle lies on the Global Cycle End Excess Pressure Curve. A new adjustment can be applied later in the test when the error ε_2 exceeds the critical established error again. In this way, it can be ensured that the predictions closely follow the boundary Global Curves.

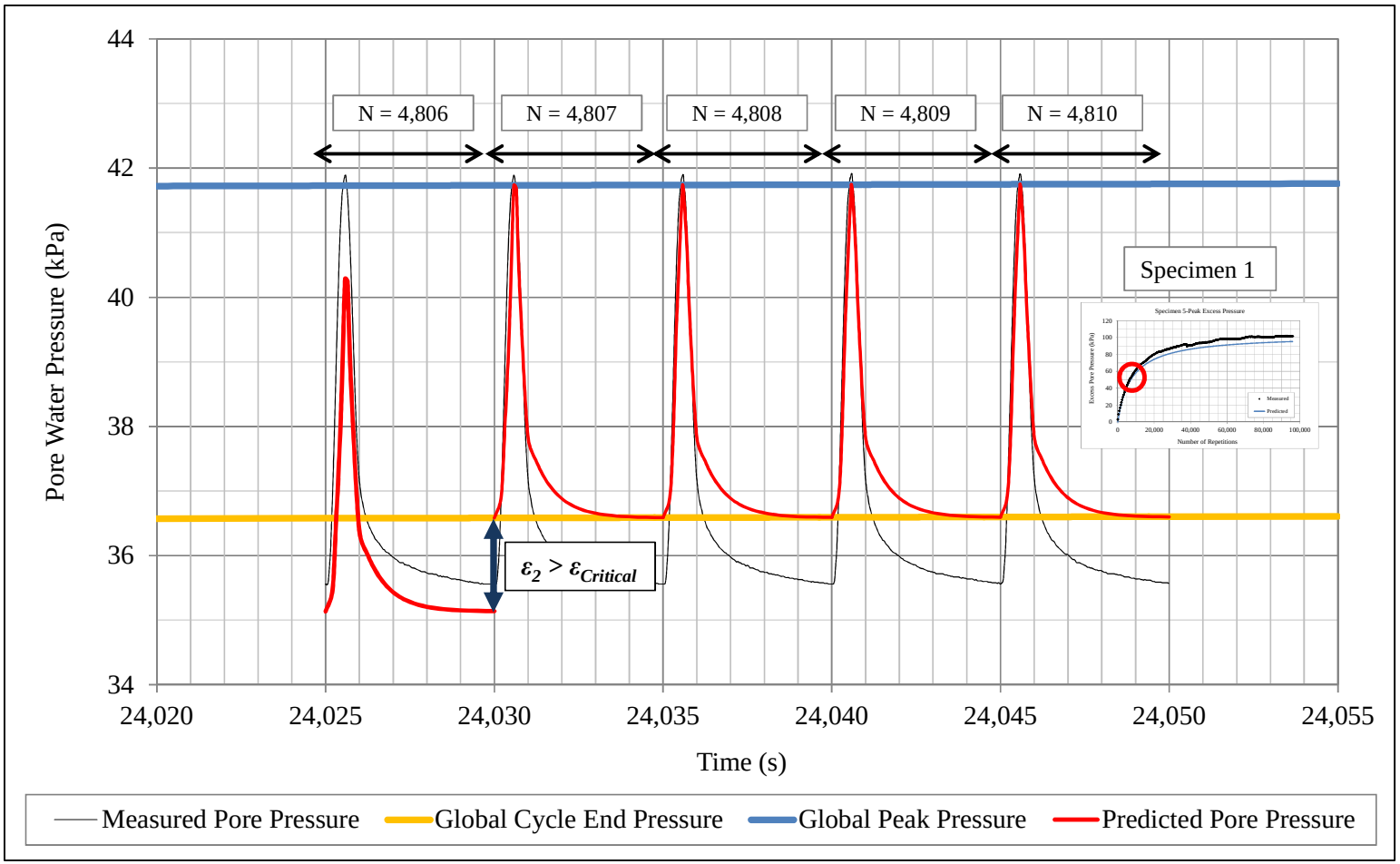

FIGURE 6-55 Example of predictions adjustment at an early stage of the test for specimen 1

Evaluation of Test Conditions Influence on the Model Regression Constants

The models proposed in previous sections require of 9 regression constants in order to predict the development of excess pore pressure. The β constant was observed to be about 0.5 for saturated conditions and 0.58 for unsaturated regardless of the influence of any other variable. The other 8 constant seem to be more affected by the test conditions as indicated by their range of variation.

Due to the time demanding nature of the tests performed (as explained in Chapter 4), only two levels for each variable were controlled in this study. The limited amount of data available did not allow for the development of models that relate the regression constants to the test conditions. However, a general analysis looking into the impact that varying test conditions may bring to the mentioned regression parameters was conducted. Valuable conclusions that can be taken into account for future research efforts aimed at enhancing the proposed models were obtained.

Influence of Test Conditions on the Global Pressure Curves Parameters

The regression coefficients a_p, a_1, a_2, b_p, b_1 and b_2 presented in Table 6-2 from previous sections, are presented below to facilitate the analysis. It was explained earlier in this report that the *a* parameter is nothing but the reciprocal of the maximum excess pore pressure $\Delta u_{w\,max}$ to be achieved for particular conditions. Also, it was mentioned that the *b* parameter is related to the maximum time $t_{\,max}$ that takes for the material to reach $\Delta u_{w\,max}$.

As presented in Figures 6-33 and 6-34, the value of $\Delta \boldsymbol{u}_{\boldsymbol{w\,max}}$ increases as the *a* parameter decreases. Similarly, it was observed in Figures 6-35 and 6-36 that t_{max} increases with the value of *b*.

In order to analyze from a rational point of view the influence of the test variables upon the variation of the *a* parameter, the $\Delta u_{w\,max}$ values corresponding to the estimated *a* parameters were obtained and are presented along in Table 6-9.

TABLE 6-9 Regression coefficients for the global curves

Specimen	1	2	3	4	5	6
$S\%_{AP}$	81	79	78	80	83	80
$S\%_{AC}$	75	76	95	96	78	73
$S\%_{AT}$	77	77	100	100	82	77
$\psi_{mo}\,(kPa)$	157	157	0	0	157	157
$\theta_{net/eff}\,(kPa)$	509	344	509	344	509	344
$t_D\,(s)$	4	4	4	4	8	8
a_p	0.0090	0.0157	0.0199	0.0398	0.0177	0.0233
a_1	0.0103	0.0164	0.0260	0.0936	0.0295	0.0243
a_2	0.0107	0.0167	0.0270	0.0981	0.0307	0.0252
b_p	359.2	613.9	391.2	180.3	452.7	3716.2
b_1	388.4	714.8	425.7	1016.9	2028.7	3873.0
b_2	400.3	732.4	440.1	1703.0	3449.3	3906.8
$\Delta u_{p\,max}(kPa)$	111	64	50	25	56	43
$\Delta u_{1\,max}(kPa)$	97	61	39	11	34	41
$\Delta u_{2\,max}(kPa)$	94	60	37	10	33	40

Now, an analysis on the a parameters in terms of $\Delta u_{w\,max}$ can be conducted. Figure 6-56 represent the influence of the bulk stress upon the $\Delta u_{w\,max}$ values obtained from the a parameters.

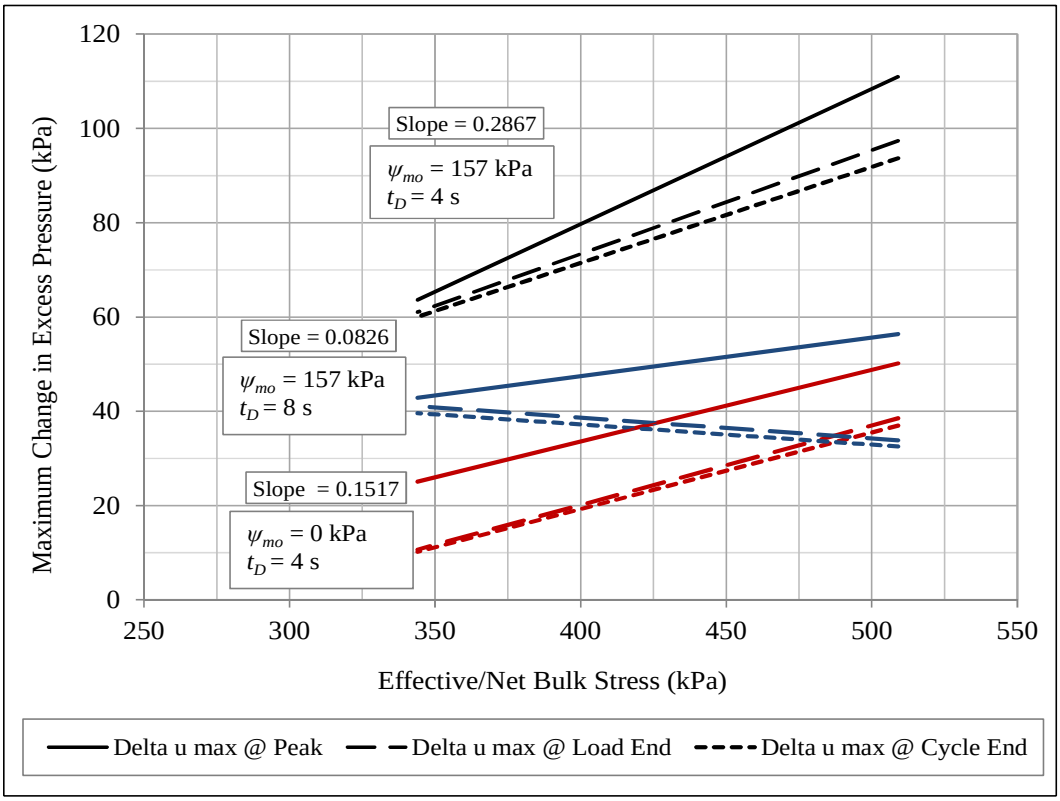

FIGURE 6-56 Influence of bulk stress on $\Delta u_{w\,max}$

It should be noted in Figure 6-56 that three lines are plotted for each test condition. Each line was constructed using only the two ending point corresponding to high and low levels of the variable evaluated. The three lines correspond to the maximum excess pressure reached by the Peak, Load End and Cycle End Global Excess Pressure Curves as indicated in the legend. Except for the dashed blue lines corresponding to the Load End and Cycle end maximum pressures, it is observed that in general, the maximum pressure values tend to

increase with the bulk stress level. This observation suggests that the *a* parameter follows a rational trend under the effects of the bulk stress.

The slopes presented in the figures correspond to the lines for the maximum excess pressure at the peak. In other word, correspond to the continuous lines. By comparing the slopes, it can be said that the more significant impact of the bulk stress is registered for the unsaturated specimen tested at low level of dwelling time. The increment in maximum pressure change when increasing the bulk stress is around 50kPa, by far more important than changes observed for the other two sets of lines.

The fact that the maximum excess pressure values reached by the Load End and Cycle End Global Curves at high stress levels ended up being lower than those observed at low stress levels may be explained by the initial conditions of the test specimens. The mentioned points corresponding to ψ_{mo}=157 kPa and t_D=8s at high stress level correspond to Specimen 5. From

Table 6-9, it is observed that the degree of saturation for Specimen 5 is higher compared to the rest of unsaturated specimens. This may lead to believe that even when the same matric suction was applied during conditioning, equilibration was never achieved by the specimen. Therefore, the real matric suction for that specimen could have been lower than what was actually believed. Also it was observed that in general the changes in excess pore pressure appear to be greater at higher than at lower applied initial matric suctions. Therefore, if Specimen 5 was properly equilibrated to 157kPa then the maximum excess pressure would have been higher. In that case, the three points in Figure 6-59

corresponding to Specimen 5 would be shifted upwards which would result in all lines pointing upwards. As a general conclusion, considering the questioning arose about Specimen 5, the effect of the bulk stress seems positive in terms of $\Delta \boldsymbol{u}_{\boldsymbol{w\,max}}$ and logically negative when translating the effects in terms of *a* parameters.

Figure 6-57 shows the influence of the initial matric suction ψ_{mo} on the $\Delta \boldsymbol{u}_{\boldsymbol{w\,max}}$ achieved. In this case, the influence of suction is clear. The values for $\Delta \boldsymbol{u}_{\boldsymbol{w\,max}}$ increase with ψ_{mo} regardless of the stress level imparted to the specimens. Therefore the influence of the initial matric suction ψ_{mo} on the *a* parameter is significant.

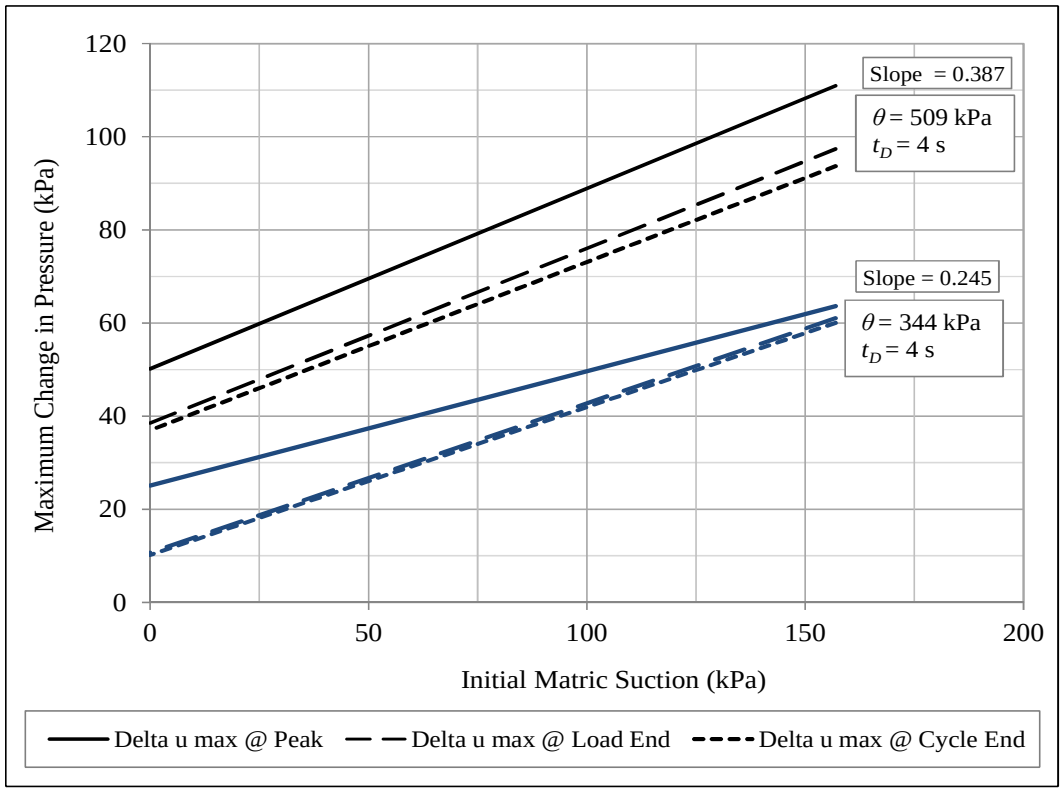

FIGURE 6-57 Influence of initial matric suction on $\Delta u_{w\,max}$

Note that parameters for Specimen 5 are not involved in this plot because test results corresponding to a low level of initial matric suction and the same level of dwelling time, needed for an eventual comparison were not obtained.

Figure 6-58 shows the influence of the dwelling time t_D on the $\Delta \boldsymbol{u}_{\boldsymbol{w\,max}}$ achieved. At a first glance, it seems based on the slope of the black lines that the effect of dwelling time is significant. However, it should be recognized that Specimen 5 is again involved in the analysis. For the reasons previously explained, it is expected that the lower points in the black lines would shift upwards if the specimen reached proper equilibration under the suction applied during the conditioning stage. Therefore, the conclusions about this figure should be cautiously stated.

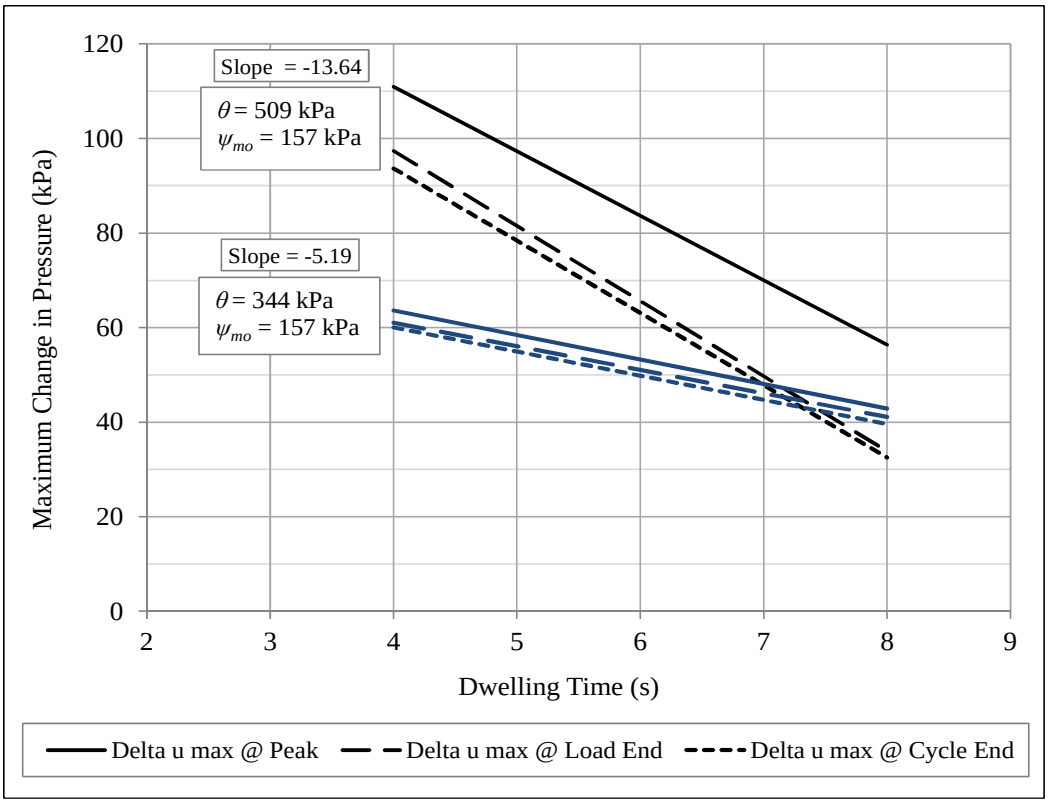

FIGURE 6-58 Influence of dwelling time on $\Delta u_{w\,max}$

It appears evident that regardless or the stress level, the maximum change in excess pressure to be reached decreases with increasing dwelling times. This means that the *a* parameter increases with dwelling time. However, when comparing the line slopes in Figure 6-58 to those observed in Figures 6-56 and 6-57, it is readily apparent that even when some effect of the dwelling time exist the effect imparted by the bulk stress and initial matric suction are more significant.

In order to reinforce the observations obtained from the figures presented above, correlation matrixes were developed to find the statistical coefficient of correlation between the variables in study and the *a* parameter. The results of the correlation matrixes are summarized in Table 6-10.

TABLE 6-10 Coefficients of correlation between variables and the *a* parameter

	a_p	a_1	a_2
a_p, a_1, a_2	1	1	1
t_D	-0.029	-0.164	-0.164
θ	-0.564	-0.413	-0.410
ψ_{mo}	-0.666	-0.675	-0.676

The results shown in Table 6-10 provide support to the conclusions obtained from the figures. The negative values mean that the parameter tends to decrease as the variable level increases. It should be noted that coefficients of correlation close to +/- 1 indicate a strong correlation and as the values approaches 0 the level of correlation between the parameters and the variables decreases as well. According to the coefficients of correlation presented, apparently the highest effect upon the *a* parameter is imparted by the initial matric suction followed by the bulk stress. Both variables seem to be potential predictors

for the development of relationships to estimate the *a* parameter. Even when the dwelling time also shows to be correlated to *a*, according to the values observed in the table it does not seem to be as important as the other two variables.

Therefore, the suggested dependence of *a* on the mentioned predictive variables is expressed in the following equation and should be considered for future research.

$$a = f(\psi_{mo}, \theta) \tag{6-41}$$

Figure 6-59 shows the influence of the bulk stress on the *b* parameter. In general, the trends indicate that the higher the bulk stress, the lower the *b* parameter. In terms of time, it means that when the applied stress is higher, the time that the specimen takes to reach the maximum excess pore pressure is shorter which is logically reasonable. Also, an interaction between dwelling time and bulk stress can be inferred. At high dwelling times it seems that the influence of the bulk stress becomes more important as suggested by the slope of the blue continuous line.

It was surprising to find a reversed trend for the red continuous line. It would be reasonable to expect the *b* parameter decreasing with increasing bulk stress as observed for the rest of the lines. The lower point of the red line corresponds to Specimen 4 which was tested for a short number of repetitions. It is likely that the reduced number of data points compared to the rest of the tests resulted in the presence of uncertainty when the regression parameters were estimated. A replicate of the test could have been useful to double check the

results. However, as previously mentioned, due to the time demanding nature of the test, it was not possible to run replicates for this study.

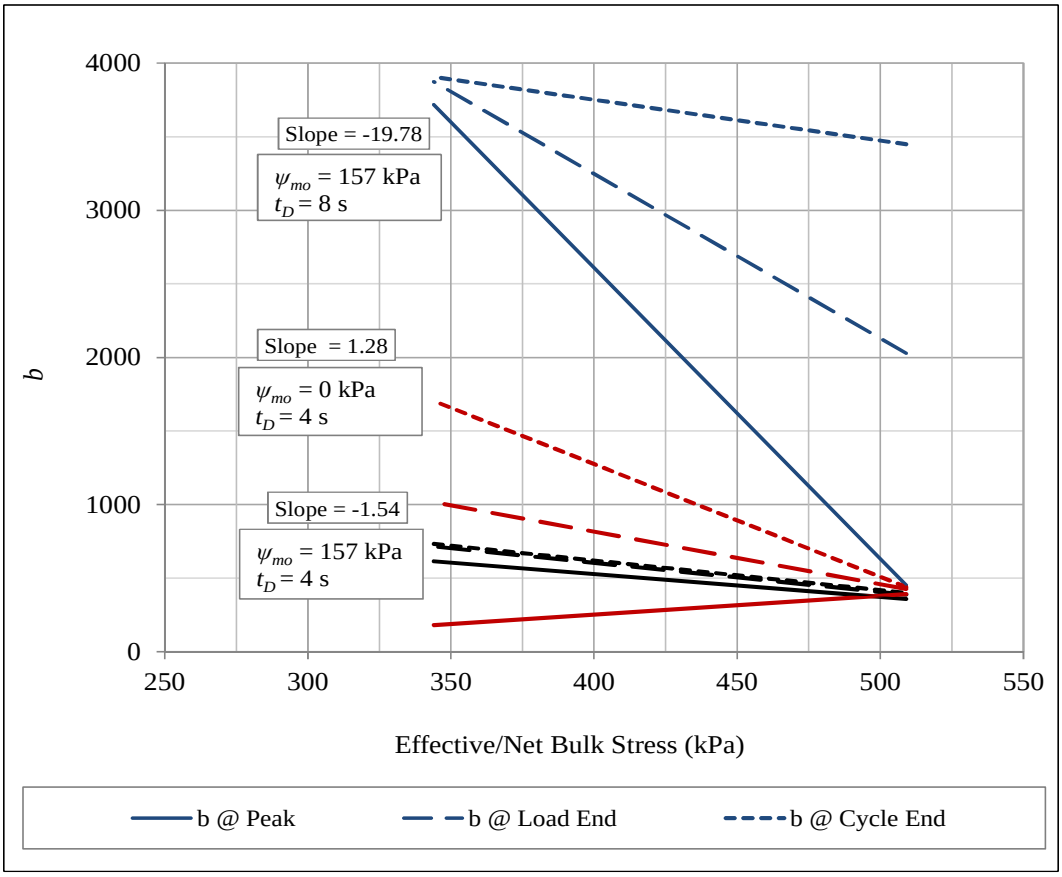

FIGURE 6-59 Influence of bulk stress on the *b* parameter

Again, the uncertainty about the validity of the *b* parameters at low levels of suction, bulk stress and dwelling times remains present since the results obtained under those conditions correspond to Specimen 4. As previously commented, probably the limited data available to define pressures development for that specimen could have induced error in the estimation of parameters. Therefore, it could be possible that the initial matric suction does not have effect on the *b* parameter regardless of the stress level. Better conclusions may be obtained when analyzing the correlation matrixes for this parameter.

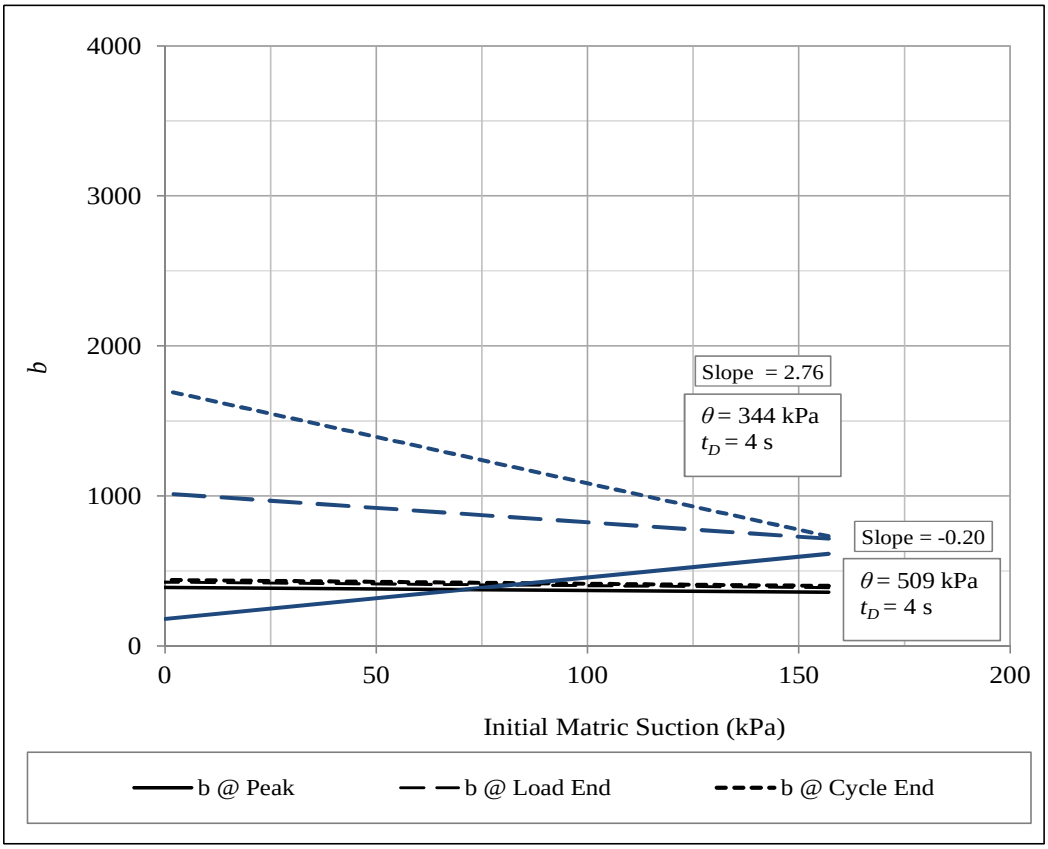

FIGURE 6-60 Influence of initial matric suction on the *b* parameter

Figure 6-61 shows the influence of the dwelling time on the *b* parameter. This time, there seems to be no doubt about the high impact of the dwelling time upon the time required to reach the maximum excess pressure. Regardless of the bulk stress level, the time to reach the maximum excess pore pressure is dramatically increased with dwelling time.

It is also observed that the continuous black line that corresponds to the peak excess pressure is not affected significantly. It means that regardless of the dwelling time the peak pressure at high bulk stress is reached at early stages of repetitive loading. However, it should also be taken into account that the end

point of the black continuous line at 8 seconds of dwelling time correspond to Specimen 5 which might probably provide misleading information.

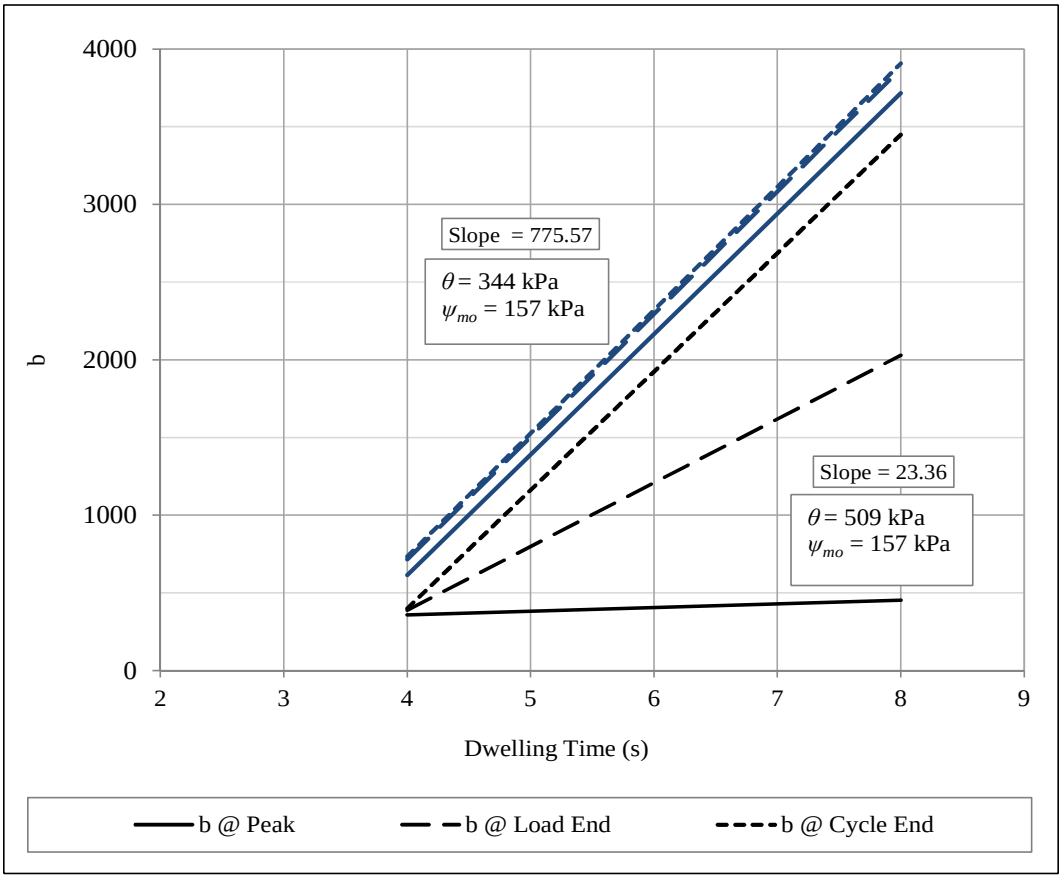

FIGURE 6-61 Influence of dwelling time on the *b* parameter

In order to validate the conclusions obtained from the figures, correlation matrixes were obtained again to analyze the relationship between the test conditions and the *b* parameter. Table 6-11 shows a summary of the correlation matrixes developed.

TABLE 6-11 Coefficients of correlation between variables and the *b* parameter

	b_p	b_1	b_2
b_p, b_1, b_2	1	1	1
t_D	0.644	0.886	0.949
θ	-0.444	-0.374	-0.241
ψ_{mo}	0.379	0.394	0.349

The results observed in the Table 6-11 confirm that there is a strong positive correlation between the *b* parameter and the dwelling time. Also, it indicates that there might be a medium to low influence of bulk stress and matric suction that would need to be considered to determine the time required to reach maximum pressures. However, it is clear that the dominant variable on this parameter is without discussion the dwelling time. Therefore, the b parameter could be expressed as a function of the controlled variables as follows:

$$b = f(t_D, \psi_{mo}, \theta) \tag{6-42}$$

Influence of Test Conditions on the Parameters Governing the Unloading Phase

The regression coefficients m and n are fundamental to describe the soil response during the unloading phase occurring within the i^{th} cycle. Therefore, it is necessary to understand the impact of the variables controlled during the test upon the mentioned parameters.

The parameters m and n are necessary to estimate the denominator p for the exponential function that describes the pore water pressure dissipation as seen in Equation 6-22. At the same time, p varies with the number of cycles applied to

the material. Figure 6-62 shows the variation of p with the number of cycles for different values of the parameter m and keeping n constant.

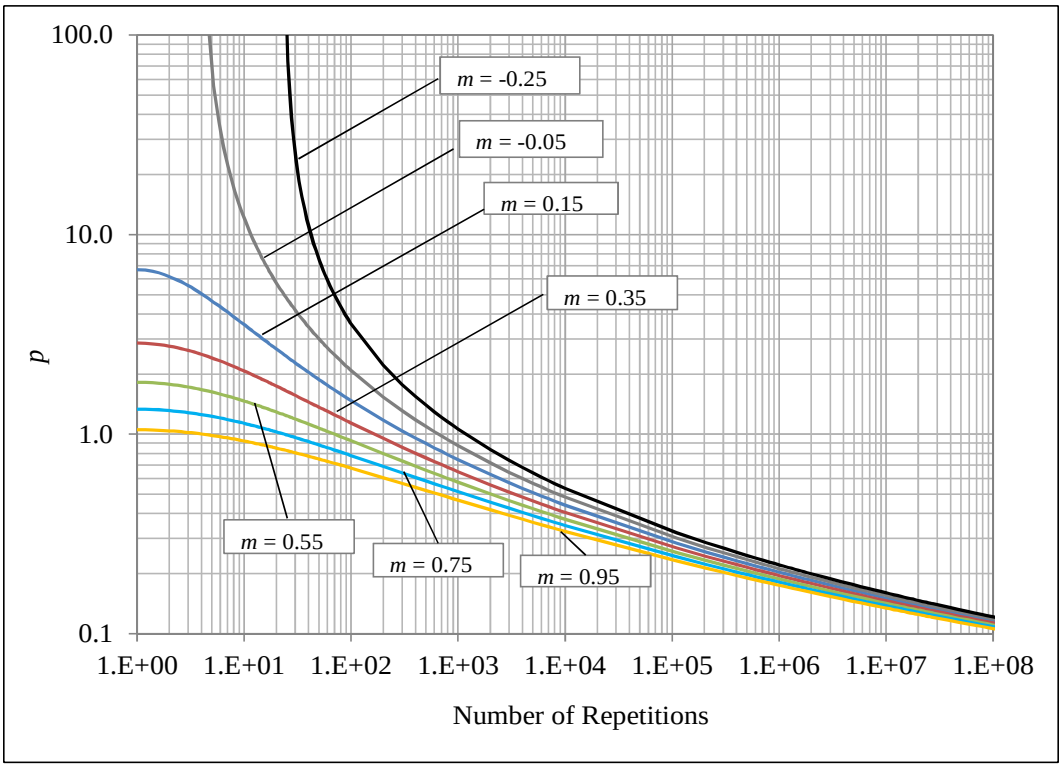

FIGURE 6-62 Variation of p with number of cycles and different m values

It can be observed that p decreases as m increases. At the same time, p decreases with the number of cycles. According to Equation 6-22, as p decreases, the exponential factor decreases as well. It means that as p decreases, the intercept of the same equation (equal to the pore water pressure at the end of the loading phase) will be also reduced.

Figure 6-63 shows the impact of varying m in terms of pressures. In order to develop the curves presented in the figure, Equation 6-22 was evaluated keeping n constant, assuming an intercept of 4 kPa which corresponds to the pore water pressure present at the end of the loading phase and using t = 4 seconds.

The results obtained are the values of pore pressure remaining after 4 seconds of rest. Such values were then normalized by the intercept and plotted as percentages. The final values represent the percentage of the pore pressure at the beginning of the unloading phase that is left for dissipation. In other words the plotted values are the residual pore pressures after 4 seconds of dwell expressed as a percentage of the pore pressure at the beginning of the dwelling time.

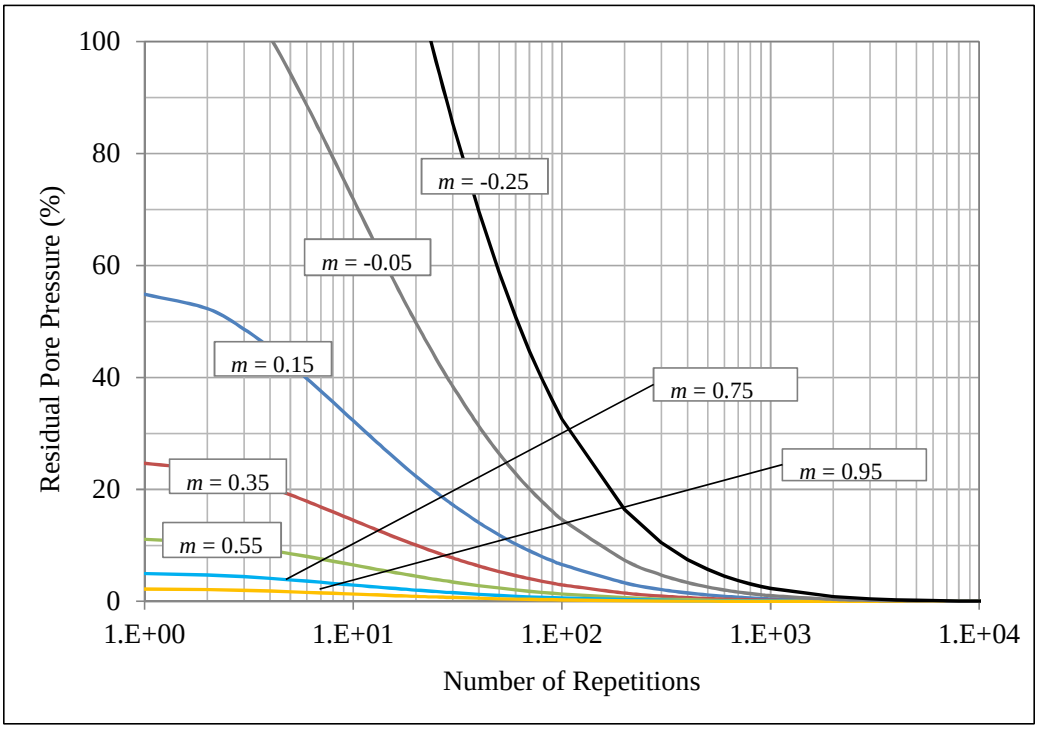

FIGURE 6-63 Residual pore pressure percent for different *m* values

It can be observed that the residual pore pressure percent left after 4 seconds of unloading phase decreases as m increases. The first impression indicates that the m parameter appears to be related to the capability of the material to dissipate pore pressures. Such capability can be related to the initial matric suction which is related at the same time to the coefficient of permeability. However, this plot is not enough to determine the relationship between m and the

variables controlled in the testing program. The values of m obtained for every single specimen were plotted against the controlled variables. Table 6-12 conveniently recalls the values for m and n previously presented.

TABLE 6-12 Parameter m and n obtained for all specimens

Specimen	Parameter			
	m	n	S_e/S_y	R^2_{adj}
1	-0.170	0.022	0.034	0.999
2	-0.195	0.021	0.052	0.997
3	-0.176	0.024	0.022	0.999
4	0.729	0.018	0.058	0.997
5	0.407	0.008	0.101	0.990
6	-0.229	0.011	0.010	1.000

Note that the m values obtained for the specimens tested are almost within the whole range displayed in Figure 6-63. This means that at some point, some of the specimens tested were able to dissipate the totality of the pore pressure left at the instant the load was completely removed; and at some point, some others did not dissipate pressures at all.

Figure 6-64 shows the variation of m with the bulk stress applied during the test. According to the plot here seems to be interaction of the variables affecting the soil response. Apparently at low levels of suction, the bulk stress level plays an important role in determining the percent of pressure to be released by the material. At low levels of suction and dwelling time, the bulk stress seems not to be affecting the m value. However, when high levels of both suction and dwelling time, the bulk stress plays again an important role. It is hard to determine

the predominant variable as a lot of interaction seems to occur. The results from a correlation matrix presented later in the document helped to define preliminary conclusions regarding the effect of bulk stress on m.

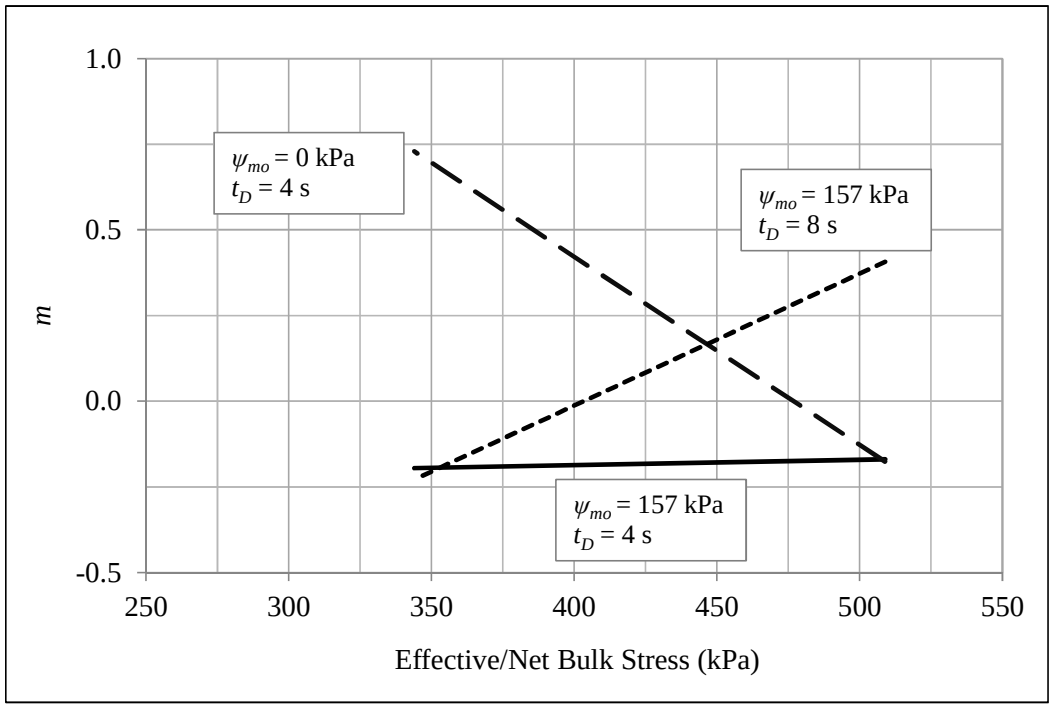

FIGURE 6-64 Influence of bulk stress on the *m* parameter

Figure 6-65 shows the variation of m with initial matric suction. Again, interaction between the bulk stress level and the initial matric suction is observed. At low bulk stress levels the effect of matric suction upon the capability of the material for pore pressure dissipation is observed. The influence of suction is reasonable since it is highly related to the hydraulic conductivity of the material which decreases as suction increases. Therefore it might be reasonable to believe that the capability for pore pressure dissipation is reduced for unsaturated materials. However it appears that at high levels of bulk stress the matric suction

and possibly the hydraulic conductivity do not play an important role in determining the capability of the material to dissipate pore water pressure.

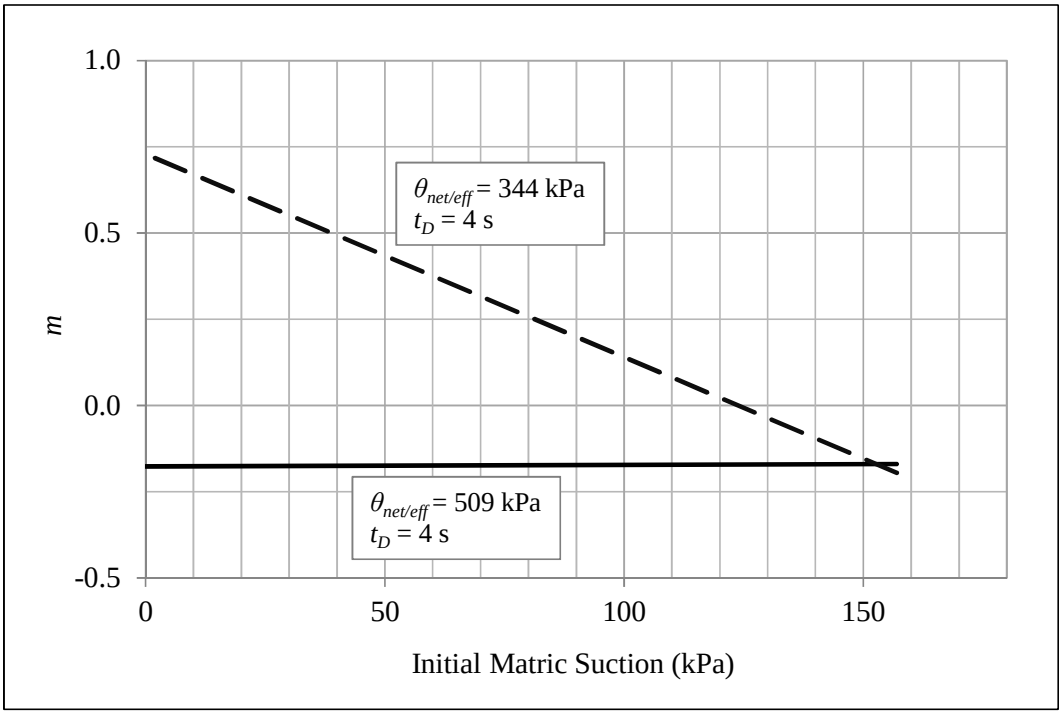

FIGURE 6-65 Influence of initial matric suction on the *m* parameter

Figure 6-66 shows the variation of m with dwelling time. Interaction of variables is observed again. At low bulk stress levels it appears not significant the influence of the dwelling time. On the other hand, at high bulk stress levels, the dwelling time appear to have some influence on the capability of the material to release pressure. However, when comparing the slope of the line for high bulk stress level with the slopes of the lines from Figures 6-64 and 6-65, it can be concluded that if there were any effect of dwelling time then it would be less significant than the effect of bulk stress and initial matric suction.

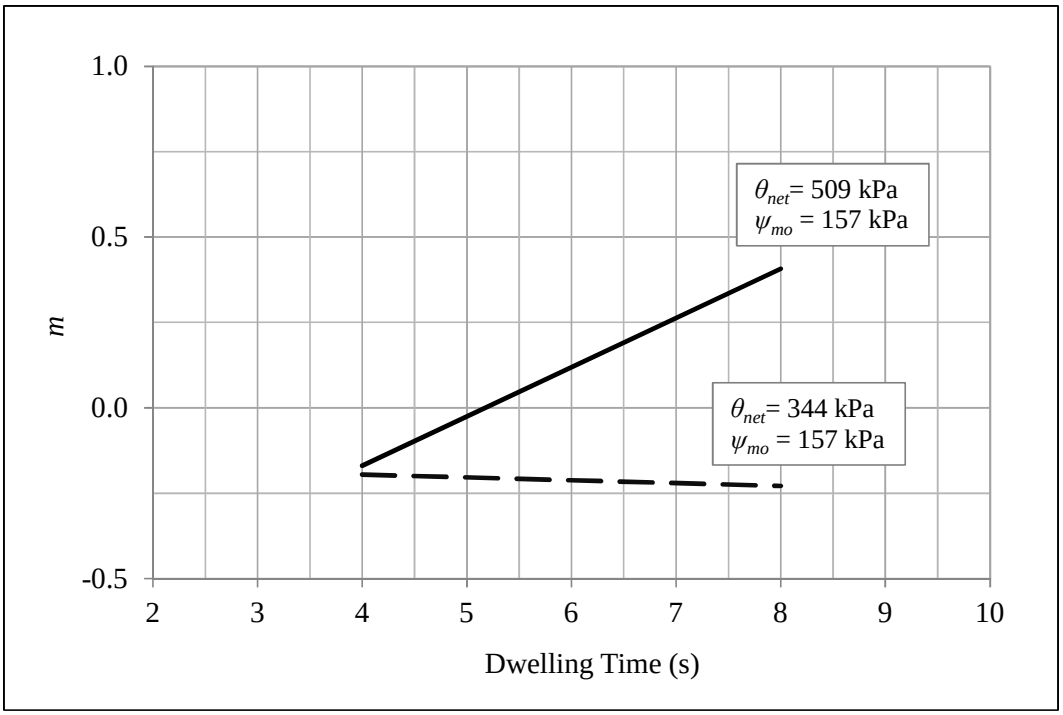

FIGURE 6-66 Influence of dwelling time on the *m* parameter

In order to reinforce the conclusions, a correlation matrix was developed to statistically evaluate the influence of the controlled conditions on the m parameter. Table 6-13 present the results of the correlation matrix.

TABLE 6-13 Correlation matrix for the m parameter

	m	t_D	θ	ψ_{mo}
m	1			
t_D	0.053	1		
θ	-0.110	0	1	
ψ_{mo}	-0.411	0.5	0	1

Results from Table 6-13 suggest that even when the coefficient correlation is low, the dominant variable for the m parameter is the initial matric suction. The

influence of the bulk stress seems to be irrelevant. It can be concluded that the initial matric suction definitely affects the m parameter.

In addition, since the hydraulic conductivity is highly correlated with soil suction, it is likely that the *m* parameter can be also function of the soil permeability. Figure 6-67, shows the relation between the initial matric suction applied to the specimens in this study and their corresponding hydraulic conductivities. The higher the matric suction, the lower the hydraulic conductivity.

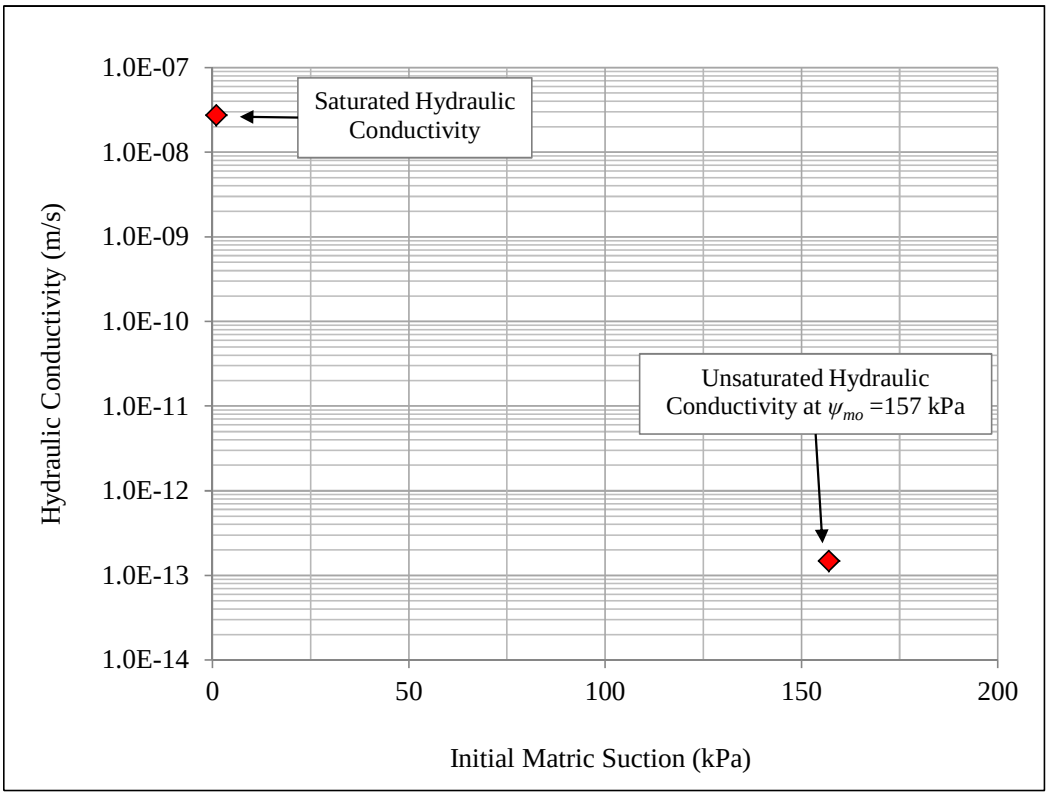

FIGURE 6-67 Initial matric suction versus hydraulic conductivity

Therefore, the hydraulic conductivity as predictive soil property should be investigated particularly when dealing with different soil types.

Given the interactions observed in Figures 6-64 to 6-66, the influence of the both bulk stress and dwelling time deserves to be further investigated in future studies. Based on the results of the analysis, the relationship of the m parameter and the controlled variables can be established as follows:

$$m = f(\psi_{mo}) \tag{6-43}$$

Figure 6-68 shows the variation of p with the number of cycles for different values of the parameter n and keeping $m$constant.

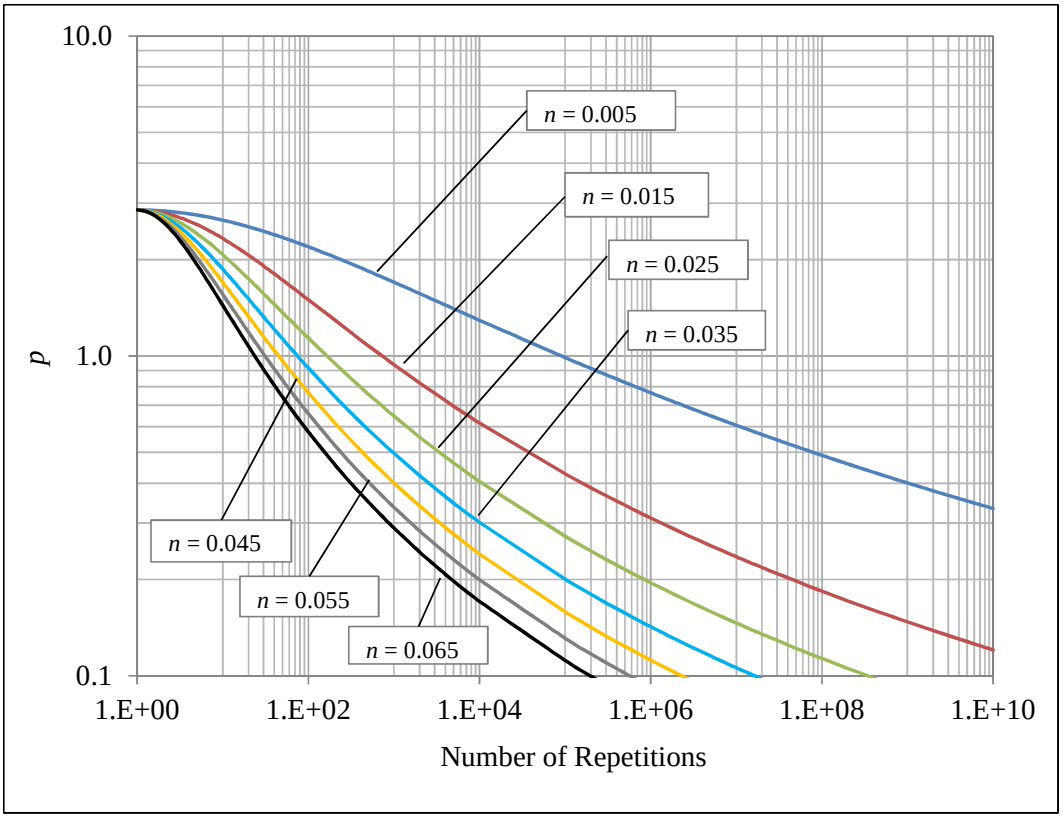

FIGURE 6-68 Variation of p with number of cycles and different n values

It can be observed that p decreases as n increases. At the same time, p decreases with the number of cycles. Apparently when n increases the degradation rate of p with number of cycles increases as well. In order to

understand the implications of varying n, its effect should be analyzed in terms of pore pressures. Figure 6-69 shows the impact of varying n in terms of residual or cycle end pore pressure. The range of n encountered for the specimens tested fall within the band delimited by the blue and black lines in Figure 6-69. In order to develop the curves presented in the figure, Equation 6-22 was evaluated keeping m constant, assuming an intercept of 4 kPa which corresponds to the pore water pressure present at the end of the loading phase and using t = 4 seconds. The results obtained have the same meaning as those obtained for Figure 6-63. Such values were then normalized by the intercept and plotted as percentages.

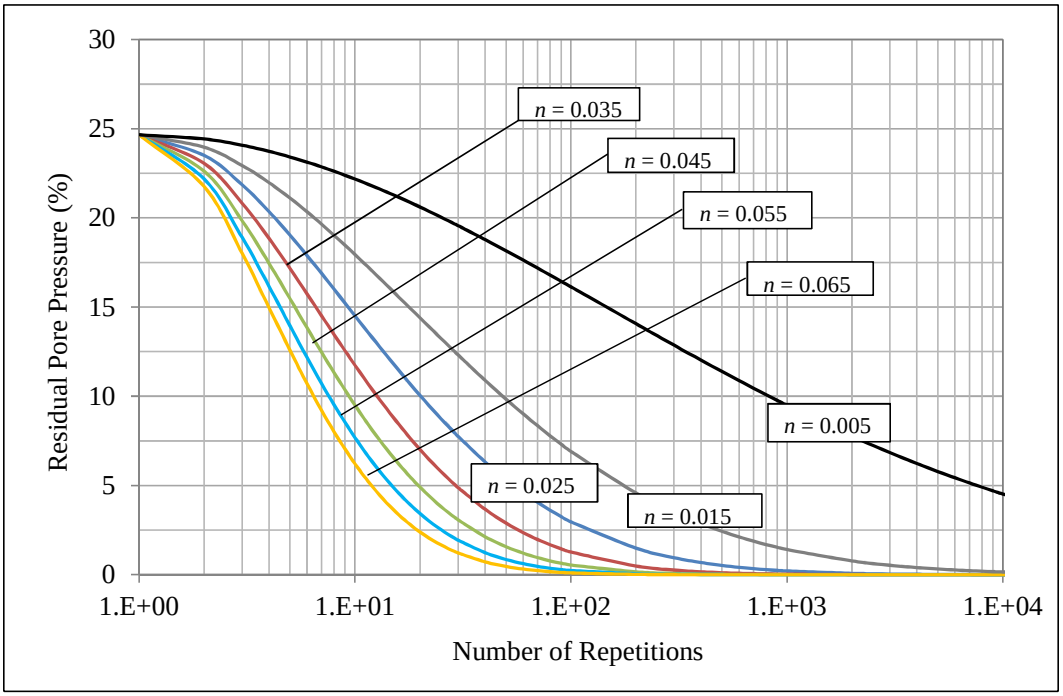

FIGURE 6-69 Residual pore pressure percent for different n values

It can be observed that rather than giving information about the capability of the material to dissipate pore pressure, the n parameter indicates how fast the material stabilizes in such a way that the percentage of residual pore pressure left

after at the end of the unload period, becomes constant. In general, the higher the n, the faster the specimen achieves stable conditions.

Even when saturated specimens are assumed to have all the pores filled with water, in reality there will always remain some air voids .inside the specimen. Obviously the presence of air voids in unsaturated specimens is more significant. Therefore, both saturated and unsaturated specimens, at different levels, are prone to experience further plastic strain which explains why all specimens experience such stabilization of the residual pore pressures. When the initial plastic strain stabilizes, it appears that most of the deformations experiences by the specimens are resilient and therefore the rate of pore pressure accumulation becomes marginal and steady when the maximum excess pore pressure is reached.

Figure 6-70 shows the variation of n with the bulk stress applied during the test. The influence of the bulk stress seems not to be significant upon the number of repetitions needed for the excess pressure of the soil to stabilize. In the figure, different from the two upper lines which point upwards with increasing bulk stress, the lower dashed line points downwards. The uncertainty about parameters obtained for Specimen 5 appears one more time as the lower dashed line ending point at high bulk stress correspond to such specimen. At high bulk stress level, it is reasonable to expect faster stabilization of the material. Therefore the trend obtained for the lower line could be questionable.

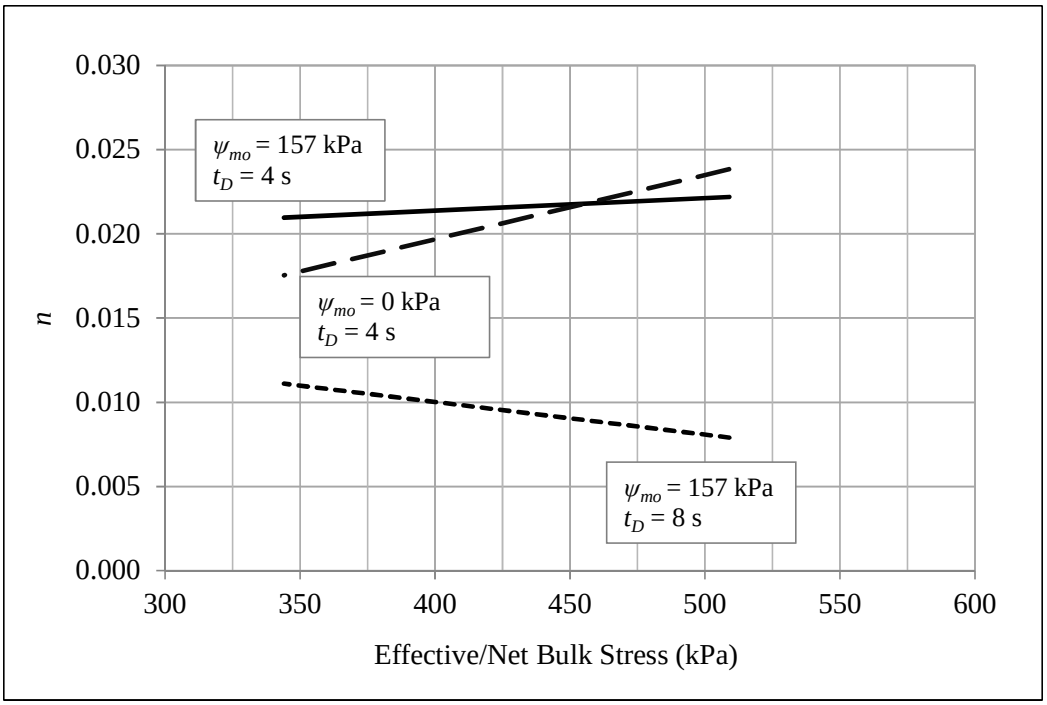

FIGURE 6-70 Influence of bulk stress on the *n* parameter

Based on the two upper lines, apparently at low initial matric suction level the influence of bulk stress upon the *n* parameter is more important than at low initial matric suction level.

Figure 6-71 shows the influence of the initial matric suction on the *n* parameter. It is observed that the effect of initial matric suction upon *n* does not seem to be significant as the slopes of the lines are not high. Apparently some interaction takes place between the initial matric suction and the bulk stress level. However, it was previously explained that only 16,000 load repetitions were applied to Specimen 4 which might condition the validity of the parameters obtained; and the point at low matric suction level for the lower dashed line corresponds to such specimen. Therefore, the two lines in reality could be parallel instead of showing interaction of variables but that has to be investigated in the

future. In general, regardless of the validity of results from Specimen 4, it is clear that the effect of initial matric suction is not significant on the *n* parameter.

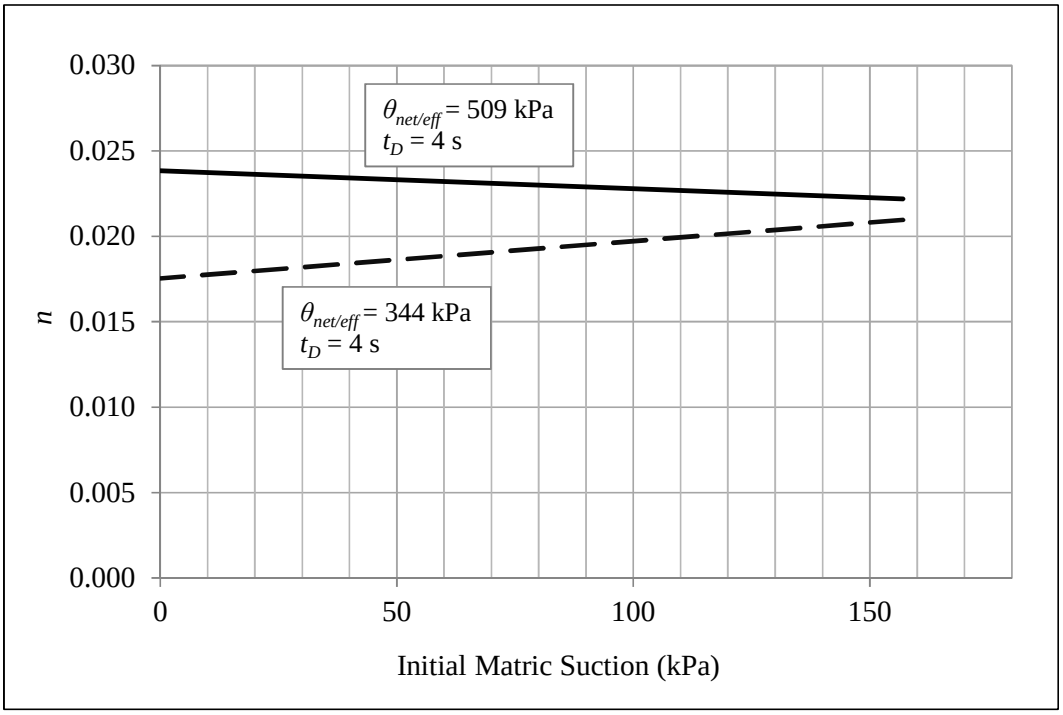

FIGURE 6-71 Influence of initial matric suction on the *n* parameter

Figure 6-72 shows the influence of the dwelling time on the *n* parameter. It is obvious that the effect of dwelling time is much more significant than bulk stress or initial matric suction. The higher the dwelling time, the lower n parameter and the longer the time required for the excess pore pressure of the specimen to stabilize. Again, a possible interaction is suggested since the two lines cross each other. However, it should be considered that Specimen 5 is involved in the analysis and the issues related to that specimen were already discussed earlier in the text.

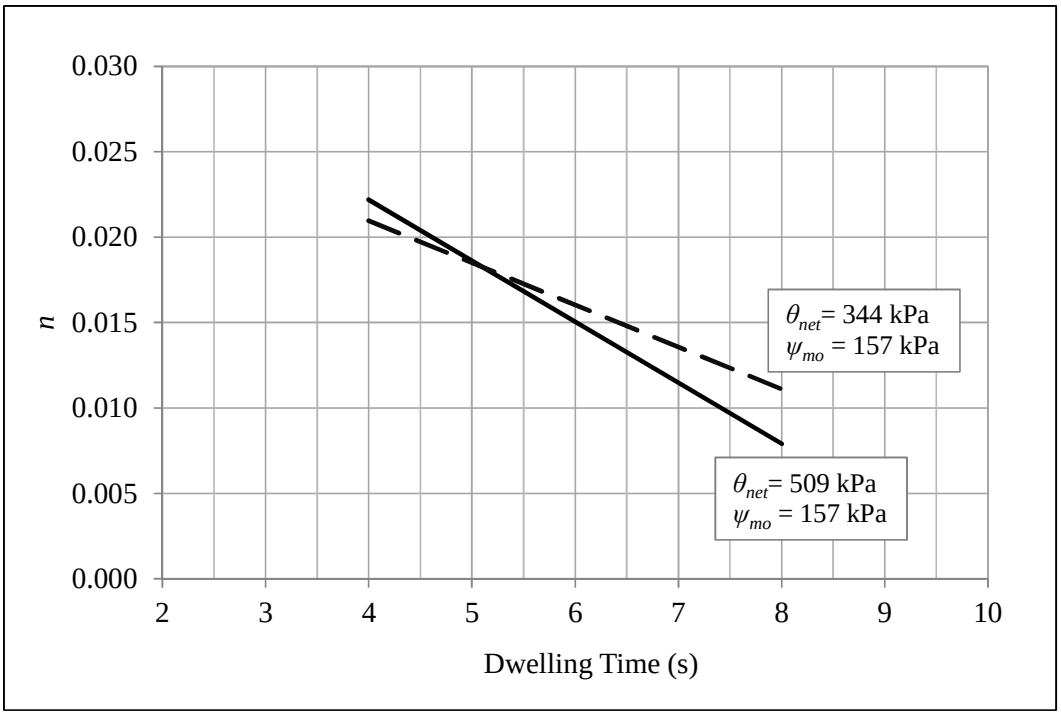

FIGURE 6-72 Influence of dwelling time on the *n* parameter

In order to confirm the observations commented after he analyzing the figures, a correlation matrix was developed again to statistically check the relation between the *n* parameter and the controlled variables. Table 6-14 shows the results of the correlation matrix.

TABLE 6-14 Correlation matrix for the *n* parameter

	n	t_D	θ	ψ_{mo}
n	1			
t_D	-0.934	1		
θ	0.123	0	1	
ψ_{mo}	-0.413	0.5	0	1

It is concluded from the results in Table 6-14 that the dominant variable affecting n is the dwelling time with a coefficient of correlation of –0.934. This

observation matches the conclusions obtained from the plots. Also, it appears that the initial matric suction has a medium to low correlation with the *n* parameter. The influence of bulk stress appears to be negligible. Therefore, the relationship of the n parameter and the controlled variables can be established as follows:

$$n = f(t_D, \psi_{mo}) \quad (6\text{-}44)$$

As a general conclusion, some valuable evidence of strong correlation between the regression constants required for the application of the proposed models, and the test conditions were obtained. Such observations are expected to be useful in future research efforts aimed at establishing predictive functions to express the parameters in terms of the soil properties.

The first impression indicates that the m parameter appears to be related to the capability of the material to dissipate pore pressures. Such capability can be related to the initial matric suction which is related at the same time to the coefficient of permeability. However, this plot is not enough to determine the relationship between m and the variables controlled in the testing program. The values of m obtained for every single specimen were plotted against the controlled variables.

Effect of Pore Water Pressure Buildup upon Resilient Modulus

In order to evaluate the effect of positive pore water pressure buildup, the excess pore water pressure predictions were utilized to estimate the resilient modulus for the soil in study at different number of repetitions along the pavement service life. As discussed in the literature review, the resilient modulus predictive model

proposed by Cary 2008 is the only one that takes into account the changes in pore water pressure occurring in the soil as result of dynamic load (*1*). Such equation is presented again as follows:

$$M_R = k_1 \cdot p_a \cdot \left(\frac{\theta_{net} - 3 \cdot \Delta u_{w-sat}}{p_a} \right)^{k_2} \cdot \left(\frac{\tau_{oct}}{p_a} + 1 \right)^{k_3} \cdot \left(\frac{\left(\psi_{m_0} - \Delta \psi_m \right)}{p_a} + 1 \right)^{k_4} \quad (6\text{-}45)$$

Where,

p_a = atmospheric pressure

k_1, k_2, k_3 *and* k_4 = regression constants

$\theta_{net} = \theta - 3u_a$, net bulk stress

Δu_{w-sat} = buildup of pore water pressure under saturated conditions, in this case $\Delta \psi_m = 0$

τ_{oct} = octahedral shear stress

ψ_{m_0} = initial matric suction

$\Delta \psi_m$ = relative change of matric suction with respect to the initial matric suction due to buildup of pore water pressure under unsaturated conditions, in this case $\Delta u_{w-sat} = 0$

The parameters k_1, k_2, k_3 *and* k_4 were obtained from resilient modulus testing in previous studies. Table 6-15 presents the regression parameters for the soil evaluated.

TABLE 6-15 Regression parameters for the resilient modulus predictive model

Parameter	Value
k_1	1480.3
k_2	0.420
k_3	-2.982
k_4	1.650

Using the predicted accumulated excess pore pressures obtained and the parameters presented in Table 6-15, the resilient modulus at different number of repetitions were estimated. Table 6-16 presents the results obtained for each specimen. It should be noted that both the predicted excess pore pressure and resilient modulus are presented in pounds per square inch, psi, as this is the unit commonly used in pavements design when dealing with such properties.

Also, the results were plotted and presented in Figure 6-73. It was observed that the effect of excess pore pressure build up upon the resilient response is more significant on unsaturated specimens than on saturated specimens. This reflects the higher pore water pressures developed by the unsaturated specimens. The most significant decrease in resilient modulus is observed for the unsaturated Specimen 2 which was subjected to a low bulk stress level and dwelling time of 4 seconds. For that specimen, the resilient modulus decreases from about 64,000 to about 40,500 psi after 1 million load repetitions as a result of the excess pore pressure development. On the other hand, for the same conditions, when subjected to high bulk stress, Specimens 1 experienced a decrease in resilient modulus for about 20,000 to 8,000 psi. The significant effect of the bulk stress level on the resilient response is evident.

TABLE 6-16 Estimated resilient modulus for the tested specimens

Specimen	1		2		3		4		5		6	
N	Δu_w	M_R	Δu_w	M_R	Δu_w	M_R	Δu_w	M_R	Δu_w	M_R	Δu_w	M_R
1	0.00	20,288	0.00	64,237	0.00	4,330	0.00	13,710	0.00	20,288	0.00	64,237
10	0.02	20,270	0.01	64,204	0.02	4,329	0.04	13,696	0.03	20,278	0.00	64,232
100	0.20	20,110	0.12	63,908	0.18	4,317	0.36	13,584	0.28	20,192	0.03	64,181
1,000	1.79	18,710	1.05	61,301	1.48	4,219	1.91	13,026	2.13	19,531	0.33	63,695
10,000	8.95	12,928	5.18	50,249	5.22	3,918	3.34	12,480	6.37	17,891	2.24	60,446
100,000	14.89	8,787	8.55	41,870	6.99	3,763	3.60	12,373	7.94	17,224	5.28	54,723
1,000,000	15.95	8,116	9.15	40,453	7.24	3,741	3.63	12,362	8.15	17,135	6.10	53,015

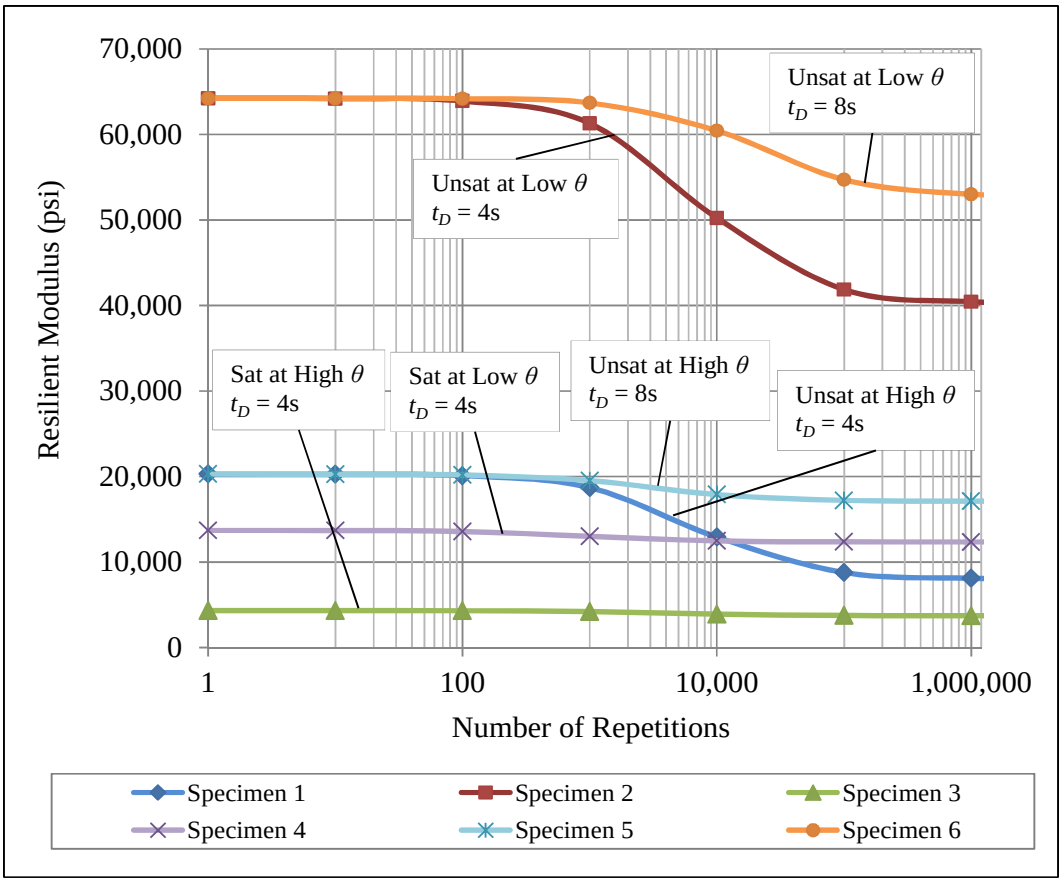

FIGURE 6-73 Influence of pore water pressure buildup on the resilient modulus

When looking at Specimens 4 and 5, it can be concluded that the change in resilient modulus due to pore water pressure buildup is not as significant as it is observed on unsaturated specimens. According to Table 6-16, the decrease at high bulk stress level is of about 600psi. At low bulk stress level, the change is about 1,400psi. This observation leads to conclude that the loss of resilient response in the saturated soil rather than being due to the development of pore water pressure under constant applied stress; it may mainly be a consequence of any significant increase in the external applied stress.

Also, when comparing Specimen 1 to 5 as well as Specimen 2 to 6, the effect of the dwelling time is evidenced. For longer dwelling times, the

degradation of the stiffness due to the development of excess pore water pressure will be lower than for shorter dwelling times. As a general conclusion, the effect of pore water pressure development appears to be more significant on unsaturated specimens rather than on saturated specimens.

Pore Water Pressure Buildup as Indicator of Changes in Stiffness

Saying a material has a high stiffness does not say anything about its elasticity. However it indicates something about its elastic modulus. Within the elastic range, a stiff material does not deform much when a stress is applied and therefore, such material has a high elastic modulus. The resilient modulus of a material is actually an estimate of its modulus of elasticity when subjected to transient loads.

When dealing with soils, not all the strain produced by application of stresses is pure elastic. There is always a plastic component in the strains that is not considered when estimating the resilient modulus. As seen in Figure 6-73, the initial resilient modulus for unsaturated soils appears to represent a stiff material. However, plastic deformations are observed to be more important in unsaturated soils at early stages of repeated loading.

Therefore, to consider that the unsaturated soils at earlier stages of loading are stiffer than the same material at advanced stages of loading based on the resilient response observed, might be a misleading conclusion.

The resilient response reflected by the estimates obtained using the model proposed by Cary suggest that resilient strains on unsaturated specimens progressively increase with number of repetitions up to about 100,000 load applications. After that, the resilient strains appear to stabilize resulting in a constant modulus. Hence, according to the predictions given by the model, changes in the initial resilient modulus with number of repetitions seem to be more significant under unsaturated conditions than under saturated conditions.

The pore water pressure buildup occurs as a consequence of deformations in the soil structure subjected to external stresses and indicates a progressive stiffening of the material. According to the predictions of the model, as the dynamic loading progresses, the plastic strains seem to be reduced until almost all deformation experienced by the material becomes pure elastic. Therefore, the proposed pore water pressure buildup models may indicate not only the maximum development of pore pressure but also the progressive change in the stiffness of the material until it reaches a steady state.

Such observations regarding a hypothetic progressive increase of resilient strain with number of repetitions until reaching a steady state seem to be in agreement with findings from some researchers but do not coincide with observations presented in other studies.

Seed et al. in 1962 studied the resilient characteristic of subgrade soils (*4*). He found that resilient strains progressively increased with number of load applications when the age of soil specimens at initial loading was 3 days or more. For specimens tested not later than 1 day after being prepared, the resilient strain

was observed to decrease reaching stable conditions. Apparently, the initial stiffness of the material seems to be highly influenced by thixotropic properties. However, as stated by Seed et al., since the number of stress repetitions in practice far exceeds the number of load applications in the laboratory, it is apparent that resilient response determined under relatively small number of stress repetitions may represent a misleading picture of the actual resilient characteristics of a subgrade soil (4).

Thixotropy seems to explain the estimates obtained when using the model proposed by Cary as it was developed using experimental results from pre-conditioned specimens (*1*). Such pre-conditioning stages in the laboratory usually last more than 3 days. Besides, in the field, roads are not supposed to be subjected to traffic loading right after the subgrade is compacted. Enough time is available between subgrade compaction and the beginning of traffic loading for the soil to develop additional stiffness due to thixotropy effects. In such case, the predictions obtained using the model proposed by Cary may reflect field conditions (*1*).

In 2006, El-Badawy measured plastic and resilient deformations on different subgrade materials commonly encountered in the state of Arizona (*43*). Different from what is commonly assumed in pavement analysis, El-Badawy results suggest that the resilient strain is not necessarily constant with an increase in the number of load repetitions. Especially at moisture conditions dry of optimum and under intermediate to high external applied stresses, El-Badawy found the resilient strain to increase with number of load applications for 2 out of the 4 subgrades tested without reaching an apparent steady condition. For other

subgrade soils, the resilient strain was observed to be fairly constant or to reach steady state after a dramatic decrease. Such results were observed within a range of 10,000 load applications which seem to be low compared to the number of repetitions expected in the field. Even when defined patterns of changes in resilient strain with number of load applications were not identified, it was shown by El-Badawy that assuming a constant resilient strain after several hundred of repetitions may not be always a correct approach for pavement analysis.

Different from Seed et al. and El-Badawy, Uzan in 1998 suggested that at relatively low stress levels, the modulus and hence the resilient strain is fairly constant during repetitive testing (*4, 43, 44*). Such conclusion was formulated from testing results of a very plastic clay subjected to about 100,000 load applications. Even when Uzan suggested a constant resilient response for the material tested in his study, he also recommended to apply a larger number of load repetitions, of the order of 50,000 or more, in order to better characterize the total deformation of the material subjected to traffic loading.

The resilient modulus testing protocol NCHRP 1-28A calls for 1,000 repetitions to condition the specimen by eliminating the initial plastic deformations (*37*). After conditioning, the repeated loading stage is conducted for a maximum of 2,000 repetitions for subgrade materials. As result, a resilient modulus is obtained at early stages of repeated loading. As indicated by the red line in Figure 6-74, the Mechanistic-Empirical Pavement Design Guide adjusts the initial resilient modulus simulating variations due to environmental changes along the time (*7*). Such initial modulus may not be representative of the actual

stiffness for unsaturated soils at advances stages of repeated loading as explained by the yellow and light blue lines in Figure 6-73.

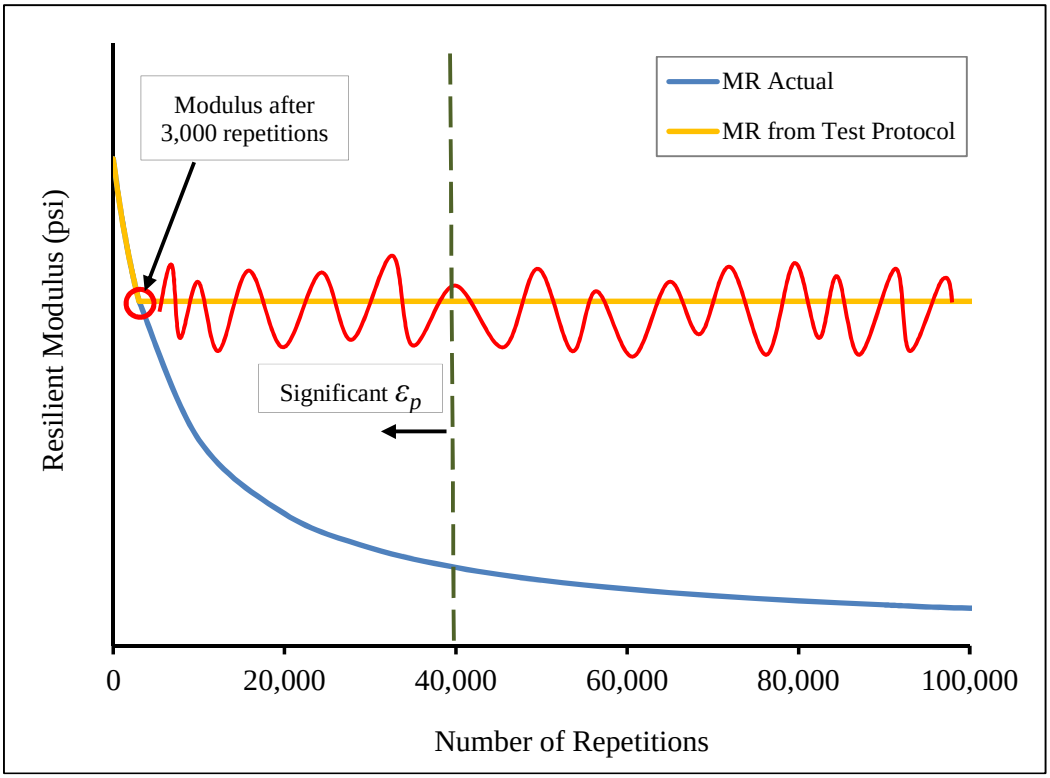

FIGURE 6-74 Modulus obtained from testing protocol versus actual modulus

Results from this investigation suggest that a much bigger number of repetitions might be needed for specimen conditioning in order to obtain more realistic modulus values as the resilient strain at early stages of loading seems not to be representative of the actual soil resilience. Such conclusion may also find support in the results presented by Seed et al. and El-Badawy as previously discussed (*4*, *43*).

Given that long specimen conditioning stages may result impractical, the models proposed in this study become a good alternative to estimate resilient modulus values at advanced stages of loading. By integrating such models into

the resilient modulus predictive techniques, more realistic design values can be obtained under both saturated and unsaturated conditions.

As a general conclusion it is evident that further research on resilient strain changes with number of load repetitions is needed especially at advanced stages of loading in order to determine the suitability of using resilient modulus values measured following the currently available testing protocols.

General Discussions of Results and Findings

The present study revealed important findings and opened new possibilities for future research. Probably this is the first time a laboratory testing program is directed to evaluate the pore pressure response of a subgrade material subjected to conditions that simulate vehicular traffic. The successful measurement of excess pore water pressure for up to 6 specimens under unsaturated and saturated conditions was a difficult goal to achieve due to the complications involved related to testing equipment and time demanding nature of the test.

The firs notable findings were observed when measuring the excess pore pressure developed in the specimens subjected to dynamic load. When performing dynamic load test in the laboratory it would be expected to observe that the development of excess pore pressure for saturated specimens is higher than for unsaturated specimens. The reasoning may indicate that pore pressure should develop significantly in soil structures with pores filled with water. On the other hand it might be believed that since the voids present in unsaturated specimens are not only filled with water but also with important volumes of air, the pore

pressure response should result less significant than the response in saturated specimens.

Contrary to the common beliefs, it was observed from the laboratory test results, that unsaturated specimens tend to develop higher excess pore pressure levels than saturated specimens. Actually, some recent research efforts found in the literature arrived to similar conclusion as discussed in Chapter 2 (*34 and 35*). Even the author observed the same behavior when conducting resilient modulus test on a granular base material. Therefore, the results of this study validate the observations presented in previous research efforts.

In earlier sections of this document, Figure 6-32 which summarizes the testing results was presented. The same figure is conveniently presented again for the purpose of elaboration on this discussion. Figure 6-75 presents the predicted curves obtained as result of fitting the laboratory measured data to Equation 6-13. Such equation was found be the best among several evaluated, for representing the laboratory measured data, by means of a comprehensive statistical analysis using a powerful software package.

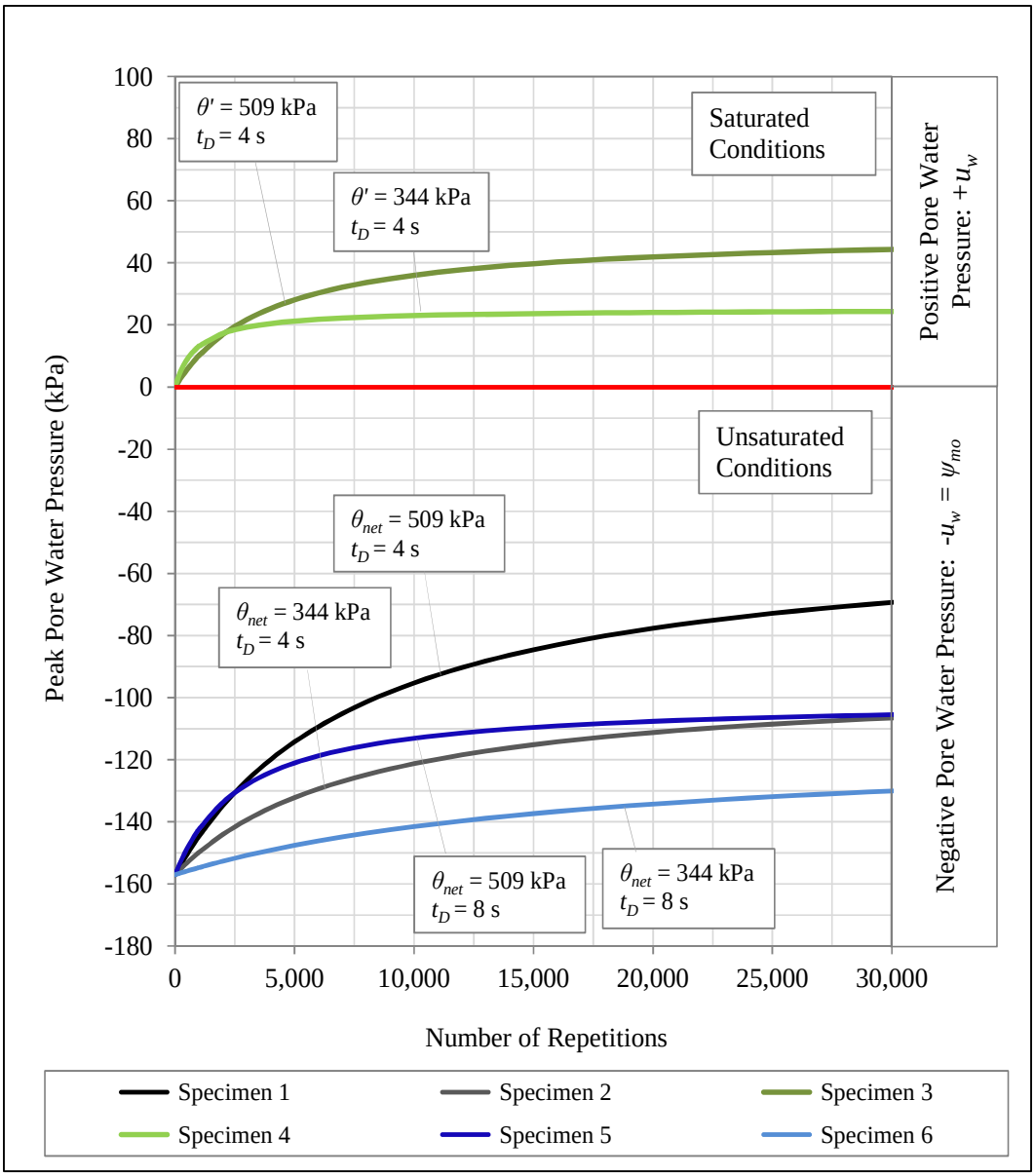

FIGURE 6-75 Results of regression analysis for the global peak pressure curves

It should be noted that the curves presented in the figure, correspond to the peak excess pore pressure curves. As can be observed, the saturated specimens started developing positive pore water pressure from a reference initial matric suction of 0kPa. The unsaturated specimens were conditioned to an initial matric

suction of 157kPa. Therefore the reference starting origin for those specimens in the figure is equal to the negative value of the initial matric suction.

It is observed that the saturated Specimens 3 and 4 are expected to develop pressures of roughly 45 and 25kPa at maximum as predicted using Equation 6-13. The unsaturated Specimens 1 and 2 tested at the same conditions except for the initial matric suction are expected to develop pressures of about 110 and 65kPa respectively. Such maximums are not appreciated in the plot because of the scale utilized in the x-axis. However the results can be corroborated in Table 6-4. The difference in developed excess pore pressure between saturated and unsaturated specimens is evident and reflects a significant effect of the initial matric suction.

The possible explanation for this phenomenon as suggested in previous research studies is related to two causes. One possible reason for the unsaturated specimens showing higher excess pore pressure than saturated specimen is the presence of pressurized air within the pores that exerts pressure on the pore water. Another possible reason can be related to the reduction of the void ratio experienced by the specimens during the conditioning stage. The combined effect of the two mentioned causes is to the judgment of the author the explanation of such phenomenon. High levels of air pressure within the pores inducing pressure on the pore water inside reduced voids with low hydraulic conductivities appears to be a reasonable physical explanation. However further research should be directed to corroborate if similar responses are observed in the field.

Another significant finding is the excess pore pressure steady state achieved by the specimens for the conditions applied for testing. Even when for

some specimens the tests were terminated before approaching to a state of excess pressure stabilization, most of them showed clear trends towards eventual achievement of constant maximum pressures. Besides, all data showed good to excellent quality of fit to Equation 6-13 which captures the eventual steady state observed.

Figure 6-75 shows at least Specimen 4 reaching the steady state of pressure development. Figure 6-75 was intended to show the progressive development of excess pore water pressure at early stages in the test. Due to the scale utilized in the x axis, it is not possible to observe the achievement of excess pore pressure steady state on the other specimens. Therefore, the predicted curves are displayed in Figure 6-76 using a larger scale in the x axis in such a way the final steady state of maximum excess pressure can be appreciated for all specimens.

It should also be noted that saturated specimens reached the steady state at a lower number of repetitions than unsaturated specimens. This finding is in agreement with the observations presented by Yang et. al in 2008 (*35*). He suggested that specimens tested at low initial matric suctions reach a steady state faster than those tested at higher initial matric suctions. Yang et. al did not observed the unsaturated specimens reaching a steady state probably because the number of repetitions applied during the test was only about 50,000. However, in this study unsaturated specimens were observed during the test to reach steady conditions. Also, when modeling the data, the results suggested that all specimens

subjected to the stress levels contemplated in the laboratory testing program, would eventually reach an excess pore pressure steady state.

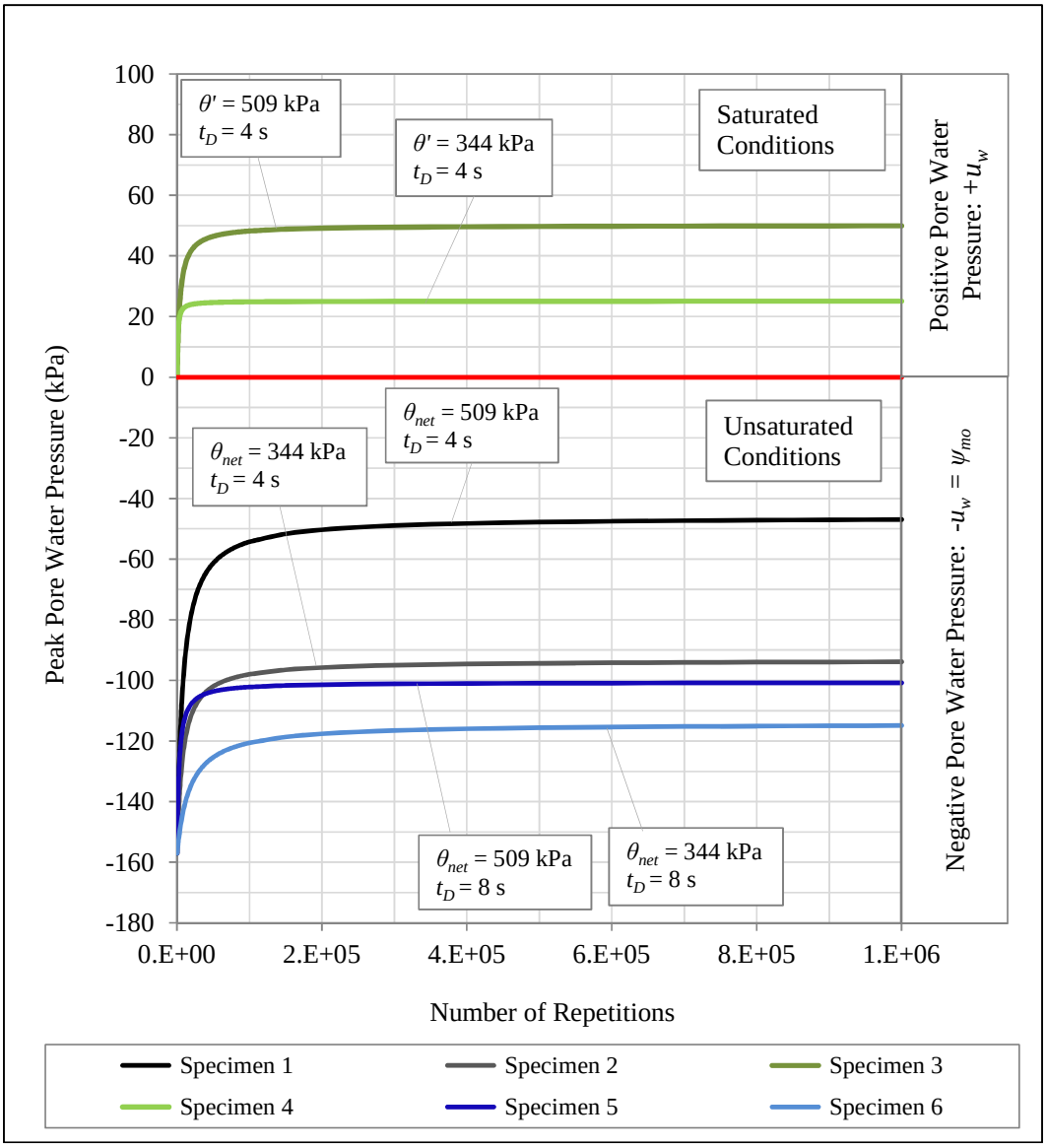

FIGURE 6-76 Results of regression analysis for the global peak pressure curves extrapolated to advanced stages of loading

The next findings reflected by the laboratory testing is the dependency of the results on the external stress level applied or bulk stress as well as the dwelling time. As expected with anticipation, it was observed and

determined that the maximum excess pore pressure to be reached by the soil is dependent upon the level of stress imparted. The higher the bulk stress, the higher the accumulated excess pore water pressure.

Apparently, the bulk stresses imparted were below critical levels that may lead to failure. This explains why all the specimens achieved the steady state at some point rather than maintaining a sustained development towards critical maximum excess pore pressure levels. However; an important question, that can be matter of future research, arises about what kind of stress level would lead to failure of the material due to accumulation of excess pore pressure.

As previously mentioned, the initial matric suction, which is directly related to the initial degree of saturation of the specimen, is determinant for the development of excess pressures. At degrees of saturation lower than optimum conditions, the increase of excess pore pressure appears to be more significant but probably not sufficient to lead the soil to failure due to development of excess pore pressure. Nonetheless, it is likely that at degrees of saturation above optimum conditions and getting close to saturation, the development of excess pore pressure may take down the initial matric suction and, cross the frontier towards saturated conditions. From then on, the possibility of sustained development of excess pore pressures towards failure condition will depend on the external dynamic stress level imparted.

The next figures, try to depict the stress paths followed by the specimens subjected to dynamic load in the laboratory testing program

conducted for this study. Figure 6-77 shows the stress path for the constant water content test conducted on the unsaturated specimens.

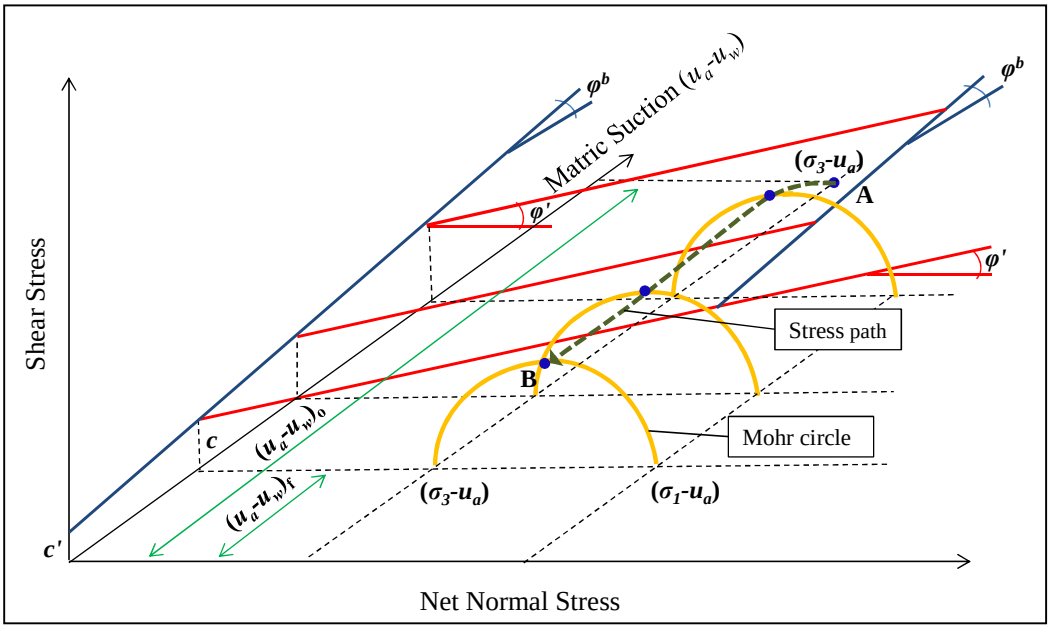

FIGURE 6-77 Constant water content test on unsaturated specimens

The stress path shown in Figure 6-77 applies to the unsaturated specimens tested in this study that reached steady states without reaching saturation. In other words, the schematic shown above applies to Specimens 1, 2, 5 and 6.

The characteristic of the dynamic load test performed is the control of constant stress levels. The air phase during the constant water content test performed is allowed to drain and therefore, no air pressure is developed. The principal stresses remained constant during the test. Since the failure envelope is always higher than the shear stresses applied, the only ways for the specimens to reach failure are by either further increase of the principal stresses or by development of excess pore pressure bringing the specimen to saturated domains

followed by the decrease in the effective stresses. Evidently neither one nor the other took place during testing.

During the tests the principal stresses were kept constant and as the suction decreased due to the development of excess pore pressure, the failure envelope shifted downwards. Therefore, the stress path started at point A with the specimens subjected to initial conditions. Then, with application of the dynamic load, the stress path describe by the dashed green line was followed until point B which corresponding to the end of the dynamic load test. Point B represents the point at which excess pore pressure steady state conditions were reached. As observed, at the stress levels imparted for this study the specimen is never exposed to failure risk by plastic flow.

For saturated specimens, failure was neither reached. Figure 6-78 shows the stress path followed during the test. As discussed in Chapter 4, since there is no need to apply the axis translation technique, undrained test was conducted on saturated Specimens 3 and 4.

As observed in the test, none of the two saturated specimens reached failure. The tests started after consolidation at point A with a certain applied effective confining pressure. Then the dynamic deviator stress is applied and the next point reached I the stress path is point B. At the end of the test at point C, the excess pore pressure developed made the effective stresses to decrease but not enough to bring the specimen to failure condition.

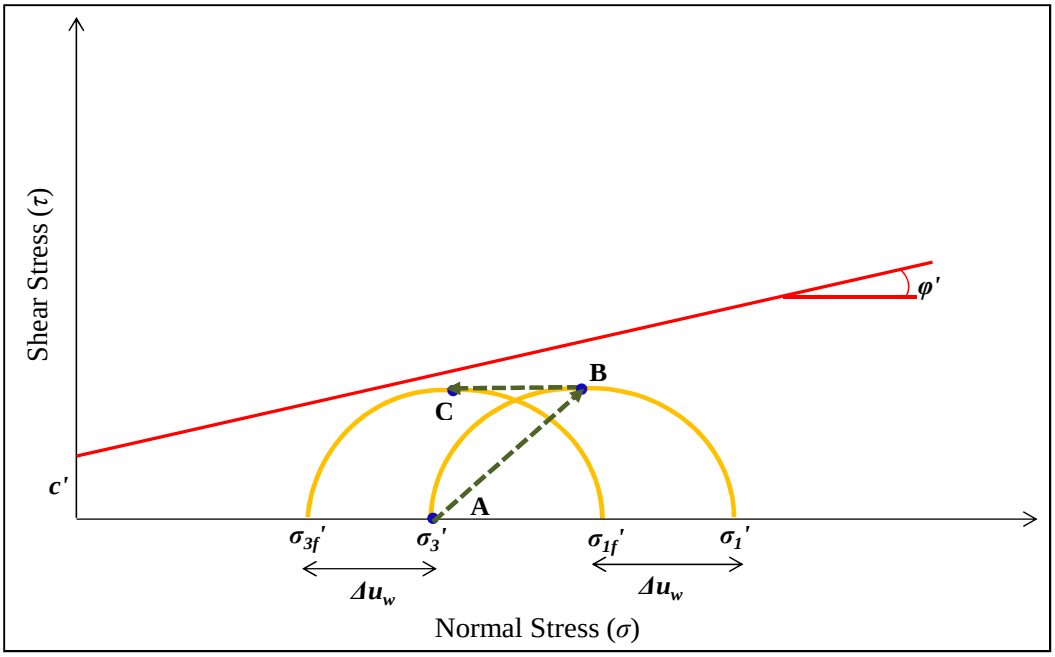

FIGURE 6-78 Undrained test on saturated specimens

The results observed in this study show the importance of refining the methodology followed when applying the unsaturated soils principles for the design of pavements. It is recognized that following effective stress approaches for saturated soils in the design of pavements may result over conservative. However, the use of the unsaturated soil mechanics may also result counterproductive if the effects of dynamic load upon the response of the materials are not considered. A clear example comes from observation of the test results which suggest that underestimating the effect of excess pore pressures developed under dynamic loading upon the initial stiffness of the material could lead to assume wrong modulus for design. By taking into account the effects of dynamic excess pore pressure development, the actual long term stiffness of the unbound materials could be accurately estimated. Therefore, within the non-

destructive spectrum of the soil response, the models developed in this study can contribute to enhance the predictions of pavement performance.

However, the conditions reproduced in the laboratory and shown in the previous figures are not the only ones likely to occur in the field. Different stress states acting on the soil may result critical and lead to failure by plastic flow. Figure 6-79 shows an example of how unfavorable conditions can affect the response of the soil subjected to traffic loading.

In Figure 6-79, the responses of the soil to different conditions are hypothesized. In the lower part of the figure, the three yellow lines represent the response of the soil to three different bulk stress levels for an unsaturated specimen at relatively high initial matric suction. Such response reproduced in the figure is similar what it was observed in the test results for unsaturated specimens. In that case, the soil is not at risk of reaching failure conditions even though the stiffness of the material undergoes degradation.

A second case is represented in the upper part of the figure, where the blue curves correspond to saturated specimens subjected to three different stress levels and with zero initial matric suction. Obviously the effective bulk stress 1 correspond to the lowest level of stress, effective bulk stress 2 correspond to a medium level of stress and effective bulk stress 3 correspond to a high and critical level of stress. The two curves representing soils subjected to effective bulk stresses 1 and 2 can be representative of the responses observed in the lab for the specimens tested in this study. As observed, both curves indicate that failure conditions were not reached but obviously the stiffness of the soil might

experience degradation. However, the third curve subjected to the highest level of stress, experiences plastic flow as the accumulated excess pore pressure reached the critical stress excess pore pressure established by the black dashed line. Such response was not observed in the laboratory but can easily occur if critical levels of external stresses are imparted to the soil.

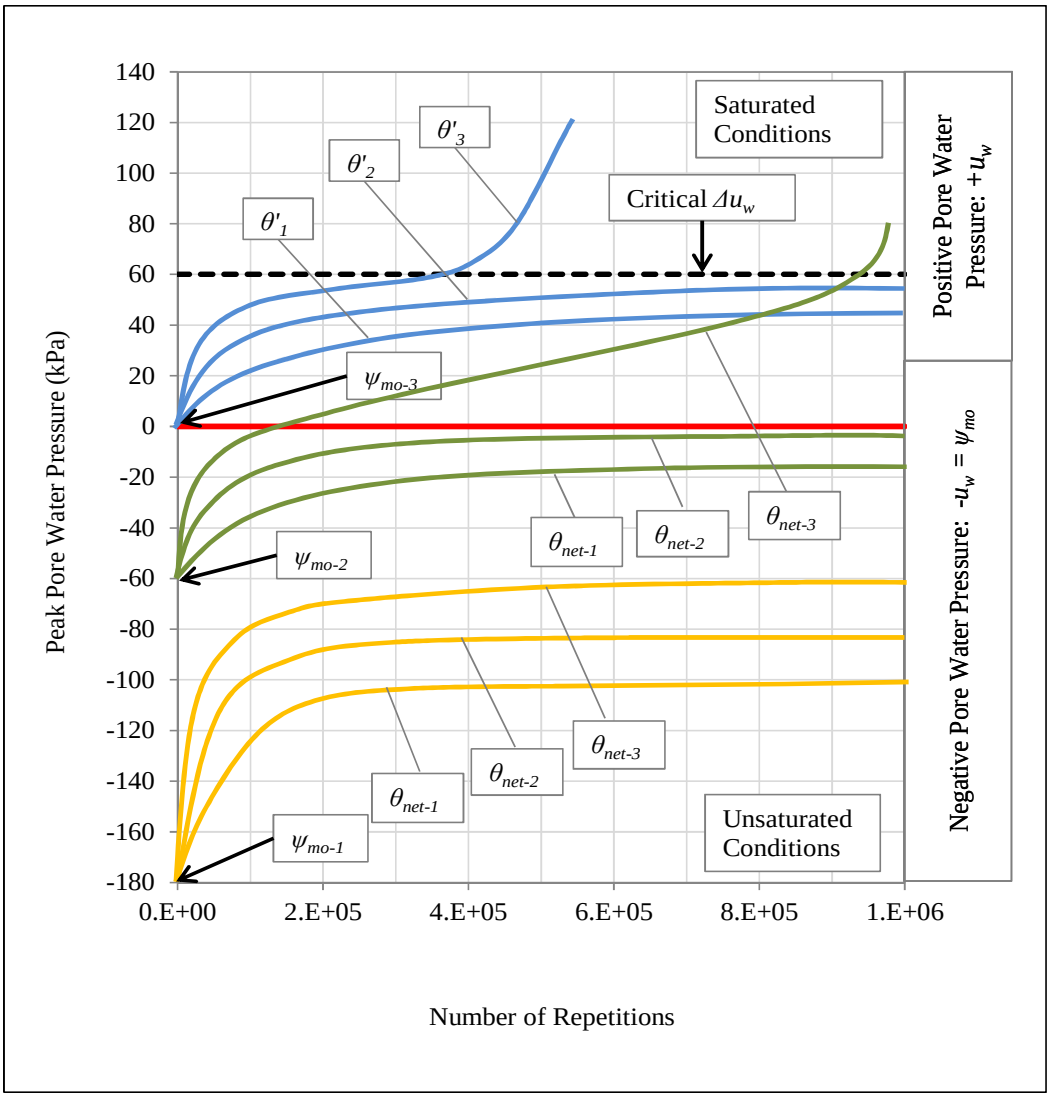

FIGURE 6-79 Effect of critical conditions on the soil response

A third case is hypothesized for the green curves. The two lower green curves correspond to soils subjected to net bulk stresses 1 and 2. Such stresses are

not critical and therefore the excess pore pressure reaches a steady state after certain number of load repetitions. Again, the response of those materials corresponds to a non-destructive range where no significant plastic deformations occur even when the material experiences stiffness degradation. However the third curve hypothesizes the case where the specimen experiences significant development of excess pore pressure that brings it from unsaturated condition towards saturated domains. After that, depending on whether the applied stress level is critical, further dynamic loading may direct the specimen towards the line of critical excess pore pressure and hence fails due to plastic flow.

Figure 6-80 shows the stress path of the hypothesized case represented by the green curve for net bulk stress 3. The mechanism of a hypothetical failure is described by the stress path starting at point A of Figure 6-80a. Point A represents the state of the specimen after completion of the conditioning stage where it is subjected to a constant net confining stress.

Then, the stress path goes towards point B under constant applied stresses. At point B, the excess pore pressure developed by the action of dynamic loading equals the initial matric suction. Plastic deformations were supposed to take place in such a way the air inside the soil pores where squeezed out and as consequence of densification the soil becomes saturated. At point B the failure envelope shifted downwards as a result of the suction reduction.

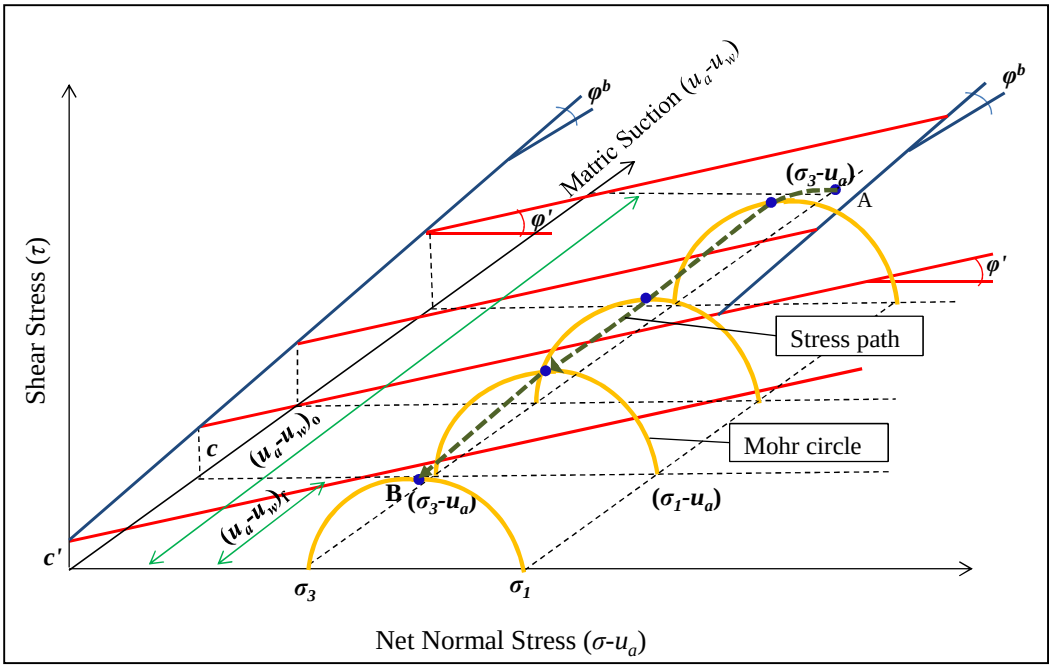

a) From unsaturated to saturated domain

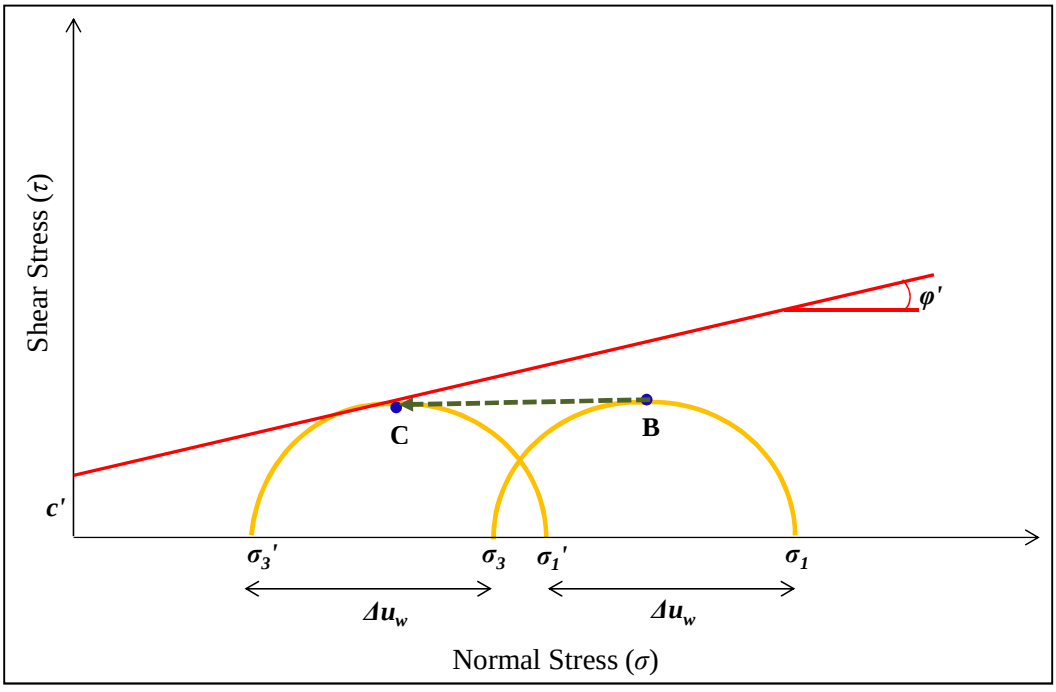

b) Towards failure envelope

FIGURE 6-80 Stress path for an unsaturated soil towards failure

Figure 6-80b shows the effective stress path from point B to point C. Point B was reached after certain number of dynamic load cycles. Further loading forces the stress path towards failure conditions as a consequence of further development of excess pore water pressure. As observed, the pore pressure increment affects the principal stresses making the Mohr circle shift to the left and reaching failure. Even when such behavior was not observed in the laboratory, it is likely to occur under applied critical conditions.

The example shown in the previous figure is intended to depict how important is the excess pore pressure development under traffic load as it might lead the soil to reach failure conditions. It also emphasizes the need to properly define the influence of the applied external stresses and the initial matric suction, as well as their interaction over a wider range for both variables.

It was demonstrated that the characterization of the excess pore pressure development can be useful not only to enhance pavement design procedures but also to understand and prevent potential failure due to significant plastic deformations.

If the critical levels of excess pore pressure for granular bases and subgrade materials are known, the models proposed in this study would be useful to delimitate the boundaries for safe stress states in such a way potential failure due to excessive development of pore water pressure can be prevented.

The results obtained also rises questions regarding the convenience of compacting unbound materials at optimum conditions. It could be possible that

compacting subgrades at conditions below optimum results to be a better practice for dealing with potential harm due to development of excess pore pressures.

As part of the results obtained from this study, two models for prediction of the accumulated excess pore pressure resulting from traffic load were proposed. Such models have the ability to capture the effect of the bulk stress applied, the initial matric suction and the dwelling time through the use of regression parameters. Due to the complexity and time demanding nature of the test, a limited number of tests were available for analysis. Therefore, it was not possible to develop relationships between the test conditions and the soil properties. Nonetheless, the degree of influence that the controlled variables have upon the predictions was established from the analysis of data.

The models are capable of predicting not only the accumulated residual pore pressures and the accumulated peak responses but also are capable of estimating the excess pore pressure at any time within the load pulse with reasonable accuracy. The models simulate the response of the soil during the entire duration for any particular cycle. Reasonable uncertainty was observed in the predictions as the inherent marginal error present at each cycle accumulates with the number of repetitions. However, the model capability for detailed simulation would be a tremendous help not only to understand how the test conditions influence the pore pressure response but also to study the influence of properties inherent of different materials like plasticity index or hydraulic conductivity.

Another important aspect of the models proposed is that the particular characteristics of traffic loading conditions were considered for their development. Therefore, with further enhancement of these models and since the effect of the load configuration given by loading and dwelling times are contemplated, it will be possible to predict the excess pore pressure development at any time during the pavement service life considering the influence of factors like vehicle speed and traffic volume observed in particular highways through the use of the *ADT*.

The implementation of this model also results helpful to overcome testing limitations. It is widely known that testing for unsaturated soils is a challenging task. Even measurement of positive pore pressures are not actually contemplated within the pavement design practices. Therefore the introduction of unsaturated soil mechanic principles into the design of pavements increases even more the level of complexity in the analysis relative to common practices. One of the primary motivations for this study was to enhance the resilient modulus predictive techniques. Replacing the need of measuring such difficult response as pore water pressured by a convenient predictive model addresses the testing limitations issue. The model proposed contributes to overcome such difficulties that may lead the pavement designers to avoid the application of unsaturated soil mechanics principles.

Also, as it was shown in previous sections, there is an evident effect of the pore water pressure buildup upon the resilient response of the soil. Such effect is more significant under unsaturated conditions as the excess pore pressure appear

to degrade the stiffness of the material under repeated load. The resilient moduli obtained by following the currently available testing protocol appear to be a misleading indicator of the soil stiffness under unsaturated conditions. A good and realistic indicator of the changes in soil stiffness is the pore water pressure buildup. Therefore, the implementation of the proposed pore water pressure buildup models in the resilient modulus predictive techniques will contribute to predict and make reasonable use of the estimated resilient modulus values obtained either for unsaturated or saturated materials.

With the contribution of future research directed towards both the expansion of the testing results database and the enhancement of the models proposed in this study, the predictive techniques developed may become a powerful tool to assess the pore pressure response of unbound materials for pavement engineering.

CHAPTER 7. SUMMARY AND CONCLUSSIONS

Study Objectives

The primary objectives of this study were aimed at answering the following questions:

1) What is the relative importance of matric suction and externally applied loads on the buildup of pore water pressure in plastic materials subjected to dynamic loading?

2) How important is the dwelling time (time between applied loads) in the buildup/dissipation of pore water pressures of saturated and unsaturated soils subjected to dynamic loading? Can it be related to vehicle speed or daily traffic?

3) Is it possible to find a model capable of predicting the buildup/dissipation of pore water pressures that is suitable to saturated and unsaturated soil conditions?

4) How important is the buildup of pore water pressure on the resilient modulus when the material is saturated or unsaturated?

5) Does the buildup of pore water pressure indicate changes in the stiffness of the material?

In order to answer the posted questions, the following objectives were pursued:

- Obtain measurements of pore water pressure buildup under repeated load for a low plasticity soil under both saturated and unsaturated conditions (two levels of suction) and at different levels of deviator stress and dwelling times.

- Find suitable mathematical models for the prediction of dynamic pore water pressure buildup considering the variables controlled in the laboratory testing program.
- Assess the importance of the pore water pressure buildup/dissipation on the resilient modulus of unsaturated soils subjected to dynamic loading conditions.
- Assess the importance of the pore water pressure buildup as indicator of changes in the stiffness of the material.

These objectives were accomplished as follows:

- Measurements of development of excess pore pressure were obtained for a clayey sand with plasticity index of 7 at high and low levels of bulk stress, initial matric suction and dwelling time. The test conditions comprised both saturated and unsaturated conditions. The results were used to generate the proposed models for prediction of excess pore pressure developed on soils subjected to traffic load.
- The results from the laboratory testing program were used to develop models for the prediction of excess pore water pressure under traffic loading. Two general models were proposed: the first one applies to the loading phase of the cyclic load and the second applies to the unloading phase. The models are primarily function of time or number of repetitions and the effects of the testing conditions such bulk stress, initial matric suction and dwelling time are reflected in the regression coefficients obtained.

- The effect of pore water pressure buildup upon the stiffness of the material was evaluated by using the predictions to obtain the variation in resilient modulus with time or number of load repetitions. This was accomplished by using a model developed by the same author capable of capturing the effect of the dynamic variation of pore water pressure upon the resilient response of the material (*1*). The results indicated that the influence of pore water pressure is important even under unsaturated soil conditions.

The models proposed showed to be an important refinement and a step forward in the implementation of unsaturated soil mechanics principles into practice. Also the potential use of the models as an alternative way to overcome testing limitations adds merit to the results of the work.

Conclusions

The general achievements presented above indicate that the main goals established for this study were successfully attained. In the next section, conclusions obtained from key sections of this study are detailed.

Literature Review

After searching the published literature it was concluded that there were no antecedents in the development of models for prediction of excess pore water pressure developed in saturated or unsaturated soil subjected to traffic loading.

Most researchers directed their research efforts towards the evaluation of the effect that testing conditions have upon the development of excess pore pressure from a general point of view. Only Ansal an Erken proposed a model for

prediction of pore pressure development as function of the stresses acting on the soil (*25*).

Results observed by Minh Thu et al. and Yang et al. are in agreement with some of the findings of this study (*34* and *35*). They suggest that the development of pore water pressure is more significant for soils tested under unsaturated conditions than those tested under saturated conditions. The results obtained in this research effort confirm the findings presented by the mentioned authors for the range of test conditions used.

Among the parameters affecting the development of excess pore water pressure that were not evaluated in this study but were pointed out by authors in the literature are: the effect of varying the confinement, effects of loading time, effect of soil type and also the disturbance of the material as reflected by the over consolidation ratio (*OCR*). Such parameters deserve attention in future efforts aimed at the enhancement of the proposed models.

Dynamic Loading Testing

Improvements to the triaxial testing systems were implemented for the purposes of this study. The two advanced triaxial testing devices used were provided with new bottom pedestals especially designed for unsaturated soil testing conditions.

The manufacturing of the bottom pedestals was in response to the difficulties encountered when trying to condition specimens of greater dimensions. As observed during a pilot testing performed at the beginning of the study, the time for saturation and consolidation of the 4-inch diameter specimens

was unreasonably long. It was then decided to reduce the size of the specimens in order to minimize the required times to complete the tests.

Even though the dimensions of the specimens utilized were 2.8 inches in diameter and 5.6 inches height, the time to achieve saturation was found to be about one month per specimen. Consolidation of the saturated specimens was achieved after two or three days. The equilibration of unsaturated specimens to the initial matric suction was achieved between 7 and 10 days per specimen. Furthermore, the duration of the dynamic loading stage of the test was between 5 and 10 days. Therefore, the time for full completion of the test was between 40 to 45 days for saturated specimens and between 15 to 20 days for unsaturated specimens. Needless to say, the dynamic load testing performed in this study was highly time demanding.

It is also concluded that in order to successfully run the kind of test performed in this study, it is fundamental to use triaxial systems with software and hardware capabilities to handle large amount of data. Serious difficulties were experienced with the triaxial system controllers in this study which limited the number of specimens tested.

Dynamic Loading Laboratory Testing Results

As a result of the present study, important findings were presented. Probably this is the first time a laboratory testing program is directed to evaluate the pore pressure response of a subgrade material subjected to conditions that simulate vehicular traffic.

The successful measurement of excess pore water pressure for specimens under unsaturated and saturated conditions was achieved. When performing dynamic load test in the laboratory it is expected to observe that the development of excess pore pressure for saturated specimens is higher than for unsaturated specimens. Contrary to the common beliefs, it was found that unsaturated specimens tend to develop higher excess pore pressure levels than saturated specimens. This indicates that the influence of the initial matric suction is fundamental when attempting to predict the development of excess pore water pressure. Within the range considered for this study it was found that the higher the initial matric suction, the higher the accumulated excess pore water pressure.

These findings are in agreement with results from some recent research efforts encountered in the literature (*34, 35*). High levels of air pressure within the pores inducing pressure on the pore water inside reduced voids with low hydraulic conductivities appears to be a reasonable physical explanation. However further research should be directed to corroborate if similar responses are observed in the field.

As suggested by Minh Thu et al., beyond certain maximum value, further increase of the initial matric suction might result in a reversed effect. In other words, the accumulated excess pore water pressure might decrease as the soil gets drier beyond such critical value of initial matric suction (*34*). This seems reasonable as when the soil gets dry enough the water phase becomes discontinuous which might prevent the development of excess pore water pressure. Such phenomenon needs to be investigated in future studies.

Another significant conclusion based on the findings is the fact that the excess pore pressure was observed to achieve steady state conditions even after a very large number of repetitions. Even the specimens that were terminated before approaching a state of excess pressure stabilization showed clear trends towards eventual achievement of constant maximum pressures.

It was concluded from the results that saturated specimens reached the steady state at a lower number of repetitions than unsaturated specimens. This finding is in agreement with the observations presented by Yang et. al in 2008 (*35*). He suggested that specimens tested at low initial matric suctions reach a steady state faster than those tested at higher initial matric suctions.

An important finding reflected by the laboratory testing is the dependency of the results on the external stress level applied as well as the dwelling time. It was observed and determined that the maximum excess pore pressure to be reached by the soil is dependent upon the level of stress imparted. It was found that the magnitude of accumulated excess pore water pressure increases along with the bulk stress level.

The bulk stresses imparted were below critical levels that may lead to failure. This is perhaps the reason why all the specimens achieved steady state conditions and never experienced failure due to plastic flow.

Based on the commented observations, a question arises about what kind of stress level would lead to failure of the material due to accumulation of excess pore pressure. It is concluded that further investigation to answer that question is needed.

At degrees of saturation below optimum conditions, the pore water pressure buildup is more significant but probably not sufficient to lead the soil to failure. It is hypothesized that at degrees of saturation above optimum conditions, the development of excess pore pressure may overcome the initial matric suction and may bring the soil to saturated conditions. This could increase the possibilities for the development of excess pore pressures under saturated conditions. The occurrence of such phenomenon is of course dependant on the external dynamic stress level imparted. However, it is important to note that failure condition was not achieved due to excess pore water pressure buildup even under saturated soil conditions for the high stress level used in this study and for a high number of repetitions.

The influence of the dwelling time upon the development of excess pore water pressure was also revealed by the test results. For higher dwelling times, the accumulation of excess pore water pressure seems to be decelerated. Also, at high level of dwelling time the maximum pore water pressures to be reached at advanced stages of repeated loading showed to be lower than the maximum values expected for low level of dwelling time.

Proposed Predictive Model

As a result of the present study, models were proposed to predict the excess pore pressure developed under traffic loading. The models add the pressure developed within the cycle under analysis to the excess pore water pressure previously accumulated. The model proposed to predict the accumulated excess pore pressure at any time during the loading phase reads as follows:

$$\Delta u_{wL} = \sum_{i=2}^{N-1}\left[\left(\frac{t_p}{a_p t_p + b_p}\right) - \left(\frac{t_2}{a_2 t_2 + b_2}\right)\right]\left[\frac{4{t_L}^{-\lambda-1}\beta^{\lambda+1}\lambda^2}{\left(\lambda - 1 + \lambda {t_L}^{-\lambda}\beta^{\lambda} + {t_L}^{-\lambda}\beta^{\lambda}\right)^2}\right] exp\left(-t_D.\left(m + n.Ln(i-1)^2\right)\right)$$

$$+\left[\left(\frac{{t_p}'}{a_p {t_p}' + b_p}\right) - \left(\frac{{t_2}'}{a_2 {t_2}' + b_2}\right)\right]\left[\frac{4t^{-\lambda'-1}\beta^{\lambda'+1}{\lambda'}^2}{\left(\lambda' - 1 + \lambda' t^{-\lambda'}\beta^{\lambda'} + t^{-\lambda'}\beta^{\lambda'}\right)^2}\right] \quad (7\text{-}1)$$

Where,

t_L = loading time in seconds

t_D = dwelling time in seconds

$t_p = (i-2)(t_L + t_D) + \beta$

$t_2 = (i-3)(t_L + t_D) + (t_L + t_D)$

${t_p}' = (i-1)(t_L + t_D) + \beta$

${t_2}' = (i-2)(t_L + t_D) + (t_L + t_D)$

t = time elapsed from the beginning of the i^{th} cycle; valid for 0s $\leq t \leq t_L$

β = constant that defines the time at maximum pore water pressure

λ = parameter that defines the width of the bell for the *LDR* pulse in the $(i\text{-}1)^{th}$ cycle

λ' = parameter that defines the width of the bell for the *LDR* pulse in the i^{th} cycle

$i = i$ if by evaluating the constraint presented in Equation 6-25, it is determined that the use of i' is not required; otherwise i' should be used.

$a_p, a_1, a_2, b_p, b_1 and\ b_2$ = regression coefficients from the Global Excess Pressure Curves

The parameters λ and λ' can be estimated by solving the following equations:

$$\frac{\left[\left(a_2+\frac{b_2}{t_2}\right)-\left(a_1+\frac{b_1}{t_1}\right)\right].\left(a_p+\frac{bp}{t_p}\right)}{\left[\left(a_2+\frac{b_2}{t_2}\right)-\left(a_p+\frac{bp}{t_p}\right)\right].\left(a_1+\frac{b_1}{t_1}\right)} = \frac{4{t_L}^{-\lambda-1}\beta^{\lambda+1}\lambda^2}{\left(\lambda-1+\lambda{t_L}^{-\lambda}\beta^{\lambda}+{t_L}^{-\lambda}\beta^{\lambda}\right)^2} \tag{7-2}$$

$$\frac{\left[\left(a_2+\frac{b_2}{t_2'}\right)-\left(a_1+\frac{b_1}{t_1'}\right)\right].\left(a_p+\frac{bp}{t_p'}\right)}{\left[\left(a_2+\frac{b_2}{t_2'}\right)-\left(a_p+\frac{bp}{t_p'}\right)\right].\left(a_1+\frac{b_1}{t_1'}\right)} = \frac{4{t_L}^{-\lambda'-1}\beta^{\lambda'+1}\lambda'^2}{\left(\lambda'-1+\lambda'{t_L}^{-\lambda'}\beta^{\lambda'}+{t_L}^{-\lambda'}\beta^{\lambda'}\right)^2} \tag{7-3}$$

Where,

$t_1 = (i-2)(t_L + t_D) + t_L$

$t_1' = (i-1)(t_L + t_D) + t_L$

The model proposed to predict the accumulated excess pore pressure at any time during the unloading phase reads as follows:

$$\Delta u_{wU} = \sum_{i=2}^{N-1}\left[\left(\frac{t_p}{a_p t_p + b_p}\right) - \left(\frac{t_2}{a_2 t_2 + b_2}\right)\right]\left[\frac{4{t_L}^{-\lambda-1}\beta^{\lambda+1}\lambda^2}{\left(\lambda - 1 + \lambda {t_L}^{-\lambda}\beta^{\lambda} + {t_L}^{-\lambda}\beta^{\lambda}\right)^2}\right] exp\left(-t_D.\left(m + n.Ln(i-1)^2\right)\right)$$

$$+\left[\left(\frac{{t_p}'}{a_p {t_p}' + b_p}\right) - \left(\frac{{t_2}'}{a_2 {t_2}' + b_2}\right)\right]\left[\frac{4{t_L}^{-\lambda'-1}\beta^{\lambda'+1}\lambda'^2}{\left(\lambda' - 1 + \lambda' {t_L}^{-\lambda'}\beta^{\lambda'} + {t_L}^{-\lambda'}\beta^{\lambda'}\right)^2}\right] exp\left(-t_D.\left(m + n.Ln(i)^2\right)\right)$$

(7-4)

Where,

t_L = loading time in seconds

t_D = dwelling time in seconds

$t_p = (i-2)(t_L + t_D) + \beta$

$t_2 = (i-3)(t_L + t_D) + (t_L + t_D)$

${t_p}' = (i-1)(t_L + t_D) + \beta$

${t_2}' = (i-2)(t_L + t_D) + (t_L + t_D)$

t = time elapsed from the load end within the i^{th} cycle; valid for 0s $\leq t \leq t_D$

β = constant that defines the time at maximum pore water pressure

λ = parameter that defines the width of the bell for the *LDR* pulse in the $(i\text{-}1)^{th}$ cycle

λ' = parameter that defines the width of the bell for the *LDR* pulse in the i^{th} cycle

$i = i$ if by evaluating the constraint presented in Equation 6-25, it is determined that the use of i' is not required; otherwise i' should be used.

$a_p, a_1, a_2, b_p, b_1 and\ b_2$ = regression coefficients from the Global Excess Pressure Curves

The parameters λ and λ' can also be estimated by solving equations 7-2 and 7-3.

The times t_L and t_D can be expressed in terms related to the highway traffic characteristics. The loading time t_L is a function of both the vehicle speed v_s and the effective length L_{eff} that defines de duration of the load pulse. The value of L_{eff} is function of the pavement structure, radius of tire imprint and depth to the point of interest for analysis. The following expression can be used to estimate the loading time:

$$t_L = \frac{L_{eff}}{17.6 v_s} \tag{7-5}$$

If the pavement structure under analysis, tire imprint radius and particular depth to the point of interest are known; then for the proposed models, t_L can be substituted by Equation 7-5 to estimate excess pore pressures for vehicles traveling at different speeds.

The dwelling time t_D is related to the highway traffic frequency which is determined by the Average Daily Traffic (*ADT*). If the *ADT* for the highway

under analysis is known, the following Equation can replace t_D in the proposed predictive equations:

$$t_D = \frac{86400}{ADT} - \frac{L_{eff}}{17.6 v_s} \quad (7\text{-}6)$$

As result, the models proposed in this study can be related to both vehicle speed and daily traffic which makes it a potentially useful tool for the analysis and design of pavements

Validation of the Proposed Models

Using Excel spreadsheets a simulation of the excess pore water pressure development for each one of the specimens was conducted to validate the proposed models. Table 7-1 shows the results of the validation. Except for the peak pressure corresponding to Specimen 4 the R^2_{adj} ranges from 0.63 to 0.99. This indicates that the model provides fair to excellent predictions. The S_e/S_y values and range from 0.09 to 0.61, which are considered to be good. It can be noted that the highest errors relative to the measured values correspond to Specimen 2 with 11% and 12% for the peak and cycle end pressures respectively.

The best results are observed for Specimen 6 which shows low S_e/S_y and high R^2_{adj}. Also the relative error for Specimen 6 is lower than 0.5% for both accumulated peak and cycle end pressures.

TABLE 7-1 Results of the simulations – statistical parameters

Specimen	N_{Total}	Peak Pressures			Cycle End Pressures		
		S_e/S_y	R^2_{adj}	Error %	S_e/S_y	R^2_{adj}	Error %
1	96,060	0.307	0.907	6.2	0.372	0.862	8.4
2	64,040	0.506	0.746	11.3	0.525	0.727	12.4
3	80,050	0.295	0.914	3.9	0.256	0.935	3.3
4	16,010	1.731	-1.879	0.6	0.539	0.720	6.1
5	32,020	0.614	0.631	5.5	0.441	0.809	3.8
6	47,628	0.111	0.988	0.4	0.087	0.993	0.0

It is also observed that the R^2_{adj} for the accumulated peak pressure of Specimen 4 results to be negative and the S_e/S_y value is significantly high. This is due to the fact that the measured values did not fit well to the model at an early stage of the simulation. If the first thirty predicted values are not considered, the calculated R^2_{adj} raises to 0.73. For traffic loading conditions, the results at high number of repetitions (rather than low number of repetitions) is a major concern, and hence it is concluded that the predictions are reasonably accurate.

The problem with the predictions seems to be an accumulation of marginal errors throughout the test rather than major issues when predicting the pore pressure pulse within a single cycle. Therefore, a rule to adjust the predictions along the test can be imposed when running a simulation program.

The error in accumulated residual pressure predictions ε_2 can be defined as the difference between the accumulated residual excess pore pressure Δu_{2U} obtained evaluating Equation 7-1 for $t=t_D$, and the excess pore pressure estimated

from the Global Cycle End Excess Pressure Curve at the same global time by using Equation 6-13. The expression to estimate the error reads as follows:

$$\varepsilon_2 = \Delta u_{2U} - \frac{1}{a_2 + \frac{b_2}{t}} \quad (7\text{-}7)$$

Where, $t = i.(t_L + t_D)$ and a_2 and b_2 are known parameters from the Global Cycle End Excess Pressure Curve. If ε_2 results to be greater than +/- a critical value established for a particular analysis, the corrected residual excess pore pressure $\Delta u_{2U_{Adj}}$can be obtained by applying the following equation:

$$\Delta u_{2U_{Adj}} = \Delta u_{2U} - \left(\Delta u_{2U} - \frac{1}{a_2 + \frac{b_2}{t}}\right) \quad (7\text{-}8)$$

Such correction can be implemented into a computer code in such a way that the adjustment of results can be done automatically.

General Conclusions

It was demonstrated that the characterization of the excess pore pressure development under traffic loading can be useful not only to enhance pavement design procedures but also to understand and prevent potential failure due to significant plastic deformations.

If the critical levels of excess pore pressure for granular bases and subgrade materials are known, the models proposed in this study would be useful to delimitate the boundaries so that the stress state varies within a safe range and potential failure due to excessive development of pore water pressure can be prevented.

The results obtained also rises questions regarding the convenience of compacting unbound materials at optimum conditions. It could be possible that compacting subgrades at conditions below optimum might be a better practice for dealing with potential harm due to development of excess pore pressures.

Two models for prediction of the accumulated excess pore pressure resulting from traffic load were proposed. The first one estimates the accumulated excess pore water pressure at any time during the loading phase for any particular cycle. The second one estimates the accumulated excess pore water pressure at any time during the unloading phase for any particular cycle. These models capture the effect of the bulk stress applied, the initial matric suction and the dwelling time through the use of regression parameters. The effect of the controlled variables upon the pore water pressure buildup was established from the analysis of data. Further investigation should be directed to determine mathematical relationships between the regression parameters and testing conditions as well as soil properties.

The models simulate the pore water pressure response of the soil during the entire duration of the applied cyclic load and for any particular cycle. A marginal error present at each cycle accumulates with the number of repetitions; however, reasonable uncertainty was observed in the predictions.

The model capability for detailed simulation would be a tremendous help not only to understand how the test conditions influence the pore pressure response but also to study the influence of properties inherent to different materials like plasticity index or hydraulic conductivity.

Another important aspect of the models proposed is that particular characteristics of traffic loading conditions were considered for their development, such as load configuration and dwelling time. Upon further enhancement of the models, it will be possible to predict the excess pore pressure at any time during the pavement service life considering the vehicle speed and traffic volume observed in particular highways.

The implementation of this model will be very valuable as it will help overcoming testing limitations. Testing for unsaturated soils is a challenging task and therefore, it is convenient to have models that predict the soil response. The model proposed contributes to overcome such difficulties that may lead the pavement designers to discard the application of unsaturated soil mechanics principles.

It was demonstrated that the development of excess pore pressure affects the resilient response of the material. This was determined by using the predicted accumulated excess pore water pressures at different number of repetitions, to estimate the variation of the resilient modulus with the equation proposed by the same author in 2008 (*1*). The development of excess pore water pressure appears to significantly decrease the resilient response of the material particularly under unsaturated conditions. However, conclusions regarding the stiffness of the material might be particularly misleading under unsaturated conditions if the resilient modulus at early stages of repeated loading is considered to represent the true stiffness. The stabilization of the excess pore pressure development indicates a steady state which translates into sample stiffening. Therefore, upon further

enhancement, the models proposed in this study can be used to predict more realistic resilient responses of soils.

Results of this investigation suggest that the specimen conditioning sequence stipulated in the resilient modulus testing protocol NCHRP 1-28A might be insufficient to eliminate plastic deformations in unsaturated specimens (*37*). Therefore, a much bigger number of repetitions should be applied for specimen conditioning prior to the execution of the main repeated loading stage. The estimation of resilient modulus based on the proposed excess pore water pressure predictive models may become a good alternative to avoid unreasonably long conditioning sequences.

Again, the influence of initial matric suction, bulk stress and dwelling time level upon the resilient response of the material was evaluated in this study. The initial matric suction was found to be fundamental for the prediction of accumulated excess pore water pressure as it greatly contributes to determine the maximum pressure levels to be reached. Apparently, to certain extent, the higher the matric suction the higher the accumulated excess pore water pressure.

The bulk stress clearly showed to have significant effect upon the development of excess pore water pressure. The higher the bulk stress the higher the accumulated excess pore water pressure.

The dwelling time showed to decelerate the accumulation of excess pore water pressure when increased. Also, the higher the dwelling time the lower the maximum accumulated excess pore water pressure to be reached by the soil when subjected to dynamic loading.

With contribution from future research directed towards the expansion of the testing results database and the enhancement of the models proposed in this study, the predictive techniques developed may become a powerful tool to assess the pore pressure response of unbound materials as well as the resilient modulus used in pavement engineering.

CHAPTER 8. RECOMMENDATIONS FOR FUTURE RESEARCH

In this chapter, some important recommendations aimed at the implementation of the proposed models as a fundamental part in the resilient modulus predictive techniques are provided. The recommendations are directed to attain three main purposes related to the investigation of pore water pressure build up and its effect upon the resilient response of unsaturated unbound materials.

As priority, further testing with broaden ranges for the variables controlled in this study are required to confirm the presented findings and to enhance the pore water pressure characterization of subgrade soils. In a second order, it is recommended to investigate the influence of variables that were not considered in this research effort. In a third order, it is recommended to evaluate the differences between pore water pressure measurements taken at intermediate locations and the ends of specimens. Also, a verification or comparison between the response obtained in the laboratory and the response obtained in the field is highly recommended. Finally, additional recommendations aimed at addressing questions raised from the analysis of the testing results are included.

Broaden the Range in the Variables Tested in the Present Study

Due to the time demanding nature of the test, only two levels for each variable evaluated in this study were considered. However, the findings presented in this study raised questions regarding the pore water pressure response of the material that can only be answered by broadening the range for each controlled variable.

Initial Matric Suction or Initial Degree of Saturation

One of the most surprising findings in this study was the effect that the initial matric suction has upon the magnitude of the developed excess pore water pressure. Apparently, the higher the initial matric suction the higher the accumulated excess pore pressure at the end of loading. However, it was suggested by Minh Thu et al. that there appears to be a maximum initial matric suction limit for which maximum development of excess pore pressure will occur (*34*). Beyond that limit, the maximum developed excess pore water pressure decreases. It appears that the water phase becomes discontinuous at certain suction condition and therefore, no more excess pore water pressure will develop. It seems that such relationship resembles the compaction curves, which reach maximum dry densities at optimum moisture contents. It is recommended to direct future research to study this mechanism by testing specimens at higher initial matric suctions.

Particularly, it is recommended to test specimens at initial matric suction levels higher than the maximum value used in this study in order to determine the levels that might lead to maximum changes in pore water pressure.

Also, at low levels of initial matric suction, the dynamic load may impart further compaction leading to the increase in the degree of saturation of the specimens. It would be interesting to investigate the transition from unsaturated conditions to saturated conditions under dynamic load due to such changes in the degree of saturation. In this way, the initial conditions that make the soil prone to such phenomenon may be identified.

Bulk Stress

In this study, critical levels of bulk stress were not evaluated as failure was not observed in any of the specimens. However, it was determined that the effect of bulk stress is fundamental on the characteristics of the excess pore water pressure developed. It is of interest to find critical bulk stress levels that may lead to tertiary flow due to excessive development of pore water pressure under saturated conditions. Therefore, future research efforts should consider higher levels of stresses to be imparted to the specimen.

In addition, some interaction between the initial matric suction and the bulk stress on the development of excess pore water pressure was observed in this study. Such interactions could also be taken into account for further investigation.

Effect of Dwelling Time

The dwelling time was demonstrated to be important in the prediction of pore water pressure buildup/dissipation. However, only two levels of dwelling time were used in this study. It should be recalled that the low dwelling time level considered in this study was 4 seconds. The resilient modulus testing protocol calls for a dwelling time of less than one second. It was observed that a shorter dwelling time accelerates the pore water pressure accumulation and impacts the maximum change in pore water pressure attained. By following the protocol load configuration, higher pore water pressure buildup and possibly specimen failure might be observed. Therefore, it is recommended to consider lower levels of dwelling time in future research efforts.

The general recommendation defined as priority for future research aims at encouraging the expansion of testing results database in order to enhance the proposed models by developing relationships between regression coefficients and the predictive variables.

The difficulties as well as the time demanding nature of this kind of test were discussed in this study. Therefore, it is anticipated that exhaustive research is needed before fully implementing the models into practice. However, any small step at a time is fundamental to ultimately achieve the full implementation of the models along with the unsaturated soil mechanics principles into the pavement design methodologies.

Suitability of Additional Predictive Variables

As it was mentioned in this document, several test conditions that were not evaluated in this study have high potential for being considered as predictive variables. Further investigation on the suitability of some of these variables is recommended in this section.

Variables Related to Soil Type

It must be recognized that a lot of effort was focused in the development of new models for the prediction of excess pore water pressure development under dynamic loading. However, the test results comprehend the characterization of only one soil type. Further testing on a broad range of soil types is recommended for future research in order to relate the parameters of the proposed models with properties inherent of each particular soil type.

Among the variables related to soil type, it is recommended to consider the hydraulic conductivity as priority since it is anticipated to be fundamental for the dissipation phase in plastic soils. Additionally; plasticity index, gradation or clay content could be considered as potential predictive variables.

Effect of Confining Stress

The effect of confinement was not investigated in this study. As suggested by some authors, the confining pressure may affect the pore water pressure buildup of materials (*19, 30, 31, 33*). Therefore, this is a variable that deserves to be considered in future studies.

Effect of Soil Disturbance

It has been recognized by several authors in the literature, that the degree of consolidation affects the response of cohesive soils. In this study, only normally consolidated specimens were tested. It is recommended to evaluate the response of over consolidated specimens at different *OCR* values in future research efforts.

Effect of Loading Time

The effect of loading time was not considered in this laboratory testing program. Even though no influence of this variable upon the pore water pressure buildup has been reported by some authors, further testing is recommended to be performed in order to confirm such hypothesis (*27, 38*).

Verification of Pore Pressure Response under Laboratory and Field Conditions

In the beginning of this study, the use of suction mini probes was contemplated for measuring the pore pressure buildup at intermediate locations in the soil specimen. However, the mini suction probes available in the market at that time did not have the resolution and rapid response required to collect data for dynamic load testing. In addition, such devices are easily damageable when subjected to load ranges as that considered for this study. Considering such limitations, the use of mini probes was ruled out.

It is recommended to consider the use of suction mini probes as their capabilities are enhanced with time. This will help to assess deviations of the response at intermediate points of the specimen from the response that can be measured at the ends of the specimen. In addition, suction mini probes can be used in the field to determine whether the response observed for laboratory conditions corresponds to what actually happens in the field.

Additional Recommendations

Ideal Moisture Content for Soil Compaction

As discussed in this report, there appears to be a level of moisture content that triggers discontinuity in the soil water phase. Such discontinuity may translate into absence of pore water pressure buildup. Therefore, it is recommended to investigate the suitability of using dry of optimum moisture contents for soil

compaction as alternative to prevent negative effects of pore water pressure buildup upon the resilient response of the soil.

Changes in Resilient Strain with Number of Load Applications

It was suggested by the predictions obtained using the model proposed by Cary that the resilient strain increases with number of load repetitions until reaching a steady state particularly under unsaturated conditions (*1*). Such observation implies that at early stages of loading, the resilient modulus might be a misleading indicator of the soil stiffness. As discussed earlier in the document, according to the available testing protocol, the resilient modulus is usually measured between 2,000 and 4,000 load applications. Therefore further investigation on the resilient strain changes with load repetitions especially at advanced loading stages is recommended to determine whether the currently available resilient modulus testing protocol is suitable for obtaining reliable design values.

REFERENCES

1. Cary, C. E. Resilient Modulus Testing for Unsaturated Unbound Materials. Master Thesis. Arizona State University, Tempe, Arizona, 2008.

2. Hveem, F. N., and R. M. Carmany. The Factors Underlying the Rational Design of Pavements. In *Highway Research Record 28*, HRB, National Research Council, Washington, D.C., 1948, pp. 101-136.

3. Hveem, F. N. Pavement Deflections and Fatigue Failures. In *Highway Research Record 114*, HRB, National Research Council, Washington, D.C., 1955, pp. 43-87.

4. Seed H. B., C. K. Chan, and C. E. Lee. Resilience Characteristics of Subgrade Soils and their Relation to Fatigue Failures in Asphalt Pavements. In *Conference Proceedings: International Conference on Structural Design of Asphalt Pavements*, Vol. 1, Ann Arbor, USA, 1962, pp. 611-636.

5. Witczak M.W., X. Qi, and W.M. Mirza. Use of Nonlinear Subgrade Modulus in AASHTO Design Procedure. *ASCE Journal of Transportation Engineering*, Vol. 123, No. 3, 1995, pp. 273-282.

6. Witczak, M. W., and J. Uzan. *The Universal Airport Design System, Report I of IV: Granular Material Characterization*. Department of Civil Engineering, University of Maryland, College Park, 1988.

7. National Cooperative Highway Research Program (NCHRP). *Guide for Mechanistic Empirical Design of New and Rehabilitated Pavement Structures*, NCHRP 1-37 A, Final Report, TRB, National Research Council, Washington, D.C., 2004.

8. Fredlund, D. G., and N. R. Morgenstern, Stress State Variables for Unsaturated Soils. *ASCE Journal of the Geotechnical Engineering Division*, Vol. 103, No. 5, 1977, pp. 447-466.

9. Fredlund, D. Unsaturated Soil Mechanics in Engineering Practice. *ASCE Journal of Geotechnical and Geoenvironmental Engineering*, Vol. 132, No. 3, 2006, pp. 286-321.

10. Fredlund, D.G., and H. Rahardjo. Soil Mechanics Principles for Highway Engineering in Arid Regions. In *Transportation Research Record 1137*, TRB, National Research Council, Washington, D.C., 1987, pp. 1-11.

11. Fredlund, D. G., A. T. Began, and P. K. Wong. Relation between Resilient Modulus and Stress Conditions for Cohesive Subgrade Soils. In *Transportation Research Record 642*, TRB, National Research Council, Washington, D.C., 1977, pp. 73-81.

12. Andrei, D. Development of a Predictive Model for the Resilient Modulus of Unbound Materials. Doctoral Dissertation. Arizona State University, Tempe, Arizona, 2003.

13. Witczak M.W., W.N. Houston, and D. Andrei. *Resilient Modulus as Function of Soil Moisture – A Study of the Expected Changes in Resilient Modulus of the Unbound Layers with Changes in Moisture for 10 LTPP Sites*. Development of the 2002 Guide for the Development of New and Rehabilitated Pavement Structures, NCHRP 1-37 A, Inter Team Technical Report (Seasonal 2). Arizona State University, Tempe, Arizona, 2000.

14. Yang, R. R., W. H. Huang, and Y. T. Tai. Variation of Resilient Modulus with Soil Suction for Compacted Subgrade Soils. In *Transportation Research Record 1913*, TRB, National Research Council, Washington, D.C., 2005, pp. 99-106.

15. Liang, R. Y., S. Rabab'ah, and M. Khasawneh. Predicting Moisture-Dependent Resilient Modulus of Cohesive Soils Using Soil Suction Concept. *ASCE Journal of Transportation Engineering*, Vol. 134, No. 1, 2008, pp. 34-40.

16. Parreira, A. B., and R. F. Goncalves. The Influence of Moisture Content and Soil Suction on the Resilient Modulus of a Lateritic Subgrade Soil. Presented at GeoEng - An International Conference on Geotechnical & Geological Engineering, Melbourne, Australia, 2000.

17. Zapata, C. E. and C. E. Cary. A New Generation of Resilient Modulus Characterization of Unbound Materials. Contemporary Topics in Ground Modification, Problem Soils, and Geo-Support. In *Geotechnical Special Publication No. 187: Selected papers from the 2009 International Foundations Congress and Equipment Expo*, American Society of Civil Engineers. Orlando, Florida, March, 2009, pp. 377-384.

18. Cary, C. E. and C. E. Zapata. Comparative Study of a Mechanistic Resilient Modulus Predictive Equation for Unbound Materials. Presented at The 2nd International Conference on Transportation Infrastructure, Sao Paulo, Brasil, 2010.

19. Fredlund, D. G., and H. Rahardjo. *Soil Mechanics for Unsaturated Soils*, John Wiley and Sons, Inc., New York, 1993.

20. Larew, H. G., and G. A. Leonards. A Strength Criterion for Repeated Loads. In *Highway Research Record 41*, HRB, National Research Council, Washington, D.C., 1962, pp. 529-556.

21. Sangrey, D. A. Behavior of Soils Subjected to Repeated Loading. Doctoral Dissertation. Cornell University, Ithaca, New York, 1968.

22. Sangrey, D. A., J. W. France, S. J. Poulos, and G. Castro. Cyclic Loading of sands, Silts and Clays. In *Conference Proceedings: Earthquake Engineering and Soil Dynamics*, American society of Civil Engineers, Passadena, California, 1978, pp.836-851.

23. Sangrey, D. A., D. J. Henkel, and M. I. Esrig. The Effective Stress Response of a Saturated Clay Soil to Repeated Loading. *Canadian Geotechnical Journal*, Vol. 6, No 3, 1969, pp. 241-252.

24. France, J. W., and D. A. Sangrey. Effect of Drainage in Repeated Loading of Clays. *ASCE Journal of Geotechnical Engineering*, Vol. 103, No. 7, 1977, pp. 769-785.

25. Ansal, A. M., and A. Erken. Undrained Behavior of Clay Under Cyclic Shear Stresses. *ASCE Journal of Geotechnical Engineering*, Vol. 115, No. 7, 1989, pp. 968-983.

26. Hsu, C., and M. Vucetic. Treshold Shear Strain for Cyclic Pore-Water Pressure in Cohesive Soils. *ASCE Journal of Geotechnical and Geoenvironmental Engineering*, Vol. 132, No. 10, 2006, pp. 1325-1335.

27. Brown, S. F., and A. K. F. Lashine and A. F. L. Hyde. Repeated Load Triaxial Testing of a Silty Clay. *Geotechnique*, Vol. 15, No. 1, 1975, pp. 95-114.

28. Andersen, K. H., W. F. Rosenbrand, S. F. Brown, and J. H. Pool. Cyclic and static Laboratory Test on Drammen Clay. *ASCE Journal of Geotechnical Engineering*, Vol. 106, No. 5, 1980, pp. 499-529.

29. Mendoza, M. J., and V. M. Hernandez. Pore-Pressure Build-Up Under Cyclic Loading in Mexico City Clay. In *Conference Proceedings: 13th International Conference on Soil Mechanics and Foundations Engineering*, New Delhi, India, 1994, pp. 181-186.

30. Skempton W. F. The Pore Pressure Coefficients, A and B. *Geotechnique*, Vol. 4, No. 4, 1954, pp. 143-147.

31. Bishop, W., and D. J. Henkel. *The Measurement of Soil Properties in the Triaxial Test*, Edward Arnold, Ltd., London, 1957.

32. Ogawa, S., T. Shibayama, and H. Yamaguchi. Dynamic Strength of Saturated Cohesive Soil. In *Conference Proceedings: 9th International Conference on soil Mechanics and Foundations Engineering*, Butterworths, Tokyo, Japan, 1977, pp. 317-320.

33. Kim, C., W. Hwang, Y. Choi, M. Lee, and T. Kim. Characteristics of Pore Pressure and Volume Change During Undrained Loading of Unsaturated Compacted Granite Soil. Soils and Rock Instrumentation, Behavior and

Modeling. In *Geotechnical Special Publication No. 194: Selected papers from the 2009 GeoHunan International Conference*, American Society of Civil Engineers. Hunan, China, August, 2009, pp. 50-56.

34. Minh Thu, T., H. Rahardjo, and E. Leong. Shear Strength and Pore-Water Pressure Characteristics During Constant Water Content Triaxial Tests. *ASCE Journal of Geotechnical and Geoenvironmental Engineering*, Vol. 132, No. 3, 2006, pp. 441-419.

35. Yang, S, H. Lin, J. H. S. Kung., and W. Huang. Suction-Controlled Laboratory Test on Resilient Modulus of Unsaturated Compacted Subgrade Soils. *ASCE Journal of Geotechnical and Geoenvironmental Engineering*, Vol. 134, No. 9, 2008, pp. 1375-1384.

36. Barksdale, R. D. A Compressive stress Pulse Times in flexible Pavements for Use in Dynamic Testing. In *Highway Research Record 345*, HRB, National Research Council, Washington, D.C., 1971, pp. 32-44.

37. National Cooperative Highway Research Program. Laboratory Determination of Resilient Modulus for Flexible Pavement Design. In *Research Results Digest*, No 285, Transportation Research Board of the National Academies, Washington, D.C., 2004, pp. 52.

38. Lashine, A. K. Some Aspects of the Characteristics of Keuper Marl Under Repeated Loading. Doctoral Dissertation. University of Nottingham, Nottingham, England, 1971.

39. Fredlund, D. G., and A. Xing. Equations for the Soil-Water Characteristic Curve. *Canadian Geotechnical Journal*, Vol. 31, No 3, 1994, pp. 521-532.

40. Jacquemin, S. C. Laboratory Determination of Hydraulic Conductivity for Unsaturated Cracked Fine Grained Soil. Master Thesis. Arizona State University, Tempe, Arizona, 2011.

41. Ullidtz, P. *Pavement Analysis*, Elsevier, Amsterdam, 1987.

42. Holtz, R. D., and Kovacs, W. D. *An Introduction to Geotechnical Engineering*, Prentice-Hall, Inc, New Jersey, 1981.

43. El-Badawy, S. Development of a Mechanistic Constitutive Model for the Repeated Load Permanent Deformation Behavior of Subgrade Pavement Materials. Doctoral Dissertation. Arizona State University, Tempe, Arizona, 2006.

44. Uzan, J. Characterization of Clayey Subgrade Materials for Mechanistic Design of Flexible Pavements. In *Transportation Research Record 1629*, TRB, National Research Council, Washington, D.C., 1998, pp. 189-196.

APPENDIX A

BOTTOM PEDESTALS REVISED DESIGN DRAWINGS

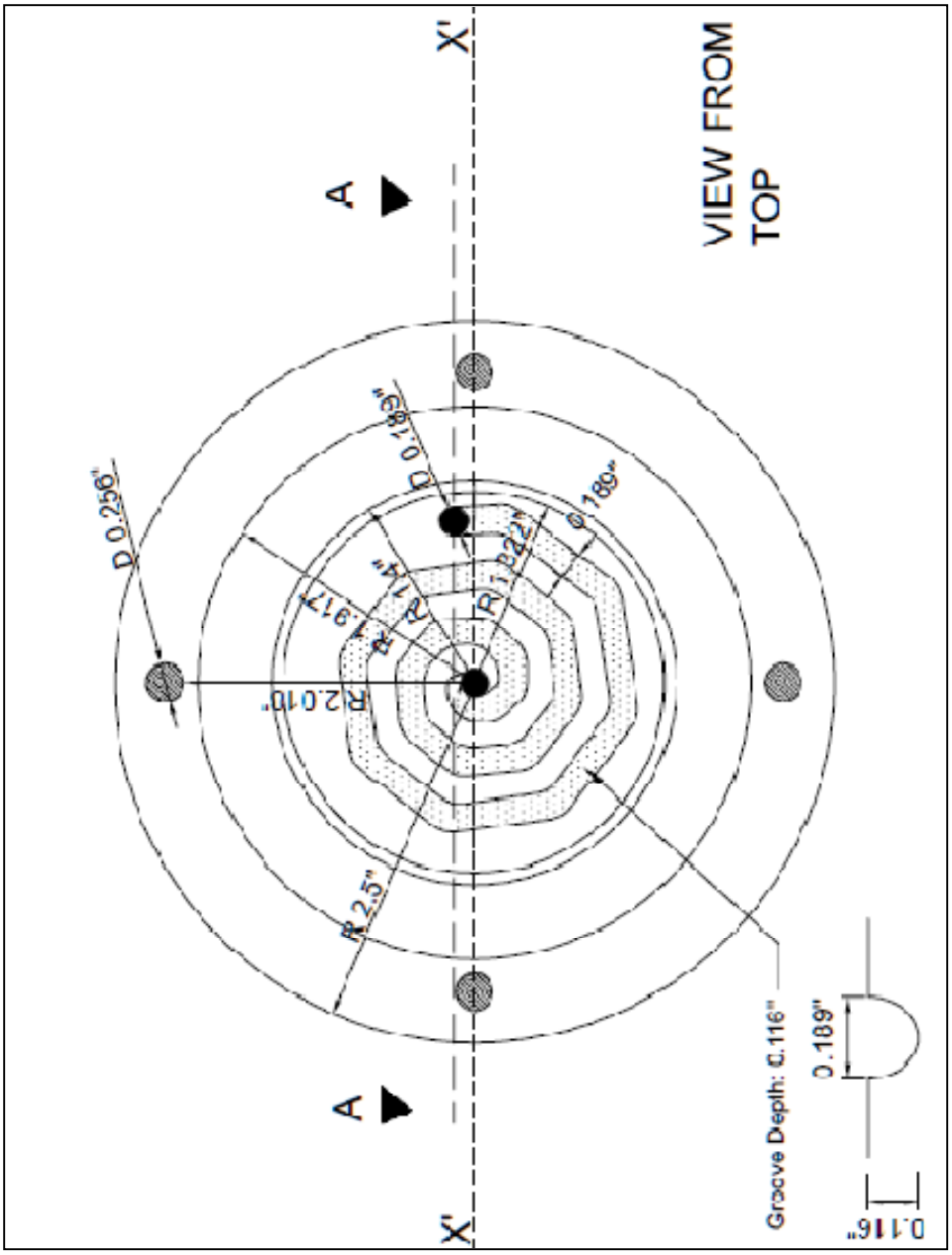

Bottom Pedestal – Design 1 – Drawing 1 of 4

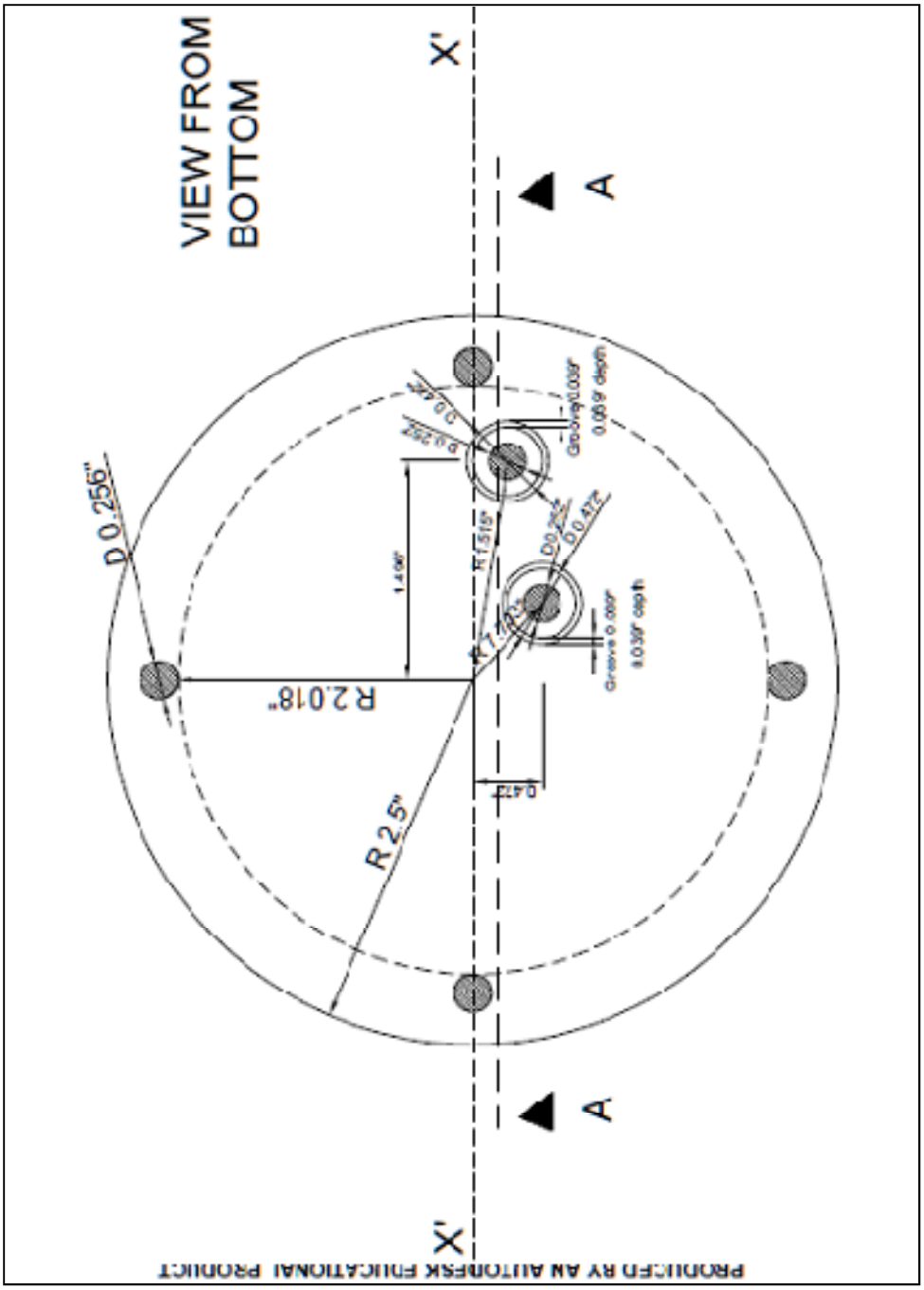

Bottom Pedestal – Design 1 – Drawing 2 of 4

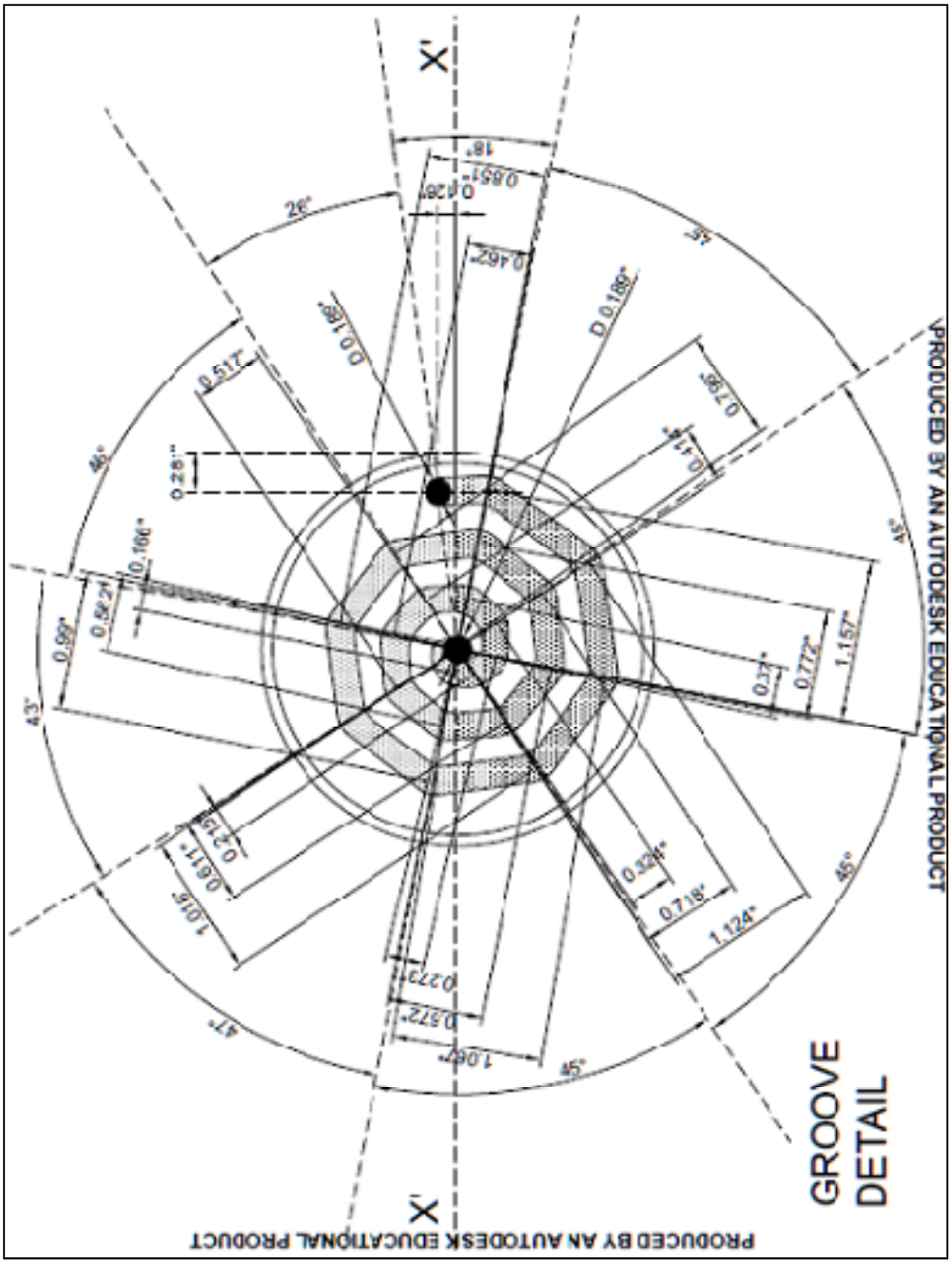

Bottom Pedestal – Design 1 – Drawing 3 of 4

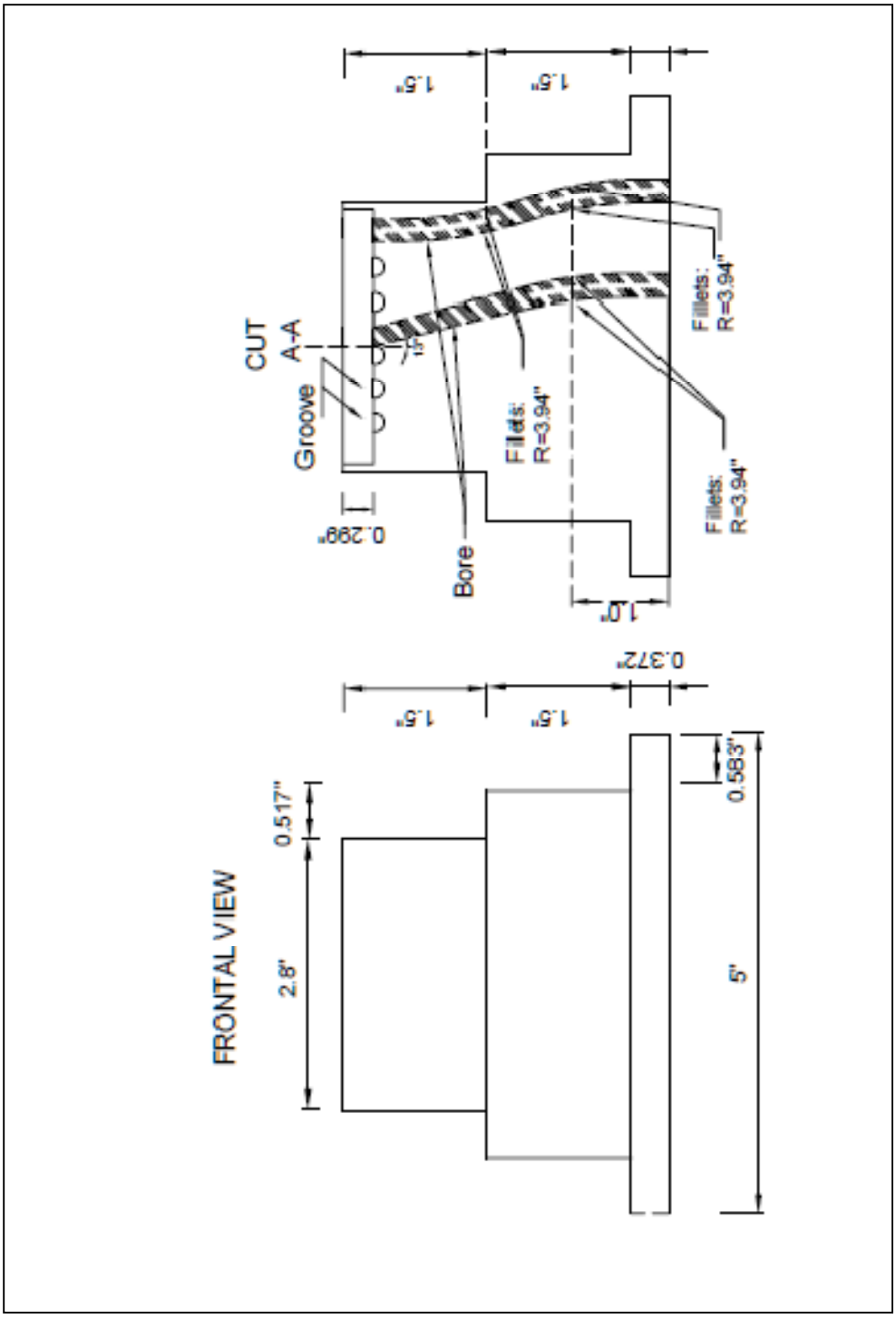

Bottom Pedestal – Design 1 – Drawing 4 of 4

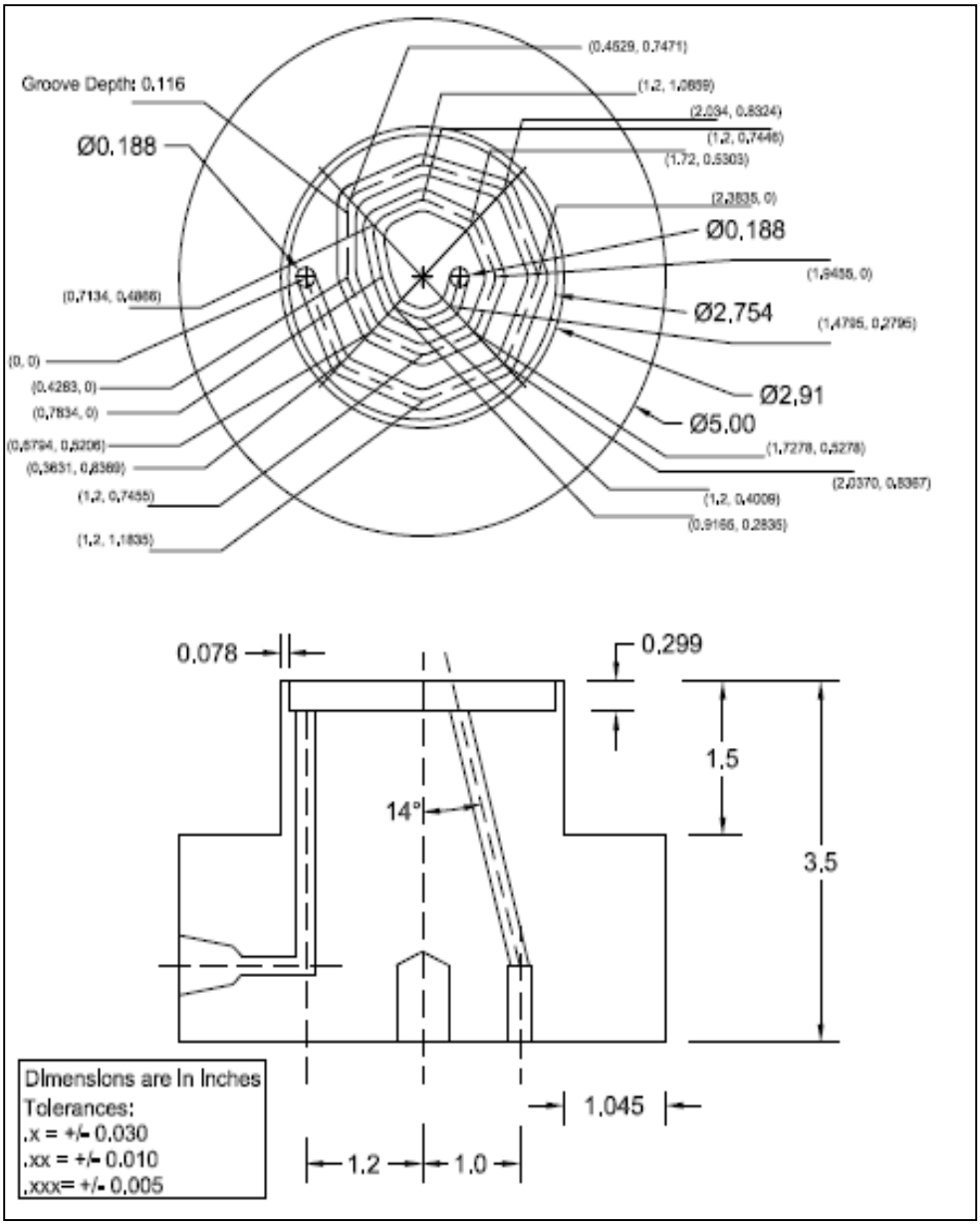

Bottom Pedestal – Design 2 – Drawing 1 of 1

APPENDIX B

GOODNESS OF FIT PLOTS FOR GLOBAL EXCESS PRESSURE CURVES

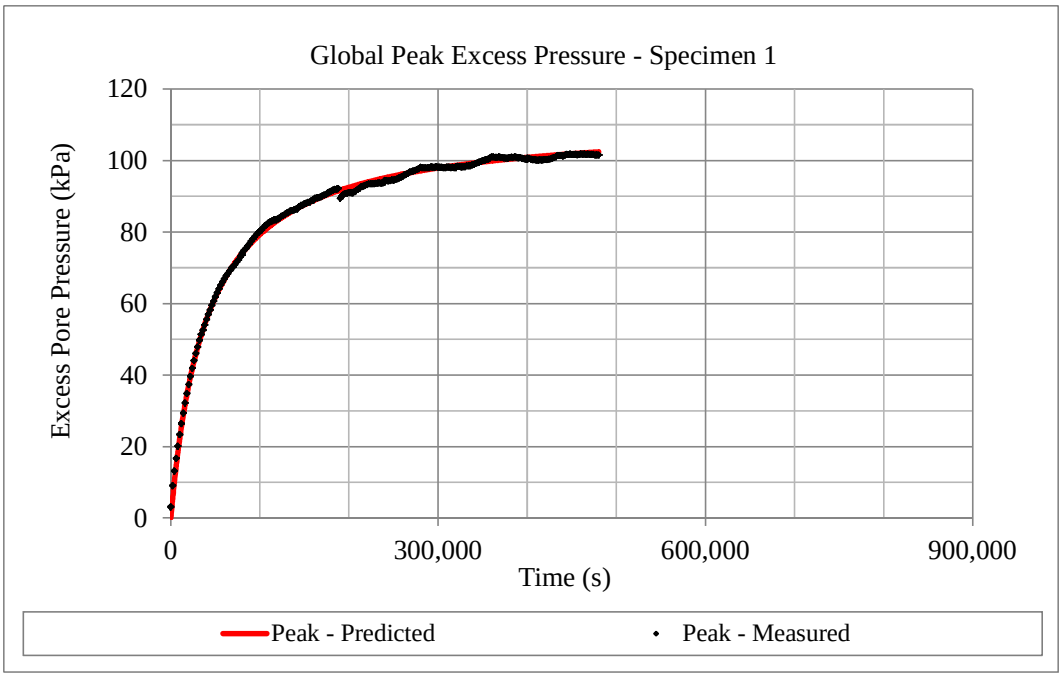
Global Peak Excess Pressure - Specimen 1
Excess Pore Pressure (kPa)
120
100
80
60
40
20
0
0
300,000
600,000
900,000
Time (s)
Peak - Predicted
Peak - Measured

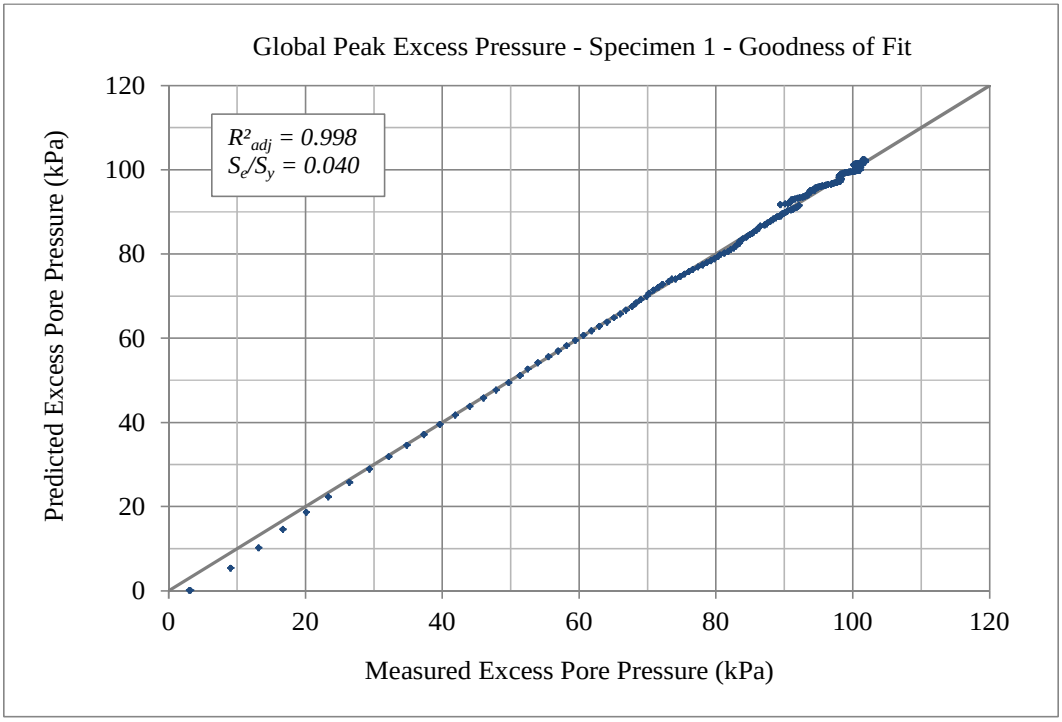
Global Peak Excess Pressure - Specimen 1 - Goodness of Fit
R^2_{adj} = 0.998
S_e/S_y = 0.040
Predicted Excess Pore Pressure (kPa)
120
100
80
60
40
20
0
0
20
40
60
80
100
120
Measured Excess Pore Pressure (kPa)

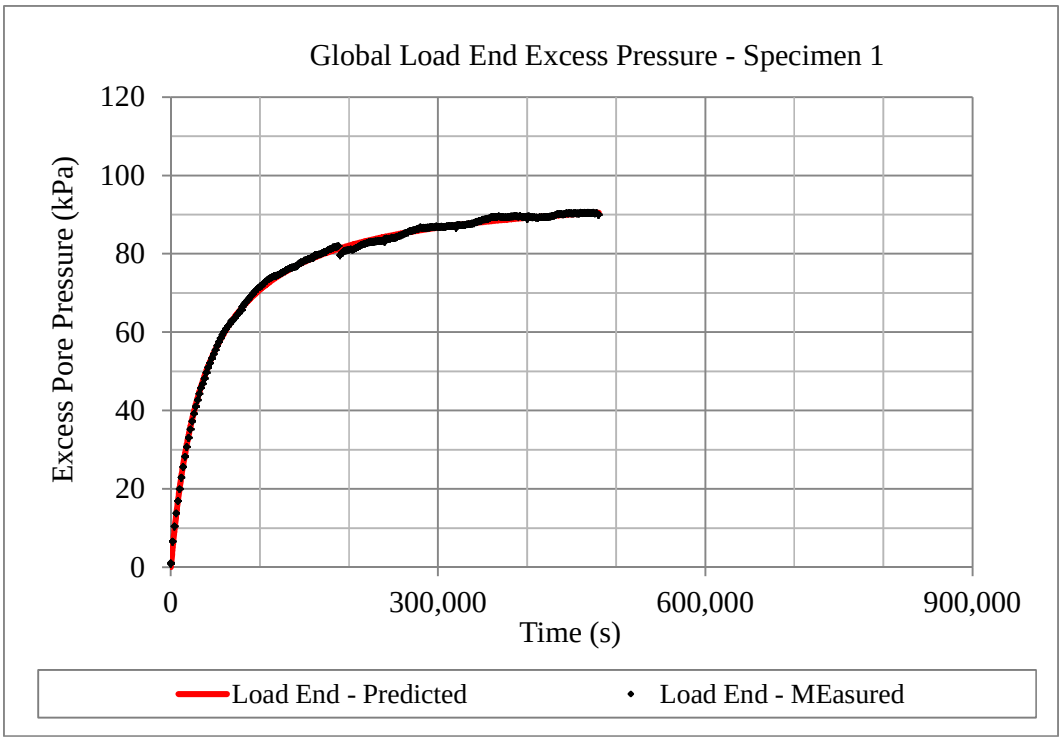
Global Load End Excess Pressure - Specimen 1
Excess Pore Pressure (kPa)
120
100
80
60
40
20
0
0
300,000
600,000
900,000
Time (s)
Load End - Predicted
Load End - MEasured

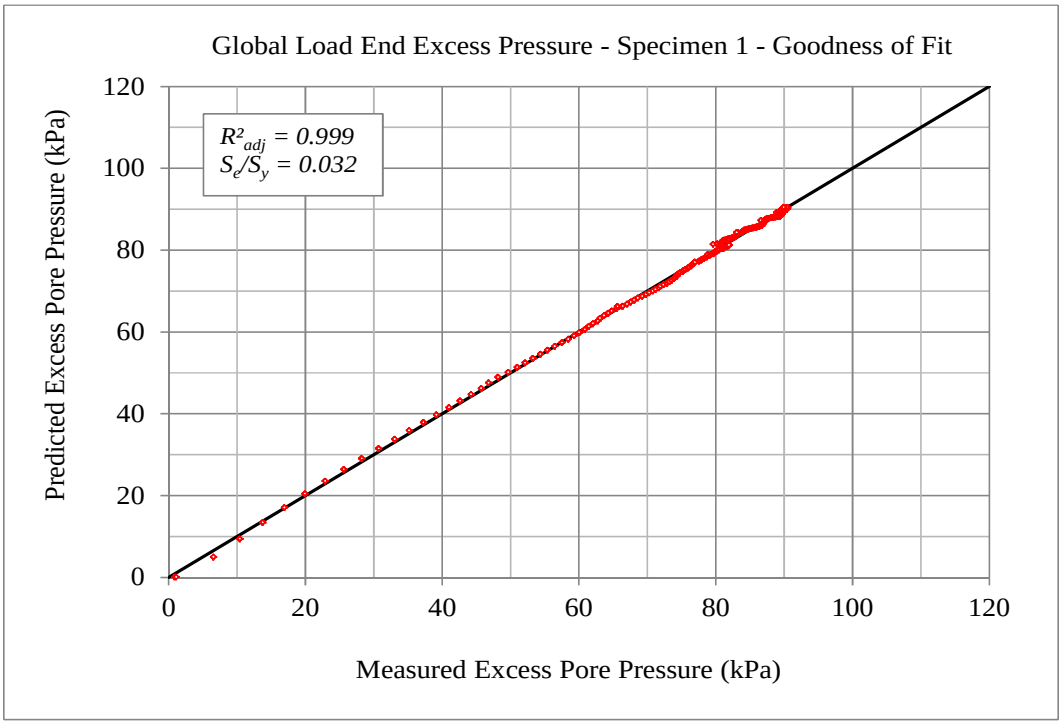
Global Load End Excess Pressure - Specimen 1 - Goodness of Fit
R^2_{adj} = 0.999
S_ϵ/S_y = 0.032
Predicted Excess Pore Pressure (kPa)
120
100
80
60
40
20
0
0
20
40
60
80
100
120
Measured Excess Pore Pressure (kPa)

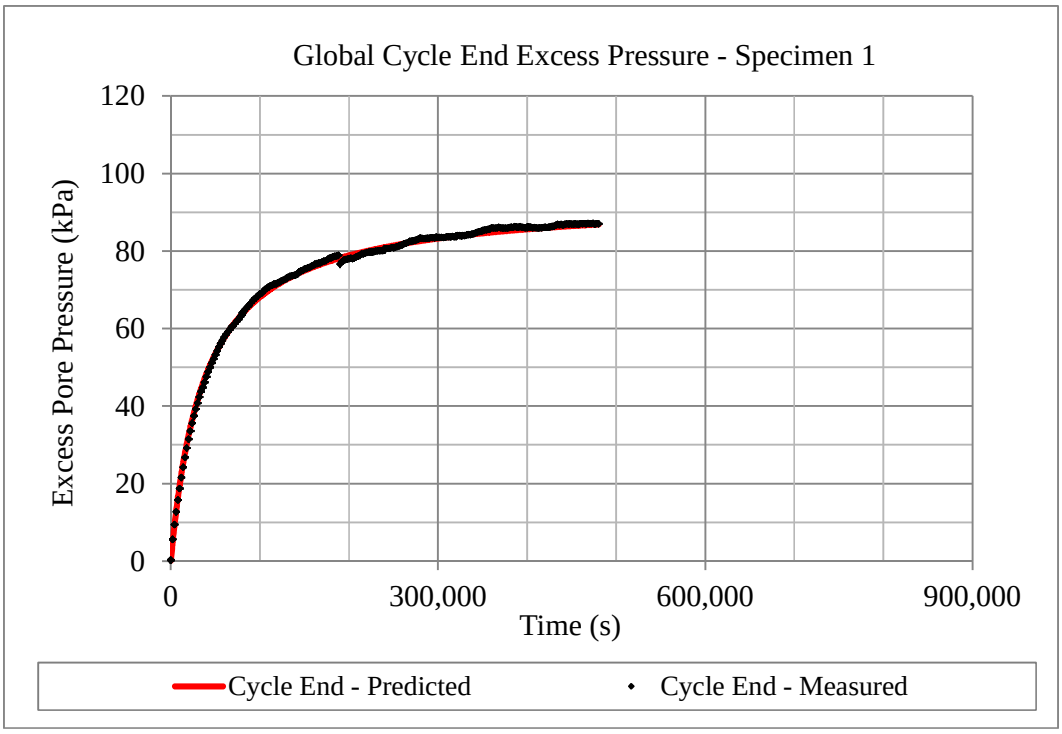
Global Cycle End Excess Pressure - Specimen 1
Excess Pore Pressure (kPa)
120
100
80
60
40
20
0
0
300,000
600,000
900,000
Time (s)
Cycle End - Predicted
Cycle End - Measured

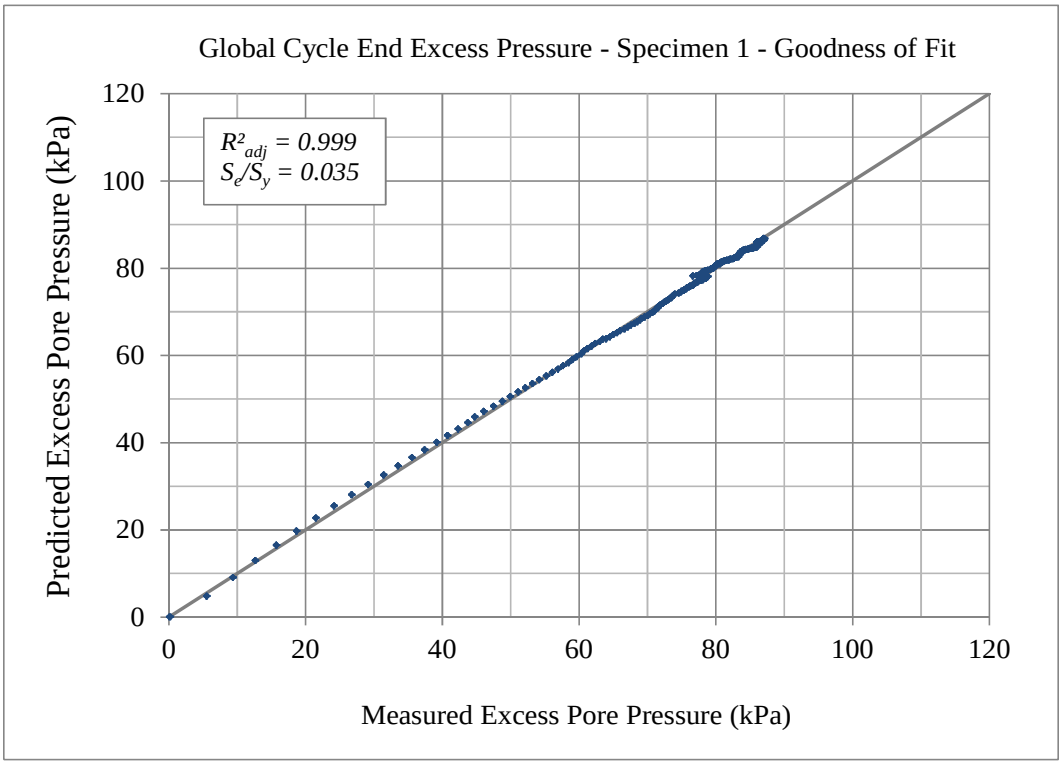
Global Cycle End Excess Pressure - Specimen 1 - Goodness of Fit
R^2_{adj} = 0.999
S_e/S_y = 0.035
Predicted Excess Pore Pressure (kPa)
120
100
80
60
40
20
0
0
20
40
60
80
100
120
Measured Excess Pore Pressure (kPa)

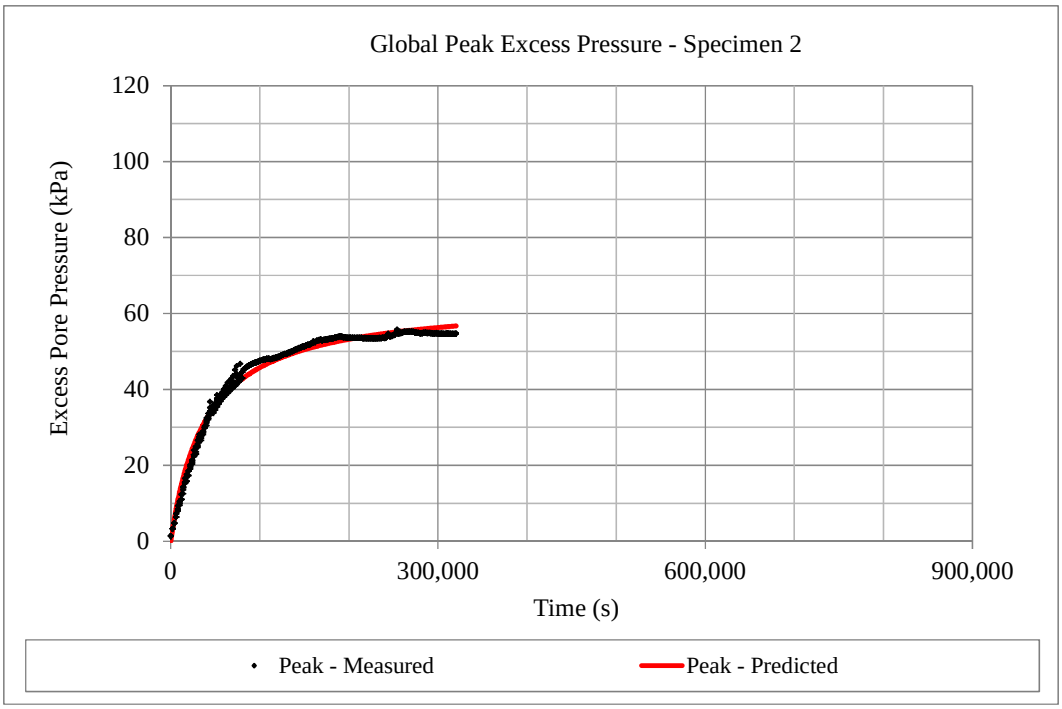
Global Peak Excess Pressure - Specimen 2
Excess Pore Pressure (kPa)
120
100
80
60
40
20
0
0
300,000
600,000
900,000
Time (s)
Peak - Measured
Peak - Predicted

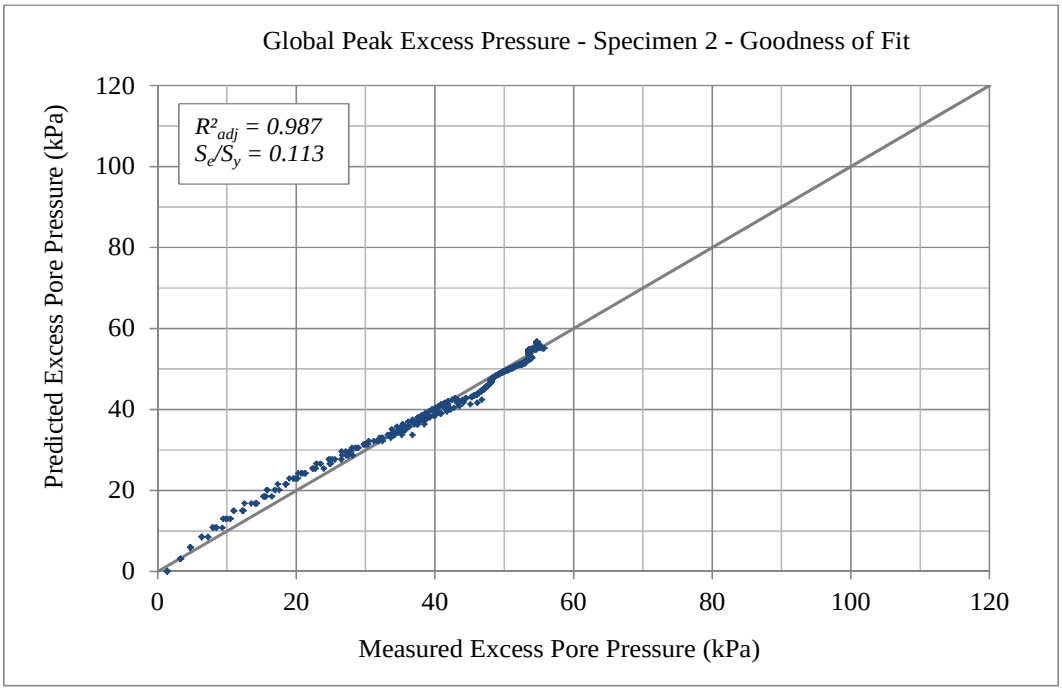
Global Peak Excess Pressure - Specimen 2 - Goodness of Fit
R^2_{adj} = 0.987
S_e/S_y = 0.113
Predicted Excess Pore Pressure (kPa)
120
100
80
60
40
20
0
0
20
40
60
80
100
120
Measured Excess Pore Pressure (kPa)

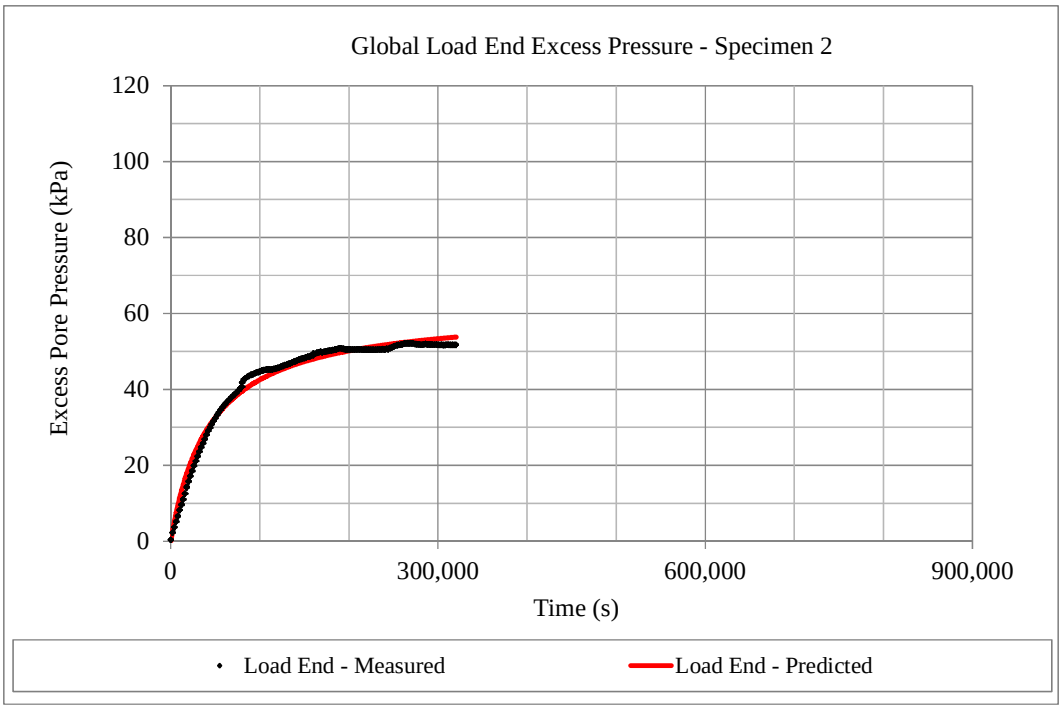
Global Load End Excess Pressure - Specimen 2
Excess Pore Pressure (kPa)
120
100
80
60
40
20
0
0
300,000
600,000
900,000
Time (s)
Load End - Measured
Load End - Predicted

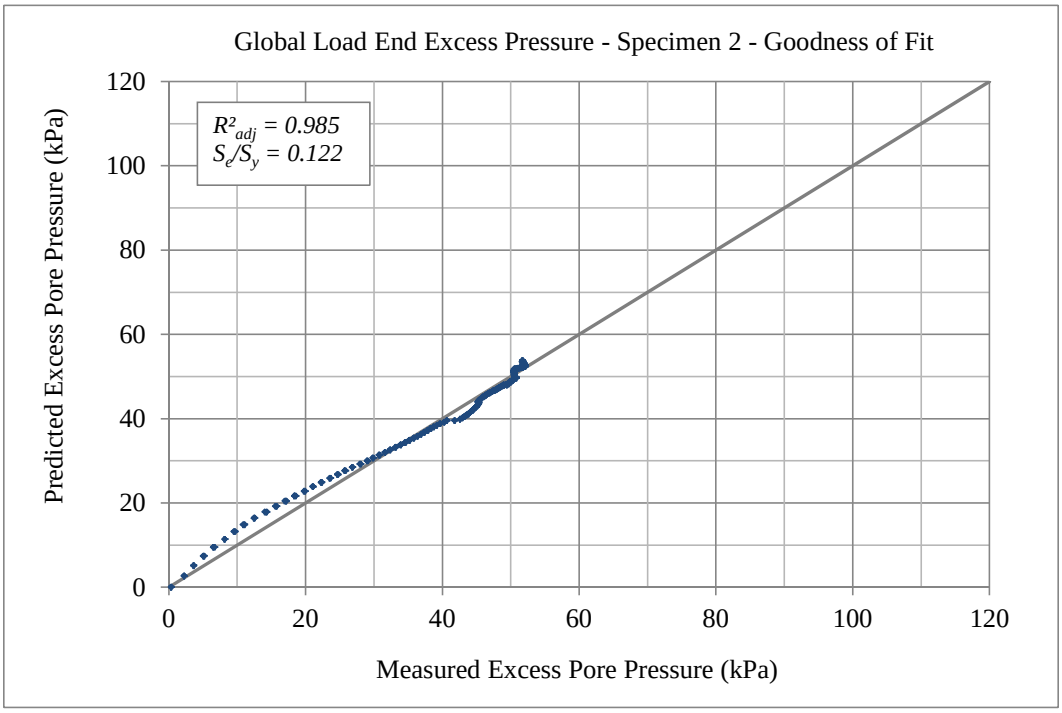
Global Load End Excess Pressure - Specimen 2 - Goodness of Fit
R^2_{adj} = 0.985
S_e/S_y = 0.122
Predicted Excess Pore Pressure (kPa)
120
100
80
60
40
20
0
0
20
40
60
80
100
120
Measured Excess Pore Pressure (kPa)

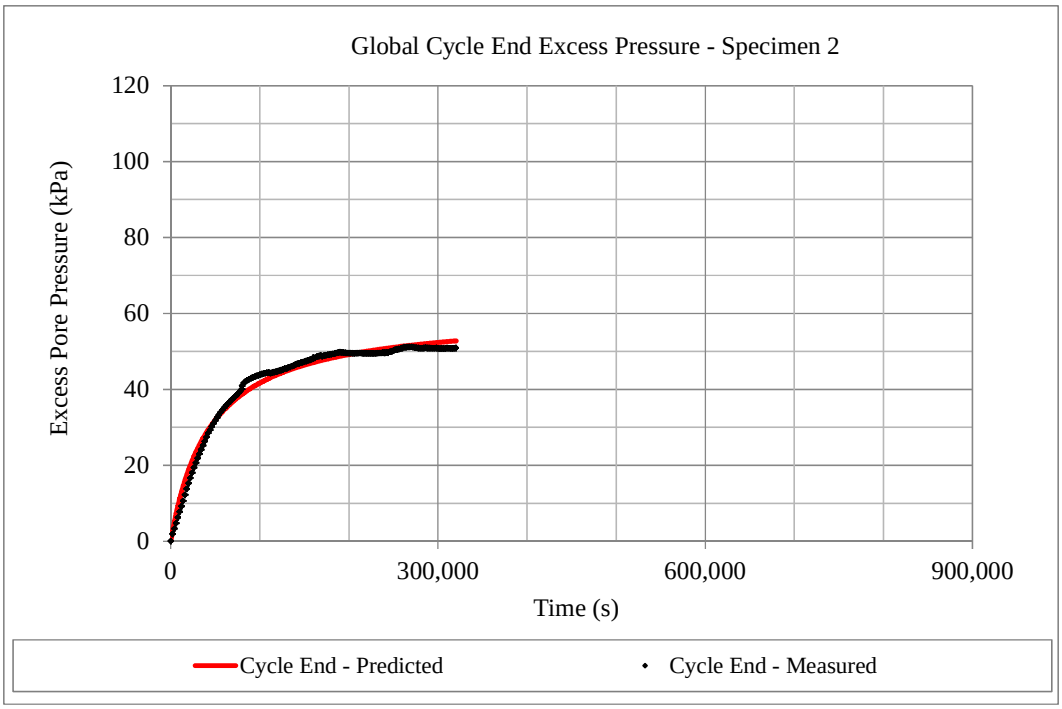
Global Cycle End Excess Pressure - Specimen 2
Excess Pore Pressure (kPa)
120
100
80
60
40
20
0
0
300,000
600,000
900,000
Time (s)
Cycle End - Predicted
Cycle End - Measured

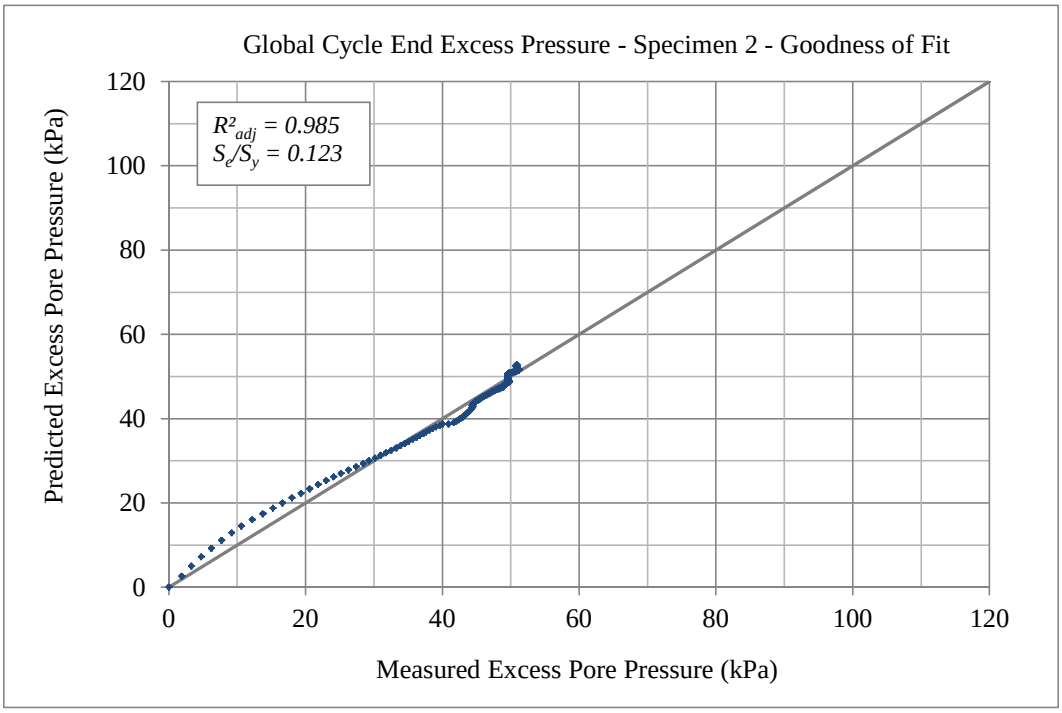
Global Cycle End Excess Pressure - Specimen 2 - Goodness of Fit
R^2_{adj} = 0.985
S_e/S_y = 0.123
Predicted Excess Pore Pressure (kPa)
120
100
80
60
40
20
0
0
20
40
60
80
100
120
Measured Excess Pore Pressure (kPa)

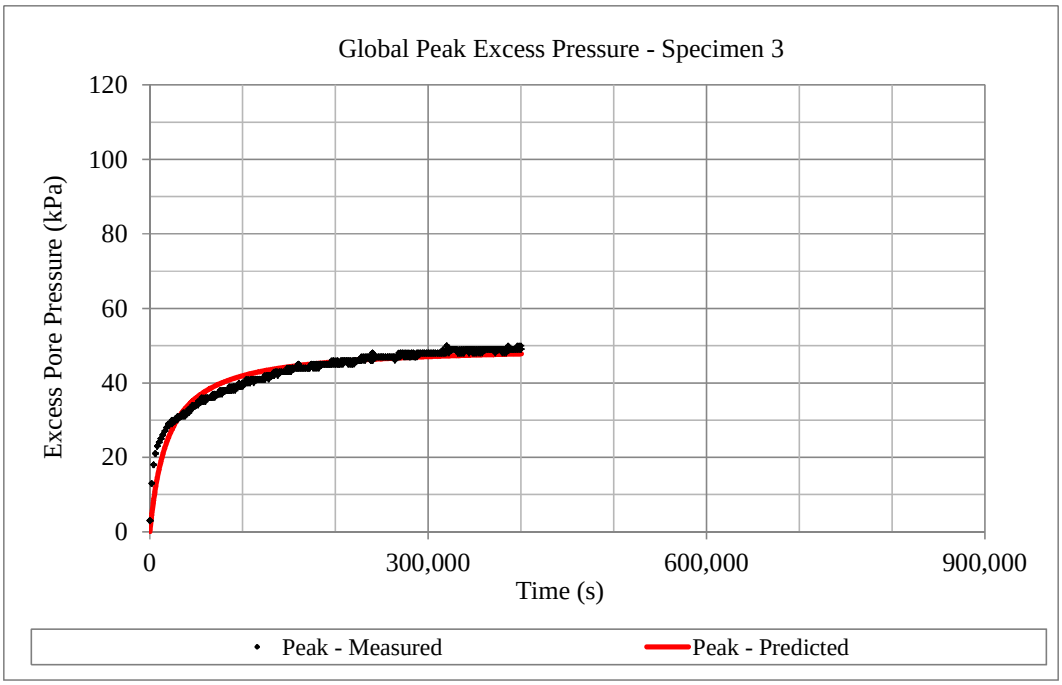
Global Peak Excess Pressure - Specimen 3
Excess Pore Pressure (kPa)
120
100
80
60
40
20
0
0
300,000
600,000
900,000
Time (s)
Peak - Measured
Peak - Predicted

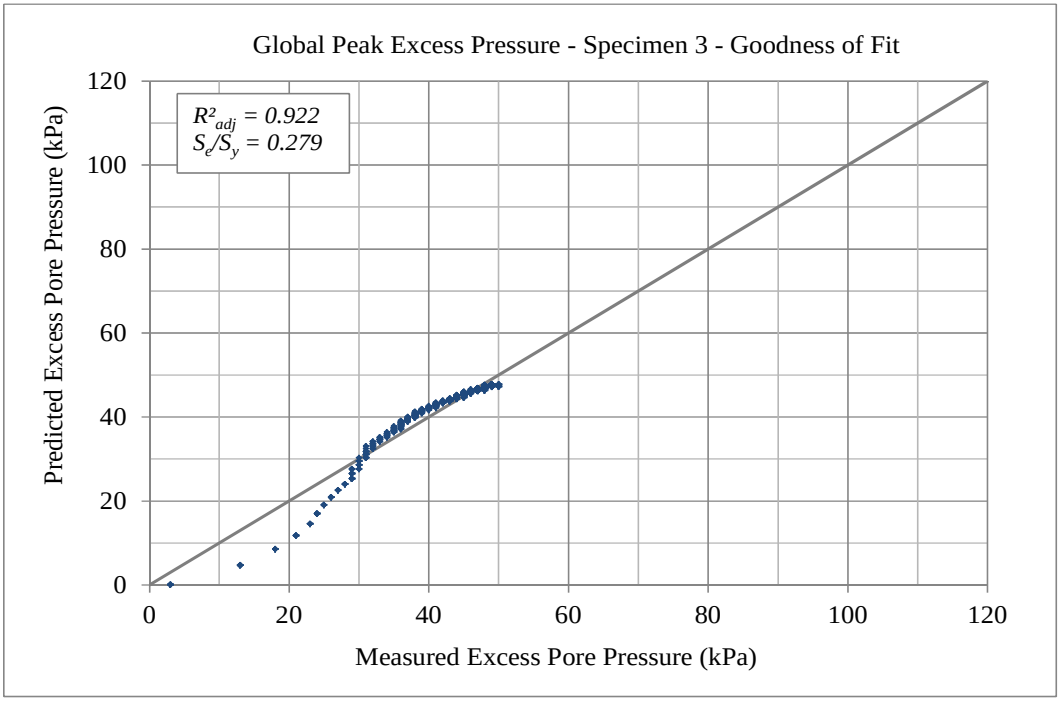
Global Peak Excess Pressure - Specimen 3 - Goodness of Fit
R^2_{adj} = 0.922
S_e/S_y = 0.279
Predicted Excess Pore Pressure (kPa)
120
100
80
60
40
20
0
0
20
40
60
80
100
120
Measured Excess Pore Pressure (kPa)

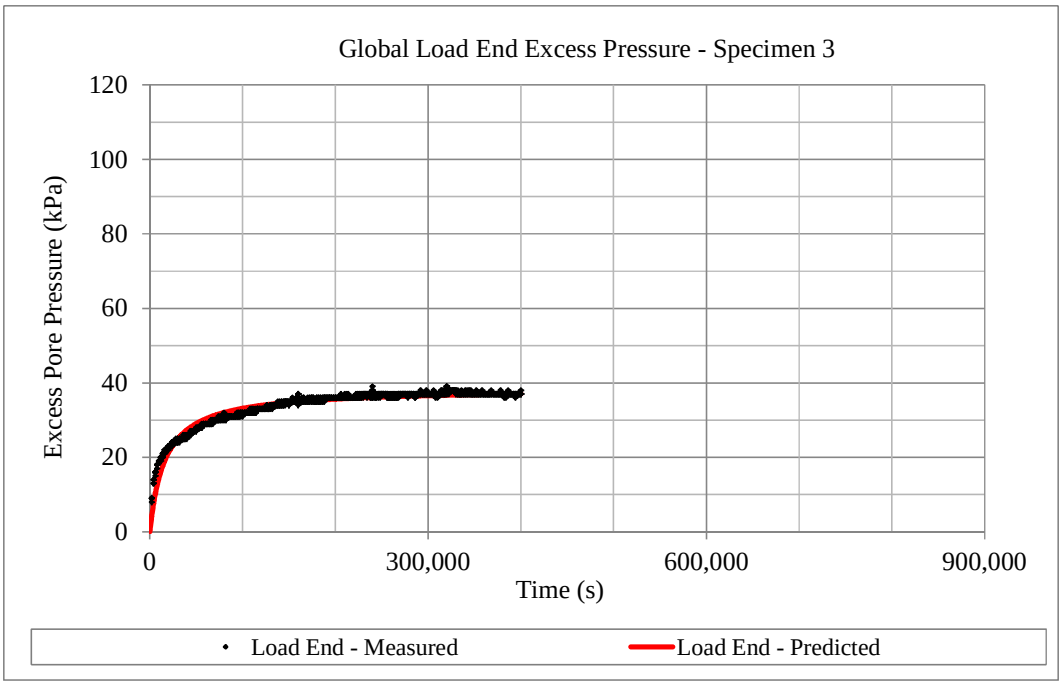
Global Load End Excess Pressure - Specimen 3
Excess Pore Pressure (kPa)
120
100
80
60
40
20
0
0
300,000
600,000
900,000
Time (s)
Load End - Measured
Load End - Predicted

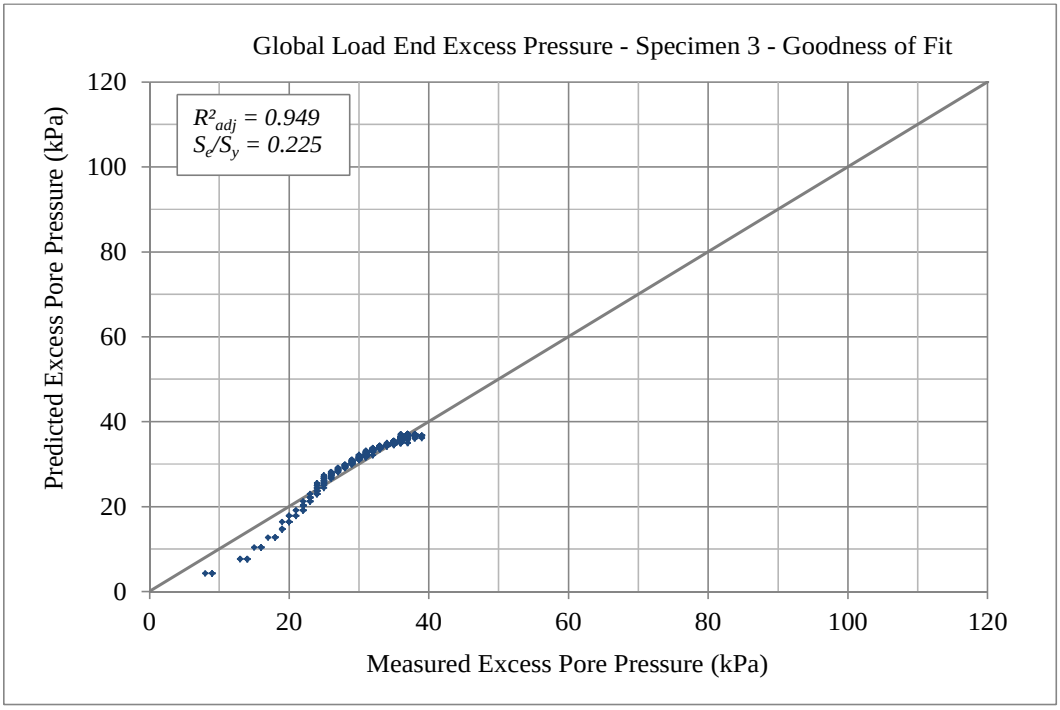
Global Load End Excess Pressure - Specimen 3 - Goodness of Fit
R^2_{adj} = 0.949
S_e/S_y = 0.225
Predicted Excess Pore Pressure (kPa)
120
100
80
60
40
20
0
0
20
40
60
80
100
120
Measured Excess Pore Pressure (kPa)

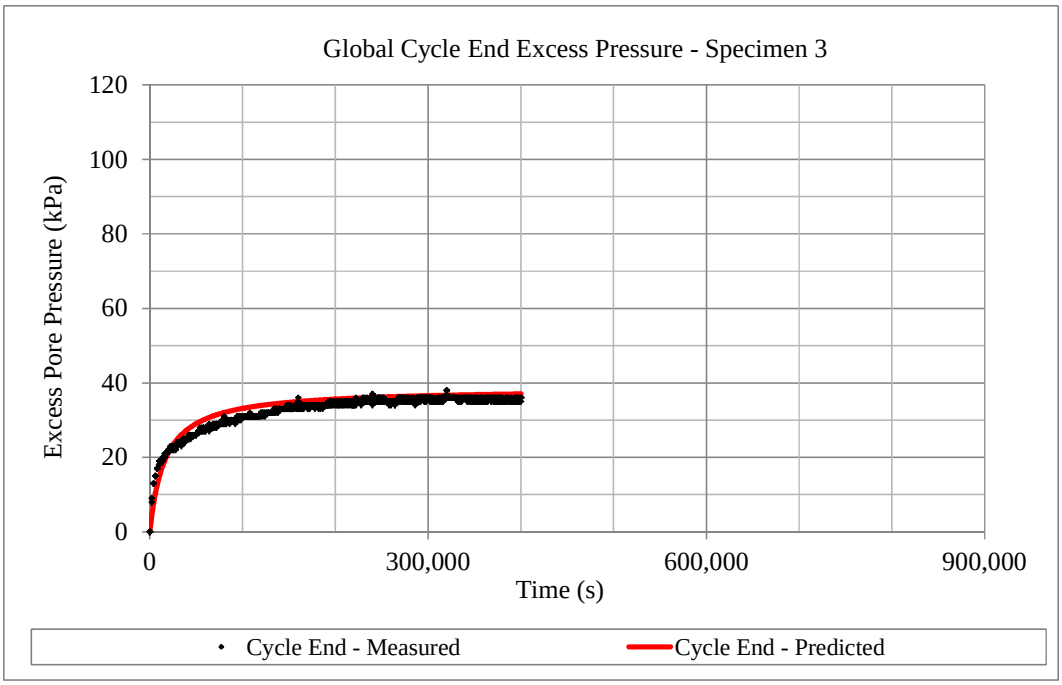
Global Cycle End Excess Pressure - Specimen 3
Excess Pore Pressure (kPa)
120
100
80
60
40
20
0
0
300,000
600,000
900,000
Time (s)
Cycle End - Measured
Cycle End - Predicted

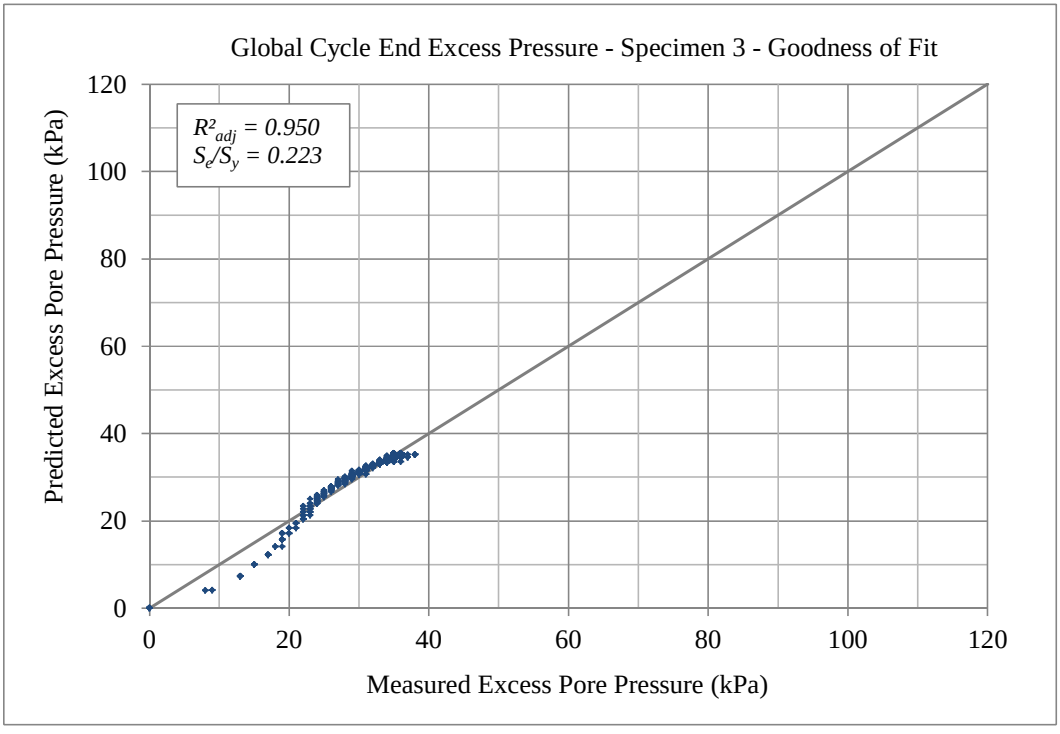
Global Cycle End Excess Pressure - Specimen 3 - Goodness of Fit
R^2_{adj} = 0.950
S_e/S_y = 0.223
Predicted Excess Pore Pressure (kPa)
120
100
80
60
40
20
0
0
20
40
60
80
100
120
Measured Excess Pore Pressure (kPa)

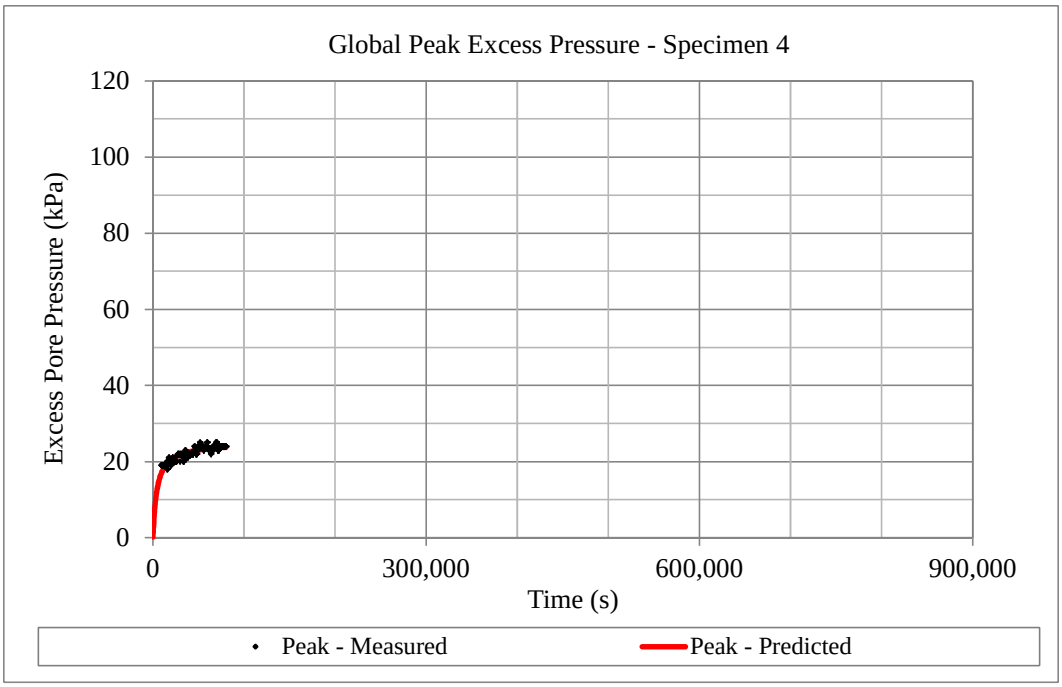
Global Peak Excess Pressure - Specimen 4
Excess Pore Pressure (kPa)
120
100
80
60
40
20
0
0
300,000
600,000
900,000
Time (s)
Peak - Measured
Peak - Predicted

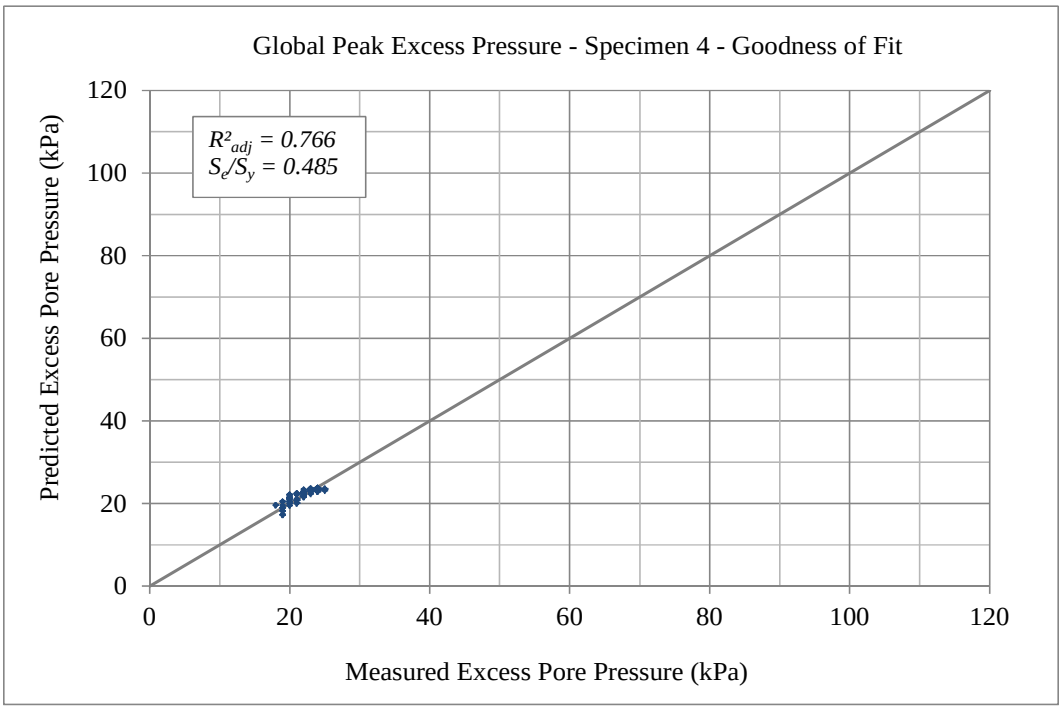
Global Peak Excess Pressure - Specimen 4 - Goodness of Fit
R^2_{adj} = 0.766
S_e/S_y = 0.485
Predicted Excess Pore Pressure (kPa)
120
100
80
60
40
20
0
0
20
40
60
80
100
120
Measured Excess Pore Pressure (kPa)

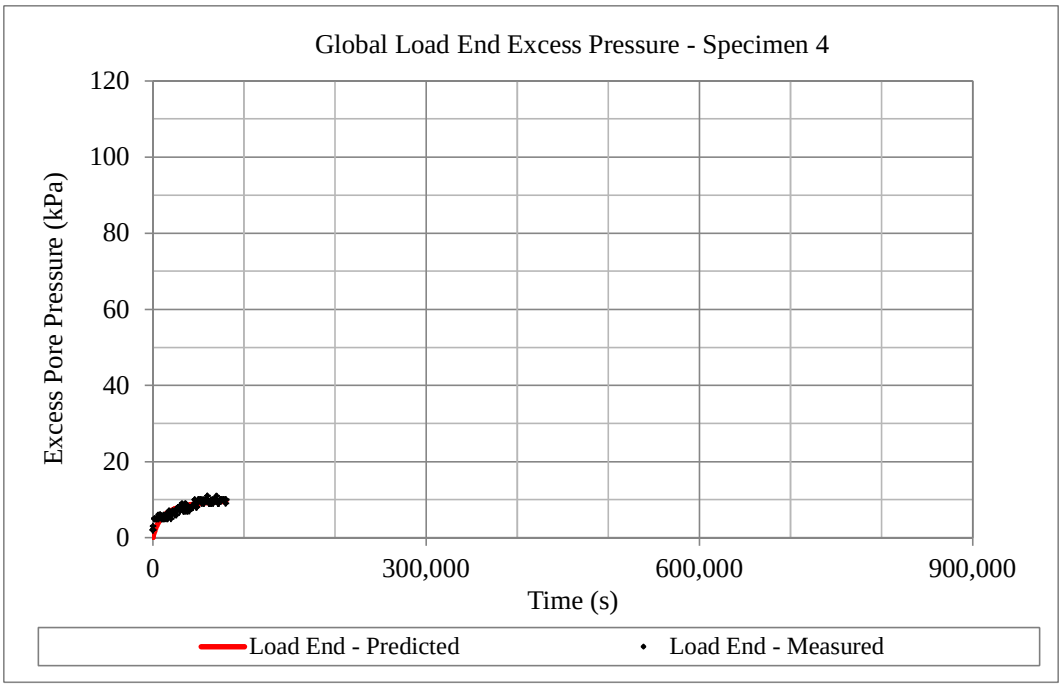
Global Load End Excess Pressure - Specimen 4
Excess Pore Pressure (kPa)
120
100
80
60
40
20
0
0
300,000
600,000
900,000
Time (s)
Load End - Predicted
Load End - Measured

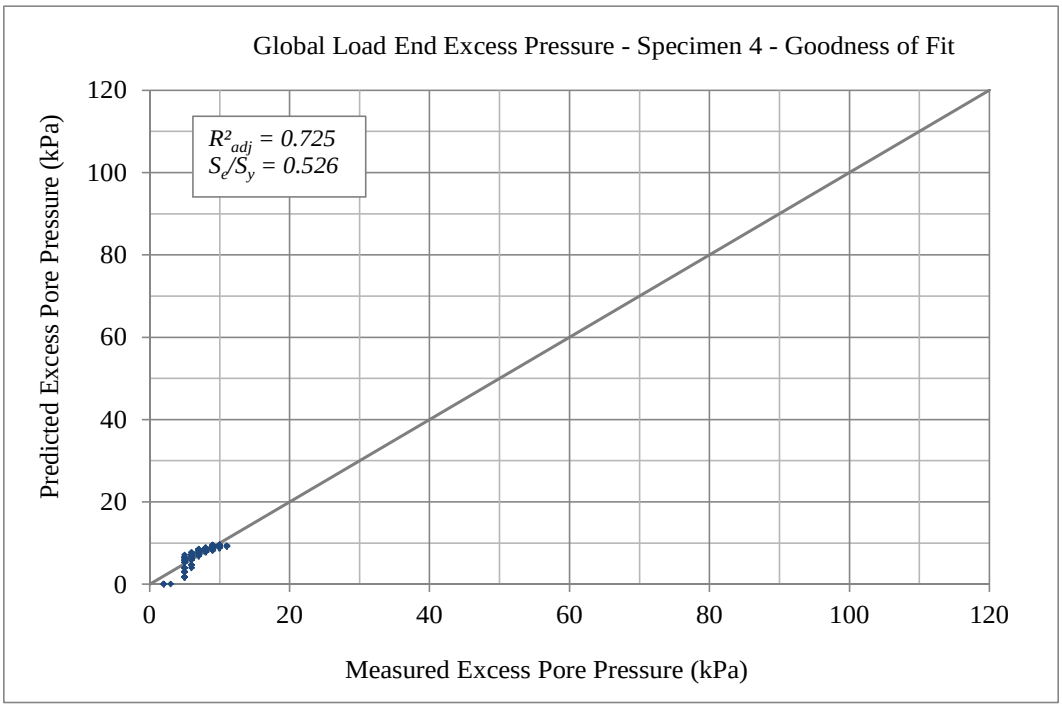
Global Load End Excess Pressure - Specimen 4 - Goodness of Fit
R^2_{adj} = 0.725
S_e/S_y = 0.526
Predicted Excess Pore Pressure (kPa)
120
100
80
60
40
20
0
0
20
40
60
80
100
120
Measured Excess Pore Pressure (kPa)

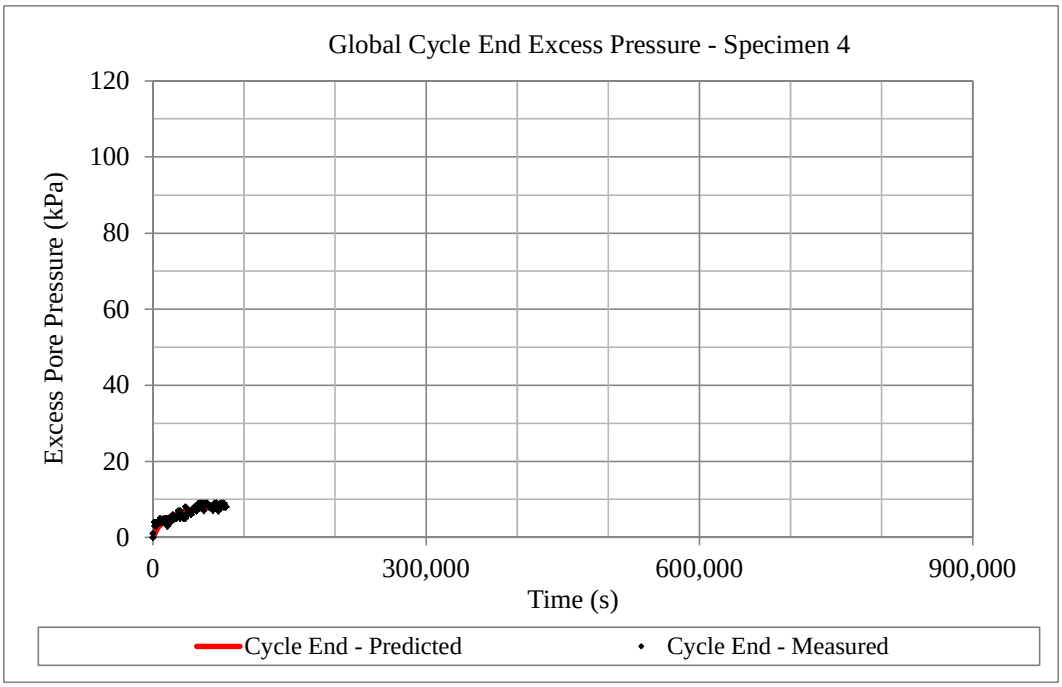
Global Cycle End Excess Pressure - Specimen 4
Excess Pore Pressure (kPa)
120
100
80
60
40
20
0
0
300,000
600,000
900,000
Time (s)
Cycle End - Predicted
Cycle End - Measured

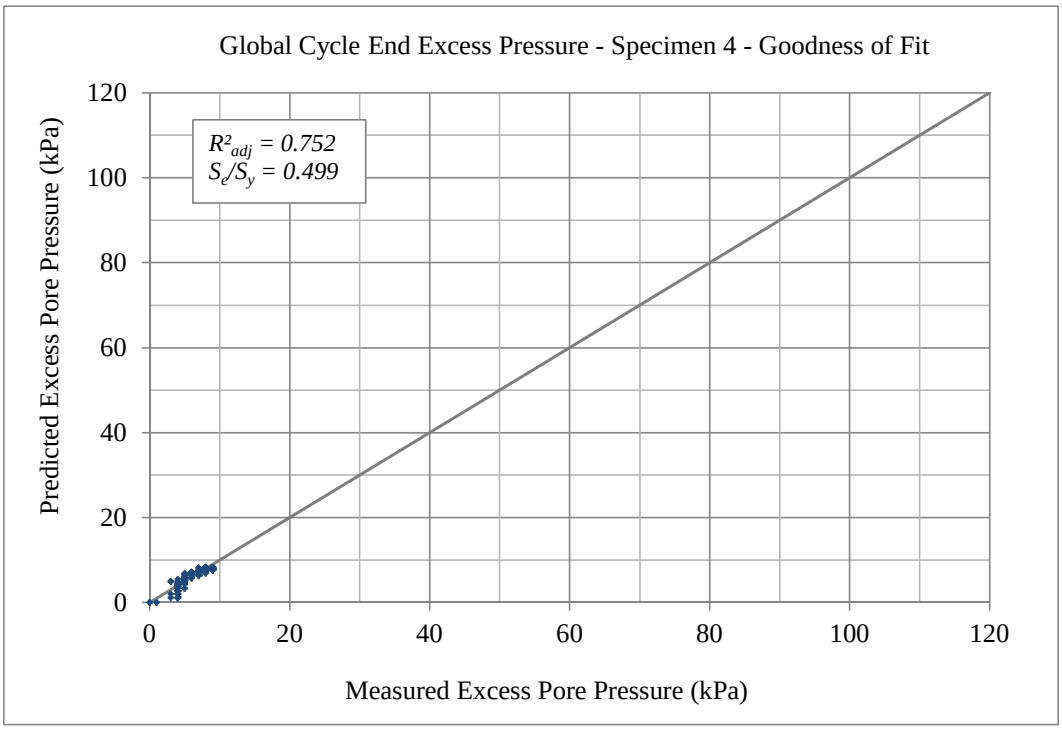
Global Cycle End Excess Pressure - Specimen 4 - Goodness of Fit
R^2_{adj} = 0.752
S_e/S_y = 0.499
Predicted Excess Pore Pressure (kPa)
120
100
80
60
40
20
0
0
20
40
60
80
100
120
Measured Excess Pore Pressure (kPa)

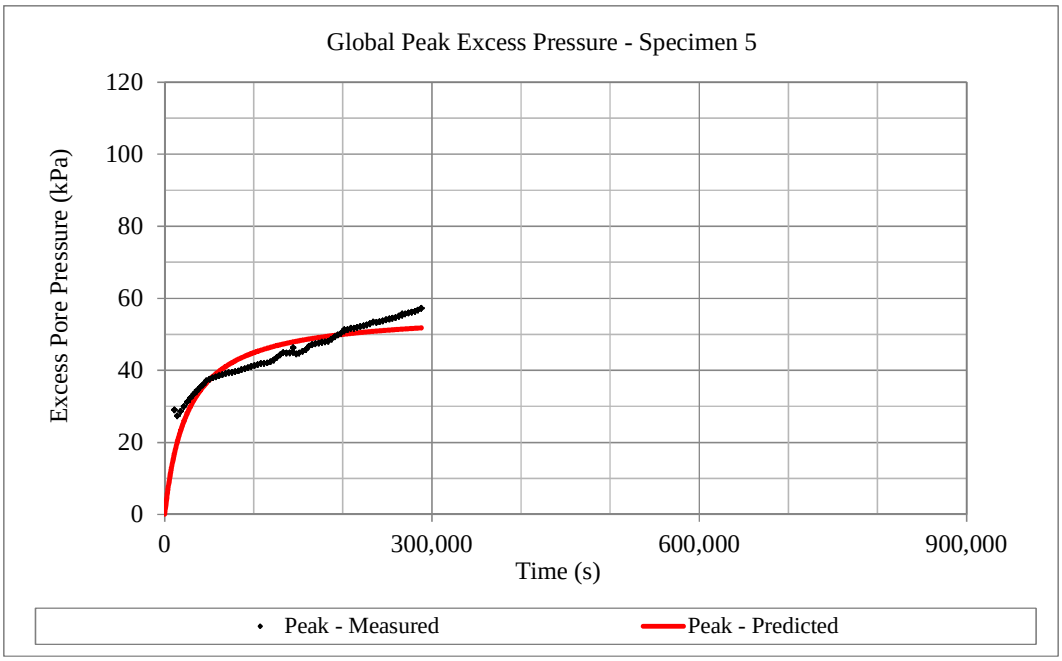
Global Peak Excess Pressure - Specimen 5
Excess Pore Pressure (kPa)
120
100
80
60
40
20
0
0
300,000
600,000
900,000
Time (s)
Peak - Measured
Peak - Predicted

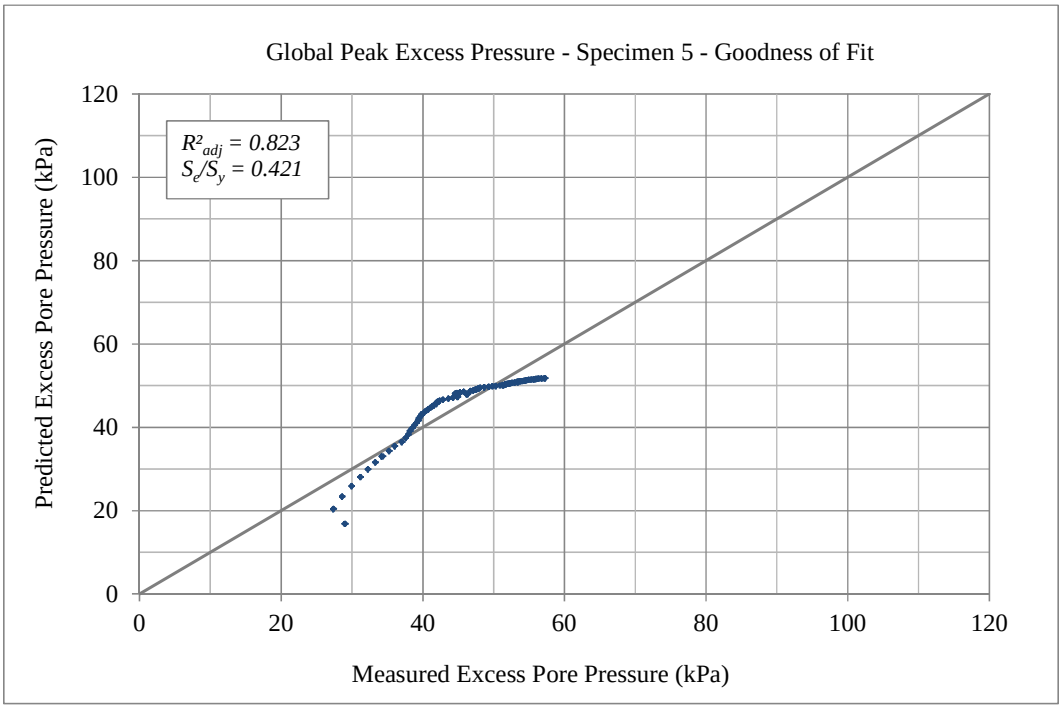
Global Peak Excess Pressure - Specimen 5 - Goodness of Fit
R^2_{adj} = 0.823
S_e/S_y = 0.421
Predicted Excess Pore Pressure (kPa)
120
100
80
60
40
20
0
0
20
40
60
80
100
120
Measured Excess Pore Pressure (kPa)

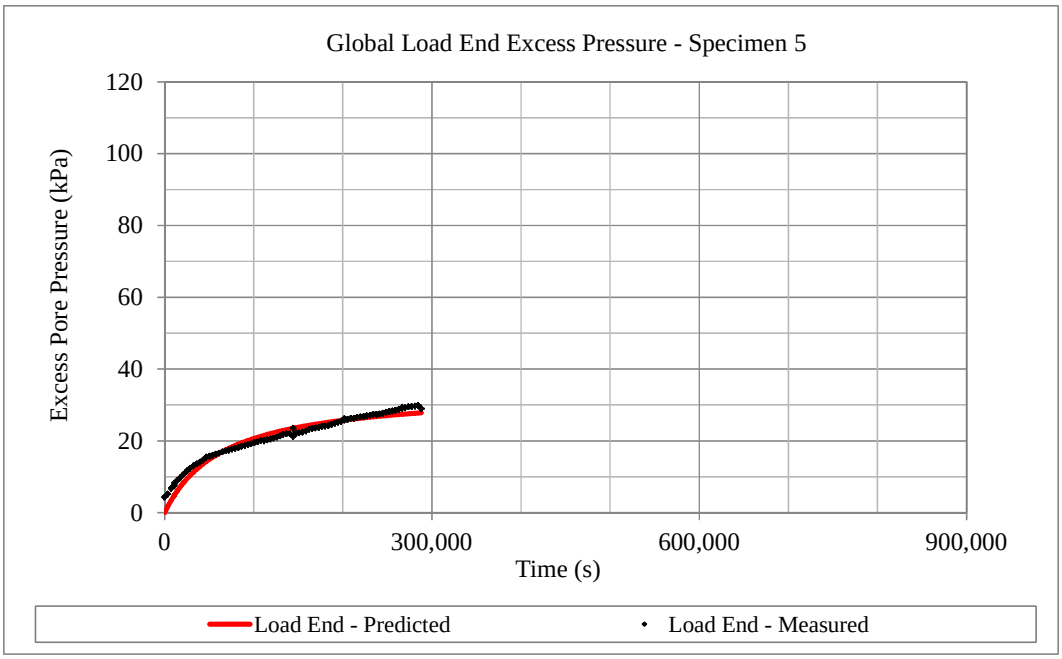
Global Load End Excess Pressure - Specimen 5
Excess Pore Pressure (kPa)
120
100
80
60
40
20
0
0
300,000
600,000
900,000
Time (s)
Load End - Predicted
Load End - Measured

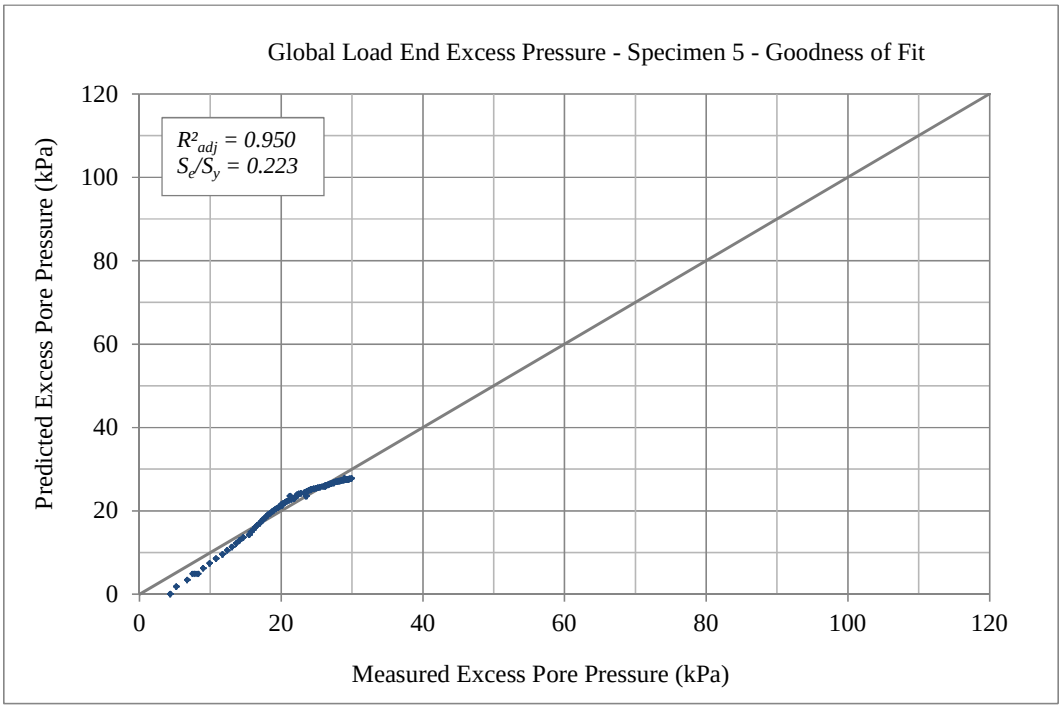
Global Load End Excess Pressure - Specimen 5 - Goodness of Fit
R^2_{adj} = 0.950
S_e/S_y = 0.223
Predicted Excess Pore Pressure (kPa)
120
100
80
60
40
20
0
0
20
40
60
80
100
120
Measured Excess Pore Pressure (kPa)

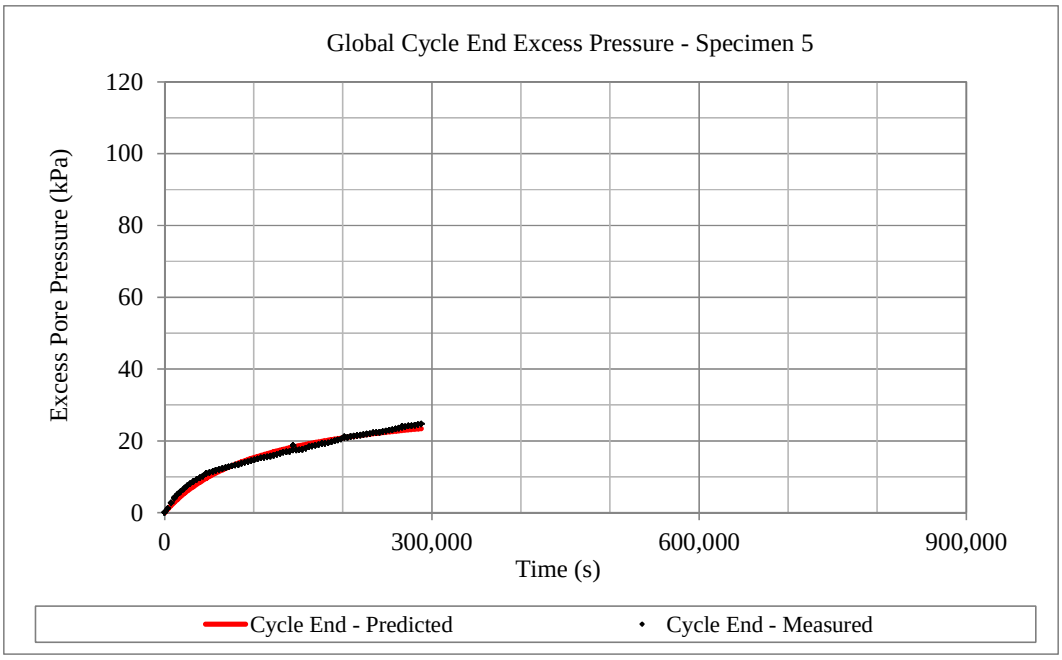
Global Cycle End Excess Pressure - Specimen 5
Excess Pore Pressure (kPa)
120
100
80
60
40
20
0
0
300,000
600,000
900,000
Time (s)
Cycle End - Predicted
Cycle End - Measured

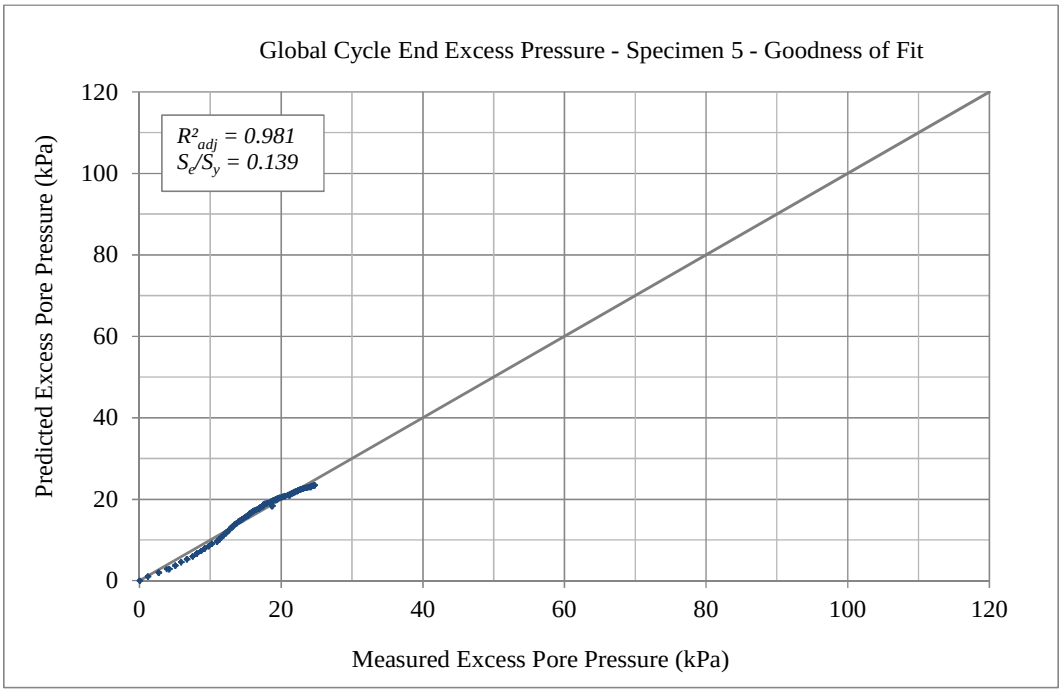
Global Cycle End Excess Pressure - Specimen 5 - Goodness of Fit
R^2_{adj} = 0.981
S_e/S_y = 0.139
Predicted Excess Pore Pressure (kPa)
120
100
80
60
40
20
0
0
20
40
60
80
100
120
Measured Excess Pore Pressure (kPa)

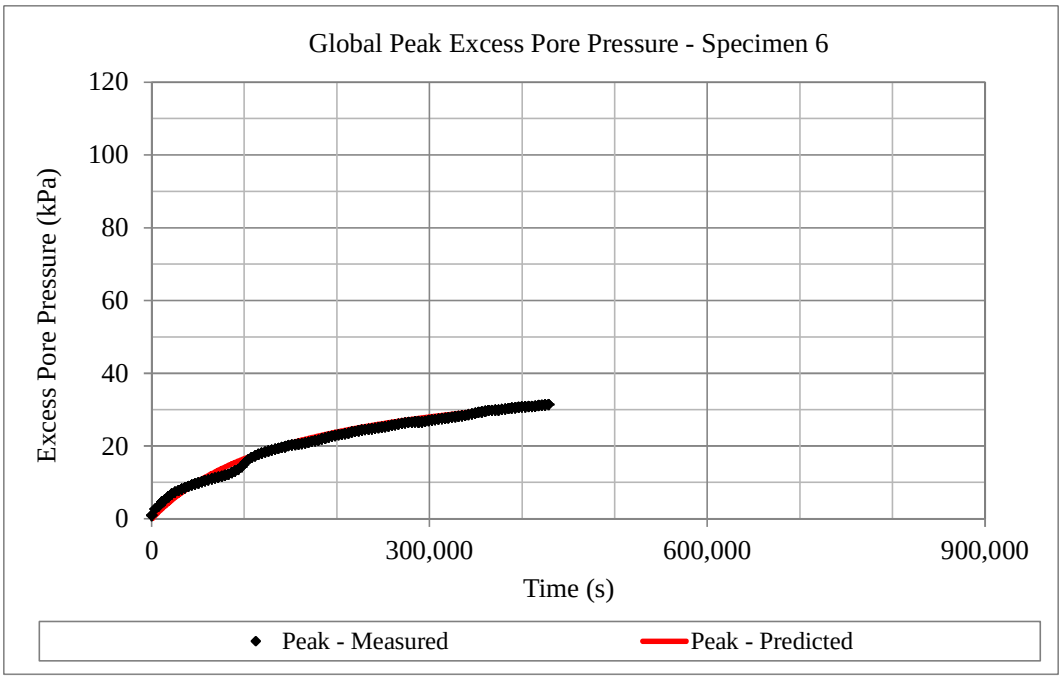
Global Peak Excess Pore Pressure - Specimen 6
Excess Pore Pressure (kPa)
120
100
80
60
40
20
0
0
300,000
600,000
900,000
Time (s)
Peak - Measured
Peak - Predicted

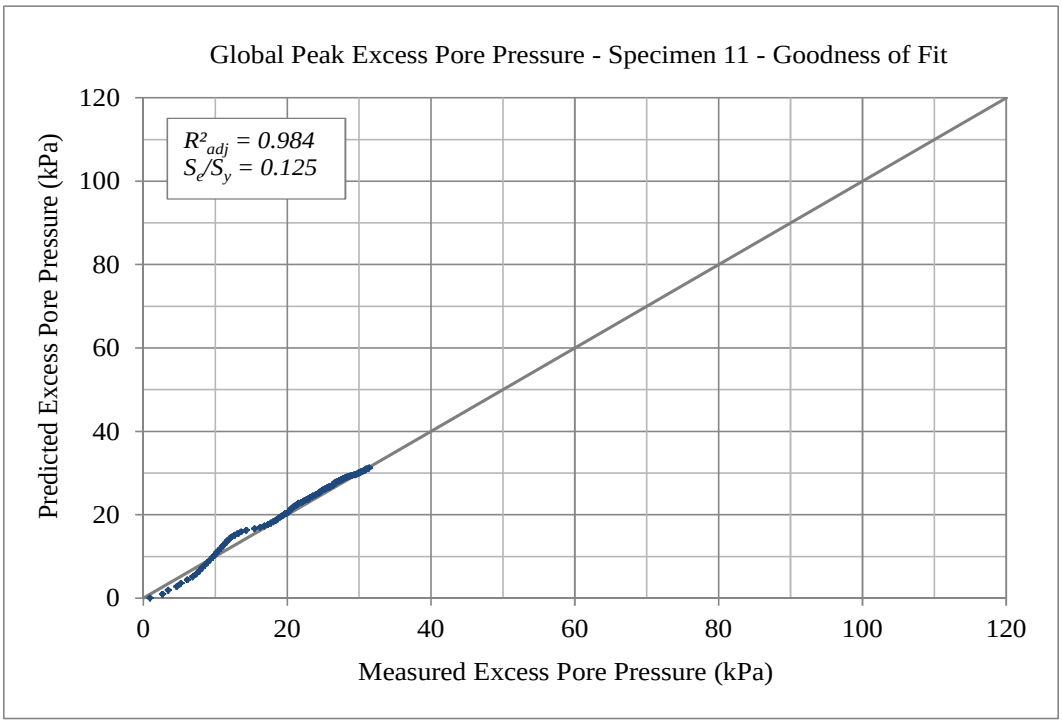
Global Peak Excess Pore Pressure - Specimen 11 - Goodness of Fit
R^2_{adj} = 0.984
S_e/S_y = 0.125
Predicted Excess Pore Pressure (kPa)
120
100
80
60
40
20
0
0
20
40
60
80
100
120
Measured Excess Pore Pressure (kPa)

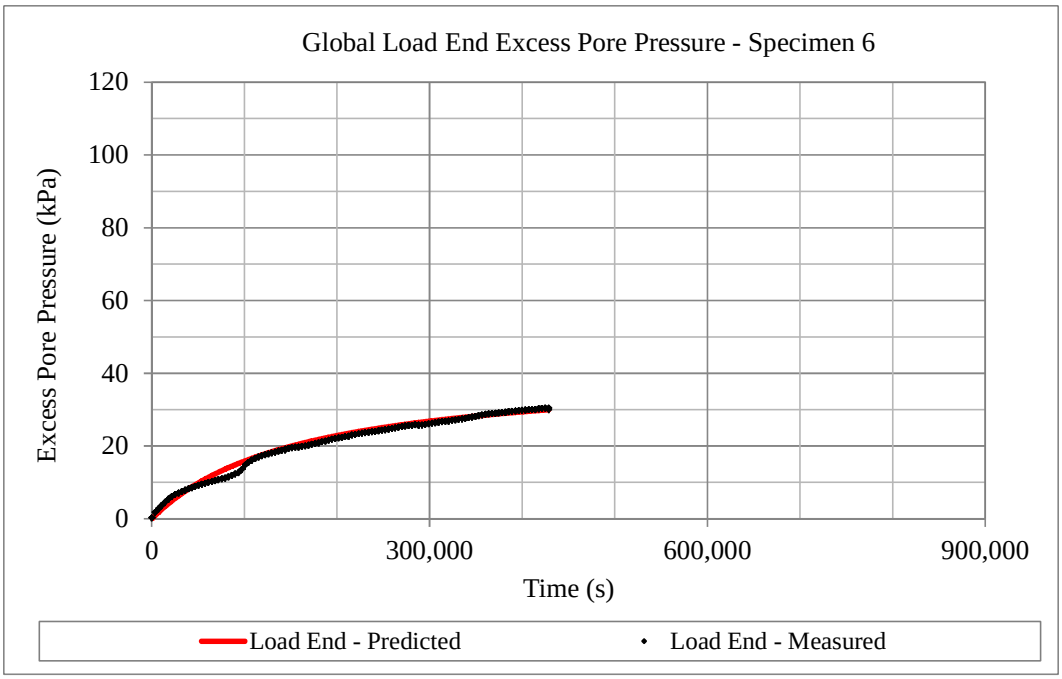
Global Load End Excess Pore Pressure - Specimen 6
Excess Pore Pressure (kPa)
120
100
80
60
40
20
0
0
300,000
600,000
900,000
Time (s)
Load End - Predicted
Load End - Measured

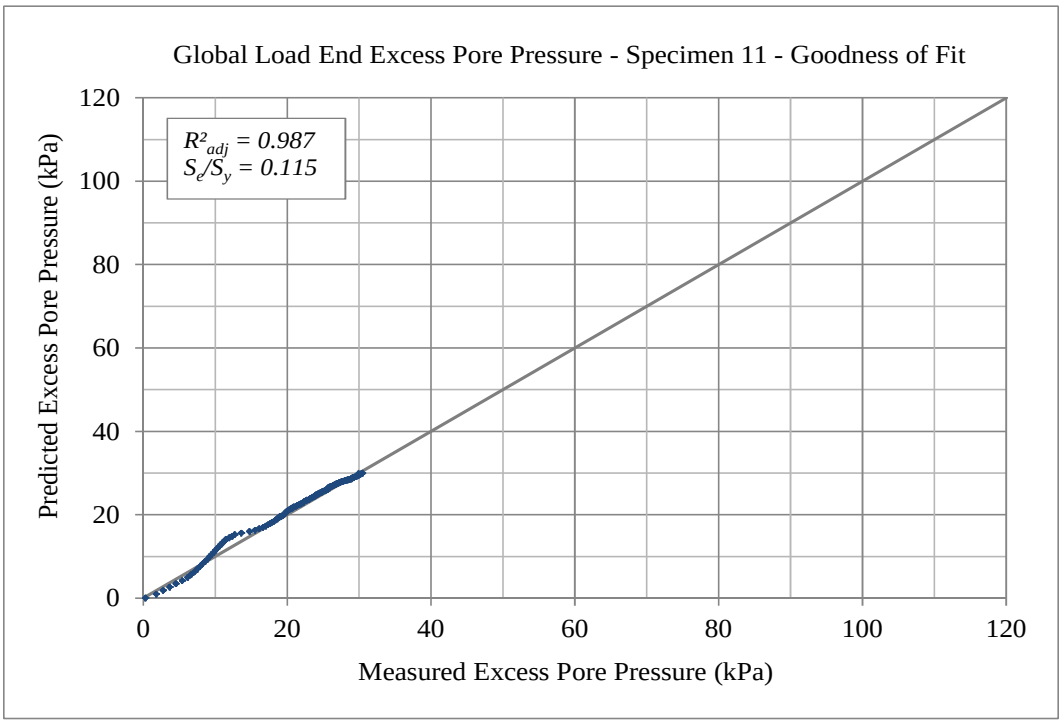
Global Load End Excess Pore Pressure - Specimen 11 - Goodness of Fit
R^2_{adj} = 0.987
S_e/S_y = 0.115
Predicted Excess Pore Pressure (kPa)
120
100
80
60
40
20
0
0
20
40
60
80
100
120
Measured Excess Pore Pressure (kPa)

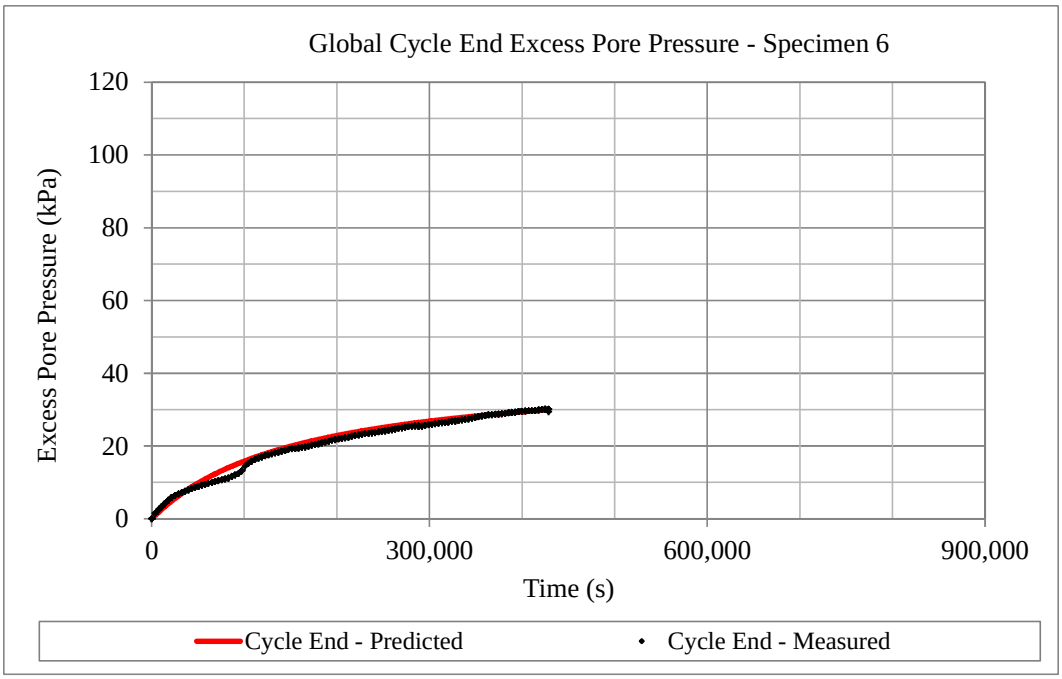
Global Cycle End Excess Pore Pressure - Specimen 6
Excess Pore Pressure (kPa)
120
100
80
60
40
20
0
0
300,000
600,000
900,000
Time (s)
Cycle End - Predicted
Cycle End - Measured

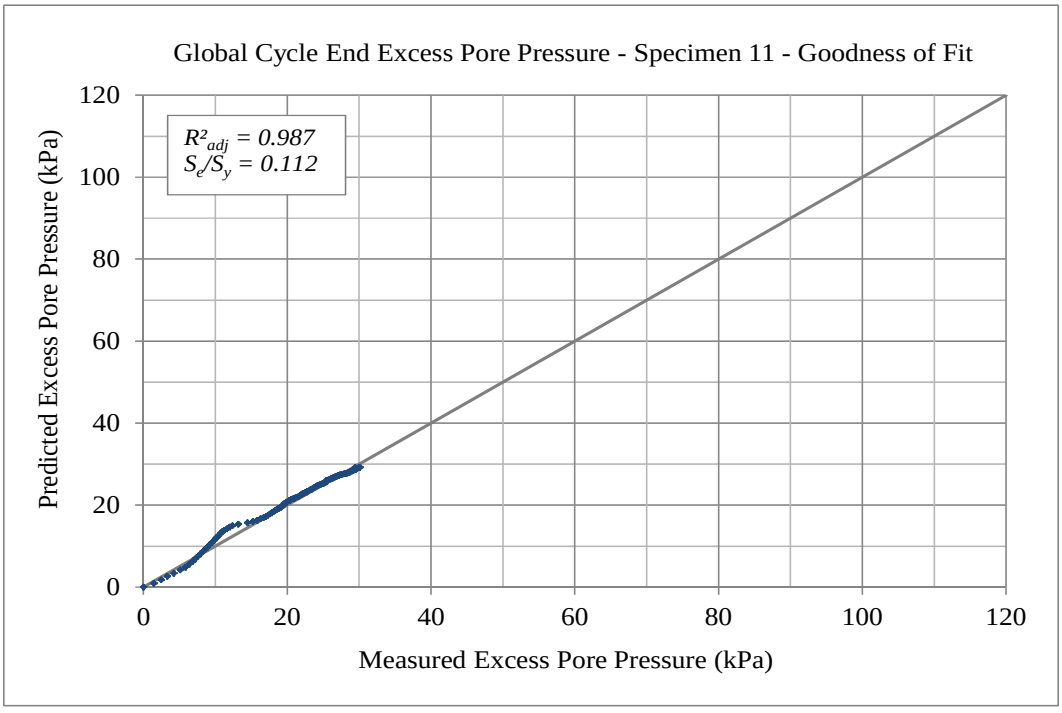
Global Cycle End Excess Pore Pressure - Specimen 11 - Goodness of Fit
R^2_{adj} = 0.987
S_e/S_y = 0.112
Predicted Excess Pore Pressure (kPa)
120
100
80
60
40
20
0
0
20
40
60
80
100
120
Measured Excess Pore Pressure (kPa)

APPENDIX C

GOODNESS OF FIT PLOTS FOR THE *p* PARAMETER

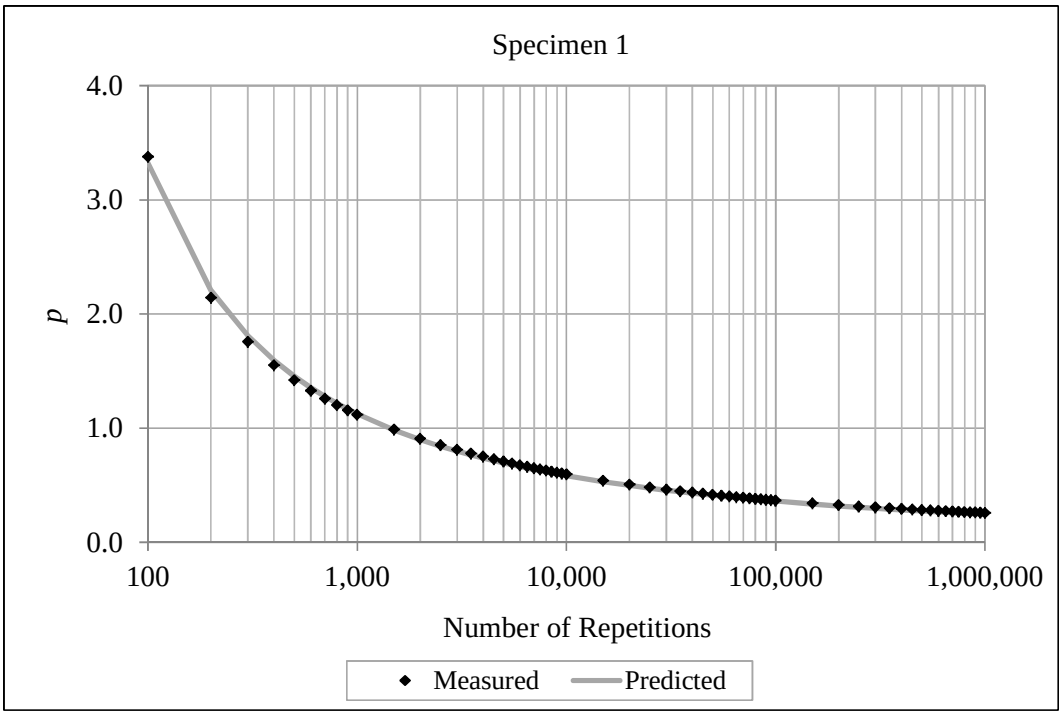
Specimen 1
4.0
3.0
2.0
1.0
0.0
p
100
1,000
10,000
100,000
1,000,000
Number of Repetitions
Measured
Predicted

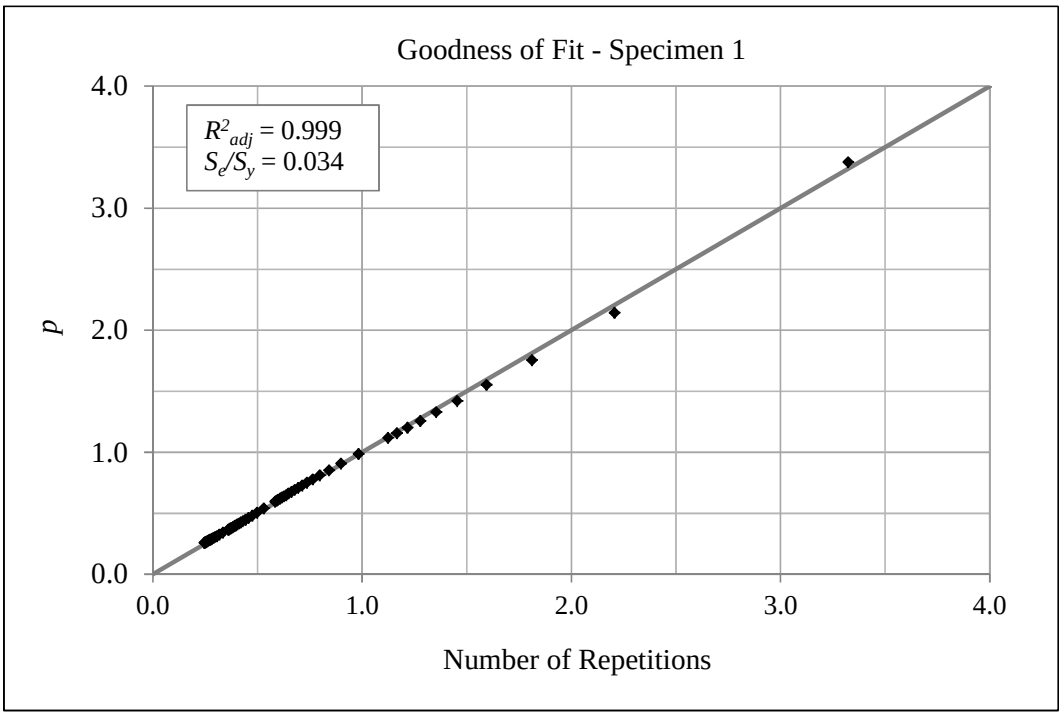
Goodness of Fit - Specimen 1
R^2_{adj} = 0.999
S_e/S_y = 0.034
4.0
3.0
2.0
1.0
0.0
p
0.0
1.0
2.0
3.0
4.0
Number of Repetitions

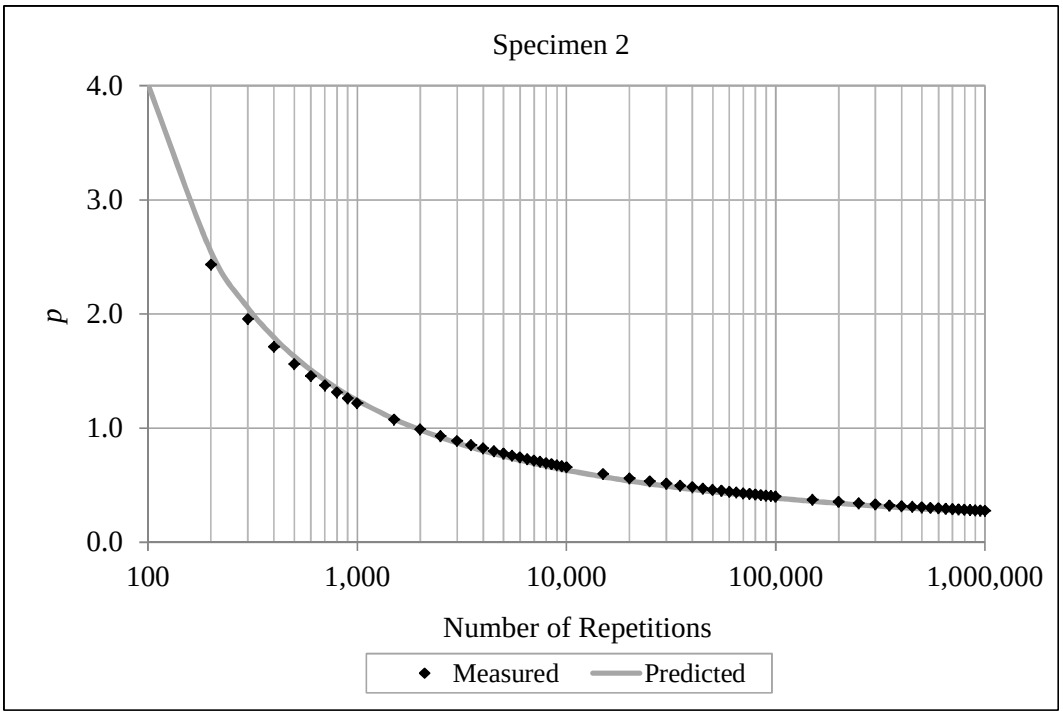
Specimen 2
4.0
3.0
2.0
1.0
0.0
p
100
1,000
10,000
100,000
1,000,000
Number of Repetitions
Measured
Predicted

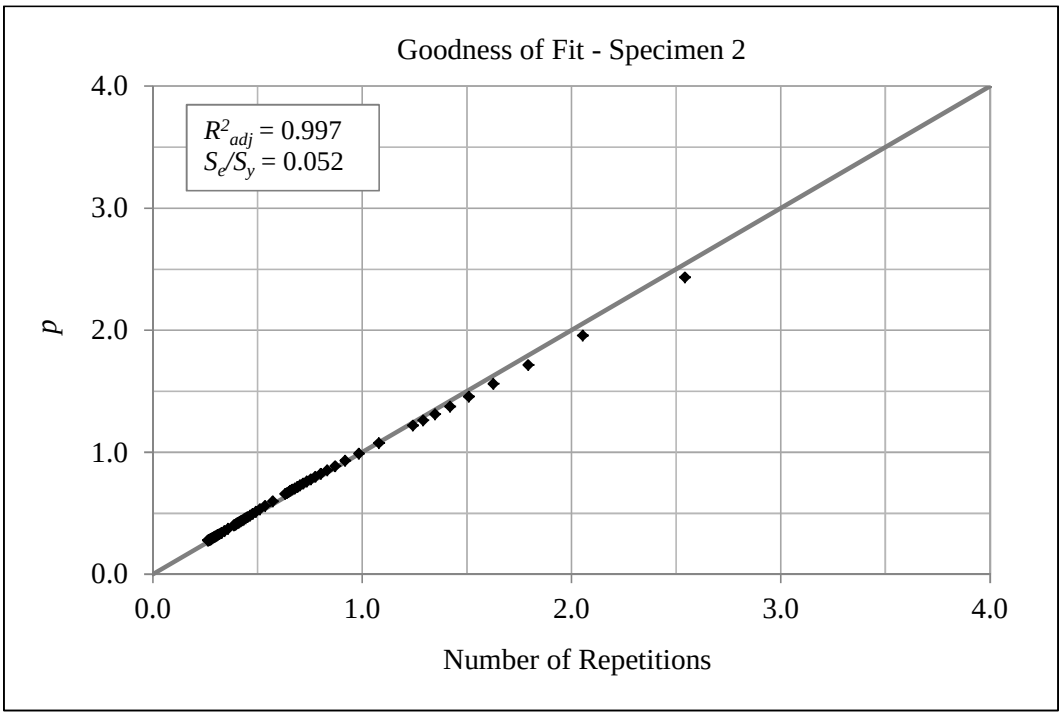
Goodness of Fit - Specimen 2
R^2_{adj} = 0.997
S_e/S_y = 0.052
4.0
3.0
2.0
1.0
0.0
p
0.0
1.0
2.0
3.0
4.0
Number of Repetitions

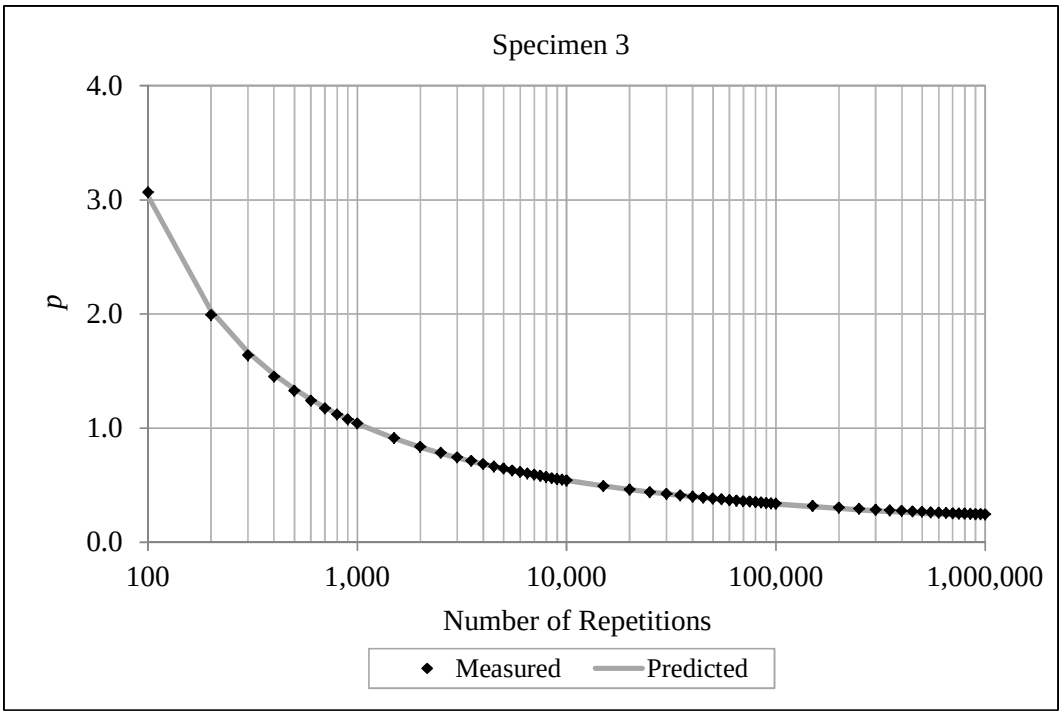
Specimen 3
4.0
3.0
2.0
1.0
0.0
p
100
1,000
10,000
100,000
1,000,000
Number of Repetitions
Measured
Predicted

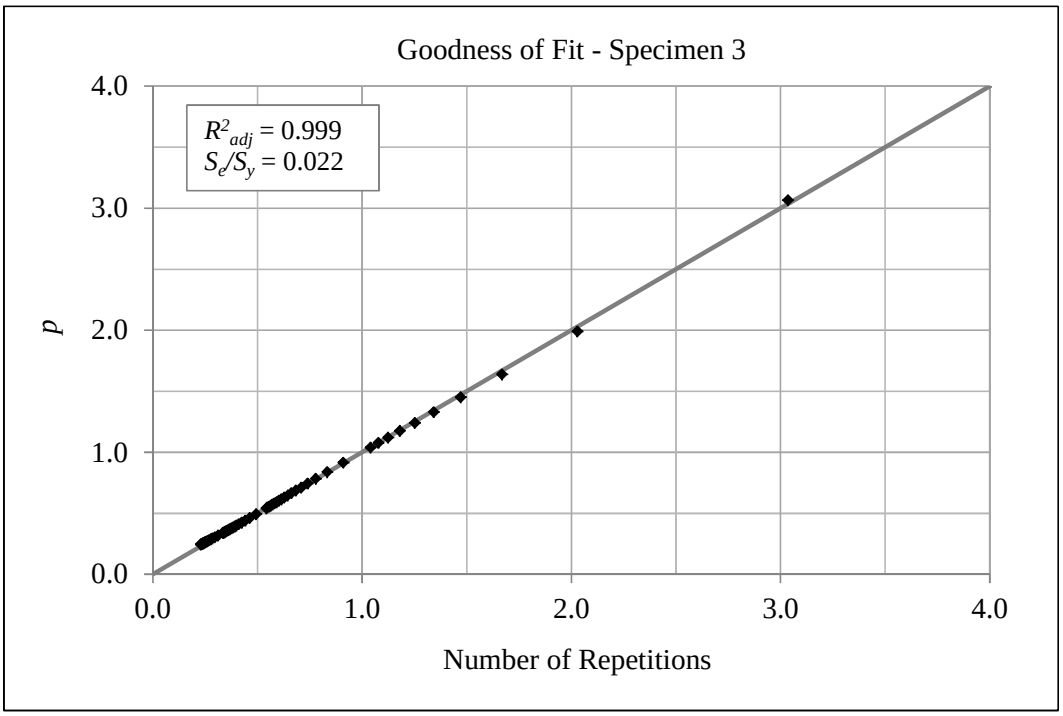
Goodness of Fit - Specimen 3
R^2_{adj} = 0.999
S_e/S_y = 0.022
4.0
3.0
2.0
1.0
0.0
p
0.0
1.0
2.0
3.0
4.0
Number of Repetitions

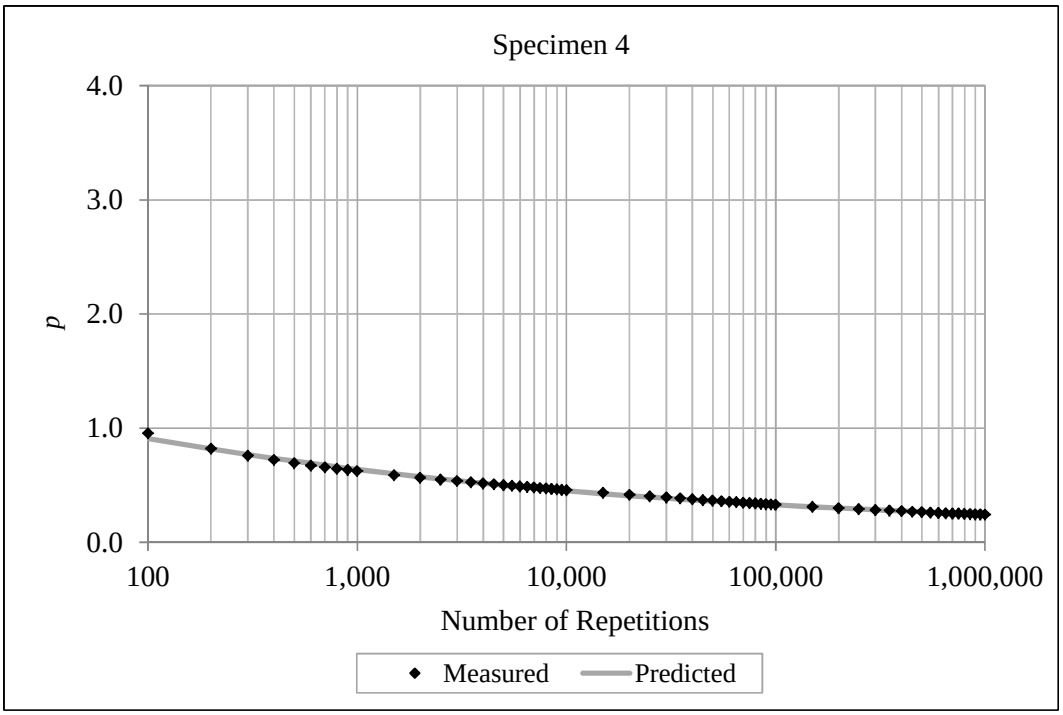
Specimen 4
4.0
3.0
2.0
1.0
0.0
p
100
1,000
10,000
100,000
1,000,000
Number of Repetitions
Measured
Predicted

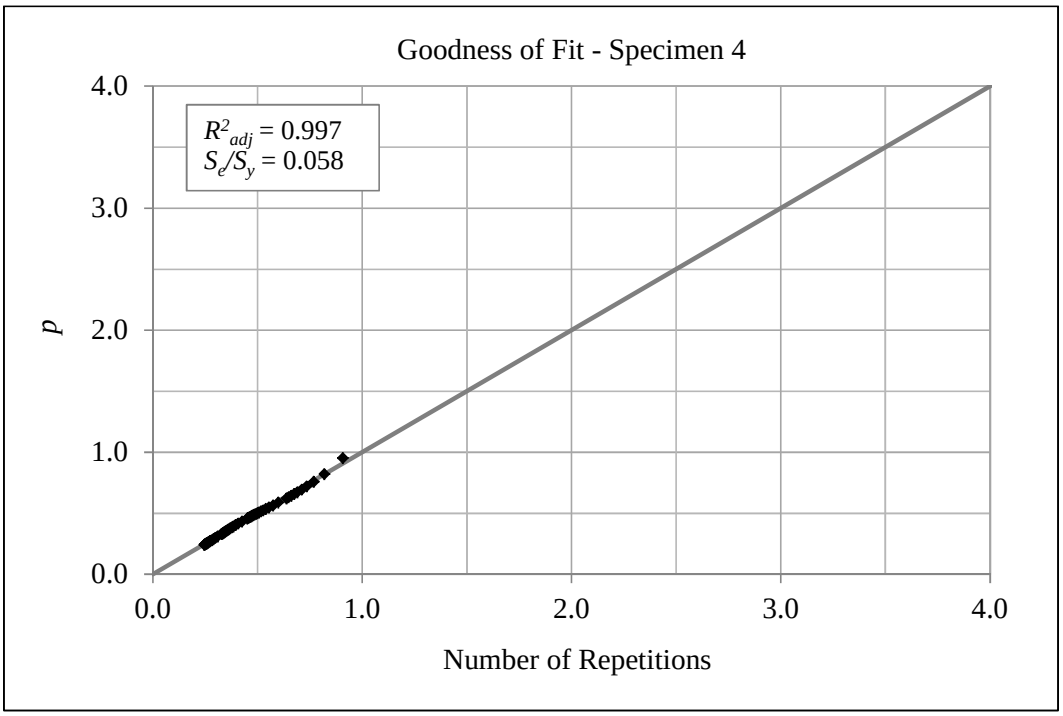
Goodness of Fit - Specimen 4
R^2_{adj} = 0.997
S_e/S_y = 0.058
4.0
3.0
2.0
1.0
0.0
p
0.0
1.0
2.0
3.0
4.0
Number of Repetitions

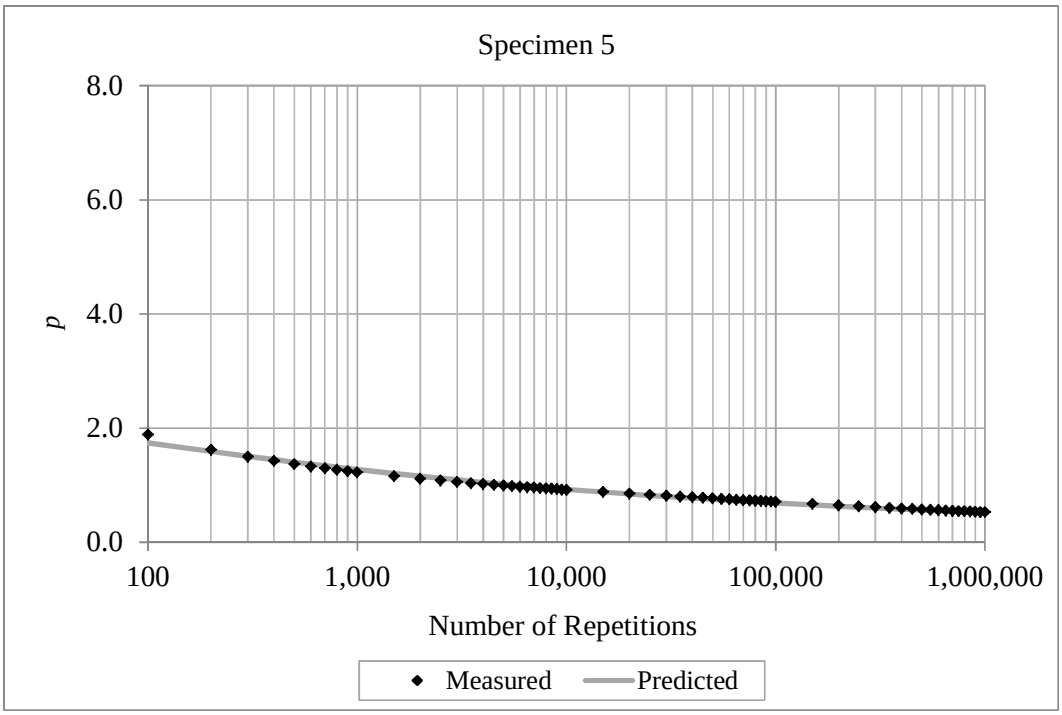
Specimen 5
8.0
6.0
4.0
2.0
0.0
p
100
1,000
10,000
100,000
1,000,000
Number of Repetitions
Measured
Predicted

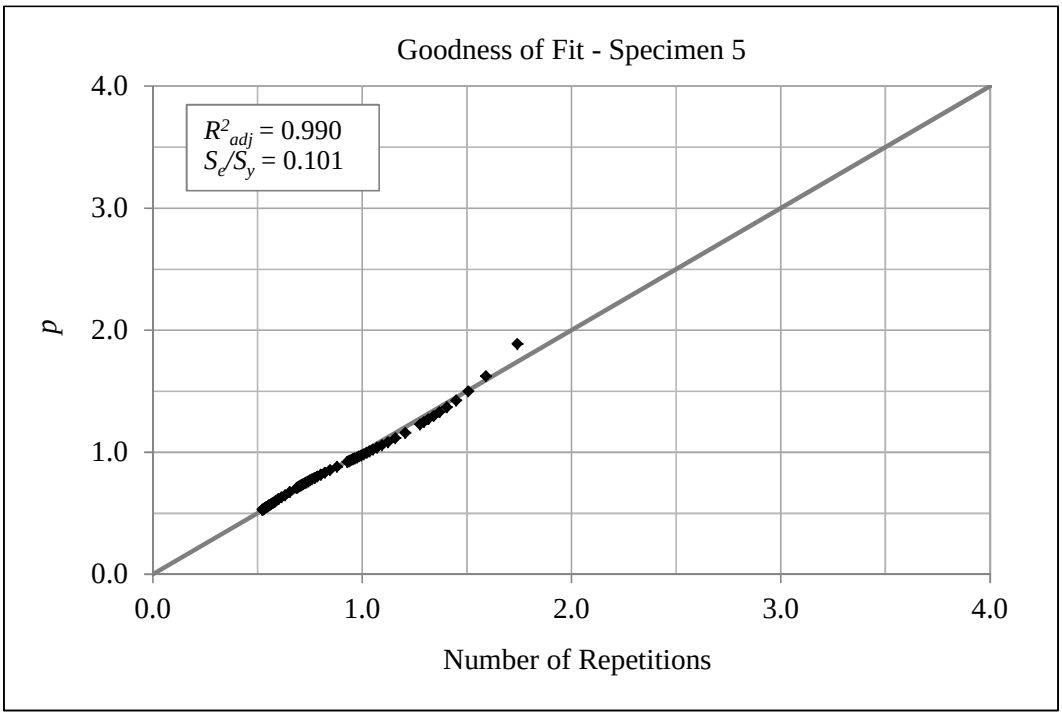
Goodness of Fit - Specimen 5
R^2_{adj} = 0.990
S_e/S_y = 0.101
4.0
3.0
2.0
1.0
0.0
p
0.0
1.0
2.0
3.0
4.0
Number of Repetitions

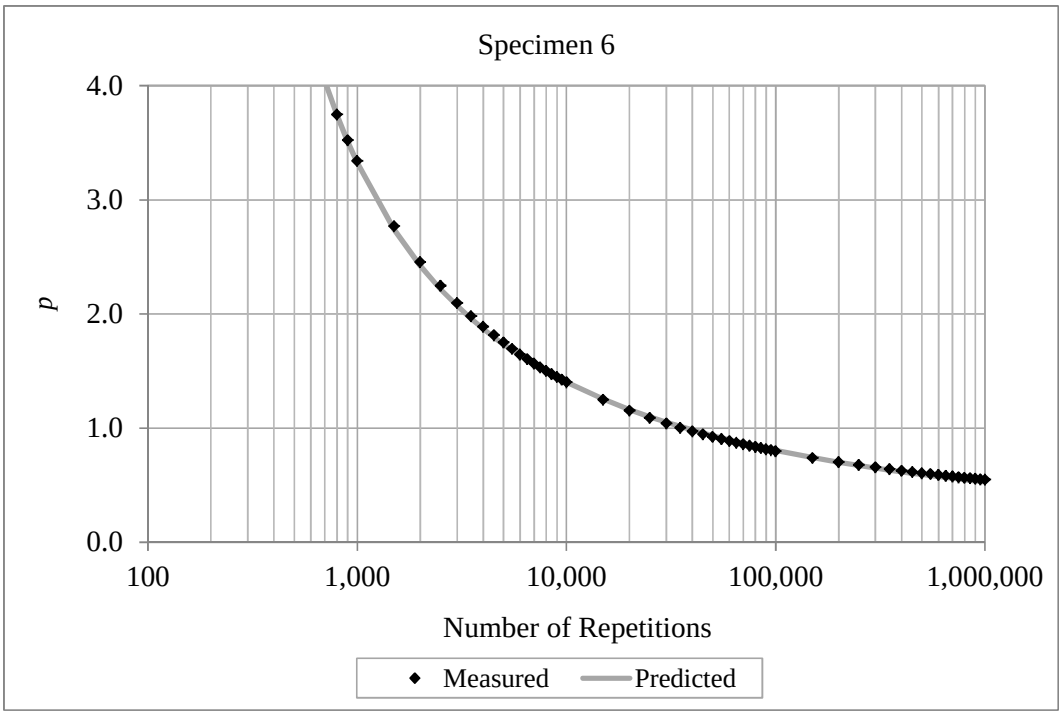
Specimen 6
4.0
3.0
2.0
1.0
0.0
p
100
1,000
10,000
100,000
1,000,000
Number of Repetitions
Measured
Predicted

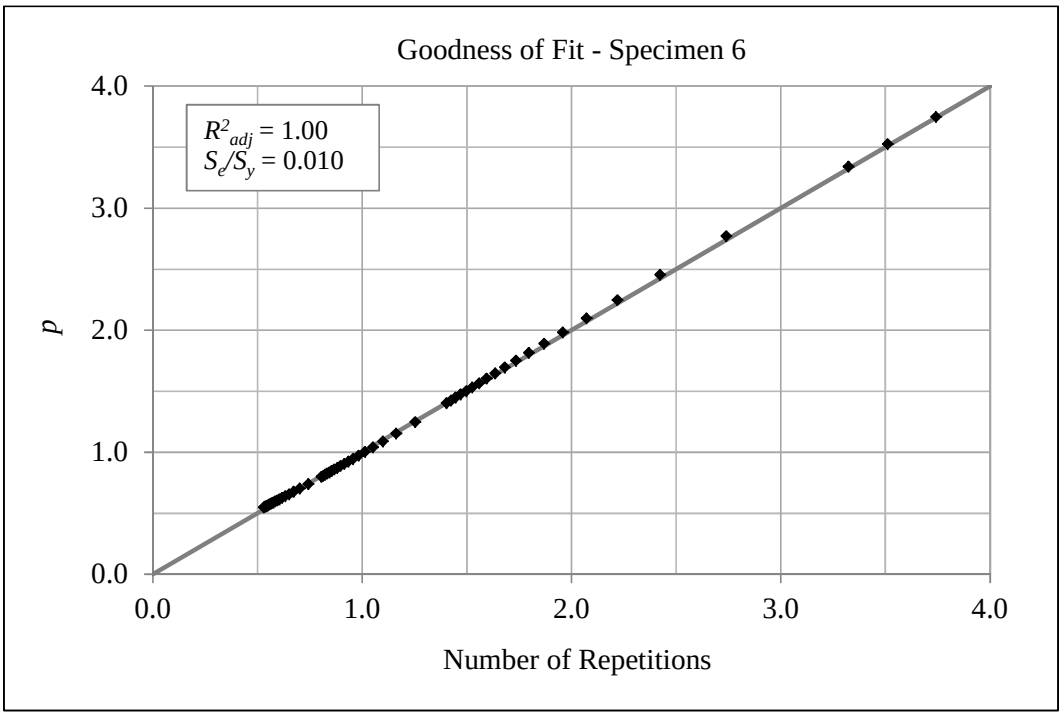
Goodness of Fit - Specimen 6
R^2_{adj} = 1.00
S_e/S_y = 0.010
4.0
3.0
2.0
1.0
0.0
p
0.0
1.0
2.0
3.0
4.0
Number of Repetitions

APPENDIX D

SIMULATION RESULTS AND GOODNESS OF FIT PLOTS

FOR THE PEAK AND RESIDUAL EXCESS PRESSURES

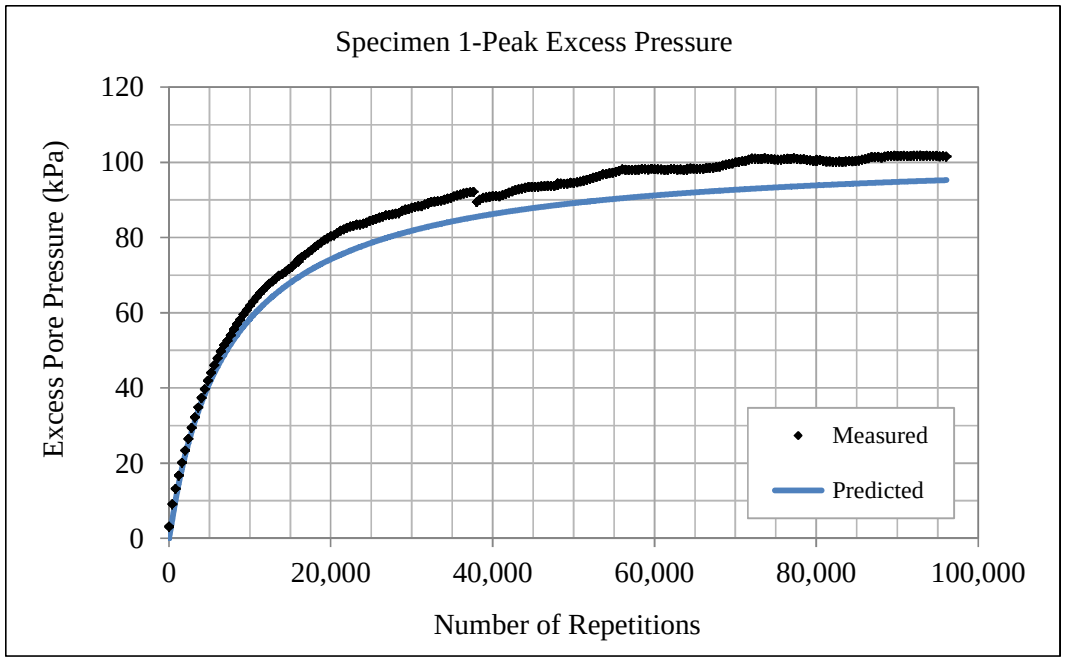
Specimen 1-Peak Excess Pressure
Excess Pore Pressure (kPa)
120
100
80
60
40
20
0
0
20,000
40,000
60,000
80,000
100,000
Number of Repetitions
Measured
Predicted

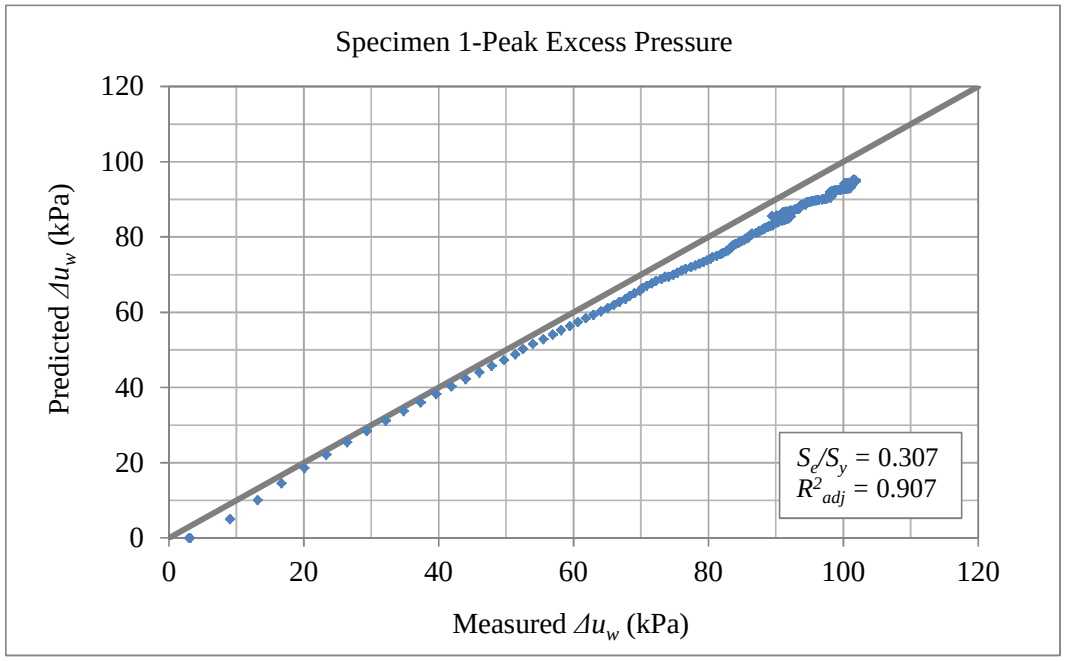
Specimen 1-Peak Excess Pressure
Predicted Δu_w (kPa)
120
100
80
60
40
20
0
0
20
40
60
80
100
120
Measured Δu_w (kPa)
S_e/S_y = 0.307
R^2_{adj} = 0.907

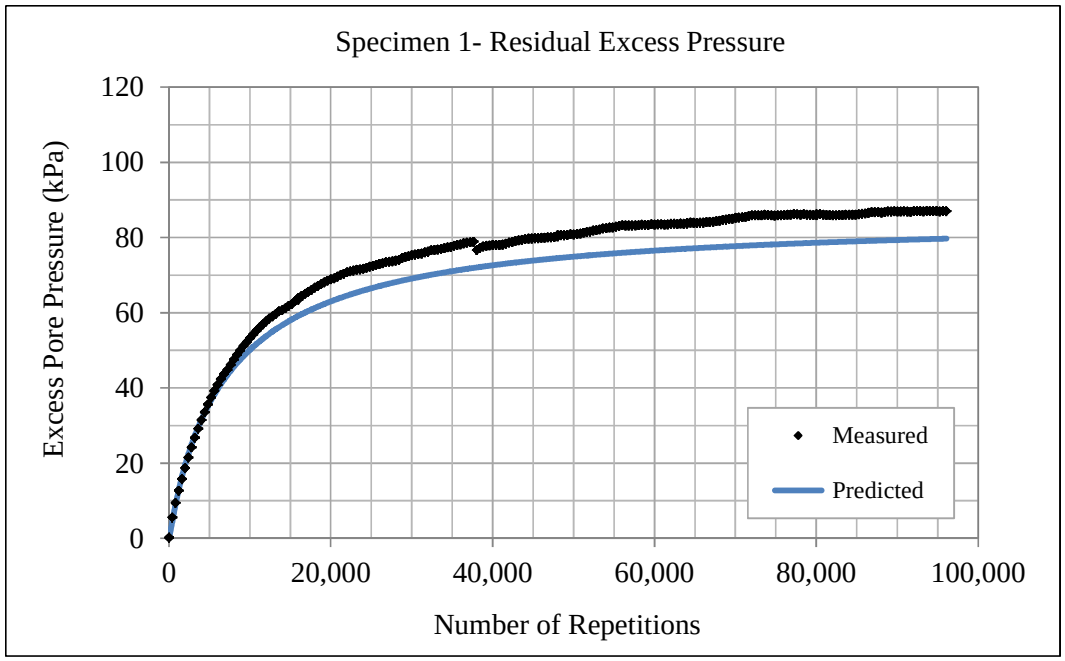
Specimen 1- Residual Excess Pressure
Excess Pore Pressure (kPa)
120
100
80
60
40
20
0
0
20,000
40,000
60,000
80,000
100,000
Number of Repetitions
Measured
Predicted

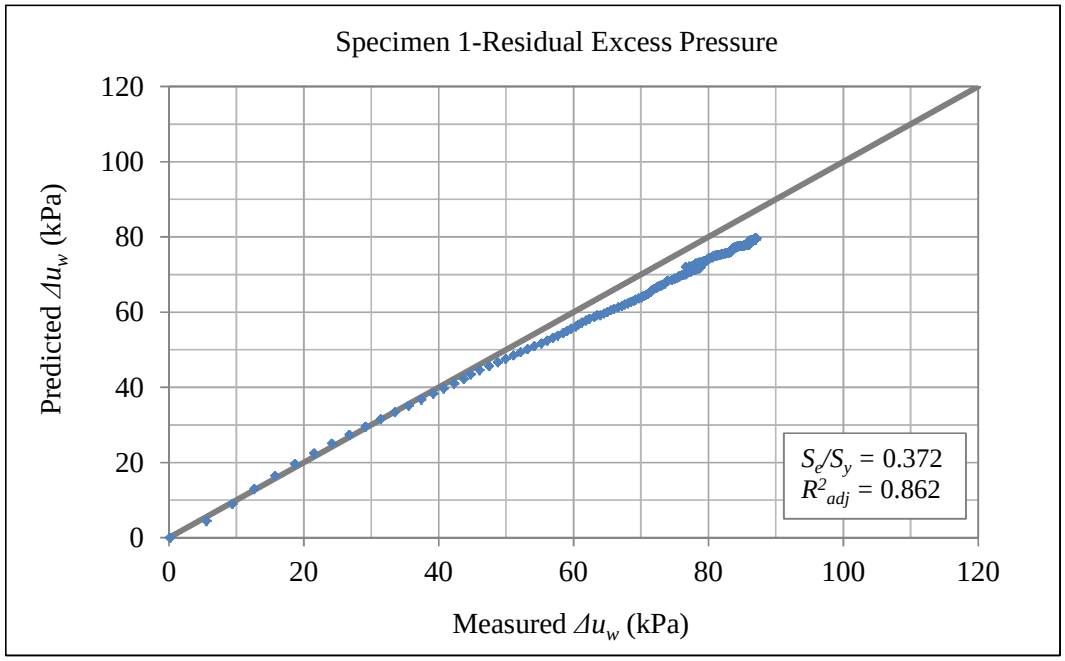
Specimen 1-Residual Excess Pressure
Predicted Δu_w (kPa)
120
100
80
60
40
20
0
0
20
40
60
80
100
120
Measured Δu_w (kPa)
S_e/S_y = 0.372
R^2_{adj} = 0.862

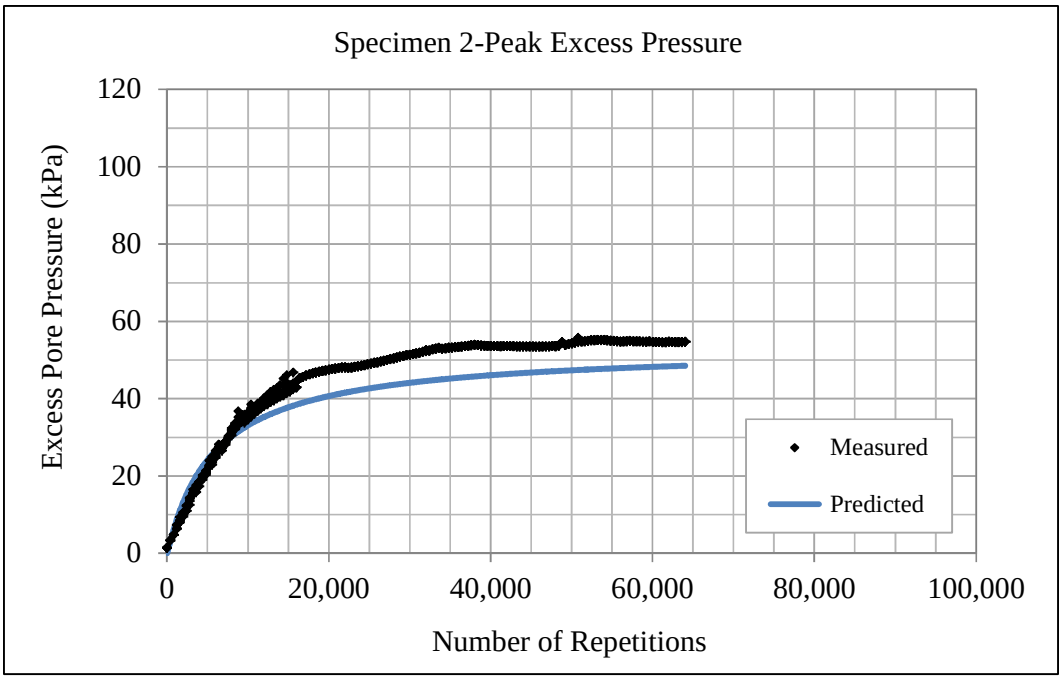
Specimen 2-Peak Excess Pressure
Excess Pore Pressure (kPa)
120
100
80
60
40
20
0
0
20,000
40,000
60,000
80,000
100,000
Number of Repetitions
Measured
Predicted

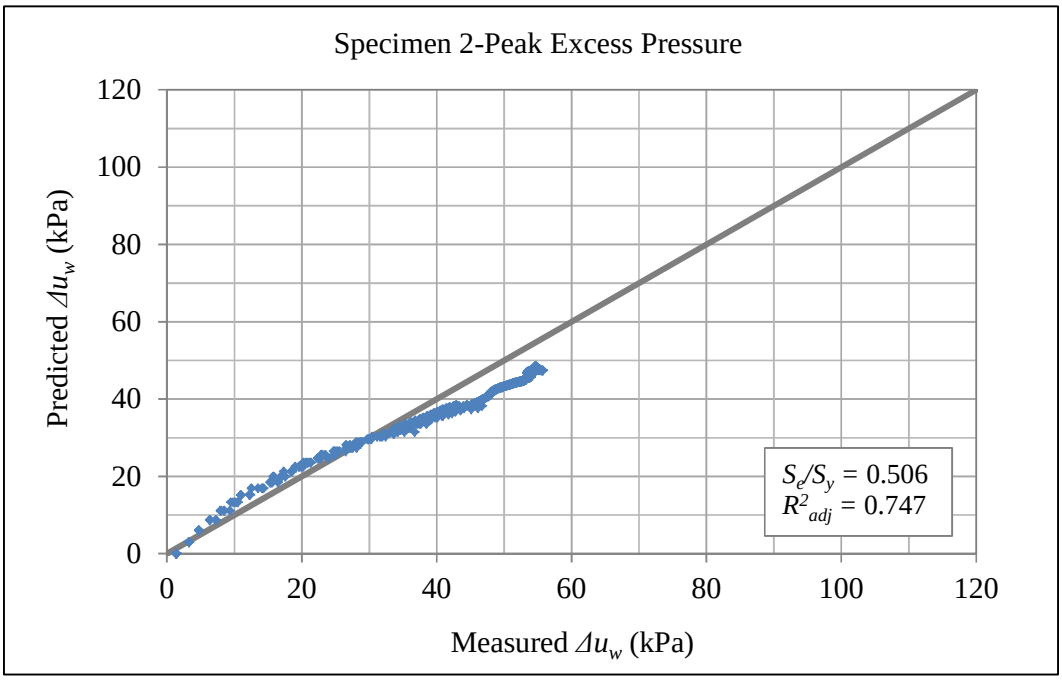
Specimen 2-Peak Excess Pressure
Predicted Δu_w (kPa)
120
100
80
60
40
20
0
0
20
40
60
80
100
120
Measured Δu_w (kPa)
S_e/S_y = 0.506
R^2_{adj} = 0.747

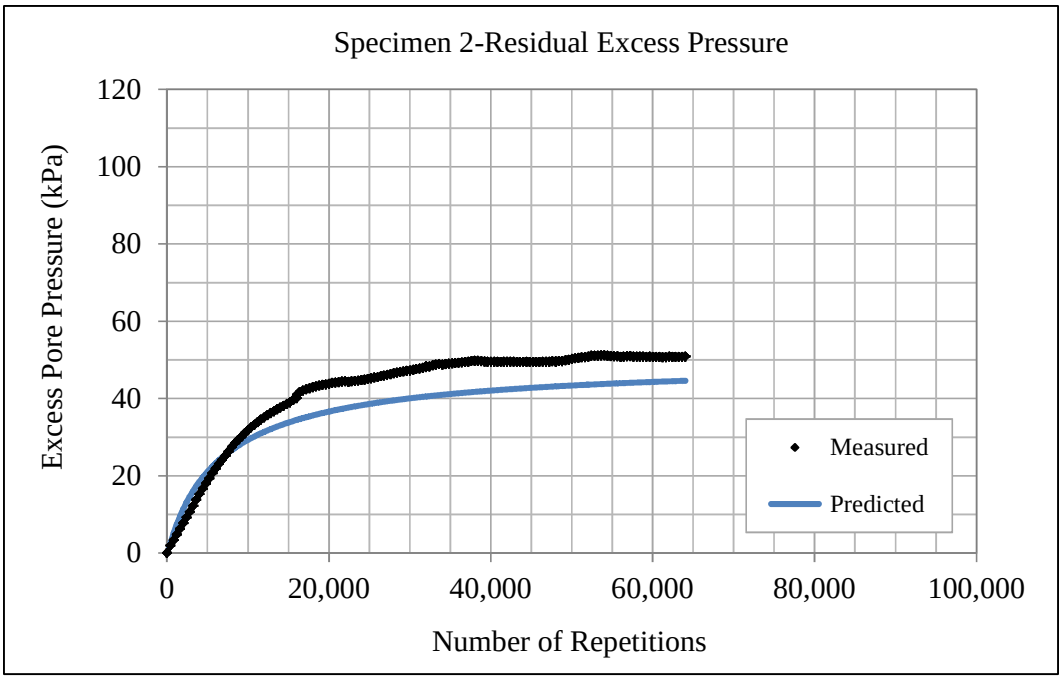
Specimen 2-Residual Excess Pressure
Excess Pore Pressure (kPa)
120
100
80
60
40
20
0
0
20,000
40,000
60,000
80,000
100,000
Number of Repetitions
Measured
Predicted

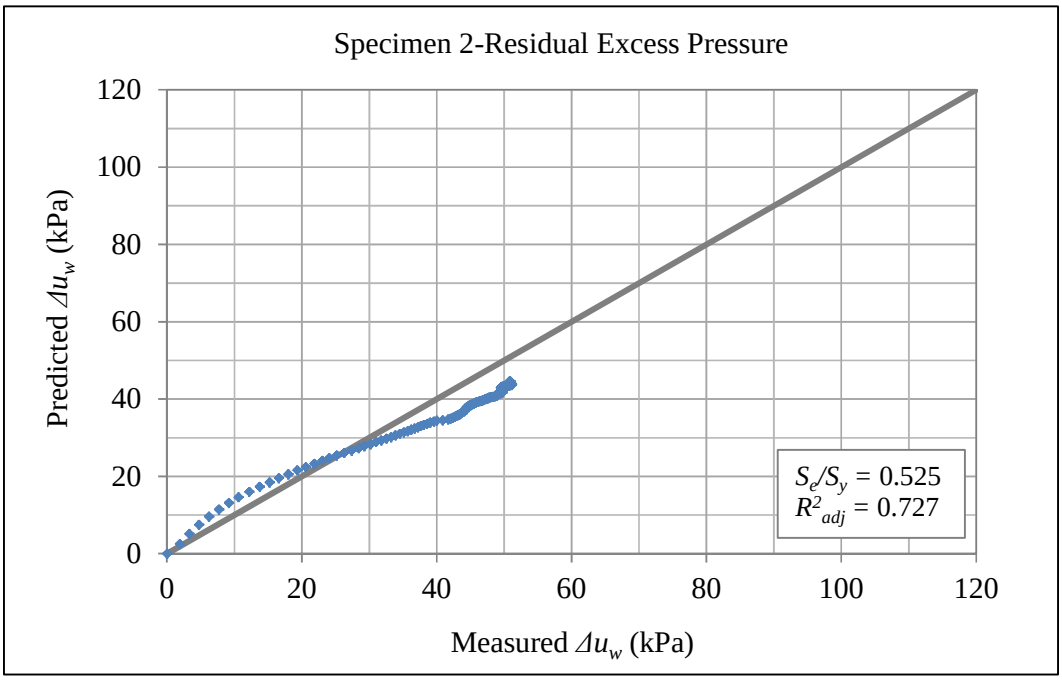
Specimen 2-Residual Excess Pressure
Predicted Δu_w (kPa)
120
100
80
60
40
20
0
0
20
40
60
80
100
120
Measured Δu_w (kPa)
S_e/S_y = 0.525
R^2_{adj} = 0.727

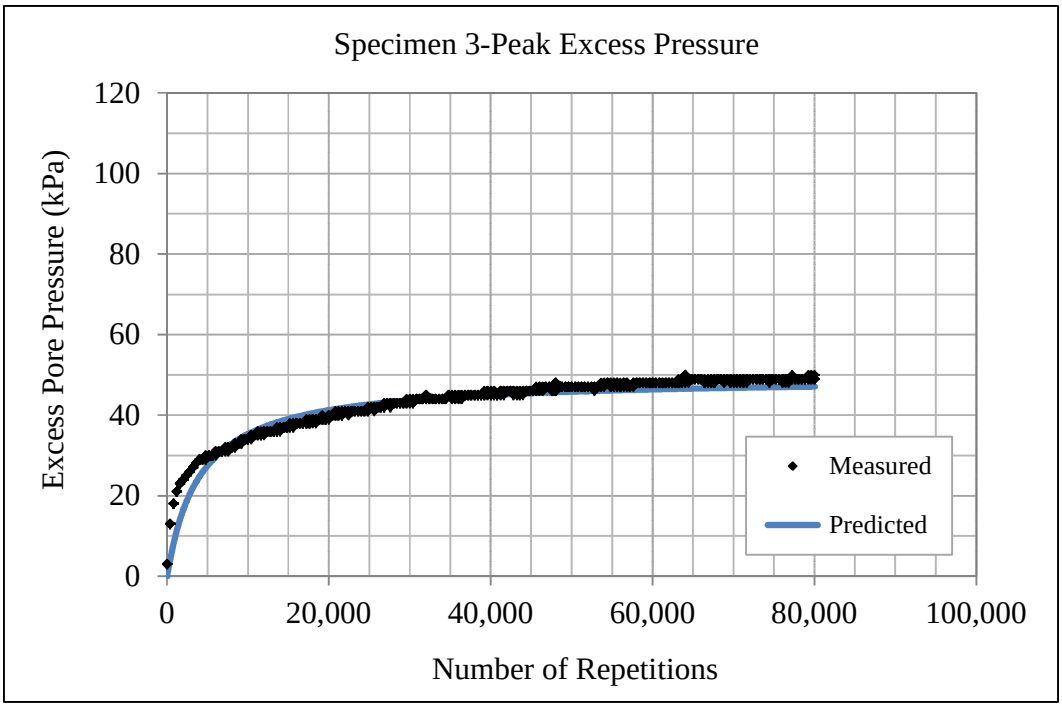
Specimen 3-Peak Excess Pressure
Excess Pore Pressure (kPa)
120
100
80
60
40
20
0
0
20,000
40,000
60,000
80,000
100,000
Number of Repetitions
Measured
Predicted

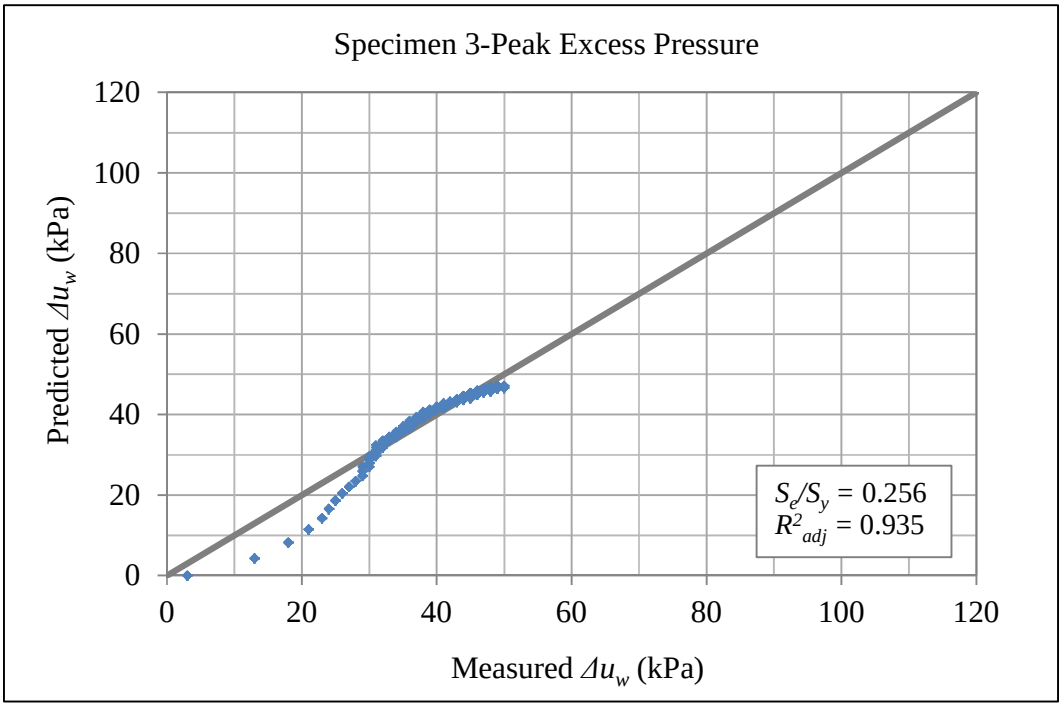
Specimen 3-Peak Excess Pressure
Predicted Δu_w (kPa)
120
100
80
60
40
20
0
0
20
40
60
80
100
120
Measured Δu_w (kPa)
S_e/S_y = 0.256
R²_adj = 0.935

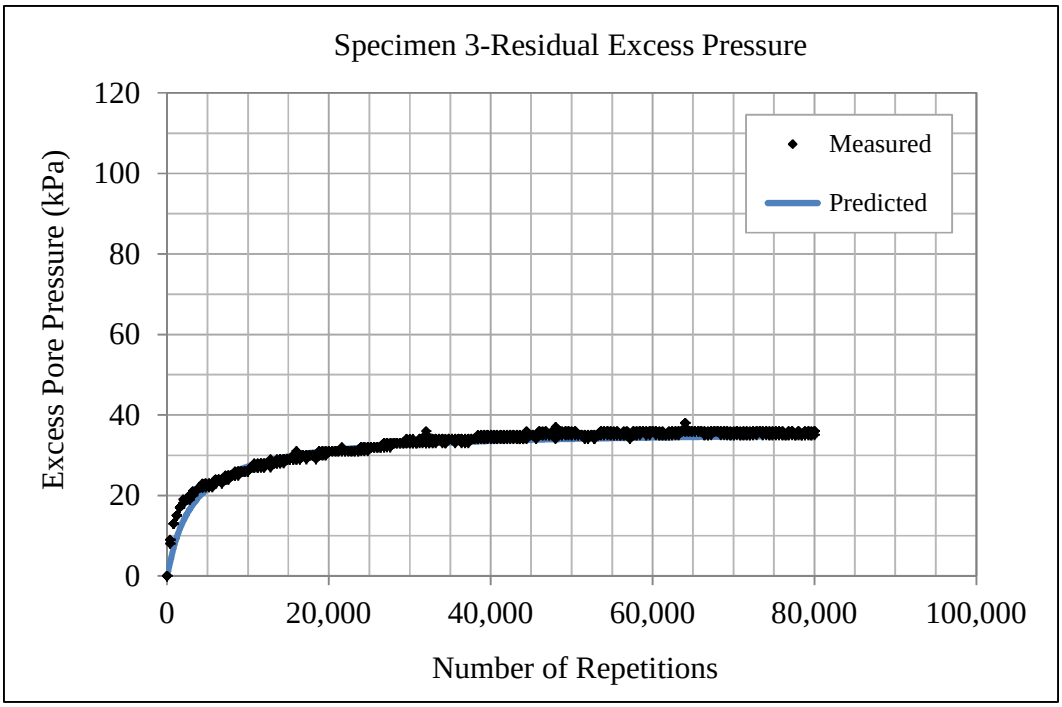
Specimen 3-Residual Excess Pressure
Excess Pore Pressure (kPa)
120
100
80
60
40
20
0
0
20,000
40,000
60,000
80,000
100,000
Number of Repetitions
Measured
Predicted

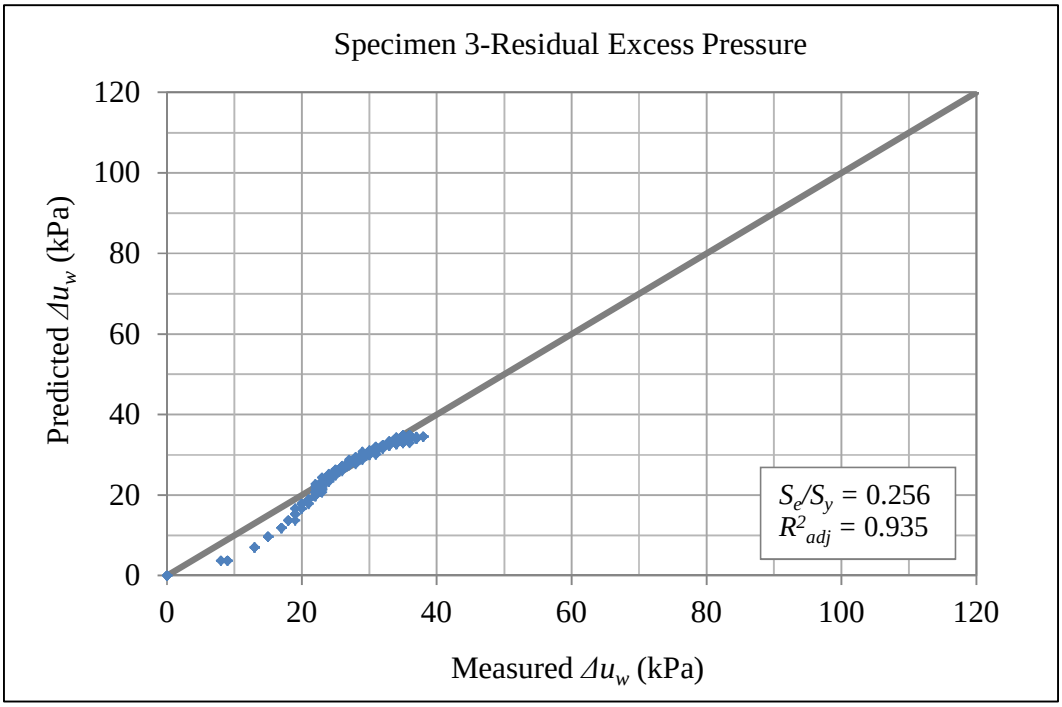
Specimen 3-Residual Excess Pressure
Predicted Δu_w (kPa)
120
100
80
60
40
20
0
0
20
40
60
80
100
120
Measured Δu_w (kPa)
S_e/S_y = 0.256
R²_adj = 0.935

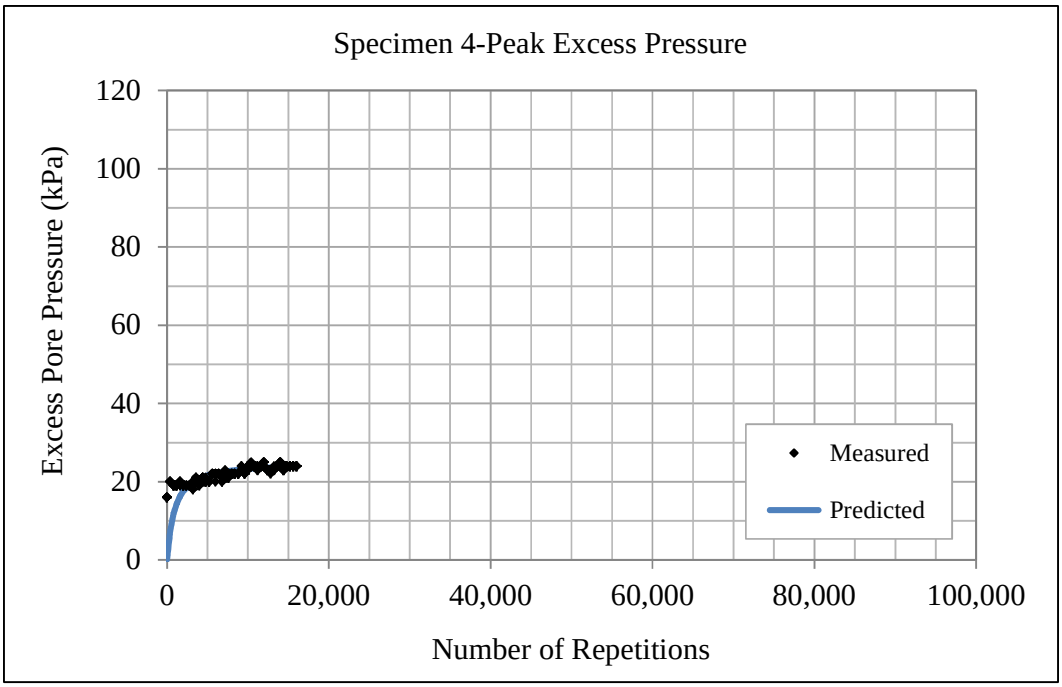
Specimen 4-Peak Excess Pressure
Excess Pore Pressure (kPa)
120
100
80
60
40
20
0
0
20,000
40,000
60,000
80,000
100,000
Number of Repetitions
Measured
Predicted

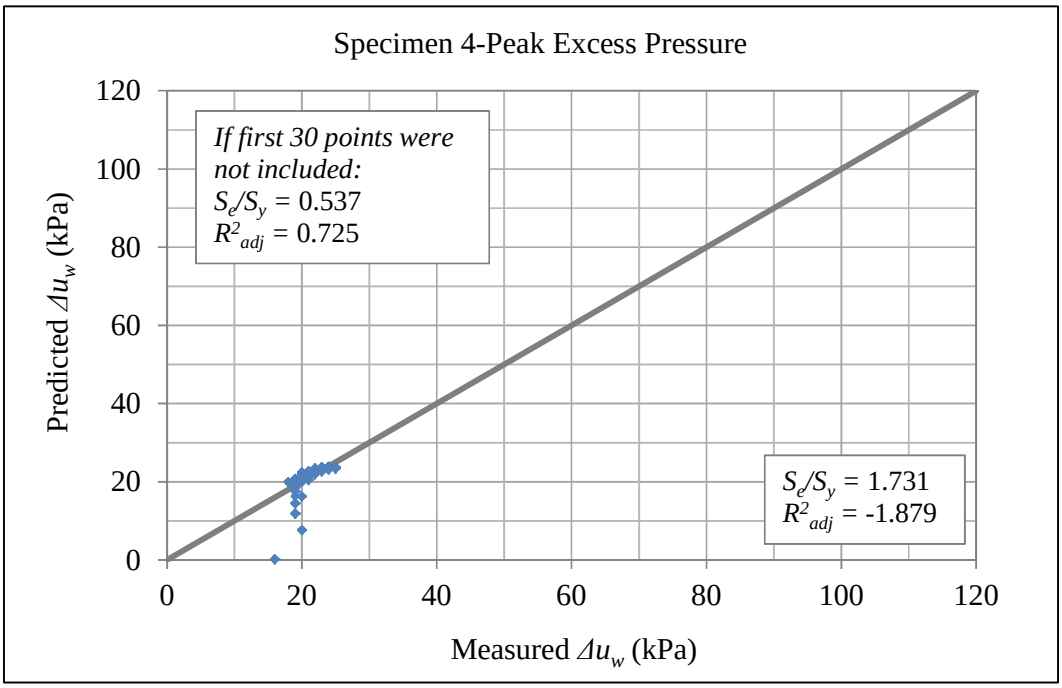
Specimen 4-Peak Excess Pressure
Predicted Δu_w (kPa)
120
100
80
60
40
20
0
0
20
40
60
80
100
120
Measured Δu_w (kPa)
If first 30 points were not included:
S_e/S_y = 0.537
R²_adj = 0.725
S_e/S_y = 1.731
R²_adj = -1.879

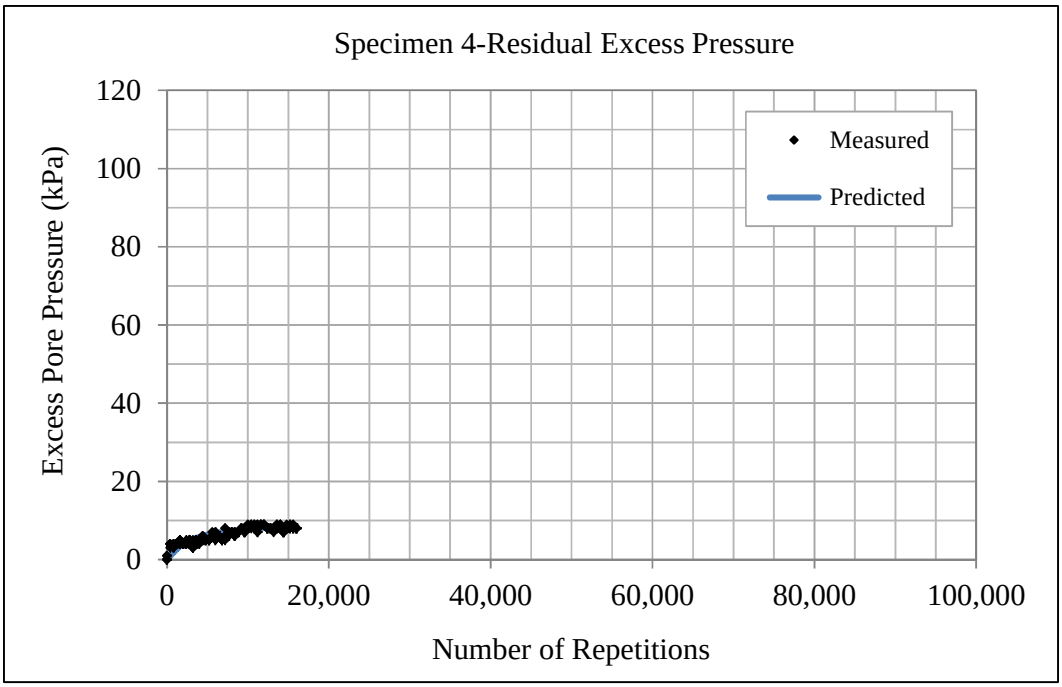
Specimen 4-Residual Excess Pressure
Excess Pore Pressure (kPa)
120
100
80
60
40
20
0
0
20,000
40,000
60,000
80,000
100,000
Number of Repetitions
Measured
Predicted

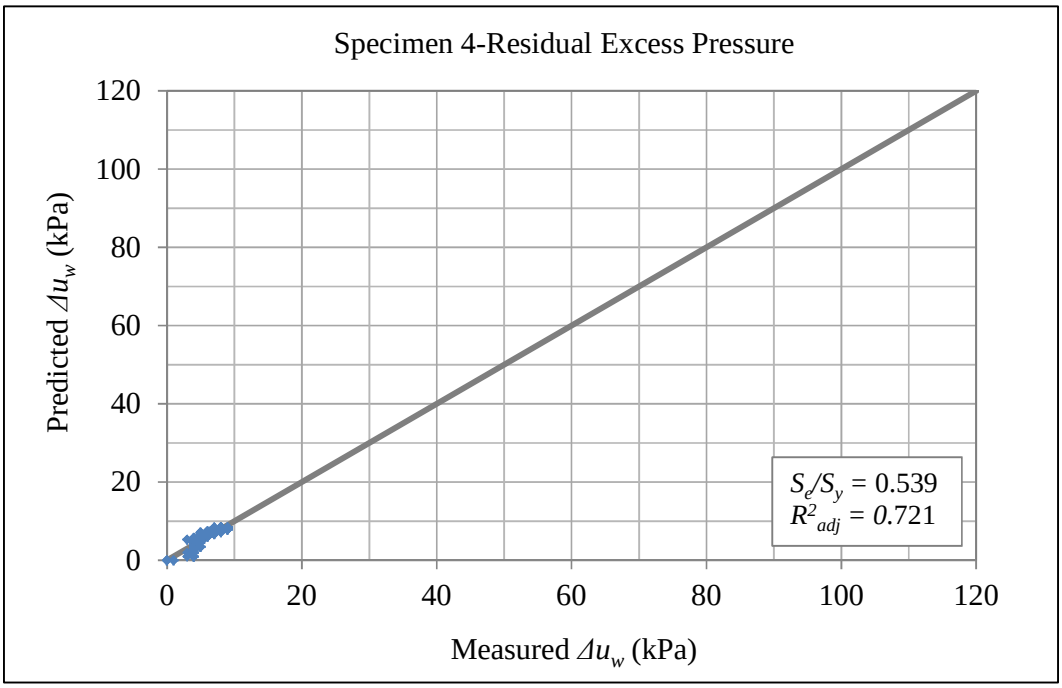
Specimen 4-Residual Excess Pressure
Predicted Δu_w (kPa)
120
100
80
60
40
20
0
0
20
40
60
80
100
120
Measured Δu_w (kPa)
S_e/S_y = 0.539
R²_adj = 0.721

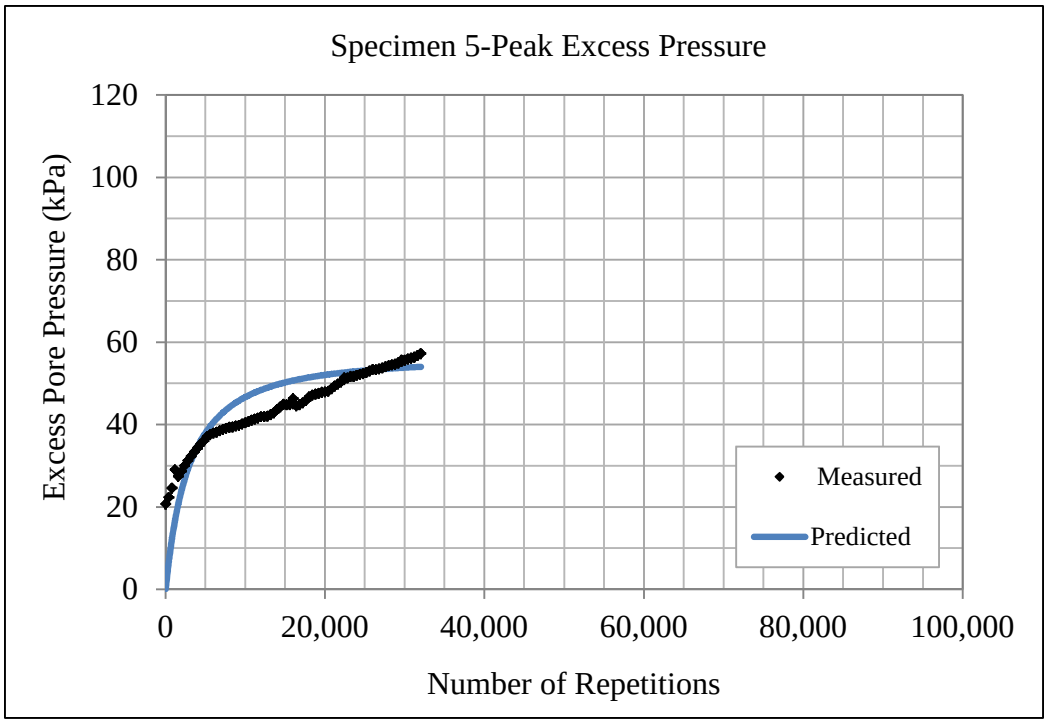
Specimen 5-Peak Excess Pressure
Excess Pore Pressure (kPa)
120
100
80
60
40
20
0
0
20,000
40,000
60,000
80,000
100,000
Number of Repetitions
Measured
Predicted

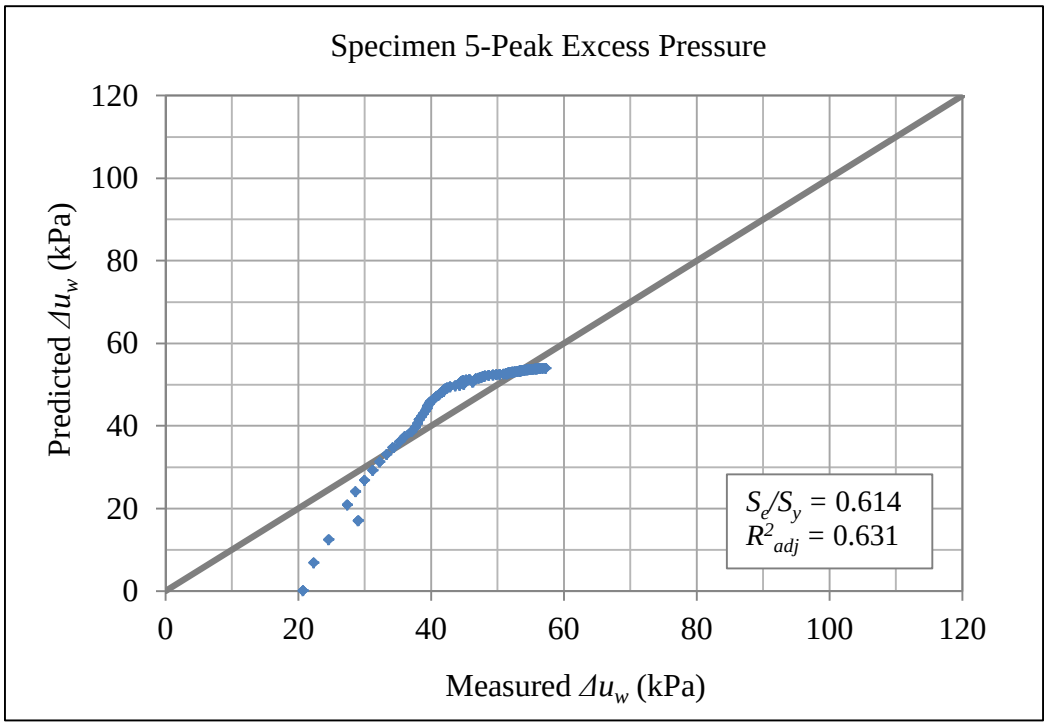
Specimen 5-Peak Excess Pressure
Predicted Δu_w (kPa)
120
100
80
60
40
20
0
0
20
40
60
80
100
120
Measured Δu_w (kPa)
S_e/S_y = 0.614
R²_adj = 0.631

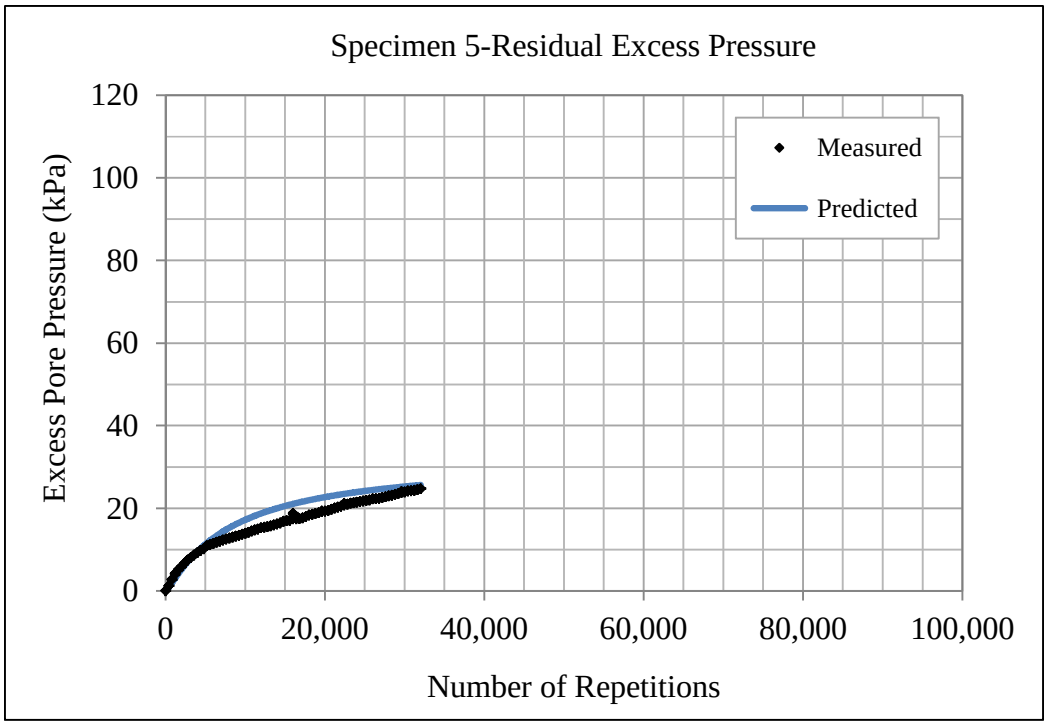
Specimen 5-Residual Excess Pressure
Excess Pore Pressure (kPa)
120
100
80
60
40
20
0
0
20,000
40,000
60,000
80,000
100,000
Number of Repetitions
Measured
Predicted

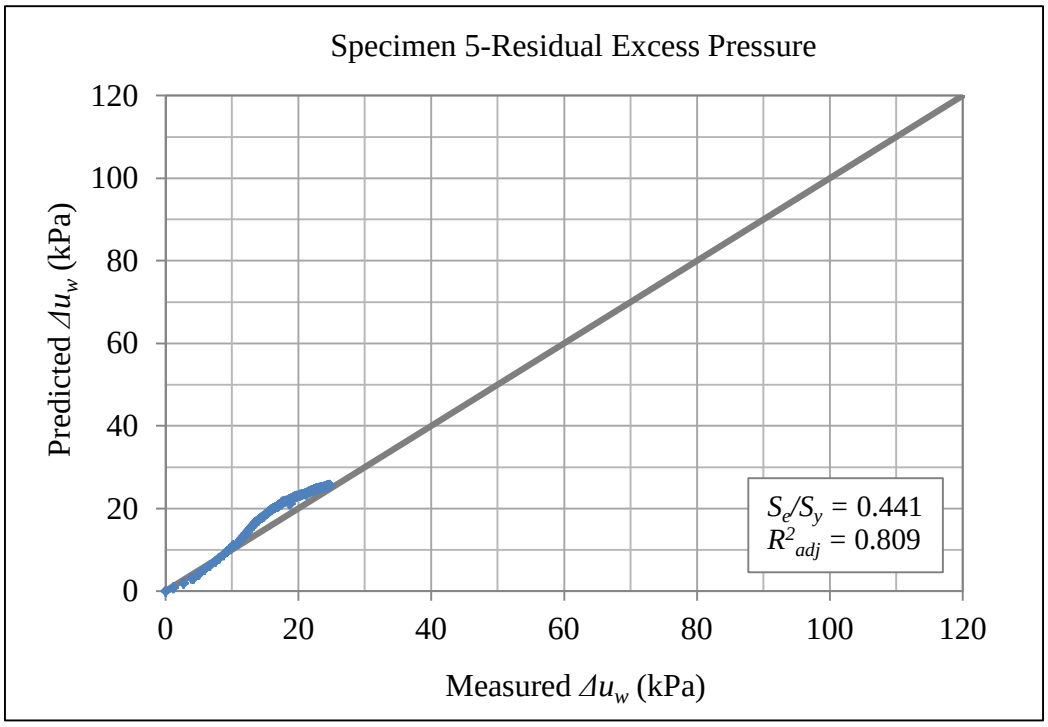
Specimen 5-Residual Excess Pressure
Predicted Δu_w (kPa)
120
100
80
60
40
20
0
0
20
40
60
80
100
120
Measured Δu_w (kPa)
S_e/S_y = 0.441
R²_adj = 0.809

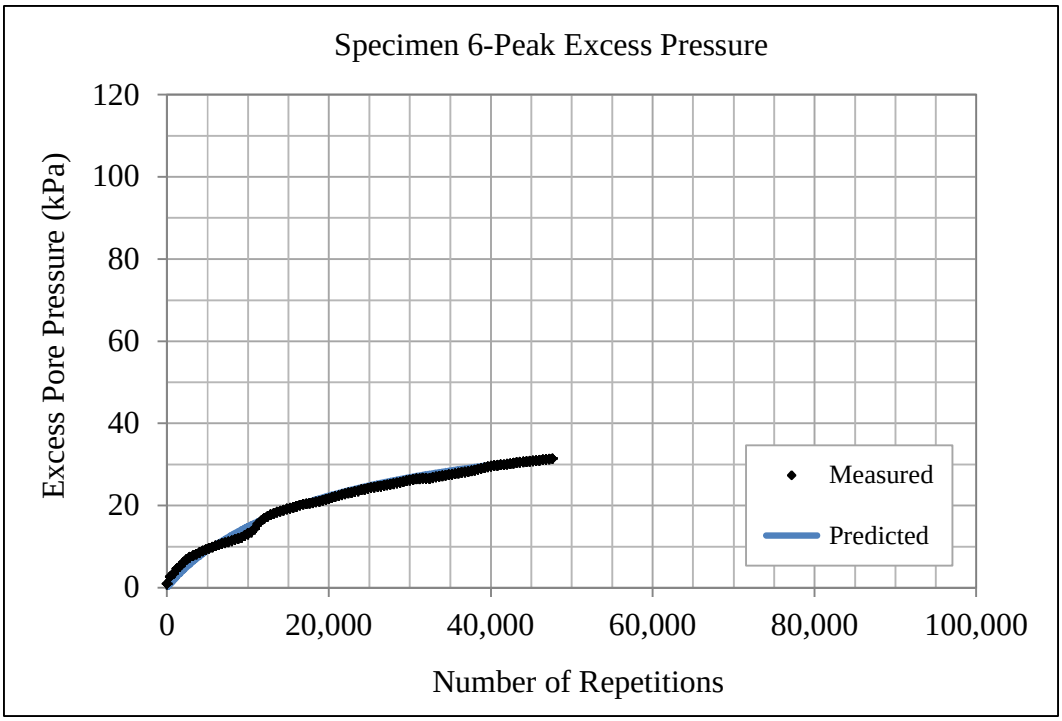
Specimen 6-Peak Excess Pressure
Excess Pore Pressure (kPa)
120
100
80
60
40
20
0
0
20,000
40,000
60,000
80,000
100,000
Number of Repetitions
Measured
Predicted

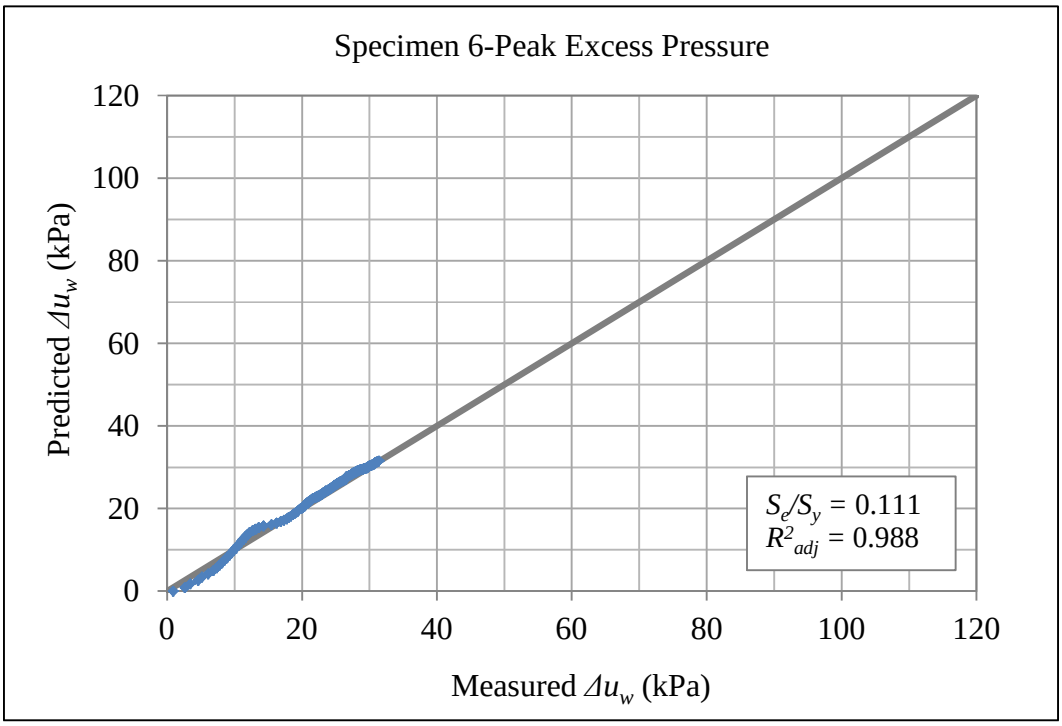
Specimen 6-Peak Excess Pressure
Predicted Δu_w (kPa)
120
100
80
60
40
20
0
0
20
40
60
80
100
120
Measured Δu_w (kPa)
S_e/S_y = 0.111
R²_adj = 0.988

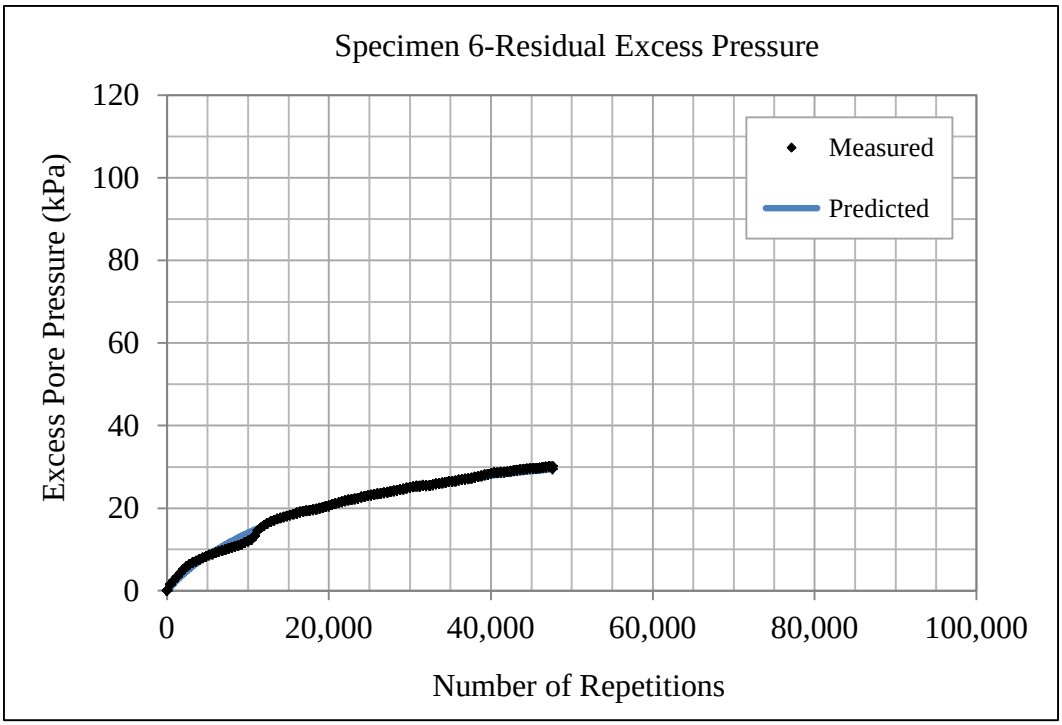
Specimen 6-Residual Excess Pressure
Excess Pore Pressure (kPa)
120
100
80
60
40
20
0
0
20,000
40,000
60,000
80,000
100,000
Number of Repetitions
Measured
Predicted

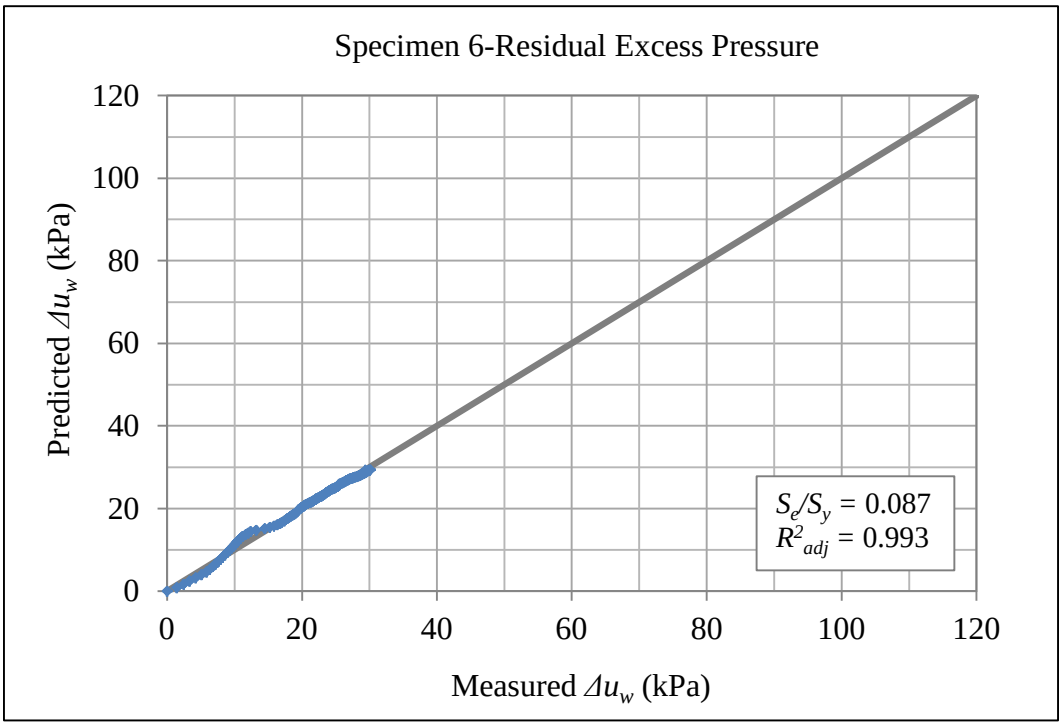
Specimen 6-Residual Excess Pressure
Predicted Δu_w (kPa)
120
100
80
60
40
20
0
0
20
40
60
80
100
120
Measured Δu_w (kPa)
S_e/S_y = 0.087
R²_adj = 0.993

APPENDIX E

EXAMPLE OF EXCESS PORE WATER PRESSURE BUILDUP SIMULATION

Spec.	**1**	
$S\%_{AC}$	75	
$\theta_{net/eff}$	509	
t_D	4	
t_L	1	
β	0.576	
a_1	0.0103	
b_1	388.45	
a_2	0.0107	
b_2	400.26	
a_p	0.009	
b_p	359.2	
M	-0.1697	
N	0.0222	
T	0.576	(Load)
T	4	(Unload)

N	t_p	t_1	t_2	t_2'	*Actual* u_p'	*Actual* u_1'	*Actual* u_2'	λ	p	*Predicted* u_p'	*Predicted* u_1'	*Predicted* u_2'	*Peak* Δu_w	*Residual* Δu_w
1	0.576	1	0	5	0.0016	0.0026	0.0125	0.000	3.324	0.0018	0.00178	0.00053	0.00180	0.00053
2	5.576	6	5	10	0.0030	0.0030	0.0125	1.136	3.324	0.0030	0.00295	0.00089	0.00357	0.00142
3	10.576	11	10	15	0.0045	0.0033	0.0125	2.082	3.324	0.0045	0.00333	0.00100	0.00588	0.00242
4	15.576	16	15	20	0.0059	0.0037	0.0125	2.538	3.324	0.0059	0.00371	0.00111	0.00831	0.00353
5	20.576	21	20	25	0.0073	0.0041	0.0125	2.829	3.324	0.0073	0.00409	0.00123	0.01085	0.00476
6	25.576	26	25	30	0.0087	0.0045	0.0125	3.035	3.324	0.0087	0.00447	0.00134	0.01350	0.00610
7	30.576	31	30	35	0.0102	0.0048	0.0125	3.190	3.324	0.0102	0.00485	0.00146	0.01627	0.00756

N	t_p	t_1	t_2	t_2'	Actual u_p'	Actual u_1'	Actual u_2'	λ	p	Predicted u_p'	Predicted u_1'	Predicted u_2'	Peak Δu_w	Residual Δu_w
8	35.576	36	35	40	0.0116	0.0052	0.0125	3.312	3.324	0.0116	0.00523	0.00157	0.01915	0.00913
9	40.576	41	40	45	0.0130	0.0056	0.0125	3.411	3.324	0.0130	0.00561	0.00168	0.02215	0.01081
10	45.576	46	45	50	0.0144	0.0060	0.0125	3.492	3.324	0.0144	0.00598	0.00180	0.02526	0.01261
11	50.576	51	50	55	0.0159	0.0064	0.0125	3.561	3.324	0.0159	0.00636	0.00191	0.02848	0.01452
12	55.576	56	55	60	0.0173	0.0067	0.0125	3.619	3.324	0.0173	0.00674	0.00202	0.03182	0.01654
13	60.576	61	60	65	0.0187	0.0071	0.0125	3.670	3.324	0.0187	0.00712	0.00214	0.03527	0.01868
14	65.576	66	65	70	0.0202	0.0075	0.0124	3.714	3.324	0.0202	0.00750	0.00225	0.03883	0.02093
15	70.576	71	70	75	0.0216	0.0079	0.0124	3.753	3.324	0.0216	0.00788	0.00236	0.04251	0.02330
16	75.576	76	75	80	0.0230	0.0083	0.0124	3.787	3.324	0.0230	0.00825	0.00248	0.04630	0.02577
17	80.576	81	80	85	0.0244	0.0086	0.0124	3.818	3.324	0.0244	0.00863	0.00259	0.05020	0.02837
18	85.576	86	85	90	0.0259	0.0090	0.0124	3.846	3.324	0.0259	0.00901	0.00271	0.05422	0.03107
19	90.576	91	90	95	0.0273	0.0094	0.0124	3.871	3.324	0.0273	0.00939	0.00282	0.05835	0.03389
20	95.576	96	95	100	0.0287	0.0098	0.0124	3.894	3.324	0.0287	0.00977	0.00293	0.06259	0.03682
21	100.576	101	100	105	0.0301	0.0101	0.0124	3.915	3.324	0.0301	0.01014	0.00305	0.06695	0.03987
22	105.576	106	105	110	0.0316	0.0105	0.0124	3.934	3.324	0.0316	0.01052	0.00316	0.07142	0.04303
23	110.576	111	110	115	0.0330	0.0109	0.0124	3.952	3.324	0.0330	0.01090	0.00327	0.07600	0.04630
24	115.576	116	115	120	0.0344	0.0113	0.0124	3.969	3.324	0.0344	0.01128	0.00339	0.08070	0.04968
25	120.576	121	120	125	0.0358	0.0117	0.0124	3.984	3.324	0.0358	0.01166	0.00350	0.08551	0.05318
26	125.576	126	125	130	0.0372	0.0120	0.0124	3.998	3.324	0.0372	0.01203	0.00361	0.09043	0.05680
27	130.576	131	130	135	0.0387	0.0124	0.0124	4.011	3.324	0.0387	0.01241	0.00373	0.09547	0.06052
28	135.576	136	135	140	0.0401	0.0128	0.0124	4.023	3.324	0.0401	0.01279	0.00384	0.10062	0.06436
29	140.576	141	140	145	0.0415	0.0132	0.0124	4.035	3.324	0.0415	0.01317	0.00395	0.10588	0.06831
30	145.576	146	145	150	0.0429	0.0135	0.0124	4.045	3.324	0.0429	0.01354	0.00407	0.11125	0.07238

N	t_p	t_1	t_2	t_2'	*Actual* u_p'	*Actual* u_1'	*Actual* u_2'	λ	p	*Predicted* u_p'	*Predicted* u_1'	*Predicted* u_2'	*Peak* Δu_w	*Residual* Δu_w
1,000	4995.576	4996	4995	5000	1.3463	0.3488	0.0097	4.427	1.125	1.3463	0.34877	0.00996	12.28	10.95
1,001	5000.576	5001	5000	5005	1.3476	0.3491	0.0097	4.427	1.124	1.3476	0.34909	0.00996	12.29	10.96
1,002	5005.576	5006	5005	5010	1.3489	0.3494	0.0097	4.427	1.124	1.3489	0.34941	0.00995	12.31	10.97
1,003	5010.576	5011	5010	5015	1.3501	0.3497	0.0097	4.427	1.124	1.3501	0.34972	0.00995	12.32	10.98
1,004	5015.576	5016	5015	5020	1.3514	0.3500	0.0097	4.427	1.123	1.3514	0.35004	0.00995	12.33	10.99
1,005	5020.576	5021	5020	5025	1.3527	0.3504	0.0097	4.427	1.123	1.3527	0.35035	0.00994	12.34	11.00
1,006	5025.576	5026	5025	5030	1.3539	0.3507	0.0097	4.427	1.123	1.3539	0.35067	0.00994	12.35	11.01
1,007	5030.576	5031	5030	5035	1.3552	0.3510	0.0097	4.427	1.122	1.3552	0.35099	0.00994	12.36	11.02
1,008	5035.576	5036	5035	5040	1.3564	0.3513	0.0097	4.427	1.122	1.3564	0.35130	0.00993	12.37	11.03
1,009	5040.576	5041	5040	5045	1.3577	0.3516	0.0097	4.428	1.121	1.3577	0.35162	0.00993	12.38	11.04
1,010	5045.576	5046	5045	5050	1.3590	0.3519	0.0097	4.428	1.121	1.3590	0.35193	0.00993	12.39	11.05
1,011	5050.576	5051	5050	5055	1.3602	0.3522	0.0097	4.428	1.121	1.3602	0.35225	0.00992	12.41	11.06
1,012	5055.576	5056	5055	5060	1.3615	0.3526	0.0097	4.428	1.120	1.3615	0.35257	0.00992	12.42	11.07
1,013	5060.576	5061	5060	5065	1.3628	0.3529	0.0097	4.428	1.120	1.3628	0.35288	0.00992	12.43	11.08
1,014	5065.576	5066	5065	5070	1.3640	0.3532	0.0097	4.428	1.120	1.3640	0.35320	0.00991	12.44	11.09
1,015	5070.576	5071	5070	5075	1.3653	0.3535	0.0097	4.428	1.119	1.3653	0.35351	0.00991	12.45	11.10
1,016	5075.576	5076	5075	5080	1.3665	0.3538	0.0097	4.428	1.119	1.3665	0.35383	0.00991	12.46	11.11
1,017	5080.576	5081	5080	5085	1.3678	0.3541	0.0097	4.428	1.118	1.3678	0.35414	0.00991	12.47	11.12
1,018	5085.576	5086	5085	5090	1.3691	0.3545	0.0097	4.428	1.118	1.3691	0.35446	0.00990	12.48	11.13
1,019	5090.576	5091	5090	5095	1.3703	0.3548	0.0097	4.428	1.118	1.3703	0.35477	0.00990	12.50	11.13
1,020	5095.576	5096	5095	5100	1.3716	0.3551	0.0097	4.428	1.117	1.3716	0.35509	0.00990	12.51	11.14
1,021	5100.576	5101	5100	5105	1.3729	0.3554	0.0097	4.428	1.117	1.3729	0.35540	0.00989	12.52	11.15
1,022	5105.576	5106	5105	5110	1.3741	0.3557	0.0097	4.428	1.116	1.3741	0.35572	0.00989	12.53	11.16
1,023	5110.576	5111	5110	5115	1.3754	0.3560	0.0097	4.428	1.116	1.3754	0.35603	0.00989	12.54	11.17